ROZPRAWA
DOKTORSKA

Dynamic control of electrostatic interactions in soft matter systems via application of external electric fields

Tomasz Szymborski

Supervisor:

dr hab. Piotr Garstecki, prof. IChF PAN

Ph.D. dissertation

prepared within the International Ph.D. in Chemistry Studies

at the Institute of Physical Chemistry of the Polish Academy of Sciences

ul. Kasprzaka 44/52, 01-224 Warszawa

Warsaw, May 2012

I would like to start by thanking my supervisor, dr hab. Piotr Garstecki, whose knowledge, enthusiasm and advice guided me throughout the research.

I would like to sincerely thank Professor Robert Hołyst for the opportunity of working in the Department of Soft Condensed Matter and providing me with interesting subject of work.

I would like to thank dr hab. Marcin Fiałkowski for numerical calculations of electric field in my free-standing smectic films experiment.

I would also like to express special thankfulness to dr hab. inż. Jan Tobiś, for developing an electro-hydrodynamical model and devoting long hours of discussions to my work. Moreover, I would like to thank dr Piotr Korczyk for image analysis in the electro-coalscence project.

Finally, I would like to acknowledge dr Carlos Drummond from CRPP-CNRS, Bordeaux, France for introducing me to the Surface Force Apparatus method.

Many thanks go to all, former and current, members of the Department of Soft Condensed Matter for their help and support during my Ph.D. studies.

List of publications from Ph.D. research

1. **T. Szymborski**, P. Korczyk, R. Hołyst and P. Garstecki

„Ionic polarization of liquid-liquid interfaces; dynamic control of the rate of electro-coalescence”

Applied Physics Letters, 99, 094101, 2011

2. **T. Szymborski**, O. Cybulski, I. Bownik, A. Żywociński, S. A. Wieczorek, M. Fiałkowski, R. Hołyst, and P. Garstecki

“Dynamic charge separation in a liquid crystalline meniscus”

Soft Matter, 2009, **5**, p. 2352-2360

3. M. Hashimoto, S. S. Shevkoplyas, B. Zasońska, **T. Szymborski**, P. Garstecki, G. M. Whitesides

„Formation of bubbles and droplets in parallel, coupled flow-focusing geometries”

Small, Vol. 4, (10), 2008, p. 1795-1805

4. N. Zięba cz, S. A. Wieczorek, **T. Szymborski**, P. Garstecki, R. Hołyst

„Thousand fold accelaration of phase separation of polymer-liquid crystal blends upon application of low frequency oscillating electric field”

ChemPhysChem, 2009, **10**, p. 2620-2622

List of publications

1. H.-G. Li, S. A. Wieczorek, X. Xin, T. Kalwarczyk, N. Zięba cz, **T. Szymborski**, R. Hołyst, J.-C. Hao, E. Górecka, D. Pociecha

“Phase Transition in Salt-Free Catanionic Surfactant Mixtures Induced by Temperature”

Langmuir, 26, 1, 2010, p. 34-40

2. X. Xin, H.-G. Li, S. A. Wieczorek, **T. Szymborski**, E. Górecka, D. Pociecha, R. Hołyst

“Incorporation of Carbon Nanotubes into lyotropic liquid crystal by phase separation in the presence of hydrophilic polymer”

Langmuir, 26, 5, 2010, p. 3562-3568

3. M. J. Woźniak, J. Ryszkowska, **T. Szymborski**, G. Chen, T. Tateischi, K. J. Kurzydłowski

“Application of phase imaging and force manipulation mode for description of dispersion of carbon nanotubes in polyol matrix”

Materials Science-Poland, Vol. 26, No. 1, 2008, p. 245-253

4. J. Ryszkowska, M. Jurczyk-Kowalska, **T. Szymborski**, K. J. Kurzydłowski

“Dispersion of carbon nanotubes in polyurethane matrix”

Physica E: Low-dimensional Systems and Nanostructures, (39), 2007, p. 124-127

List of patent applications

1. R. Hołyst, N. Ziębacz, S. A. Wieczorek, **T. Szymborski**, P. Garstecki

„Sposób przyspieszania separacji faz w układach niejednorodnych, zwłaszcza w układach polimer/ciekły kryształ i polimer/polimer”.

Patent application number: P-385743.

Biuletyn Urzędu Patentowego, 2010, 3, 13.

List of abbreviations and symbols

Abbreviations

5CB	4-cyano-4'-n-pentylbiphenyl
8CB	4-cyano-4'-n-octylbiphenyl
AC	alternative current
DC	direct current
DEP	dielectrophoresis
dyCHASE	dynamic charge separation
EF	electric field
EHD	electro-hydrodynamics
FSSF	free-standing smectic film
LC	liquid crystal
OEF	oscillating electric field
PDMS	poly(dimethylsiloxane)
PC	polycarbonate

Symbols

$\boldsymbol{A}_0$	the radius of non-deformed island
$\boldsymbol{A}$	the length of the A arm
$\boldsymbol{B}$	the length of the B arm
$\boldsymbol{A}_{max}$	maximal value of length of the A arm
$\boldsymbol{B}_{max}$	maximal value of length of the B arm
$\boldsymbol{f}$	frequency
$\boldsymbol{f}_{CR}$	critical frequency
$\boldsymbol{P}$	perimeter of the liquid crystalline island

$\boldsymbol{U}$	voltage
$\boldsymbol{N}$	the number of the arms of deformed island
$\boldsymbol{R}$	a vector with beginning in the center of the island and the end at its edge
$\boldsymbol{t}$	time
$\boldsymbol{T}$	temperature
	the angle between x axis and vector R
$_{D}$	Debye screening length
$^{-1}$	Debye screening length
	electrophoretic mobility

CONTENTS

Chapter 1 Introduction

Soft matter is a term that describes all systems that are neither solid nor liquid (or gas). In many ways these systems are more complex than both liquids and solids. Unlike liquids, they exhibit structure at many different length scales. Unlike solids, because these structures are of scales larger than atomic one, they result from forces that are weaker than inter-atomic or intermolecular electronic potentials and are thus 'softer' and more prone to change – exhibiting a marvelous plethora of symmetries and morphologies of order.

Although this description suggests mysterious and exotic systems, they are as common (or, if we include living systems, more common) than simple liquids and solids. Soft matter systems include:

i) Colloidal suspensions, a suspension of one material in a liquid, solid state or gas,
ii) Emulsions, which are a liquid droplets suspended in other liquid, stabilized by a molecules called surfactants,
iii) Foams, which are air bubbles in a liquid or a solid state (e.g. polymeric or metallic foams),
iv) Polymers – long molecules comprising many repetitive units (mers) – both as a bulk and diluted in a solvent,
v) Surfactants, an amphiphilic molecules which self-organize in water into a complex structures like micelles or tubules,
vi) Liquid crystals, which are a state of matter with a properties between liquid (they flow) and solid state (they show a long-distance arrangement)

All these materials are comprised of structures which are in size between a single nanometers up to a millimeter (this is called a meso-scale). The time scale for this systems obviously differs because of constituents of the soft matter systems are relatively large, thus diffusion processes are slower than in atomic or molecular scale (Brownian time scale for a 1 µm particle suspended in a water is ca. 1 s). A wide range of possible systems, from a liquid crystals up to aerosols, connected with the relatively long timescales gave a great model systems for a physicists, chemists and even biologists.

Science traditionally has focused on the richness of diversity of the equilibrium structures of soft matter, such as various kinds of structure formed in the mixture of water and

surfactants, structures formed in block copolymers, and others. Due to the fact that the systems of soft matter are excellent model systems, for years they are used to study the dynamics of approaching to the equilibrium and to study the processes and stationary states in non-equilibrium systems. These studies have require the provision of energy to these systems in multiple formats – as a mechanical energy (such as by mixing or shear), by stimulating the flow of heat (Benard-Marangoni convection, Rayleigh-Bernard convection) or external magnetic and electrical fields.

One of the areas of growing interest is interaction of the soft matter systems with electric field. They are extremely interesting for the following reasons:

i) electrostatic interactions decay as r^{-1}, (where r is the distance from the charged object). In soft matter systems electrostatic interactions are screened, so their strength is very strongly dependent on the local structure,
ii) in aqueous environment many soft matter systems gets its functional, structural and dynamical properties due to electrostatic charge on its surface. Many suspensions are stabilized by short-range repulsive interaction arising from the dissociation of electrical charges on the surface of colloids (micelles, lipid membranes, proteins, etc).
iii) all aqueous environment are in fact electrolyte solutions (they contain ions, even if the water is deionized, due to contamination from the tank or the air). In such a case all charged species are screened by a counter-ions. The fact of screening of charged objects with counter-ions has a huge impact on dynamics of many objects like colloids, DNA, proteins or polyelectrolytes. Moreover, aqueous environment is a natural place for live organisms, therefore studying behavior of electrolyte solutions give us a better understanding of biological systems, i.e. charged DNA strands, cell membranes and proteins,
iv) a large number of techniques involving charged objects (i.e. ions, proteins) found applications as the analytical techniques (capillary zone electrophoresis, gel electrophoresis) or in industry,
v) electrostatic interactions are the strongest in the universe yet simultaneously easy to apply and tune in the laboratory practice. The strength and shape of electric field can be easily changed by the geometry of the electrodes. The electric field can be both constant or oscillating, what gives a wide area of new phenomena (i.e. dielectrophoretic effect for frequencies of MHz)

One of the most striking phenomenon is behavior of ions in an electrolyte solution. When charged objects are placed into an electrolyte solution (i.e., a glass plate or colloids particles in water) ions with charge opposite to the charge of the surface will be attracted to the surface, whereas the ions with the same charge will be repelled. Counter-ions bind to the

surface. As a consequence of attraction and repelling of ions from the electrolytic solution and the charged surface, there is a non-uniform distribution of the ions near the surface. A layer of counter-ions will ‘bind’ to the surface due to electrostatic attraction, whereas the concentration of the co-ions will be close to zero. This phenomenon is known as a double layer. At the distance sufficiently away from the surface the electro-neutrality is established. In reality this layer of counter-ions is affected with a thermal motion, forming a diffuse double layer.

The counter-ions near the charged surface screen the electrostatic interactions between the objects. With the screening of the charge is connected a distance, known as the screening Debye length. This length is in fact a thickness of the electrical double layer. The object can be ‘un-screen’ if the counter-ions move away from the charged surface on the distance of Debye length. This movement can be done with the external electric field – applying the potential opposite to the potential of the surface will repeal counter-ions from the surface. As they reach the Debye length counter-ions will stop the screening of the object (the screening will be smaller during the movement of the counter-ions because of non-equilibrium process).

Changing the spatial distribution of ions from one equilibrium to another distribution takes a finite time. This time is the lesser when:

i) the greater the electrophoretic mobility of the ions (and thus this time is the smaller when the charge of the ions is higher),

ii) the higher the field strength, and

iii) the smaller the hydrodynamic resistance of the ions.

For a fixed set of parameters, there should be a characteristic decay time of the change. Normally macro-charges (e.g., charged colloids, domain boundaries, phase boundaries) are screened in nano-metric lengths, so on the distances larger than the nano-metric the objects do not interact with each other electrostatically.

Even a partial lifting of the effectiveness of screening results in 'switching on' electrostatic interactions between macro-charges at larger distances. This phenomenon may give an opportunity for dynamic control of power and range of electrostatic interactions in soft matter.

This Ph. D. thesis is based on two basic ideas:

i) the characteristic switching time τ is given by the ratio between the Debye screening length and the electrophoretic mobility of the screening ions,

ii) an external electric field oscillating at a frequency lower than $f_{CR}=\tau^{-1}$ causes a momentary and partial lifting of the effectivity of the screening effect. The effect is highest near the critical frequency f_{CR}.

The second assertion follows from the hypothesis that during the movement of ions between the equilibrium positions of ions are not in a position of equilibrium, and so cannot shield macro-charges with the same effectiveness as in equilibrium. Switching the polarity of the external electric field close to the critical frequency (f_{CR}) should cause 'blurring' of clouds shielding and the most effective reduction of shielding effectiveness. In fact, the hypothesis is confirmed by results of experiments performed in the course of their doctoral dissertation. In particular:

i) In the first set of experiments we used a free-standing smectic film in external electric field. The experiments were conducted for two different geometries. The first experiment was performed for the needle pierced through the free-standing smectic film, therefore around the needle I obtained a meniscus. In the second experiment on the FSSF I created an ‘island’ – a circular and thicker part of the film than the rest. On the border, both meniscus and island, there is a circular dislocation due to the jump of the thickness between the meniscus/island and the rest of the film. Liquid crystals used in experiments contained an ionic impurities (residues from organic synthesis, contaminations from the air, bottle etc.). Without external electric field and for electric field oscillating with high frequencies (i.e. f > 1 kHz) the ions are delocalized in the all island. Equilibrium distribution of ions causes that the system (FSSF with meniscus or island) is electrically neutral (for large frequencies the ions oscillate around the equilibrium positions). When the oscillations of the electric field are equal or lower than ‘critical’ the ions start to move due to force which is the effect of acting of electric field on the charges ion. When the ions—close to the dislocation line—separate over the Debye length (λ_D) they start to charge the boundary of the meniscus/island. As the frequency of the electric field is lowering, the time of acting on the ions on the border of meniscus/island increase – the ions cannot relaxate to the previous equilibrium distribution. As the result ions (negative or positive) create a localized,

macroscopic area. Such a separation of ions in external, radial oscillating electric field created an electro-hydrodynamic (EHD) instability. This EHD instability is visible as a periodic oscillations of the shape of the meniscus or the island.

I give a qualitative and quantitative description of this phenomena in Chapter 3.1 and detailed, both qualitative and quantitative, description in Chapter 3.2, together with electro-hydrodynamical model. This model was used to assess the induced charge Q and, additionally, to asses value of line tension F_σ of dislocation on the border of the island.

ii) In Chapter 3.3 I demonstrate experiments performed for liquid crystal/polymer system. These experiments were performed by dr Natalia Ziębacz and I will confront the results with the proposed mechanism of dynamic charge separation (dyCHASE) and show that dyCHASE is responsible for the acceleration of the separation process. The system used in experiments comprises of a liquid crystal and a polymer mixed together and heated above the spinodal curve. When mixture is cooled down from one-phase (stable) region to two-phase (unstable) region the spinodal decomposition occurs – it results in creating of domains of liquid crystal in polymer matrix. The size of domains of liquid crystal in polymer matrix can be measured via optical microscope or Static Light Scattering (SLS). In such a system phase separation (merging of the liquid crystal domains) occurs slowly. Application of oscillating electric field to this separated mixture results with an acceleration of phase separation, up to a 1000 times. The influence of electric field on the rate of the separation is a result of movement of ions inside the LC domains: for frequencies equal or lower than critical the ions inside the domain separate on the Debye length and electrostatically charge the domains (the ions cannot move to the polymer matrix due to high difference of viscosity between these two medium). Charged domains attract each other and merge, finally leading to a full phase separation.

This chapter demonstrate that dynamic charge separation (dyCHASE) process proposed in Chapter 3.1 and proved in Chapter 3.2 is universal in its nature.

iii) In Chapter 3.4 I demonstrate experiments on water-in-oil emulsion subjected to oscillating electric field. The goal of this experiment was to verify hypothesis that dyCHASE is a universal mechanism, thus it can be observed in a W/O emulsion. For this experiment I used a microfluidic device where I generated a tens of small water

droplets suspended in oil (hexadecane). I used a wide (5 mm) channel to fill it with water droplets.

The water droplets in oil are stabilized by the surfactants on the interface of water and oil, therefore the emulsion is stable – the time needed to merge water droplets together, thus to perform a phase separation is long. To merge two (or more) water droplets it is possible to polarize them with electric field – polarized droplets start to attract each other till the small amount of oil between them break and droplets merge together. The process overcomes the stabilization of the surfactant molecules.

The process of polarization of the water droplets can be also done due to separation of ions on the interface of water and oil. If the droplet are in electrolyte solution and the oscillating electric field is acting on them, for large frequencies ions are in the equilibrium positions. When the frequency reach the 'critical frequency' the ions will separate over the Debye length and start to charge the boundary of the droplet (as in the liquid crystal/polymer case). Charges water droplets start to attract each other, the thin film of oil becomes thin and when is a few nanometer thick it rupture and tow water droplets merge.

In Chapter 3.4 I will demonstrate that it exists a critical frequency above the rate of the coalescence process is reduced. This decreasing of the rate is related to the separation of the ions for distances shorter than Debye screening length in water. I will demonstrate that polarization of the interface water/oil is connected with the macroscopic charge separation. As a result, the dyCHASE mechanism can be applied to regulate the coalescence process in the microscale.

Chapter 2 Literature review

Chapter 2.1 Soft condensed matter – structure, properties and applications

In Chapter 2.1 I will describe the basic definitions, constituents and notions of soft condensed matter systems. 'Soft matter' encompasses systems that border between the realm of solids and liquids, i.e. systems that are often called complex fluids for exhibiting structure at a range of different length scales at the same time having the consistency of liquids. Another feature of soft materials is the periodicity of the formed structures, typically in the range 1–1000 nm. This range of length is also known as mesoscale. The name originates from the observation that unlike atomic crystals, the soft matter systems often present structures at the length-scales that are intermediate between the microscopic (atomic) and macroscopic scales, i.e. nematic phases are formed by particles ranging from molecules ca. 2–3 nm long up to ca. 300 nm long (Tobacco Mosaic Virus).

While in solid state systems dominant interactions are Columbic, in soft matter the most important are van der Waals interactions (i.e., dipole-dipole - 2 kJ mol^{-1} , dispersion forces - 2 kJ mol^{-1} and dipole-induced dipole - 0.6 kJ mol^{-1}) and hydrogen bond (ca. 20 kJ mol^{-1}). Moreover, even at equilibrium the magnitude of typical interactions between molecules in complex fluid are comparable or slightly larger than k_BT. This is why these systems are called 'soft' - because their structure is fragile and can be easily changed or destroyed by thermal fluctuations or application of external forces or fields.

The most recognizable examples of soft condensed matter systems are:

- *liquid crystals, molecules with a high anisotropy of shape. Used in displays (e.g., computer, watches and calculators),*
- *polymers, polymeric blends and polymer composites. Used in industry as construction and functional materials,*
- *colloidal solutions, a dispersion of one phase in another. Are an objects of interest in pharmaceutical (i.e. drugs) and food industry.*
- *surface active agents, a molecules with hydrophilic an hydrophobic part. Have numerous applications in industry (i.e., paints, shampoos, detergents and oil recovery).*

Soft matter systems surround us everywhere. We know milk, butter, soap and detergents from everyday use. We use liquid crystals to display information on our Liquid Crystalline Displays (LCD) or we use digital watches, calculators and cell phones. We also deal with different gels, foams and huge spectrum of polymers, widely used in modern technology. Much of the food we eat is in fact a soft matter (e.g., butter, yogurts, ice creams, and mayonnaise). In fact, human body is also a remarkable collection of numerous examples of soft matter. Nowadays, we also consider biological matter, i.e., proteins, membranes, DNA and viruses, as a big and important part of soft matter. Thus, the subjects of equilibrium and non-equilibrium properties of soft matter systems is a subject of intensive research in both academic and industrial laboratories.

Soft condensed matter—shortened frequently as soft matter—is often also referred to as a complex fluid. [1] In complex fluids molecules create mesoscopic structures, which affect macroscopic properties of the material. [2] Soft matter is a convenient way to call all materials in states of matter between a solid state and a liquid state. Soft matter systems include:

- Colloidal dispersions, where sub- or micrometer size particles of one phase are dispersed in another. Types of colloidal dispersions include liquid and solid aerosols, foams, emulsions, sols etc.
- Macromolecules, polymer melts or their solutions. Macromolecules are big molecules made of a repeat units. When placed in solution they create a statistical coil.
- Liquid crystals, also known as a fourth state of matter. When molecules possess high anisotropy, which leads to a number of states between solid state and liquid state. The most popular types of phases are: Isotropic (no long-range translational or orientational order, like in a typical liquid), Nematic (the molecules have no long-range transitional order, however they do posses long-range orientational order) and Smectic (molecules are organized in layers, in Smectic A molecules are normal to the layers).
- Surface active agents (or surfactants) are molecules with a hydrophilic ‘head’ and a long hydrophobic ‘tail’. These molecules self-organize, i.e. in a water solution hydrophobic tails are kept far from water by placing them inside a spherical structure – a micelle. For larger concentration molecules create structures called tubules.

According to [3] all soft matter systems have common things, which include:

i) Length scale between atomic and macroscopic sizes. A typical size of a colloidal particle is between 1 nm and 1000 nm, whereas self-assembled structures of surfactants are in scale of tens of nanometers and polymer chains have length between tens and hundreds of nanometers. Moreover, there are different approaches in description of the system for at different length. For instance, the polymer chain at

molecular level is characterized by covalent bonding, steric repulsion (which originates from the Pauli exclusion principle) and hydrogen bonding. When macromolecule is in a solvent the most important are geometrical factors (a high aspect ratio of a molecule) and steric repulsion when parts of the chain are close. Therefore in the scale of the macromolecule the major factors are steric repulsion and conformational entropy of the chain.

ii) The second important aspect is the one concerning the fluctuations and Brownian motion. Colloidal particles, micelles and macromolecules undergo Brownian motion, i.e. they are subjected to random forces from the thermal motion of the surrounding molecules. Typical diffusion coefficients for molecules in liquids and thermotropic LC are $D \approx 10^{-9}$ m^2 s^{-1}, for macromolecules (which dissolved have a shape of a statistical coil) $D \approx 10^{-18}$ m^2 s^{-1}, whereas diffusion coefficient for a micelle in water at room temperature with hydrodynamic radius 10 nm is $D \approx 2 \cdot 10^{-11}$ m^2 s^{-1}. Wide range of diffusion coefficients give us a next tool to tune the experiments on transport of matter, self-organization and others.

iii) The characteristics listed above contribute to the—perhaps most interesting—property of many soft matter systems that they can self assemble into organized structures. Often these structures can be changed by tuning the thermodynamic parameters of the system. Most of soft matter systems are able to move towards equilibrium. The self-assembly take place on the molecular level, yet it results in structures in mesoscale. A noticeable example of such behavior are surfactants which represent a large number of phases. Using self-assembly structures of high complexity can be created without any external fields, using entropy as the main driving force. Soft matter systems create a wide range of phases and it is easy to force and observe transitions between these phases.

iv) Soft matter systems can be used as a model system to examine non-equilibrium phenomena. Because of their structure they can be driven out of equilibrium with a variety of fields, i.e. electric field, magnetic field, light. Simultaneously their dynamics can be observed—with excellent time and spacial resolution—with variety of optical and spectroscopic techniques necessary to determine the dynamics of these processes.

Soft matter systems found wide applications in the laboratories working on the non-equilibrium physics. The understanding of systems which are in a thermal equilibrium is very good, however when a perturbation is applied (a rapid change of temperature, mechanical

perturbation or external field, i.e. electric) the understanding is still a challenging task. The complex fluid systems are excellent objects to investigate for the following reasons:

i) All complex fluid constituents (colloids, macromolecular statistical coils, micelles etc.) are in size between 1 nm and 1000 nm. The highest value of dimension, 1μm, is comparable to the wavelength of visible light. Therefore soft matter can often be easily visualized with the use of optical microscopy. Therefore, it is relatively easy to control and observe experiments conducted with the use of soft matter.

ii) The relaxation time of complex fluid τ_R is the time taken for an object to diffuse over a length scale comparable to its size and it lies in range from 1 ms up to 1 s. These times are modified by interaction (i.e. typical attractions are of the order 1 to $20k_BT$), therefore characteristic times over which non-equilibrium soft matter systems evolve are in range of 1 ms to 1 year. Thus, it is easy to choose a time scales which are most convenient or accessible for us to conduct the experiments.

iii) Relatively high shear stress can be easily achieved, therefore non-equilibrium flow (i.e. suspensions of particles in liquid, liquids with a different densities) can be studies [4].

2.1.1 LIQUID CRYSTALS

Liquids crystals were discovered in the nineteenth century by Friedrich Reinitzer [5]. This new state of matter was called liquid crystal (LC) state, as it posses properties both of a liquid and a solid state.

Liquid crystal can be divided into two main classes: thermotropic liquid crystals and lyotropic liquid crystals. Thermotropic LC are made of pure mesogens and they change phase as the temperature is changing (usually each phase is strictly correlated with a certain range of temperature – see Fig. 3). Lyotropic LC phases formulate in solution and we can regulate the degree of crystallinity by the concentration of the molecules. In this subchapter I will describe only thermotropic LC. A good overview of structure of molecules which create liquid crystalline phases, type of the phases and its application are depicted in Fig. 1.

Only molecules of a specific shape can form thermotropic liquid crystalline phases. The most typical case of LC are the rod-like molecules, which make conventional smectic and nematic phases.

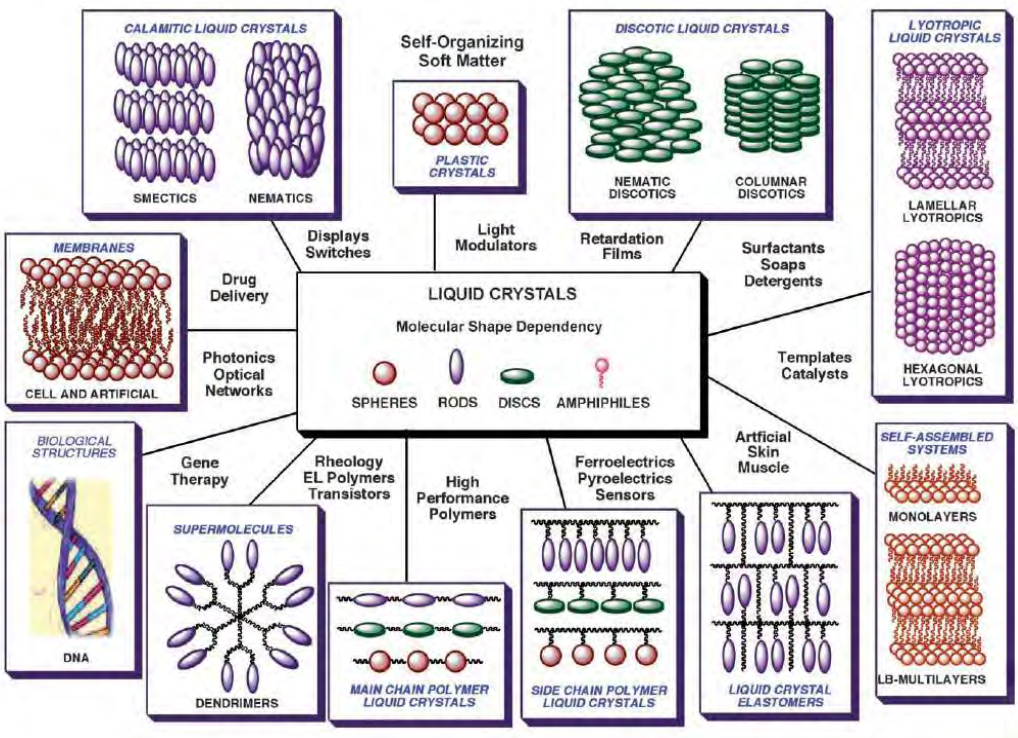

Fig. 1 Classes of liquid crystals according to their molecular structure, phases they create and application [6]

The basic structure of LC is schematically shown in Fig. 2. Typically, molecule has a rigid core made of two or more aromatic rings and linking group between them. At the ends of the molecule we can distinguish a terminal group and a side group.

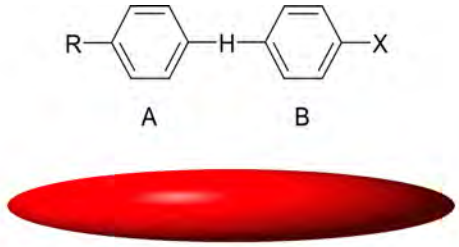

Fig. 2 A schematic picture of liquid crystal molecule. A and B are aromatic rings (rigid core), H is a linking group, X is a side group and R is a terminal group. As the side and terminal group can be long, the aspect ratio of the molecule is high. For this reason such molecules are called rod-like molecules and described in graphic form as prolate spheroid.

Structure of the 4-n-octyl-4-cyanobiphenyl (8CB)—a typical example of rod-like molecule—and its phase transition temperature is shown in Fig. 3. 8CB is a popular LC substrate and one of the best known liquid crystals nowadays.

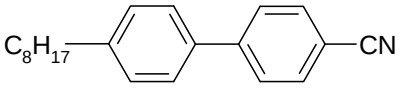

Cr 21.25 ℃ SmA 33.85 ℃ N 40 .85 ℃ I

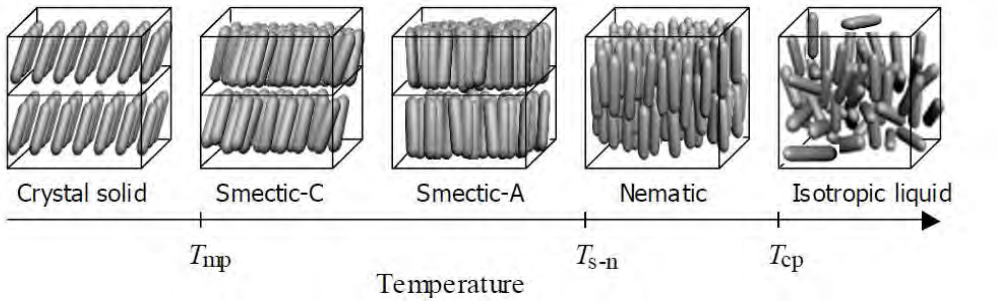

Fig. 3 A chemical structure of 4-n-octyl-4-cyanobiphenyl (8CB) and temperatures of its phase transitions (where Cr – crystalline phase, SmA – Smectic A phase, N – nematic phase and I – isotropic phase). 8CB is a very convenient LC for experiments with SmA since this phase is in room temperature, i.e. between 21.25 ℃ and 33.8 5 ℃.
At the bottom graphical scheme of phase transition of a rod like molecule as a function of temperature (note: 8CB liquid crystal, presented above, does not possess SmC phase). [7]

There are two basic orders of the molecules in materials: positional order and orientational order. The nematic liquid crystal is a phase without any long range translational order. In this phase, molecules tend to be parallel to each other. The preferred direction of parallel orientation is characterized by so called director, denoted by a unit vector *n*. The nematic LC is shown in Fig. 4a. As we decrease the temperature, molecules of LC start to segregate into layers and this is a smectic phase. The smectic phase exhibits a one-dimensional order. Molecules can re-arrange in single layer, yet they cannot 'jump' from one layer to another. There is no correlation in position of molecules between the planes. If molecules are tilted by certain angle we have phase smectic C (SmC) and if they are perpendicular to the plane, it is a Smectic A (SmA) phase (see Fig. 4b and 4c).

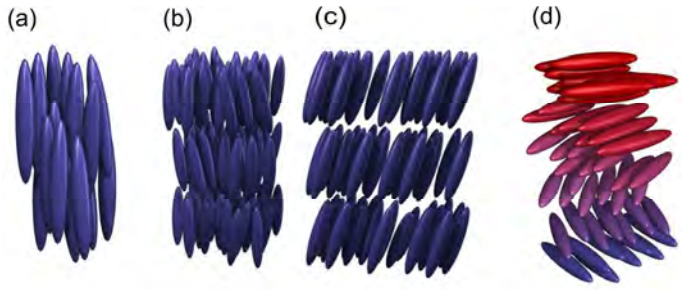

Fig. 4 The most popular phases in rod-like mesogens: (a) nematic (N) phase, (b) smectic A (SmA) phase, (c) smectic C (SmC) phase, (d) cholesteric phase. Source of the pictures: http://barrett-group.mcgill.ca/teaching/liquid_crystal/LC02.htm

If the molecule of LC has a non-symmetrical carbon atoms, the liquid crystal as a phase show a helical structure. The molecules in cholesteric phase (Fig. 4d) are arranged in thin layers, the molecules lie in the layers and are parallel to each other. The director rotates along the helical axis continuously and uniformly.

At the very beginning of research on LC materials people thought that only rod-like molecules can create LC phases. In the sixties, however it was shown that disk-like molecules also show LC phases. Discotic LC are classified, in a simplest way, as columnal phase and nematic phase (see Fig. 5).

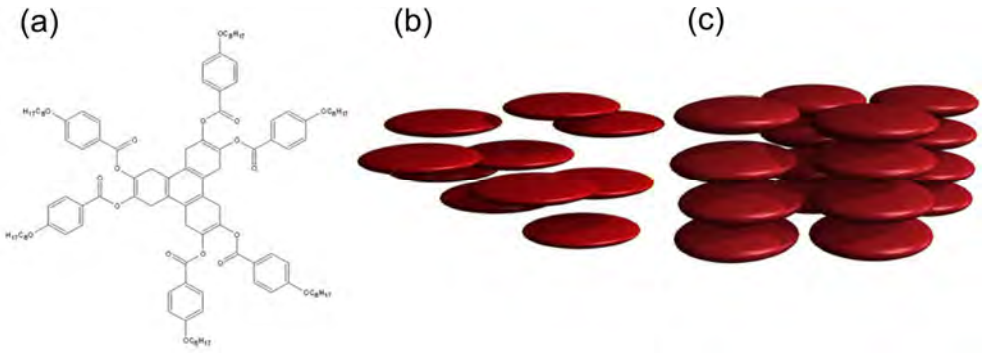

Fig. 5 Structure and phases of disk-like mesogens: (a) a chemical structure of a disc-like molecule, (b) nematic phase, (c) columnar phase. Source of the pictures: http://barrett-group.mcgill.ca/teaching/liquid_crystal/LC04.htm

Orientational order is one of the most important features of LC. Because of it, LC posses anisotropic properties: different responses to external fields (magnetic, electric), shear etc. In rod-like molecules we can consider orientation of the long molecular axis, a unit vector $\hat{a}$ (see Fig. 6). This vector is attached to the molecule and parallel to the long molecular axis. The average orientation of unit vector $\hat{a}$ is defined as:

$$S = \left\langle \frac{1}{2}(3\cos^2\theta - 1) \right\rangle \tag{1}$$

where θ is the angle between the long molecular axis of an individual molecule and the director $\vec{n}$ (Fig. 6).

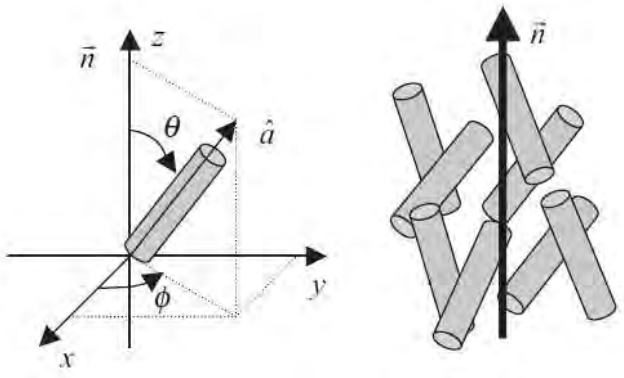

Fig. 6 Diagram showing the orientation of the rod-like molecule and the director $\vec{n}$. [8]

In the isotropic phase, all molecules are oriented randomly and S=0. In an ideal macroscopically ordered nematic LC state:

$$\cos^2\theta = 1$$
$$\therefore S = 1 \tag{2}$$

Liquid Crystals in smectic phase possess an interesting feature: due to their layered structure we can span LC in smectic phase into a free-standing film. First experimental observations of thin films made of thermotropic liquid crystals were performed by Friedel in 1922. [9] Free-standing smectic films (FSSF) are stretched on the stiff frame, usually made of steel or glass, and contacting from both sides with air. Smectic films are usually a few tens on nanometer thick, the thinnest FSSF was two layers of liquid crystal molecule. FSSF are surprisingly stable, they can be pierced with a glass fiber or steel needle without breaking. They can vibrate like a drumhead, their structure can be changed by varying the temperature of environment. We can induce hydrodynamic flows inside the film, or, by applying external electric field, electro-hydrodynamic instabilities. Thermotropic films, while kept under vacuum, can be preserved for months. [10] [9] Free-standing smectic film in two main geometries are depicted in Fig. 7. In Fig. 7a we see FSSF spanned on a circular frame, whereas in the Fig. 7b it is spanned between two parallel edges. Process of spanning depends on the experimental system, but the general idea is the same: a small amount of LC material is placed on the edge of the frame and then a metal or glass slide/spatula moves on the frame creating the film.

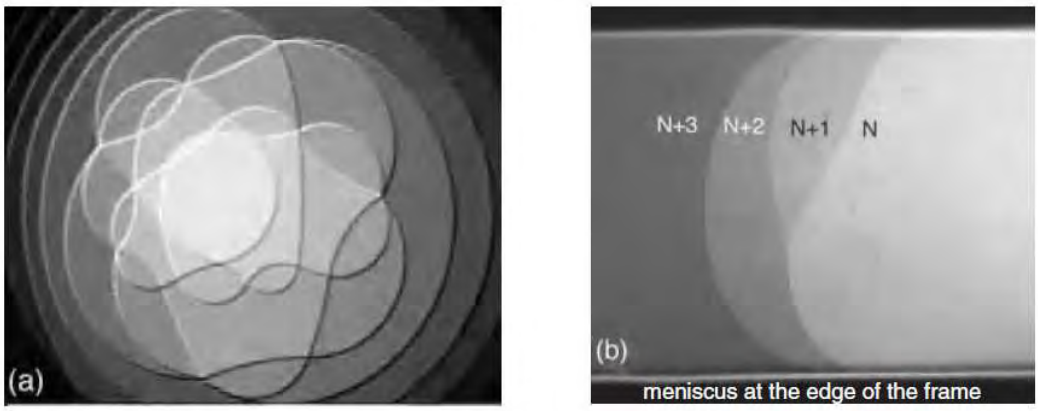

Fig. 7 Free standing films, visualized in reflected light *via* optical microscopy (a) thermotropic liquid crystal of a smectic A (SmA) phase of eutectic mixture S2 (b) lyotropic liquid crystal of a L_α phase of mixture $C_{12}EO_6$ and water. Due to different thickness of the films we observe variation in colors. Each step corresponds to a change in the thickness of the film by one or several molecular layers. [10]

More information about free-standing smectic films will be given in experimental part of this thesis.

2.1.2 COLLOIDAL DISPERSIONS

A colloidal dispersion is a heterogeneous system in which we have two phases: a dispersed one and a continuous one. The term ‘colloid’ usually is applied to a system where dispersed phase is in the size between 50 Å and 50 µm, but this is quite arbitrary. According to the International Union of Pure and Applied Chemistry (IUPAC) the term ‘colloidal’ refers to the system of dispersed particles with a dimensions between 1 nm and 1 µm. [11] Not only spherical but also ellipsoidal particles, platelets and rods can be classified as colloidal system, but only when their dimensions are in the range mentioned earlier. If all particles in the system are of the same size (or almost the same size) the system is called monodisperse, whereas if there are many sizes, then the system is called polydisperse.

A full scope of the colloidal systems and everyday examples is shown in Table 1. We can classify colloids into the dispersion phase and the dispersed phase. When the dispersed phase is a liquid and the dispersion phase is a gas, a colloidal dispersion called ‘liquid areosol’ is created. Since two gases mix together perfectly and create a uniform mixture, there is no possible dispersion in this case.

Table 1. Types of colloidal systems, depending on the dispersed and the dispersion phase, their names and examples from real life. [12]

Dispersed phase	Dispersion medium	Name	Examples
Liquid	Gas	Liquid aerosol	Fogs, sprays
Solid state	Gas	Solid aerosol	Smoke, dust
Gas	Liquid	Foam	Foams
Liquid	Liquid	Emulsion	Milk, mayonnaise
Solid state	Liquid	Sol (colloidal solution)	Colloidal gold
Gas	Solid state	Solid foam	Expanded polystyrene
Liquid	Solid state	Solid emulsion	Opal, pearl
Solid state	Solid state	Solid suspension	Pigmented plastics

Examples of the popular colloidal systems are shown in Fig. 8.

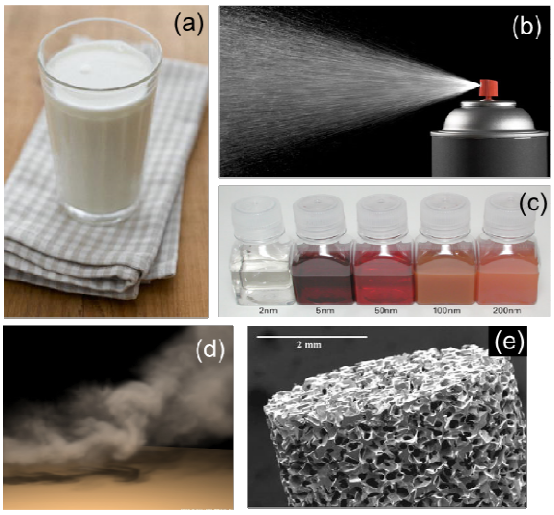

Fig. 8 Different types of colloidal solution are presented above: (a) milk is an emulsion, or liquid-liquid colloid suspension (b) spray is a liquid aerosol, (c) colloidal solution of gold, size of the particles is from 2 nm to 200 nm, (d) smoke is an example of solid aerosol whereas (e) is a metallic foam, an example of solid state and gas colloidal system (source of the pictures: Internet)

Stability of the colloids and DLVO theory

In colloidal systems surface effects, which scale as $\propto r^2$ dominate over the bulk effects, which scale as $\propto r^3$. A good example of that is a sphere with a radius of 1 cm. The surface area of such a sphere is 3.14 cm^2. However, if we put the same amount of material (i.e. latex) into a form of spheres of 0.1 µm in diameter, the surface area of this system will be 314 000 cm^2.

The issue of stability of the colloidal system is therefore obvious. One force which can destabilize colloidal system is the gravity. If particles are denser that the medium they will

sediment to the bottom, however if the medium is denser they will gather on the surface (they will create a 'cream'). As the surface of colloidal system increase, the van der Waals forces dominate and colloidal particles start to aggregate, and as the aggregates increase they sediment on the bottom of the tank. From another point of view, all particles in water solution accumulate a charge, from dissociation of chemical groups or as a result of adsorption of ions from solution. Electrostatic charge and electrochemical double layer at the interface of the particle repeal particles, thus they work against van der Waals attraction forces. The total potential between colloid particles is shown in Fig. 9. Quantitatively, this interplay between attraction and repulsion was described by DLVO (Derjaguin–Landau–Verwey–Overbeek) theory.

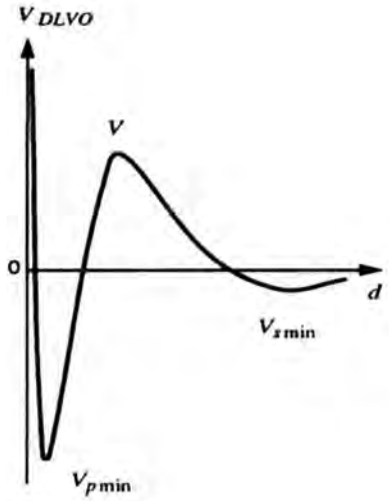

Fig. 9 Total potential in the DLVO theory is a sum of electrostatic interactions and van der Waals forces. [13]

Another way of stabilization of the colloids is steric stabilization, i.e. a surfactant layer on the surface of the colloid, or a thin layer of the polymer. If the polymer is a polyelectrolyte we have the additional electrostatic stabilization. There are also another ways to destabilize the system and to switch from the repulsive to attractive interactions:

- addition of salt to the electrostatically stabilized colloid. Increasing salt solution can reduce Debye screening length, and decrease electrostatic repulsion. As a result, van der Waals attraction forces will dominate,
- in polymerically stabilized colloid addition of a 'poor' solvent. The resulting attractive polymer/polymer interactions will lead to the attraction between particles,
- chemical or physical removal of a stabilizing polymer chains from the surface of particles,
- adding non-adsorbing polymer to cause an increase in size of the depletion interaction.

2.1.3 POLYMERS

Polymers, polymer solutions and mixtures constitute a big class of soft matter. Polymer can be divided into two main groups: natural and synthetic. Natural polymers are DNA, RNA, proteins and polysaccharides (i.e. starch). Synthetic polymers (polyethylene (PE), polypropylene (PP), poly(tetrafluoroethylene) (PTFE or Teflon®) etc.) are used in everyday use.

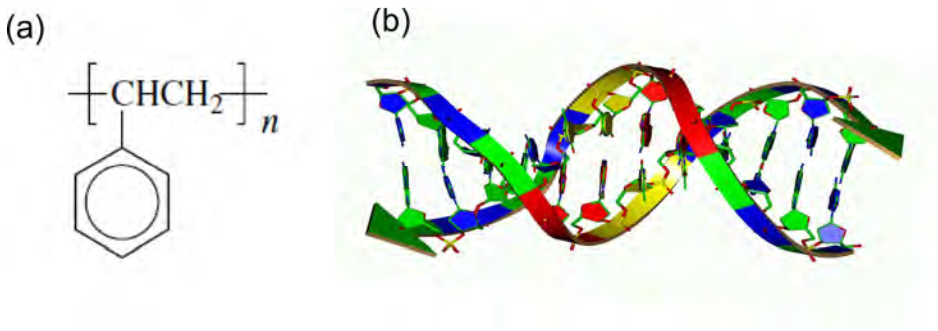

Fig. 10 An example of artificial polymer, polystyrene (PS) (a) and natural polymer (b) (biopolymer), a double DNA strand. In DNA there are four types of repetitive units, which gives two complementary pairs: A-T and C-G. Source of the pictures: Internet

Both types of polymers, natural and synthetic, mixed with a filling material like fibers, particles and clays give a new type of materials called polymer composite. If filling material is nano-sized, this type of material is called polymer nanocomposite.

It is possible to classify polymer by their molecular structure. Polymer can be linear, branched, cross-linked and network polymers. If polymer macromolecule is made of only one type of repetitive unit (A), this is a homopolymer. If we have two or more types of units (A and B), this is a heteropolymer (see Fig. 11)

…A—A—A—A—A—A—A—A—A—A—A…

…A—B—B—A—A—B—A—B—A—B—B…

…A—A—B—B—A—A—B—B—A—A—B…

Fig. 11 Homopolymer (top) with a A mer, and copolymer with random arrangement of units (middle). On the bottom an example of block co-polymer, where instead of statistical arrangement of mers we observe A—A and B—B blocks. In copolymer—in contrary to a homopolymer—two different mers, A and B, create a macromolecule.

Visualization of linear and branched polymers with one type of units is shown in Fig. 12. Each blue dot is a single unit and those polymers are homopolymers.

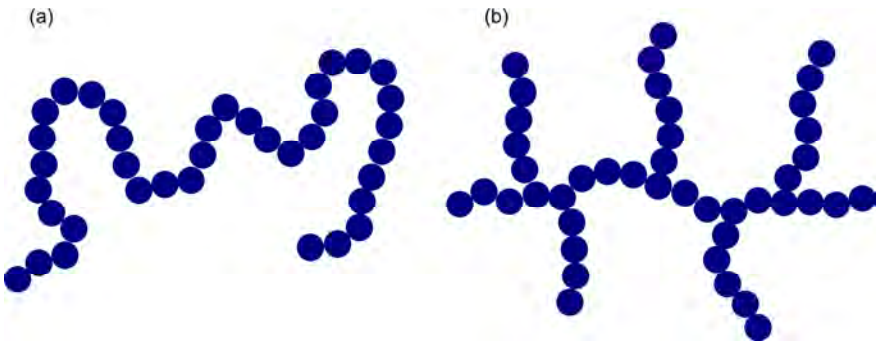

Fig. 12 Schematic representation of linear (a) and branched (b) polymer.

Polymers shows a different physical states according to their temperature. They can be:

i) liquid state – polymer melts and solutions are liquids. To obtain this we have to increase temperature or use—in most cases—organic solvent to dissolve polymers,

ii) glassy state – some polymers, like PS or PMMA do not crystallize but stay in a glassy state,

iii) crystalline state – polymers can crystallize, but very often this crystallization is not complete and we obtain a semi-crystalline material. In such material very small crystals exist in a matrix of amorphous material. Matrix can be in a glassy state or in a liquid-like state,

iv) liquid crystalline – if a polymer is a rigid molecule, it can form a liquid crystalline phase. A good example of liquid crystalline polymer is Kevlar.

An isolated, flexible polymer chain in solution is not a straight molecule (Fig. 13). Its shape become a random coil.

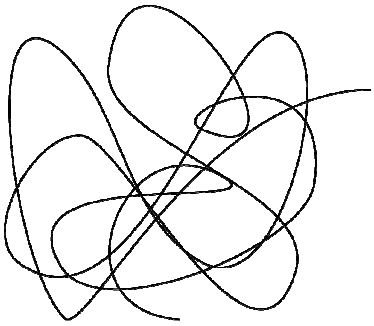

Fig. 13 Random coil of polymer macromolecule in solution.

2.1.4 AMPHIPHILIC MOLECULES AND THEIR SELF-ORGANIZATION

Surfactant molecules are amphiphilic, they have both hydrophilic and hydrophobic moieties (a hydrophilic 'head' and hydrophobic 'tail'). A general and detailed view of chemical structure of surfactant is shown in Fig. 14.

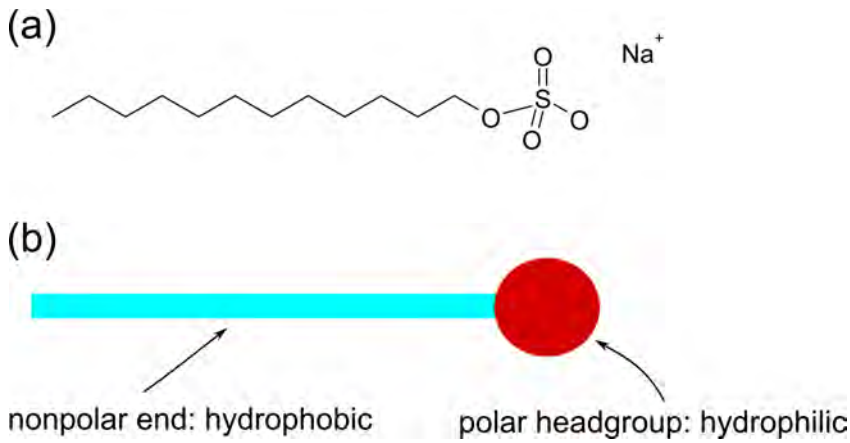

Fig. 14 Chemical structure of surfactant (SDS). Positively charged part of the molecule is called a 'head' and hydrophobic part is a 'tail'.

Ionic surfactants may be divided into two main types: anionic and cationic. Anionic surfactants have a negatively charged head whereas cationic surfactants have a positively charged head. A good example of ionic surfactant is sodium dodecyl sulphate (SDS).

Zwitterionic surfactants contain both positive and negative charges in the structure of the molecule. Usually the positive charges are a result of ionization of ammonium group whereas negative charge are connected with ionization of carboxyl group. Zwitterionic surfactants found application if cosmetic industry as they are non-irritant for skin or eyes.

Next group of surfactants are amphoteric surfactants. They can have either cationic, anionic or zwiterionic properties, depending on the pH of the solution. Moreover, a number of

nonionic surfactant exists. The hydrophilic group is usually a polyether chain, and hydrophobic tail is often an alkyl chain. Particularly important class of nonionic surfactants are fatty alcohol ethoxylates (they are abbreviated to C_mE_n where C stands for methyl and E stands for oxyethylene). The last group constitute lipids. They are a substances of biological origin, which exhibit amphiphilic behavior and possess two or more hydrocarbon tails. They are also a main component of cell membranes. [14] Organization of molecules, for low concentration of surfactants in solution, is shown in Fig. 15.

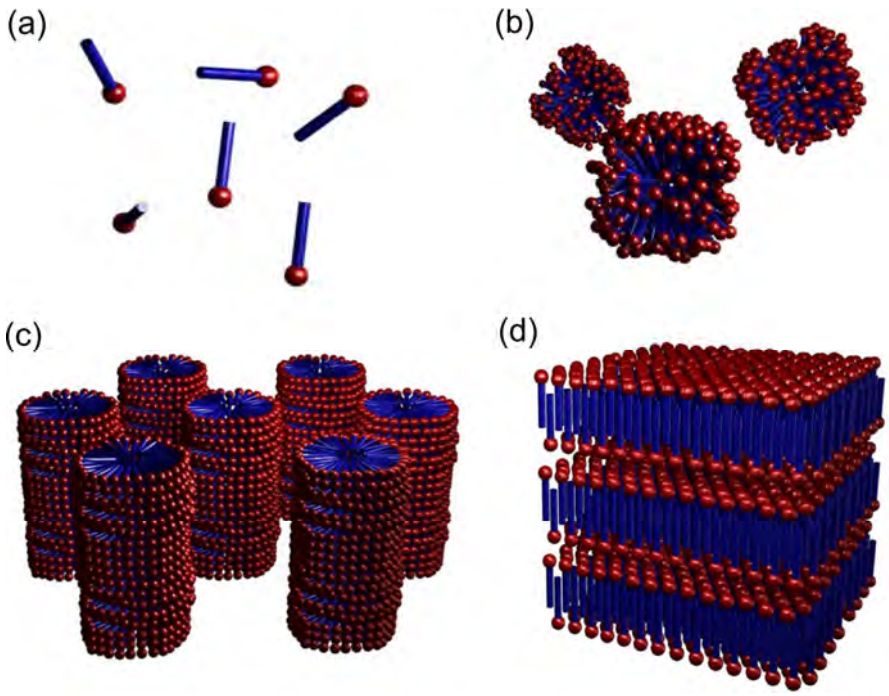

Fig. 15 (a) Amphiphile molecules in aqueous solution below CMC, (b) micelle-a spherical aggregation of molecules. In this case hydrophilic heads are on the outer surface of the micelle, (c) hexagonal structure, (d) lamellar structure: between two layers of surfactant is trapped a thin layer of water. Source of the pictures:
http://barrett-group.mcgill.ca/teaching/liquid_crystal/LC05.htm

Increasing the concentration of surfactant will initiate a start of self-organizing of molecules into a series of regular geometries. This concentration is called Critical Micelle Concentration (CMC). Above that Critical Concentration molecules of surfactant form micelles, i.e. clusters of 50 to 200 molecules. The size of micelle depends on geometric and energetic properties of molecules and the system.

The main structures associated with two-component systems (surfactant and water) are: hexagonal, lamellar and cubic phases (see Fig. 15). The hexagonal phase is composed of a close-packed array of long cylindrical micelles, which are arranged in hexagonal pattern. We distinguish in water a ‘normal’ structure where hydrophilic head is located on the outer

surface of cylinder, or ‘inverted’ when it is opposite. The lamellar phase consists alternating water-surfactant bilayers. The cubic phase is build of small micelles.

The dependency of particular phases on concentration and temperature is shown on the phase diagram (see Fig. 16).

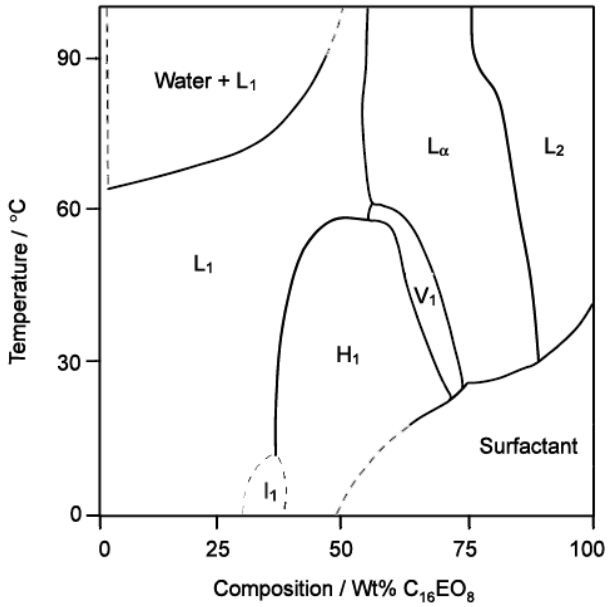

Fig. 16 Phase diagram of the non-ionic surfactant $E_{16}EO_8$. L_1 and L_2 are isotropic solutions, H_1 is hexagonal phase, V_1 is cubic, L_α is lamellar phase. [15]

Surface active agents are main component of detergents. In process of removing of dirt, fatty materials (i.e. dirt, oil and other organic or inorganic materials) are removed from surfaces and dispersed in water. As the dirt is hydrophobic, the long hydrophobic tail of amphiphile attach dirt and remove it from the surface.

Chapter 2.2

Basics of electrostatics and electrodynamics

The purpose of this chapter is to introduce the reader into the basic ideas of electrostatics and electrodynamics. At the very beginning I will present Coulomb's law for identical and different charges. Then, I will present electric field and electrostatic potential around electric charge. Next part of this chapter concerns Gauss's, Laplace's and Poisson's equations. After that I will describe Maxwell's equations which form the basis of electrodynamics. Interaction between charges and dipoles, including Keesom and London forces, are described at the end of this chapter.

Electrostatic interaction between charged particles is one of the fundamental forces of nature (i.e. they are the basis for chemical bonding) and simultaneously is one among the strongest in the Universe. Apart from biological importance (salt water forms the working fluid of living cells, nervous systems works due to ion fluxes and pH and salt regulate the associations of proteins, DNA and biopolymers), these interactions are important in technology and industry. Moreover, that electrostatic interactions in aqueous solutions are a base for corrosion science and engineering.

As a first approximation we can state that there exist four basic laws (or principles) of electrostatics. The first principle is that of charge conservation - it states that the total charge on an isolated body cannot be changed. In other words, for an isolated body eq. 3 is satisfied:

$$\sum Q_i = const. \tag{3}$$

where Q_i is i^{th} charge contained by the body.

The second principle is that charge is 'quantized' in a sense that the total charge on a body is an integral multiple of a fundamental charge. The fundamental elementary charge is the magnitude of a charge carried by an electron, i.e. $1.602 \cdot 10^{-19}$ Coulombs.

The third law is Coulomb's law, which describes the force between two point charges. The phenomenon of attracting or repulsing two objects subjected to rubbing (i.e. amber and fur) was known since ancient Greece. In 18th century it was found (due to series of simple experiments carried out by Benjamin Franklin) that there are two kinds of electric charges: positive and negative. Charles Coulomb (1736-1806) measured the magnitude of the forces between charged objects, with a use of the torsion balance which he invented. From experimental observations he created a dependency:

$$\vec{F} = \frac{1}{4\pi\varepsilon_0}\frac{q_1 \cdot q_2}{r^2} \cdot \hat{r} \tag{4}$$

where:

q_1, q_2 – charge on the examined objects (e.g. ions, spheres),

r – distance between charged objects,

$\hat{r}$ – unit vector directed from q_1 to q_2,

ε_0 – permittivity of free space, 8.85 x 10^{-12} [F·m^{-1}]

The interaction is shown schematically in Fig. 17.

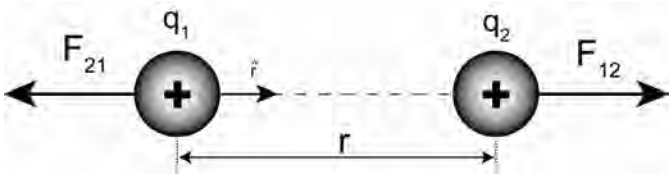

Fig. 17 The visualization of the Coulomb's law for two positive charges: the charge q_1 exerts a force F_{12} on the charge q_2 whereas the charge q_2 exerts a force F_{21} on the charge q_1. The forces are equal, yet the direction is opposite.

Coulomb's law can be also expressed in terms of energy. The law expressed as a potential energy is shown below:

$$U = \frac{1}{4\pi\varepsilon_0}\frac{q_1 \cdot q_2}{r} \tag{5}$$

This law, initially developed and tested for macroscopic objects like glass rods, ebonite rods, silk and fur cloths or charged spheres, in fact applies to a wide range of size scales, like atoms, molecules and biological cells.

Electrostatic interactions are both strong and long-ranged. In fact, the electrostatic repulsion is ca. 10^{36} times stronger than the gravitational attraction between two protons.

Important aspect of electricity is that electric charge is always conserved in isolated system. For instance, when one object is rubbed against another, i.e. glass rod against silk, no electric charge is created in this process. Because of conservation of the charge, electron adds negative charge to the silk and an equal electric charge is left on the glass rod and the value of the charge is constant. Moreover, total charge of the entire Universe is constant – only small local fluctuations are allowed (in other words, no charge can be created or destroyed).

The fourth principle of electrostatics is that of superposition. It states that the force between any two charges is unaffected by the presence of other charges. In other words, Coulomb's law between any two point charges is not affected by the presence of any other charges.

2.2.1 ELECTRIC FIELD

The electric field (EF) from a charge q is defined as the force per unit charge that produces the Coulomb force on an arbitrary unit (1 C) positive charge test. The electric field may also by defined by the relation:

$$\vec{E} \equiv \frac{\vec{F_e}}{q_0} \tag{6}$$

where $\vec{F_e}$ is the electrical force on a small charge q_0. Small charge has to test the EF at its location, the test charge should be infinitesimally small not to change the EF which it should test. It is important to remember about two characteristics of electric field:

1) electric field is a vector quantity with a magnitude directly proportional to a force and with direction given by the direction of the force on a positive test charge,

2) electric field has units of newton per coulomb (N C^{-1}), which are the same as volts per meter (Vm^{-1}) due to fact that volts are equal to Newtons times meters divided by Coulombs.

It is quite important to know how to visualize EF arround the charged object. We usually use a construction which is a visual representation of electric field as shown in Fig. 18.

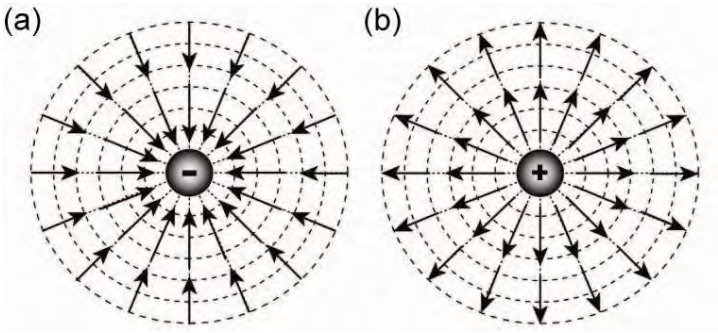

Fig. 18 Electric charge lines around two different charges (a, b), the dashed lines around charges are equipotential lines – the places where the electric potential is the same. The arrows indicate direction of the electric field. (c) Two different charges and electric field line between them.

This visualization compromises a ‘field lines‘ that point the direction of the field at each point space. There is also an arrow approach - in this case the strength of the field is indicated by the length of the arrow. In the field line approach the spacing between the lines demonstrates the strength of the field (the closer are lines the stronger is the electric field). What is also worth noticing is the fact that for both systems there is an elecrtic field between the lines or arrows. There are a few rules which are important while considering EF lines:

i) the electric field lines must orginate from the positive charges and terminate on negative charges (see Fig. 19),

ii) the net electric field at any point is the vector sum of all electric fields present at that point,

iii) electric lines never cross, since that would indicate that the field points in the two different directions,

iv) electric fields lines are always perpendicular to the surface of a conductor of equilibrium.

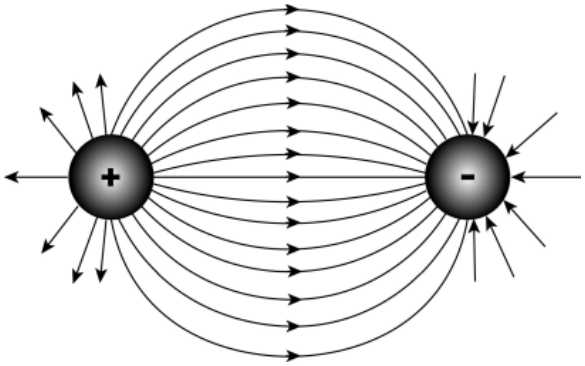

Fig. 19 Electric field lines between positive and negative charge.

If two or more different sources contribute electric fields pointing in the different directions of the same location, the total electric field is the vector sum of the individual fields, and the electric field lines always point at the single direction of the total field.

All the things described above constitute a good description of a system where we have two different or the same charges. However, the distances between charges in a group of charges are very often much smaller than the distance from the group to some point of interest. In this case, the system can be modeled as continous. It means that the system of closely spaced charges is equivalent to a total charge that is continuously distributed along some line, surface or a volume. When performing any calculations it is always convienient to use the concept of a charge density idea. There are different types of organisation of the charge (see Fig. 20):

i) linear charge density λ ($C \cdot m^{-1}$), when a charge *Q* is uniformly distributed along a line of length *l*, defined as:

$$\lambda \equiv \frac{Q}{l} \tag{7}$$

ii) surface charge density σ ($C \cdot m^{-2}$) when a charge *Q* is uniformly distributed on a surface area *A*, defined as:

$$\sigma \equiv \frac{Q}{A} \tag{8}$$

iii) volume charge density ρ ($C \cdot m^{-3}$), when a charge *Q* is uniformly disttributed throughout a volume *V*, defined as:

$$\rho \equiv \frac{Q}{V} \tag{9}$$

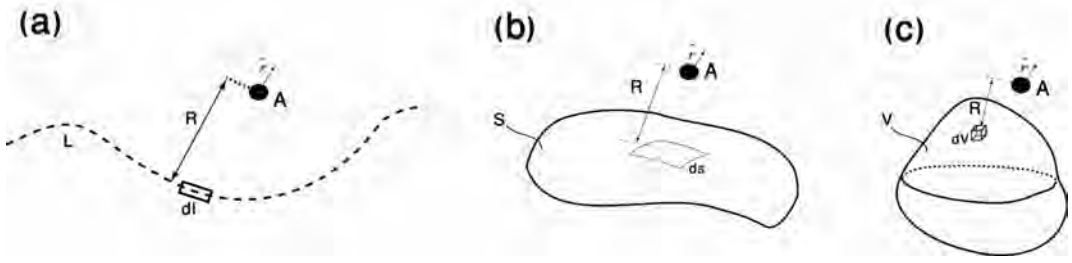

Fig. 20 Different types of distribution of the charge over (a) line, (b) surface and (c) volume.

The relevant electric field strength in the point A is then:

for a line charge $$\vec{E} = \frac{1}{4\pi\varepsilon_0}\int_L \frac{\hat{n}}{R^2}\lambda dl \quad (10)$$

for a surface charge $$\vec{E} = \frac{1}{4\pi\varepsilon_0}\int_S \frac{\hat{n}}{R^2} q_s dS \quad (11)$$

for a volume charge $$\vec{E} = \frac{1}{4\pi\varepsilon_0}\int_V \frac{\hat{n}}{R^2}\rho dV \quad (12)$$

2.2.2 ELECTROSTATIC POTENTIAL

When a test charge *q* is placed in an electric field $\vec{E}$ created by some source charge distribution, the electric force action on the test charge is:

$$\vec{F} = q \cdot \vec{E} \quad (13)$$

The force between charges described by Coulomb's law is conservative. When the test charge is moved into the field, the work done by the field on the charge is equal to the negative of the work done by the external agent causing the displacement. For an infinitesimal displacement of a charge *ds*, the work done by the electric field on the charge is:

$$w = \vec{F} \cdot ds = q\vec{E} \cdot ds \quad (14)$$

As this amount of work is done by the field, the potential energy of the charge-field system is changed by the amount:

$$dU = -q\vec{E} \cdot ds \quad (15)$$

For a finite displacement of the charge from point A to B, the change in potential energy of the system is:

$$\Delta U = U_B - U_A = -q\int_A^B \vec{E} \cdot ds \quad (16)$$

The integration performed along the path that *q* follows as it moves from point A to point B. Because the force $\vec{F}$ (see eq. 13) is conservative, this line integral does not depend on the

path taken from A to B. The potential energy per unit charge defined as $U \cdot q^{-1}$ is independent from the value *q* and has a value at every point in an electric field. This value, $U \cdot q^{-1}$, is called electric potential V:

$$V = \frac{U}{q} \tag{17}$$

The potential difference between two points A and B in an electric field is defined as the change in potential energy of the system when a test charge is moved between the points divided by the test charge *q*:

$$\Delta V = V_B - V_A \equiv \frac{\Delta U}{q} = -\int_A^B \vec{E} ds \tag{18}$$

Electric potential is a scalar characteristic of an electric field, independent from any charges that may be placed in the field. Electric potential is a measure of potential energy per unit charge, the SI unit of both electric potential and potential difference is Joules per Coulomb, which is a definition of a volt (V):

$$V \equiv \frac{J}{C} \tag{19}$$

What means that 1 J of work must be done to move a 1 C of charge through a potential difference of 1 V. [16]

2.2.3 GAUSS'S EQUATION

Integral form of Gauss equation is given by equation:

$$\oint_S \vec{E} \cdot \hat{n} da = \frac{q_{enc}}{\varepsilon_0} \tag{20}$$

where:

$\vec{E}$ - electric field,
q_{enc} - charge enclosed by a surface S,
$\hat{n}$ - unit vector perpendicular to the S surface.

The main idea of Gauss equation is that electric charges produce an electric field, and the flux of that field passing through any closed surface is proportional to the total charge contained within that surface (Fig. 21).

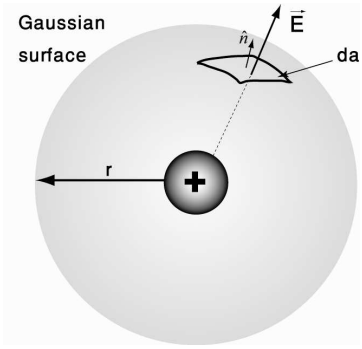

Fig. 21 Visualization of the Gauss equation for single positive charge. Gaussian surface is a virtual surface around the charge. On this surface we cut a infinitesimal area *da* and set an unity vector $\hat{n}$ perpendicular to this surface.

The differential form of Gauss equation is a mathematical description of the divergence of the electric field and the right side is the electric charge density divided by the permittivity of free space:

$$\nabla \cdot \vec{E} = \frac{\rho}{\varepsilon_0} \tag{21}$$

There are two basic problems one can solve with a use of Gauss equation:

i) for a given distribution of the electric charge inside enclosed surface, one can calculate the electric flux through a surface enclosing that charge,

ii) for a given electric flux through a closed surface, one can find the total electric charge enclosed by that surface.

For a highly symmetric distributions of charges, it is possible to find the electric field itself, not just the flux over the surface.

2.2.4 POISSON'S EQUATION

Having the Gauss law in differential form:

$$\nabla \cdot \vec{E} = \frac{\rho}{\varepsilon_0} \tag{22}$$

and knowing that

$$\vec{E} = -\nabla V \tag{23}$$

we obtain eq. (24) known as a Poisson's equation:

$$\nabla^2 V = -\frac{\rho}{\varepsilon_0} \tag{24}$$

When the total charge density is zero (in cases where the electric charge density within a body is absent, i.e. ρ=0), the expression reduces to Laplace's equation:

$$\nabla^2 V = 0 \tag{25}$$

indicating a constant electric field.

2.2.5 MAXWELL EQUATIONS

Maxwell's equations are basic equations of electromagnetism. These four basic equations (26-29) bear the name of James Clerk Maxwell (1831-1879). He was the first to state them clearly, yet Oliver Heaviside (1850-1925) was the first who expressed them in form we know today, simple and useful for engineers. In his theory of electromagnetism, Maxwell proved that electromagnetic waves are a natural consequence of the fundamental laws in four equations shown below:

$$\nabla \cdot \vec{E} = \frac{\rho_{total}}{\varepsilon_0} \tag{26}$$

$$\nabla \cdot \vec{B} = 0 \tag{27}$$

$$\nabla \times \vec{E} + \frac{\partial \vec{B}}{\partial t} = 0 \tag{28}$$

$$\nabla \times \vec{B} - \varepsilon_0 \mu_0 \frac{\partial \vec{E}}{\partial t} = \mu_0 \vec{J}_m \tag{29}$$

where:

$\vec{E}$ - is the electric field intensity

$\rho_{total} = \rho_{free} + \rho_{bound}$ - is the total electric charge density; ρ_{free} is the free charge density and ρ_{bound} is the bound charge density

$\vec{B}$ - is the magnetic induction,

$\vec{J}_m$ - is the current density resulting from the flow of charges in matter,

ε_0 - is the permittivity of free space, $8.854 \cdot 10^{-12}$ ($F \cdot m^{-1}$)

μ_0 - is the permeability of free space, $4\pi \cdot 10^{-7}$ ($H \cdot m^{-1}$)

Maxwell's equations are partial differential equations involving space and time derivatives of the field vectors $\vec{E}$ and $\vec{B}$, the total charge density ρ_{total} and the current density $\vec{J}_m$. These equations do not yield the values of E and B directly, but only after integration and after taking into account the proper boundary conditions. [17]

2.2.6 INTERMOLECULAR FORCES

Intermolecular forces can be easily understood on the basis of electrostatics, if at least one of the molecules carries a dipole moment (where dipole moment can be a result of difference of electronegativity of atoms or can be induced).
Van der Waals force is originated by dipole or induced dipole interactions between the species. We can distinguish three different types of van der Waals forces:

i) permanent dipole-permanent dipole interaction (Keesom interaction),

ii) permanent dipole-induced dipole interaction (Debye interaction),

iii) induced dipole-induced dipole interaction (London interaction). [18]

These three types of interaction are known as van der Waals interactions. They are proportional to molecular parameters that represent the polarization of molecules (polarizability, dipole moment of molecules). The combined expression of van der Waals attraction and the repulsive force is known as the 12^{-6} power low or the Lennard-Jones potential. [2]

The most basic case is a monopole-dipole interaction. For most molecules total electric charge is zero, yet quite often the electric charge is not evenly distributed (H_2O, CO etc.) and we call such molecules as 'polar'. If in a molecule we have separated charges, q^+ and q^- at a distance *d*, the dipole moment μ is given by:

$$\mu = q \cdot d \tag{30}$$

The dipole moment is a vector that points from minus to the plus (see Fig. 22).

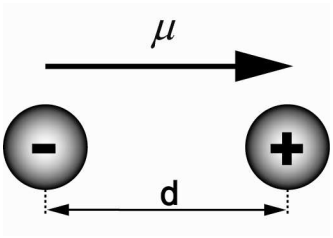

Fig. 22 The dipole moment between positive and negative charge, separated over the distance *d*. The dipole moment is directed from negative to positive charge.

A good example of monopole and dipole interaction is a molecule of water and single ion, i.e., Na^+. With the use of superposition principle—which states that if more than two charges are present, the net potential energy of a charge can be calculated by summing up the contributions of all other charges—we can calculate the potential energy between a dipole and a single charge *Q* (see Fig. 23).

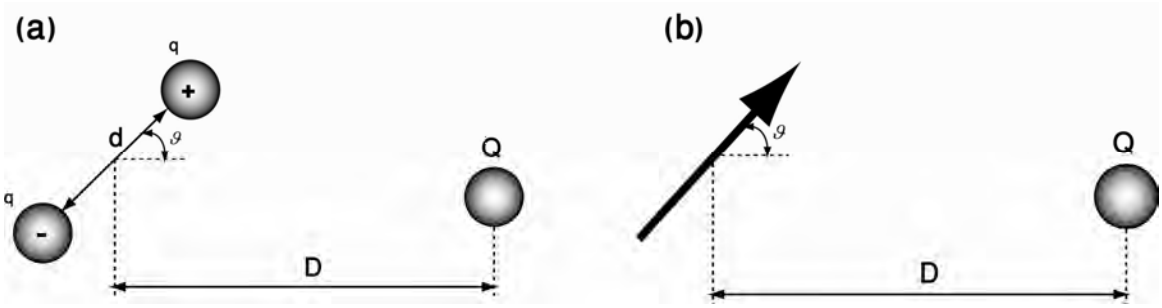

Fig. 23 The monopole-dipole interaction is shown here for a single charge and a dipole made of a negative and positive charge.

We assume that the distance between the charge and the dipole is much larger than the extension of the dipole, i.e., D≫d:

$$V(D,\vartheta) = -\frac{Q\mu \cdot \cos\vartheta}{4\pi\varepsilon_0 D^2} \tag{31}$$

In reality, a molecule with a dipole is often mobile and rotates freely. In this case the potential energy is:

$$V(D) = -\frac{Q^2\mu^2}{6(4\pi\varepsilon_0)^2 k_B T D^4} \tag{32}$$

For rotating molecule interactions decay much more faster than immobile molecule, D^{-4} instead of D^{-2}. Additionally, since $k_B T$ is in the denominator, the interaction becomes weaker with increasing temperature. [19]

Permanent dipole-permanent dipole interactions

In order to calculate interaction between two permanent dipoles we can use superposition principle to sum interactions between individual charges. A distance and three angles are used to describe position of two dipoles. Angles ϑ_1 and ϑ_2 describe the angle between the dipoles and the connecting axis, whereas ϕ is the angle between the projections of the dipoles to the area perpendicular to the connecting line (Fig. 24). The potential energy for this interaction is:

$$V(D,\vartheta_1,\vartheta_2,\phi) = \frac{\mu_1\mu_2}{4\pi\varepsilon_0 D^3}(2\cos\vartheta_1\cos\vartheta_2 - \sin\vartheta_1\sin\vartheta_2\cos\phi) \tag{33}$$

But the maximum attractive interaction is for $\vartheta_1 = \vartheta_2 = 0°$, what gives

$$V_{\max}(D) = -\frac{\mu_1\mu_2}{2\pi\varepsilon_0 D^3} \tag{34}$$

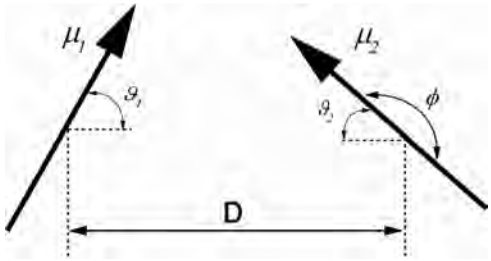

Fig. 24 Interaction between two permanent dipoles over the distance D.

When the two dipoles are allowed to rotate freely, they attract each other because they preferentially orient with their opposite charges facing each other. This thermally averaged dipole-dipole free energy is often referred as the Keesom energy (Fig. 25). The potential energy for such an interaction is:

$$V = -\frac{\mu_1^2\mu_2^2}{3(4\pi\varepsilon_0)^2 k_B T D^6} = -\frac{C_{orient}}{D^6} \tag{35}$$

In this case, the interaction energy also decreases with a temperature.

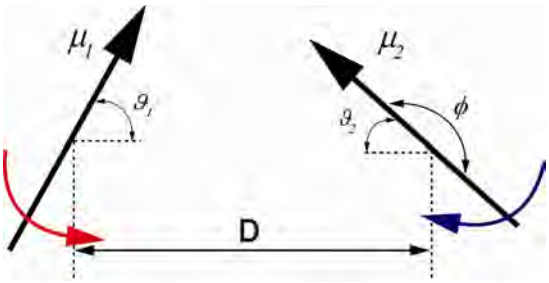

Fig. 25 Keesom interaction between two induced dipoles

Debye interaction

When a molecule with a permanent charge (polar molecule) approaches a molecule without a static dipole moment, all energies considered before will be zero. However, there will be an attractive force between these two objects, whose source is a charge shift in the non-polar molecule induced by a charged molecule. This induced dipole moment interacts with a permanent charge, and the interaction potential is:

$$V = -\frac{Q^2\alpha}{2(4\pi\varepsilon_0)^2 D^4} \tag{36}$$

where α is a polarizibility. It determines the distortion of a molecule in an external electric field. If the strength of the field is $\vec{E}$, then the molecule has an induced dipole moment:

$$\mu = \alpha \cdot \vec{E} \tag{37}$$

A molecule with a permanent dipole will interact with a polarizable molecule by inducing a dipole moment. This interaction, known as the Debye interaction, is equal to:

$$V = -\frac{\mu^2\alpha}{(4\pi\varepsilon_0)^2 D^6} = -\frac{C_{ind}}{D^6}. \tag{38}$$

London dispersion forces

All interaction described above fail when we want to describe attraction between non-polar molecules, which are clearly visible during condensation of the noble gases. The forces which are responsible for condensation of noble gases i.e., argon, are called London or dispersion forces. The origin of this dispersion force can be explained while considering an atom with its positively charged nucleus and circulating electrons with frequencies in order of magnitude 10^{15}-10^{16} Hz. The atom is therefore polar, yet its polarity changes with this immense frequency. Simultaneously, when two oscillating atoms approach they start to influence each other and the attractive orientations have higher probabilities than the

repulsive, so as an average two atoms attract each other. The interaction between two molecules with ionization energies $h\nu_1$ and $h\nu_2$ can be approximated as:

$$V = -\frac{3}{2}\frac{\alpha_1\alpha_2}{(4\pi\varepsilon_0)^2 D^6}\frac{h\nu_1\nu_2}{(\nu_1+\nu_2)} = -\frac{C_{disp}}{D^6} \tag{39}$$

Dispersion interactions increase with the polarizibilities of the molecules, and they decay as the D^{-6}. Van der Waals interactions are in fact sum of the Keesom, Debye and London interactions:

$$\begin{aligned} V_{vdW}(D) &= -\frac{C_{vdW}}{D^6} \\ C_{vdW} &= C_{orientational} + C_{induced} + C_{dispersion} \end{aligned} \tag{40}$$

All three terms contain the same distance dependency, i.e. D^{-6}, yet usually the London dispersion term is usually dominating. An interesting exception is the water molecule where strong permanent dipole is combined with the small size of a molecule.

Chapter 2.3

Electrostatics in soft condensed matter

In this chapter I will present the importance of electrostatics in the soft matter systems. At the very beginning I will describe aqueous electrolytes, and phenomenon of the solid state-liquid interface. The most important aspects of the interface phenomenon was described as Debye-Hückel theory, Gouy-Chapman theory and Poisson-Boltzmann theory. Thereafter, I will describe colloids in aqueous solution and I will review the stability of colloids in terms of double layer and DLVO theory. After that, I will show how these theories are used in description of polyelectrolytes. At the end, I will present biological application of the electrostatics: DNA, proteins and animal cells.

Most known solids when immersed into high-dielectric constant liquid, for instance water, release ions. As a result, these objects becomes electrically charged on the surface. This phenomenon, however, is known also for non-solid state objects, like droplets or bubbles – even oil droplets and air bubbles in water are charged. There are five possible mechanisms to accumulate an electric charge on a surface [20]:

i) **Ionization of surface groups**: when a surface contains acidic groups (e.g. carboxylic group COOH,), their dissociation gives rise to a negatively charged surface. When a basic groups (e.g. hydroxyl group OH) are on the surface, their dissociation gives positive charge (Fig. 26).

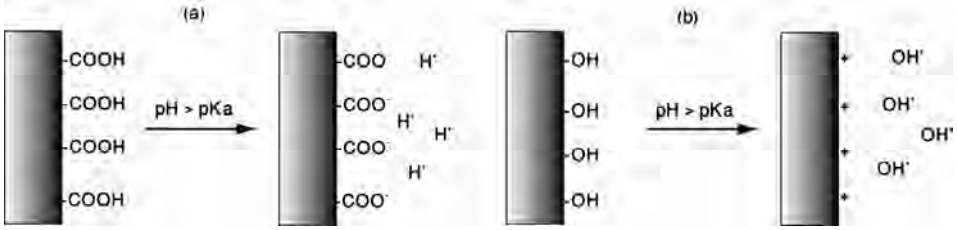

Fig. 26 surface charge can be obtained when chemical groups on the surface dissociate a) carboxylic groups dissociate in high pH and negative charge is present on the surface, b) hydroxyl groups dissociate in low pH and positive charge is created on the surface. In both cases pH has to be higher than pKa (typically, most of the groups is ionized when pH ≥ pKa + 1,5).

The magnitude of the surface charge depends on the properties of the aqueous environment (i.e. pH of the solution) and also on the strengths of the surface groups. At the point of zero charge (PZC) , the surface charge is equal to zero. It is usually done by decreasing or increasing the pH of the solution. Metal oxides can have positive or negative surface charge depending on the pH. Moreover, a glass slide placed in aqueous solution obtains negative charge due to ionization of silanol group (-SiOH).

ii) **Differential dissolution of ions from surfaces of sparingly soluble crystals**: this mechanism occurs for instance when we put AgI (silver iodide) crystals into aqueous environment. Dissolution of AgI occurs until the product of ionic concentration equals the solubility product:

$$[Ag^+][I^-] = 10^{-16}\ (mol/L)^2$$

If equal amounts of Ag^+ and I^- are to dissolve, their concentrations would be equal:

$$[Ag^+] = [I^-] = 10^{-8}\ (mol/L)^2$$

and the surface has no charge. Silver ions dissolve preferentially, leaving a negatively charged surface. If we introduce Ag^+ ions in another form, i.e. $AgNO_3$ solution, the preferential solution of silver ions is suppressed. It means that for certain concentration the charge on the surface is zero. Addition of Ag^+ ions –for instance in a form of $AgNO_3$ solution—gives us positively charged surface due to fact that iodide ions are preferentially dissolved.

iii) **Isomorphic substitution**: it is popular in materials which can exchange ions. Good example of that are clays (e.g. montmorillonite, bentonite) with their layered structure. They may exchange an adsorbed intercalated or structural ion with one of lower valency. For instance, Al^{3+} may replace Si^{4+} in the surface of the clay and as a result we obtain charged surface. A point of zero charge can be reached by decreasing the pH of the solution.

iv) **Charged crystal surfaces**: occurs when a crystal is broken and surfaces with different properties are exposed to aqueous environment. In some clays (e.g. kaolinite) the exposed edges contain $Al(OH)_3$ groups which take up H^+ ions and as a result we obtain positively charged edge. Under the same conditions basal surface may be negativelly charged. The flat surface is negatively charged and the edges are positively charged at low pH, whereas at high pH the positive charge on the edges is decreasing.

v) **Specific ion adsorption**: a good example of that is adsorption of surfactants (surface active agents) on the surface of solid state immersed in solution. Cationic surfactants (with a positively charged 'head') can absorb into negatively charged surfaces, and even to yield net positive charges on the surface. Anionic surfactants (which possess negatively charged 'head') can absorb into a positively charged surface.

We can assess the work we have to perform to separate an ion pair in vacuum or air and in a high-dielectric constant liquid, like water. In high polar liquid (for water ε_r =80 in 25 °C) this work is ca. $6 \cdot 10^{-21}$ J. This value is very close to the kinetic energy of a free ion, i.e. $k_B T$ which is $4.12 \cdot 10^{-21}$ J in 25 °C. However, if the same experiment is conducted in non-polar or weakly polar medium, like vacuum, air or hexane, the required work will be ca. 100 kT. It is the high dielectric constant or polar nature of the solvent which allows this ion to dissociate from the surface. In the air or non-polar liquids (ε_r =1÷2) the dissociation does not occur, therefore main interest is in processes at the interface of the solid state and water interface. [12] The other reason, for that is the fact that water constitutes the environment for all living organisms.

2.3.1 ELECTROLYTES

Any molecule that can dissolve in polar liquids, that can dissociate into ions and carry an electrical current is called an electrolyte. Strong electrolytes are substances that dissociate completely and are fully ionized in solution. Substances that dissociate only partly are called weak electrolytes. The degree of dissociation can be represented by the equilibrium constant K:

$$MX \xrightarrow{K} M^+ + X^- \tag{41}$$

where the K constant is defined as:

$$K = \frac{[M^+][X^-]}{[MX]} \tag{42}$$

As strong electrolyte has a large K, usually K > 0.1 whereas for a weak electrolyte K < 0.1. knowing that

$$pK = -\log_{10} \tag{43}$$

A strong electrolyte has a pK < 1, whereas a weak pK > 1.

2.3.2 THE ELECTROCHEMICAL DOUBLE LAYER

As shown above, surface charges cause an electric field. A glass slide in water solution with free ions (i.e. dissolved NaCl) becomes charged on the surface. Electric charge generated by the charges on the surface will attract counter ions. The layer of surface charges and counter ions is called electric double layer. [21] The simplest model, called Helmholtz model, the electric double layer is created when counter ions bind to the surface due to electrostatic forces between them and the charged glass slide. This single layer on the surface is called Helmholtz layer, in order to honor Hermann Helmholtz. Helmholtz layer, a relatively simply model, is quite useful in describing basic features of such a system. Unfortunately, it failed in more complicated cases, i.e. the description of the capacitance of an electric double layer. The next step in modeling was performed by two scientists: Louis Gouy and David Chapman. In the years 1910-1917 they created a new, better model which took into account thermal motion of the ions. In this model thermal fluctuation tend to drive the counter ions away from the surface.

As a result, they created a diffuse layer: it is more extended than the layer in Helmholtz theory and goes into a bulk solution (see Fig. 27)

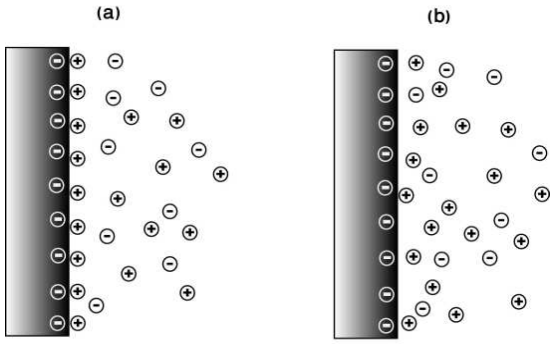

Fig. 27 Helmholtz (a) and Gouy-Chapman (b) model of electrical double layer.

Stern model (see Fig. 28) combines model of Helmholtz and Gouy-Chapman. In this model we divide the double layer into two parts: the first one is Stern layer and it is “pinned” to the surface, and the second is diffuse layer. Stern layer is located directly on the surface and is immobile, whereas diffuse layer (or Gouy-Chapman layer) consists of mobile ions that obey statistics of Poisson-Boltzmann. [19]

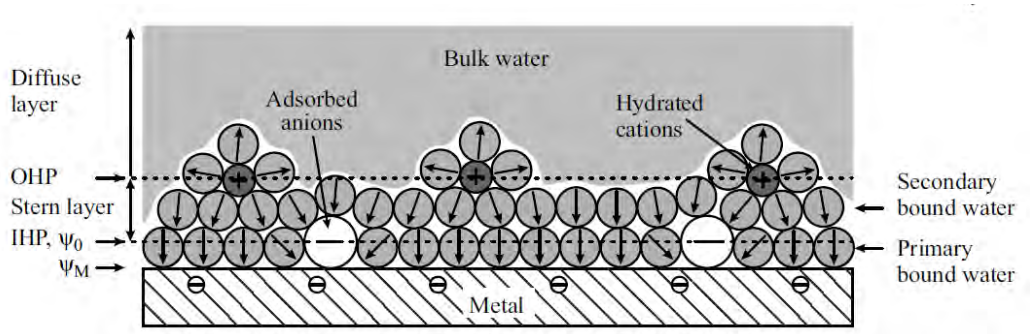

Fig. 28 Detailed description of the Stern layer at a metal surface. The inner (IHP) and the outer (OHP) Helmholtz planes are visible. [19]

A value strictly correlated with a double layer is the one known as the Debye length λ_D (also known as κ^{-1}). An equation is showing dependency between initial potential and the distance from the surface:

$$\psi(x) \cong \psi_0 \exp(-\kappa x) \tag{44}$$

This simple equation explains the physical meaning of the Debye length. This length is in fact a thickness of the electrical double layer. According to the equation (44) Debye length is the distance where the potential falls like 1/e (where e is the Neper's number).

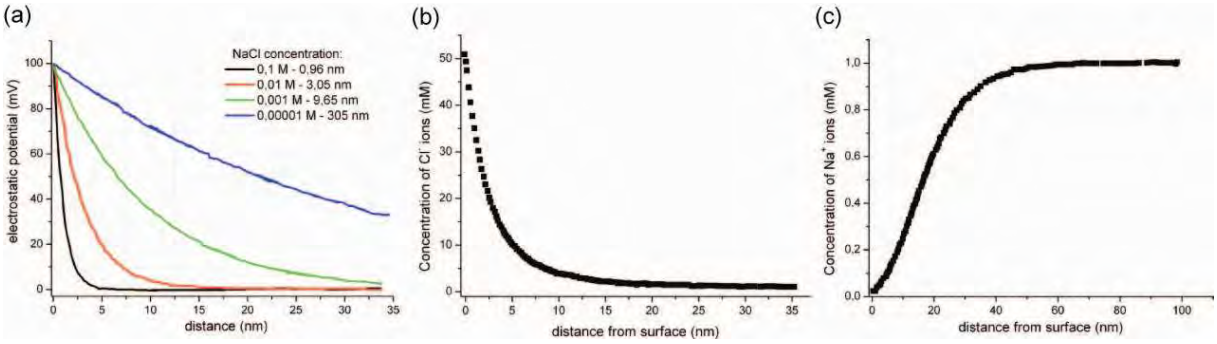

Fig. 29 Electrostatic potential from the surface for different concentration of electrolyte (from 0.1 M to 0.00001 M NaCl) (a). Inset: next to concentration value we see corresponding Debye length. Initial potential is +100 mV. The potential decreases exponentially. [12]
(b, c) Calculation of concentration of the co- and counter-ions for a flat surface with initial potential +100 mV. [12]

Fig. 29a demonstrates how different concentration of electrolyte influences the decay of initial potential on charged plate. For each concentration the Debye length is equal to the distance from the surface at which the potential has fallen to value 100/e which gives 37 mV. Once the distribution next to a charged surface is known, it is possible to use the Boltzmann

distribution to calculate the corresponding distribution of counter- and co-ions. The results of such a calculations are shown on Fig. 29b and c.

Using this equation one can assess (sometimes with high accuracy) the ion distribution next to charged, flat surfaces immersed in aqueous electrolytes. Counter ions are pulled toward the charged surface—due to electrostatic attraction—reaching quite high concentration near to the surface. Contrary to that, co-ions are expelled from the volume near-to-the-surface also due to electrostatic repelling. The Debye length decreases with increasing salt concentration – the more ions are in solution the more effective is the screening of surface charge. The general equation for calculating Debye length, for ions of higher valency is shown below:

$$\kappa^{-1} = \frac{1.0586 \times 10^{13}}{[\sum_i C_i(B) Z_i^2]^{0.5}} \tag{45}$$

The concentration has to be given in particles per m^3, and Z_i is the valency of the i^{th} ion sort. For 1:1 electrolytes and 21 °C Debye length can be easily calculated as:

$$\kappa^{-1} = \frac{0.305}{\sqrt{M}} \tag{46}$$

where M is concentration in M/Liter.

In water Debye length cannot be longer than 960 nm. Due to dissociation of water the ion concentration cannot decrease below 10^{-7} M. In laboratory practice we assume that even in distilled water the Debye length is only a few hundreds of nanometers; the reason for that is dissolved CO_2 which is converted to carbonic acid and is partially dissociated.

Debye length has also a second, very important meaning: it is also a screening or shielding distance. A test charge that is closer to the charged surface than κ^{-1} interact with this charge via electrostatic force. A charge that is further than Debye length from the surface does not ‘see’ the charge, because it is screened by the ions (they weaken interactions, attraction or repulsion) near to the surface [22].

Another useful length is Bjerrum length l_B, which is defined as:

$$l_B = \frac{e^2}{\varepsilon k_B T} \tag{47}$$

For soft materials the thermal energy, which is associated with $k_B T$, is comparable to the typical energy associated with deformation and structural degrees of freedom in the system. The Bjerrum length is the distance for which the thermal energy is equal to the Columbic energy between two unit charges. At room temperature (ca. 300K) and the dielectric constant of water ($\varepsilon \approx 80$), l_B is about 7Å [23].

2.3.3 POISSON-BOLTZMANN (PB) THEORY

One of the basic problems is calculating electric potential ψ near a charged planar surface immersed in an electrolyte. A plane surface (at least in atomic scale) with a electric charge σ which is homogenously distributed over the plane is analyzed. The charge is in contact with a liquid, because the source of the charge comes from ionized groups or adsorbed ions. The surface charge generates a surface potential defined as:

$$\psi_0 = \psi \tag{48}$$

for a boundary condition:

$$x = 0 \tag{49}$$

Charge density on the surface and electric potential are related together with the Poisson equation:

$$\nabla^2 \psi = -\frac{\rho}{\varepsilon \varepsilon_0} \tag{50}$$

What can be written as:

$$\frac{\partial^2 \psi}{\partial x^2} + \frac{\partial^2 \psi}{\partial y^2} + \frac{\partial^2 \psi}{\partial z^2} = -\frac{\rho}{\varepsilon \varepsilon_0} \tag{51}$$

where ρ is a local electric charge density (C m^{-3}).

Information about spatial distribution of the ions we can obtain from the Boltzmann equation:

$$c_i = c_i^0 \cdot \exp\left(\frac{-W_i}{k_B T}\right) \tag{52}$$

where:

W_i - is a work required to bring an ion in solution from infinite distance to a certain position closer to the surface,

c_0 - is the bulk concentration of the salt.

This equation tells how the local concentration of the ion c_i depends on the electric field – if the potential of the surface is positive, the probability of finding negative ion nearby is higher than positive one.

The electric work required to bring a cation to a place with an electric potential ψ is:

$$W^+ = e\psi \tag{53}$$

whereas the work required to bring an anion to a place with an electric potential ψ is:

$$W^- = -e\psi \tag{54}$$

The local anion and cation concentrations, i.e. c^- and c^+ are related to the local potential ψ by the Boltzmann factor:

$$\begin{aligned} c^- &= c_0 \cdot \exp(\frac{e\psi}{k_B T}) \\ c^+ &= c_0 \cdot \exp(\frac{-e\psi}{k_B T}) \end{aligned} \tag{55}$$

The local charge density is:

$$\rho = e(c^+ - c^-) = c_0 \cdot (\exp(-\frac{e\psi(x,y,z)}{k_B T}) - \exp(\frac{e\psi(x,y,z)}{k_B T})) \tag{56}$$

The potential ψ is a function of x, y and z. Comparing equation (56) with the Poisson equation we obtain:

$$\nabla^2\psi = \frac{c_0 e}{\varepsilon\varepsilon_o} \cdot (\exp(-\frac{e\psi(x,y,z)}{k_B T}) - \exp(\frac{e\psi(x,y,z)}{k_B T})) \tag{57}$$

and knowing that:

$$\sinh = \frac{e^x - e^{-x}}{2} \tag{58}$$

Poisson—Boltzmann equation is derived:

$$\nabla^2\psi = \frac{2c_0}{\varepsilon\varepsilon_0} \cdot \sinh(\frac{e\psi(x,y,z)}{k_B T}) \tag{59}$$

2.3.4 DEBYE-HÜCKEL APPROXIMATION

Let's consider very simple case, with infinitely extended planar surface, the potential cannot change in the y and z axis, so the differential coefficients must be equal zero. The Poison-Boltzman equation in the direction normal to the plane *x* is given as follows:

$$\frac{d^2\psi}{dx^2} = \frac{c_0 e}{\varepsilon\varepsilon_0} \cdot \left(\exp(\frac{e\psi(x)}{k_B T}) - \exp(-\frac{e\psi(x)}{k_B T}) \right) \tag{60}$$

For 'low' potentials it is possible to expand the exponential functions into a series and neglect all except the first (linear) term:

$$\frac{d^2\psi}{dx^2} = \frac{c_0 e}{\varepsilon\varepsilon_0} \cdot \left(1 + \frac{e\psi}{k_B T} - 1 + \frac{e\psi}{k_B T} \pm \ldots \right) \approx \frac{2c_0 e^2}{\varepsilon\varepsilon_0 k_B T} \cdot \psi \tag{61}$$

This is called the 'linearized Poisson-Boltzmann equation' also known as the 'Debye-Hückel approximation'. The general solution for this is:

$$\psi(x) = C_1 \cdot \exp(-\kappa x) + C_2 \cdot \exp(\kappa x) \tag{62}$$

where C_1 and C_2 are constants defined by the boundary conditions and κ^{-1} is Debye length.

Poisson-Boltzmann theory consists of several assumptions. Firstly, the finite size of the ions in solution was neglected. It is especially important close to the surface, where the concentration of the ions can be very high (Fig. 27).

Secondly, PB theory is a mean field theory. It means that each ion interacts with average electrostatic field of all ions around. However, it is not always true under certain conditions: ions can carry only a single charge. When they carry multiple charge, in particular di- or ever trivalent ions, they can lead to a strong deviations from the PB theory. Moreover, the surface charge is assumed to be homogenous and 'smeared out', but in reality it is formed by individual ions, which are absorbed on the surface or comes from the charged groups. In PB theory we do not consider the influence of non-Coulombic interactions. Each ion has a hydratation shell (due to electrostatic interaction between ion and electric dipole of water molecule). If the ions are very close to each other or just approach each other, hydratation shell overlaps and as a result changes the interaction. The next issue that we assume is that the solvent has constant permittivity but the very high concentration of counter-ions near the charges surface can change the permittivity. The most basic assumption in the PB theory is that the surface is flat on the molecular scale. Usually it is good assumption, but for instance in biological systems it fails.

Analyzing all assumptions above mentioned we can think that PB theory should give imprecise results. The reason why PB theory give surprisingly good results is because errors partially compensate each other. To sum up, the Gouy-Chapman theory provides quite good predictions for monovalent salts in aqueous solutions, for concentration lower than 0.2 M and for potentials lower than 50-80 mV.

2.3.5 COLLOIDS AND DLVO THEORY

While studying spheres immersed in electrolyte, it is very noteworthy to know how the double layer looks like. If the radius of the particle R_p is much more larger than the Debye length κ^{-1}, we can assume that we consider flat surface with a double layer. If it is not a case, it is necessary to consider PB theory in spherical geometry:

$$\frac{d^2\psi}{dr^2}+\frac{2}{r}\frac{d\psi}{dr}=\left(\exp(\frac{e\psi(x)}{k_BT})-\exp(-\frac{e\psi(x)}{k_BT})\right) \tag{63}$$

where r is the radical coordinate. The boundary conditions are:

$\psi(r=R_p)=\psi_0$ for a surface potential ψ_0

$\psi=0$ for $r\to\infty$

For low potentials (less than 25 mV), we can linearize differential equation to a form:

$$\frac{d^2\psi}{dr^2}+\frac{2}{r}\frac{d\psi}{dr}=\kappa^2\psi \tag{64}$$

Solved linearized PB equation in differential form (1.23):

$$\psi(r)=\psi_0\cdot\frac{R_p}{r}\cdot\exp(-\kappa(r-R_p)) \tag{65}$$

For high potentials we have to solve PB equations in radial coordinates. According to [19] no analytical solution has been reported, however a good approximation for large κR_p can be done:

$$e^{y/2}=\frac{1+\alpha\cdot\exp(-\kappa(r-R_p))\cdot\frac{R_p}{r}}{1-\alpha\cdot\exp(-\kappa(r-R_p))\cdot\frac{R_p}{r}} \tag{66}$$

The stability of colloids (e.g. gold nanoparticles) depends strongly on the concentration of ions in solution. The gold nanoparticles are negatively charged via mechanisms explained before. Charged nanoparticles repeal each other with electrostatic forces. Increasing the salt concentration, the electrostatic repulsion will decrease. In the absence of this repulsion nanoparticles can approach each other to a distance of a few Angstroms. In small scale van

der Waals forces will play a role, and attraction will be a major force, and as a result, nanoparticles will aggregate.

Quantitatively, this process can be described with DLVO theory. This name comes from the names of scientists who developed this theory: Derjaguin, Landau, Verwey and Overbeek. DLVO theory describes two forces: the attractive van der Waals force and the repulsive electrostatic double-layer force. As the van der Waals forces are in an advantage, the colloidal suspension aggregates, whereas electrostatic repulsion forces are in an advantage the colloidal suspension is highly stable. Analyzing these two forces, it is possible to approximate the energy per unit area between two infinitely extended solids separated by a gap *x*:

$$V^A(x) = 64 \cdot c_0 \cdot k_B \cdot T \cdot \kappa^{-1} \cdot \alpha^2 \cdot \exp(-\frac{x}{\kappa^{-1}}) - \frac{A_H}{12\pi x^2} \tag{67}$$

where

$$\alpha = \frac{\exp(\frac{e\psi_0}{2k_BT}) - 1}{\exp(\frac{e\psi_0}{2k_BT}) + 1} = \tanh(\frac{e\psi_0}{4k_BT}) \tag{68}$$

DLVO theory predicts than for a very small distances van der Waals forces are always dominant. The van der Waals forces for a small distances are always attractive, no matter what medium is between objects we measure. Thermodynamically, this system is unstable, and tends to aggregate however kinetics of this may be very slow. A good example is a gold colloid made by Michael Faraday in 1857, Faraday's original sample was still stable during the WWII [24].

2.3.6 POLYELECTROLYTES

Polyelectrolytes (PEL) are macromolecules which bears a dissociating ionic groups (see Fig. 30). They constitute a very interesting subject of research in soft condensed matter systems: from one point of view they show properties typical of polymer systems, yet they posses very strong influence of electrostatic forces. PEL once dissolved in a polar solvent, i.e. water, the ion pairs dissociate by creating a charged chain with dissolved counterions around them (see Fig. 30a). Polyelectrolytes can be divided into three main groups:

i) natural, e.g., DNA,

ii) modified natural, e.g. cellulose, chitin derivatives,

iii) artificial polymers, e.g. poly(styrene sulfonic acid), poly(diallyldimethylammonium chloride).

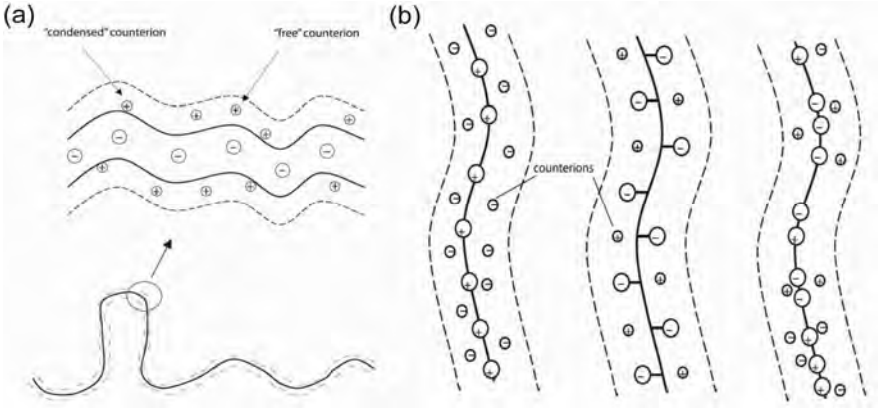

Fig. 30 Schematic view of polyelectrolyte (a) view of a macromolecule (down) and detailed view of the core (top) and counterions around ionized chain of PEL (b) for different types of polyelectrolytes: polycations, polyanions and polyampholytes [24].

Growing interest in PEL is caused by their application in technology (sensors, biosensors, multilayer thin films), as well as in biology: all proteins and DNA are charged so PEL is easy and convenient model. In recent years a technique called Layer-by-Layer (LbL),also known as electrostatic self-assembly (ESA), became very popular for preparing thin films [25]. Typical procedure of LbL is shown in the Fig. 31. The first step is to expose a charged surface to a solution of a polyion of opposite charge, in the case of negatively charged substrate it will be a solution of polycations. The method of making multilayers is relatively fast, single step can last between 1 min and 1 h. The amount of adsorbed polyelectrolyte is self-limiting. The surplus of PEL solution adhered to the surface can be removed by simple washing. Under optimal conditions, PEL with charges opposite than a surface are adsorbed and the amount of the charges of PEL is higher than the stechiometric number on the surface.

As a result, the sign of the surface charge is reversed, and when the substrate is exposed to a second solution with PEL of opposite charge, another polyion layer is adsorbed. Also in this case, adsorption reverses the sign of the surface. The experimental setup may be very simple (a two bakers filled with solution of polycationionic PEL and polyanionic PEL) or highly sophisticated: an automated arm controlled with computer. Single cycle can be repeated many times resulting in multilayer composite of positive and negative layers of polymer.

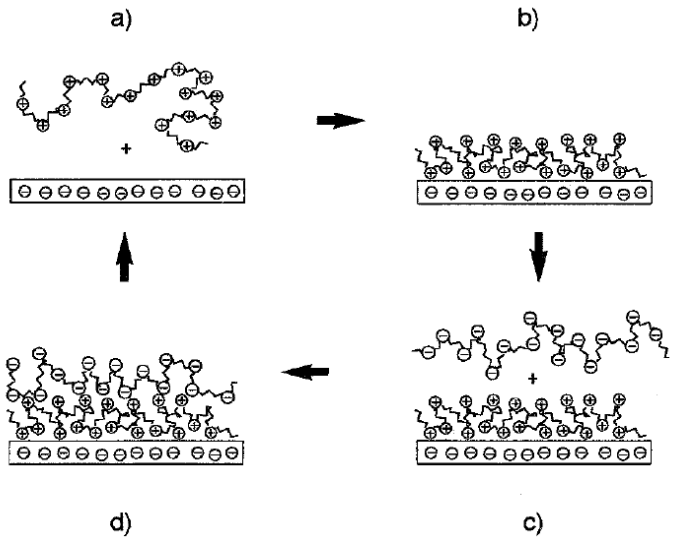

Fig. 31 General scheme for Layer-by-Layer technique: a charged surface (in this case negatively charged) is immersed into solution with cationic polyelectrolyte (a). Due to electrostatic force between the surface and the PEL, it is deposited on the surface (b). The next step is immersing of the surface with cationic layer of the PEL to a solution of anionic polyelectrolyte (c). Layer of cationic PEL is screening the charge of the surface and next layer is formed with electrostatic interaction between positively and negatively charged PEL (d). All cycle can be repeated. [25]

2.3.7 ELECTROSTATICS IN BIOLOGICAL SYSTEMS

Nucleic acids are crucial elements of storage and transfer of information in the cells. Deoxyribonucleic acid (DNA) contains the instructions for protein synthesis. DNA (see Fig. 32) from the chemical point of view is a natural polymer with a negative phosphate charges. Because negative charges repeal each other, DNA is relatively expanded in water. When salt, i.e. NaCl is added to this solution it is dissociated into Na^+ and Cl^- ions. The positive ions Na^+ surround negatively charged DNA due to electrostatic interactions, and as a result they shield its charge. This shielding weakens repulsion between negative charges on the DNA and it becomes more ‘compact’. One of the astonishing examples of electrostatic effect in biology is DNA-packaging process in cell nucleus. The total length of DNA is about two meters and the total negative charge is ca. 10^{10} e, what gives one elementary charge per 1.7 Å. DNA strand is stored in the cell nucleus with a diameter of less than 10 µm.

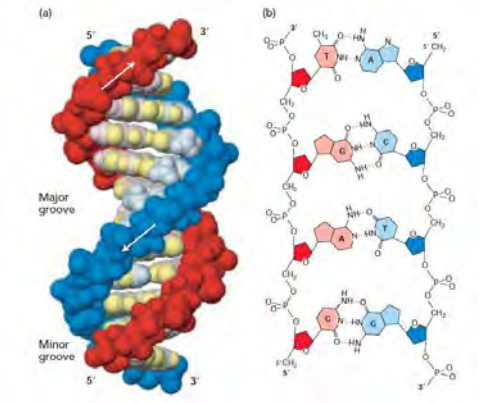

Fig. 32 The DNA double helix (a) space-filling model of B DNA, the most common DNA in the cells. (b) chemical structure of DNA double helix [26]

This storage process involves a special, positively charged proteins called histones. Each DNA molecule wraps around histones and forms a structure called nucleosome (see Fig. 33)

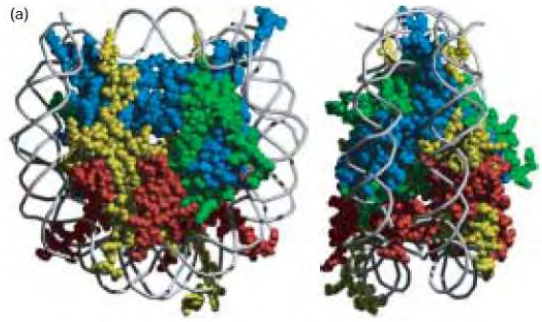

Fig. 33 Nucleosome: a DNA chain wrapped around globular protein charged positively, called histone, shown from the top and from the side. [26]

This structural organization allows DNA to be compacted into the microscopic constraints of the cell nucleus.

Proteins

Of the over 300 known amino acids only 20 are building blocks of the proteins. Each amino acid—except for proline—has a carboxyl group, an amino group and a side chain (R) bonded to the α–carbon. At pH=7.4, the carboxyl group is dissociated, forming a carboxylate ion and amino group is protonated.

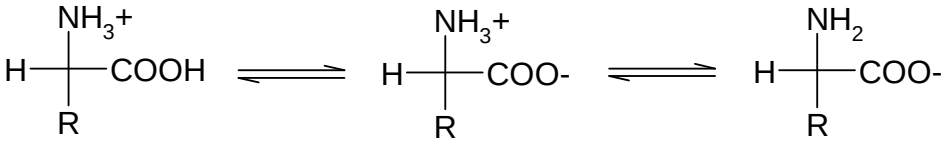

Fig. 34 Alanine in different pH. At low pH (left) amine group is ionized, at pH ca. 5.7 both groups are ionized and at high pH (right) only carboxylic group is ionized.

At neutral pH, alanine exists in dipolar form in which amino and carboxyl groups are ionized. Thus, the net charge is zero. This 'neutral' pH is known as isoelectric point (pI). At pI the sum of negative and positive charges equals zero. At physiologic pH, all amino acids have a negatively (COO^-) and positively (NH_3^+) charged group. Glutamate, aspartane, histidine, arginine and lysine have additional potentially charged groups in their side chains.

Ionic interactions, like negatively charged carboxyl groups in the side chain of aspartate or glutamate and positively charged groups in the side chain of lysin, can stabilize tertiary structure of the protein.

Concentration cell (Resting potential)

A good model of a concentration cell is a mammalian cell. Biological cell membrane is more permeable to K^+ ions than Na^+ or Cl^- ions. The hydrolysis of ATP (Adenosine-5'-triphosphate) drives the pumping of ions across the membrane. For example, the concentration of K^+ ions inside an inactive nerve cell is ca. 20 times bigger than outside, and concentration Na^+ is 10 times bigger outside the cell. The difference in concentration of ions results in a transmembrane potential difference, which is about -62 mV. The negative sign is a result of negative potential inside the cell. This potential difference is also known as the resting potential of the cell membrane. This potential plays a big role in the transmission of nerve impulses. Upon receiving of an impulse (also known as action potential) a site in the nerve cell membrane becomes transiently permeable to Na^+ ions and the transmembrane potential changes. To propagate along the nerve cell, the action potential must change the transmembrane potential difference by at least 20 mV, to values that are less negative than -40 mV. Propagation occurs when an action potential in one site of the membrane triggers an action potential in an adjacent site, with sites behind the moving action potential returning to the resting potential. [27]

Chapter 2.4

Electrokinetics

Electrokinetics was discovered over 100 years ago, and since then electrokinetic phenomena are widely used in industry and technology. In the past years electrokinetics gained a new interest due to rapid developments in lab-on-chip systems. In this chapter I will describe the most popular electrokinetic phenomena: electrophoresis, electro-osmotic flow (EOF), dielectrophoresis and others. At the end of this chapter I will show the basic applications, both industrial and academic.

Electrokinetic phenomena (EP) is a general term, which involve the migration of a charged particle or a charged surface relative to the surrounding liquid. The liquid medium is usually an electrolyte solution. EP are correlated with the electrochemical double layer on the interface of one phase, for instance on colloid surface or on the surface of glass capillary. EP constitute a result of motion and electric interactions in the electrochemical double layer. Electrokinetic phenomena may be classified in many ways, one of the most popular is to classify them according to driving force and the ensuing motion. The driving force can be represented by externally applied electric field (or to be more specific, the difference of potential). Another driving force can be gradient of pressure, also a gravitational or centrifugal field. [28] [29] The most known electrokinetic phenomena are: electrophoresis, electro-osmosis, streaming potential, sedimentation potential, dielectrophoresis and different types of electrohydrodynamic instabilities.

2.4.1 ELECTROPHORETIC EFFECT

Electrophoresis is the most known type of electrokinetic phenomena. It is defined as the movement of a charged object (a colloid particle, protein or ion) relative to a stationary liquid phase driven by external electric field. (see Fig. 35)

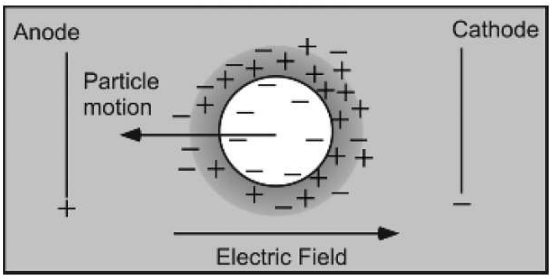

Fig. 35 Electrophoresis is a movement of charged object in external electric field. In this case a colloid particle with a negative charge on the surface is moving in the liquid medium to a positive electrode, an anode.

A charged object in an electric field experiences a force:

$$\vec{F} = q \cdot \vec{E} \tag{69}$$

In a viscous medium a friction between this object on fluid takes place, and the object moves with a velocity *v*. Electrophoretic mobility μ is a measure of the velocity of the object in external electric field:

$$\mu = \frac{\vec{v}}{\vec{E}} \tag{70}$$

The force is

$$\vec{F} = q \cdot \vec{E} = 6\pi\eta R v \tag{71}$$

and mobility:

$$\mu = \frac{q}{6\pi\eta R} \tag{72}$$

Where *R* is a radius of the particle and η is viscosity of the solvent. Values of electrophoretic mobility of most popular ions are presented in Table 2.

As mentioned earlier, the force acts on the particle when it possesses an electric charge. If the object is in electrolyte solution (and almost all real systems are electrolytes) an electrochemical double layer creates around the object. The electrophoretic mobility of the particle depends on the properties—more precisely on the thickens compared to the size of the object—of the double layer.

Table 2. Electrophoretic mobility and bare ion radii of typical ions in 25 ℃ [28]

Ion	Electrophoretic mobility $\times 10^{-8}$ $[m^2 V^{-1} s^{-1}]$	Bare ion radius [nm]
H^+	36.3	—
Na^+	5.19	0.095
K^+	7.62	0.133
Ca^{2+}	6.17	0.099
OH^-	20.48	0.176
Cl^-	7.91	0.181

This is described as the ratio of the thickness of double layer or the Debye length, κ and the radius of particle a. There are two cases:

i) The double layer is thin, compared to the particle:

$$\kappa \cdot a \gg 1 \tag{73}$$

In case of a thin double layer the electrophoretic mobility is given as:

$$\mu = \frac{\varepsilon \zeta}{\eta} \tag{74}$$

where ζ is a Zeta potential (a potential at the end of the Stern layer). This is known as the Helmholtz-Smoluchowski limit.

ii) The double layer is thick, compared to the size of the particle:

$$\kappa \cdot a \ll 1 \tag{75}$$

when a particle has a thick double layer, the net force acting on the particle constitutes the difference between two forces: Columbic force and the friction force (or the drag force given by the Stokes law). It is because the forces which act on the double layer are not felt by the particle itself. As the electrophoretic mobility can be given as:

$$\mu = \frac{q}{6\pi \eta R} \tag{76}$$

The Zeta potential can be given as:

$$\zeta = \frac{q}{4\pi \varepsilon R} \tag{77}$$

Combining these two expressions we obtain electrophoretic mobility, referred also as the Hückel-Onsager limit:

$$\mu = \frac{2\varepsilon\zeta}{3\eta} \tag{78}$$

2.4.2 ELECTRO-OSMOTIC FLOW

Contrary to the electrophoresis, in electro-osmosis (EO) we have a movement of electrolyte solution relative to a stationary charged surface. A typical example of electro-osmosis is an electro-osmotic flow (EOF) in a thin capillary. This is an important issue in capillary zone electrophoresis (CZE). A typical electro-osmotic flow through a capillary is shown in Fig. 36

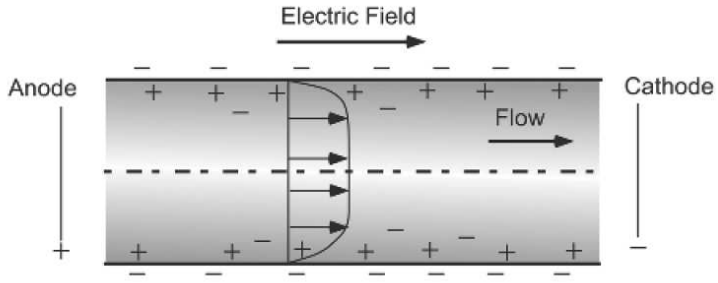

Fig. 36 A typical example of the electro-osmotic flow (EOF) in a thin capillary. [20]

The electro-osmotic flow is defined as:

$$v_{\mathrm{EOF}} = \frac{\varepsilon \cdot \zeta}{4\pi\eta} \tag{79}$$

where:

ζ – Zeta potential, measured at the plane of shear, close to the interface between liquid medium and solid state,
η – viscosity of the medium.

A double layer exists near the walls of the capillary. When we apply an electric field across the capillary, cations in the diffuse part of double layer migrate in the direction of the cathode. The diameter of the capillary is small therefore the migrating ions carry a water molecule with them (they are surrounded by solvent, in this case a water molecules). The result we obtain is a net flow of a liquid medium (in the case of CZE is typically a buffer solution) in the direction of negative electrode. The Zeta potential is inverse to the concentration of the

electrolyte: when we increase the concentration of the electrolyte we decrease the electro-osmotic flow.

Another interesting feature of EOF is a flow profile in the channel or a pipe. In a channel, the frictional forces cause a laminar or a parabolic flow profile. The flow velocity is the highest in the very center of the tube and approaches zero near the wall. This velocity gradient has a big practical importance in chromatography, because it results in significant band broadening.

In case of electro-osmosis, where the driving force constitutes a difference of the potential there is no drop of the pressure. Flow velocity is uniform across the entire capillary or a tube, except for a distance which is very close to the wall where velocity also approaches to zero. (Fig. 37)

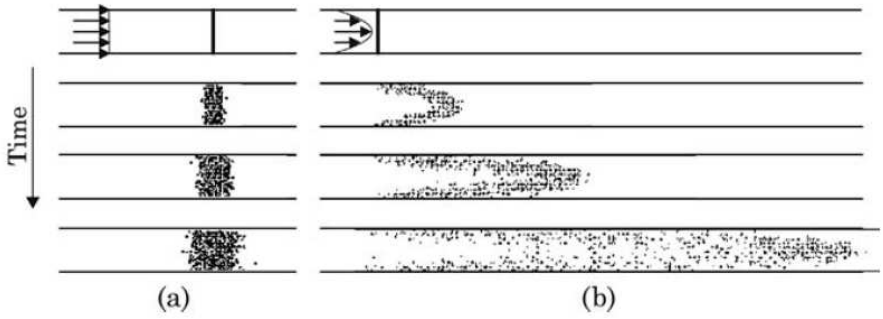

Fig. 37 Particle distribution in two channels is a good visualization of the flow profile: (a) an uniform velocity profile, which is typical for electro-osmotic flow (b) parabolic velocity profile, which is a normal profile for a pressure driven flow. [30]

2.4.3 STREAMING POTENTIAL

Let's consider a system with a charged walls and electrolyte solution which is made to flow with a pressure gradient. In such a system an electric field is created. A good example of that is a negatively charged thin capillary and an electrolyte solution is pumped through (Fig. 38). Electrolyte flows like that are usually made in narrow micro-channels (quite often capillary are used) connected with two reservoirs. The conditions to obtain streaming potential are: the concentration of electrolyte is the same and there is no net current flowing through the system. In this case the steady-state electric field is developed between two reservoirs. The streaming potential is considered to be an opposite to the phenomenon of electro-osmosis.

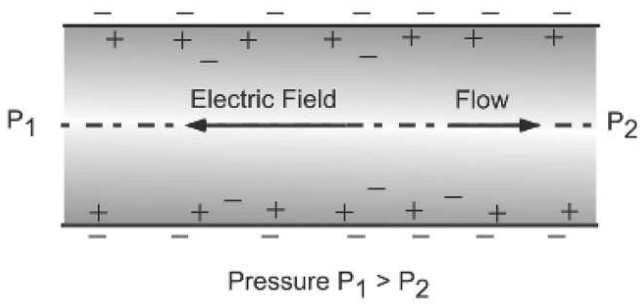

Fig. 38 An electric field is created when we apply a pressure gradient of electrolyte between charged capillary walls. [20]

2.4.4 SEDIMENTATION POTENTIAL

Sedimentation potential is created when charged particles (i.e. colloids) move relatively to a liquid. This phenomenon is sometimes known as the Dorn effect or migration potential. The movement of the particles can be in gravitational field (see Fig. 39) or in artificially created centrifugal field.

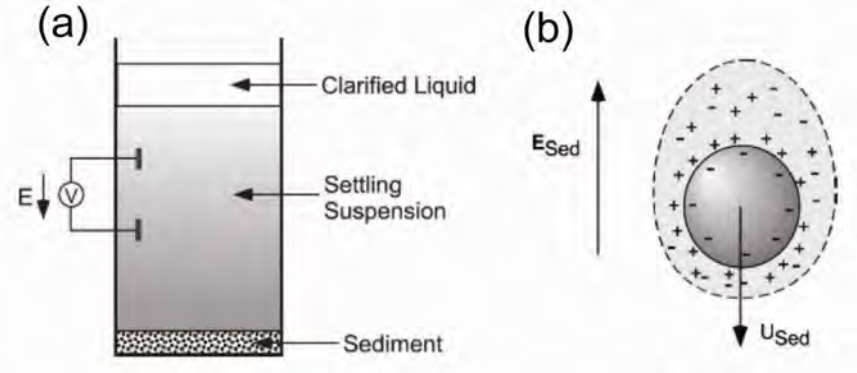

Fig. 39 (a) Sedimentation potential created by colloid suspension in a gravitational field. (b) detailed view of sedimentation of a charged colloidal particle in an electrolyte solution driven by gravity. [20]

In the system shown in Fig. 39 at the very beginning the potential difference is zero. As the colloidal particles sediment, the concentration of charged colloids increase at the bottom of the tank. As a result, we obtain a potential difference between two points: one of them is located near the surface, and the second near to the bottom of the tank. [20] The detailed view of charged colloidal particle under the gravitational force is shown in Fig. 39b. The electrical double layer surrounding each particle is distorted by the liquid flow around the particle, and it is known as relaxation effect. The electrolyte solution behind each particle

carries an excess of ions compared to the concentration of ions in front of the particle. The total current must be zero, an induced electric field is set up and the net current is zero. When we place two electrodes in the tank we are able to measure induced electrical potential gradient.

2.4.5 DIELECTROPHORETIC EFFECT (DEP)

The term dielectrophoresis (DEP) was used for the first time in 1951 by Herbert A. Pohl. Applying an electric field to a polarizable particle causes formation of a dipole inside the particle. Simultaneously, a certain free charge is accumulated on the surface as a response to that dipole.

Let's analyze the particle in uniform or non-uniform electric field. In uniform EF forces applied to the particle are equal and opposite, so there is no net force working on the particle. If the EF is non-uniform, then the forces on one side of the particle will not be equal to the forces acting on the other side, and a net force will be working on the particle. This net force is called dielectrophoretic force, and the equation for time averaged dielectrophoretic force is shown in equation (80). [31]

$$\left\langle \vec{F}_{\mathrm{DEP}} \right\rangle = \pi \varepsilon_m a^3 \,\mathrm{Re}\left[\frac{\tilde{\varepsilon}_p - \tilde{\varepsilon}_m}{\tilde{\varepsilon}_p + 2\tilde{\varepsilon}_m} \right] \nabla \left| \vec{E} \right|^2 \tag{80}$$

where $\tilde{\varepsilon}$ indicates the complex dielectric permittivity:

$$\tilde{\varepsilon} = \varepsilon - i\frac{\sigma}{\omega} \tag{81}$$

σ – conductivity of the particle or the surrounding medium,

ω – the frequency of changes of the electric field (i.e. frequency of the AC signal).

The most important feature of dielectrophoresis is a fact that the expression (80) has the Clausius-Mossotti (CM) formula inside. CM formula has a negative or positive sign and dielectrophoretic force is a vector, therefore a change of CM sign will result in a change of direction of the force. If real part of CM factor is positive, then DEP force is also positive and the force acts in the direction of the increasing field gradient. The attractive force acts on the side, where the electric field has the biggest value. The particle moves toward the region of the highest value of the electric field – this process we call positive dielectrophoresis (p-DEP). If value of real part of CM factor has a negative sign, the value of the DEP force is also negative. The particle is repelled from regions of a high electric field down the field gradient.

This is referred as negative electrophoresis (n-DEP). [31] A typical case of particle in non-uniform EF is shown in Fig. 40.

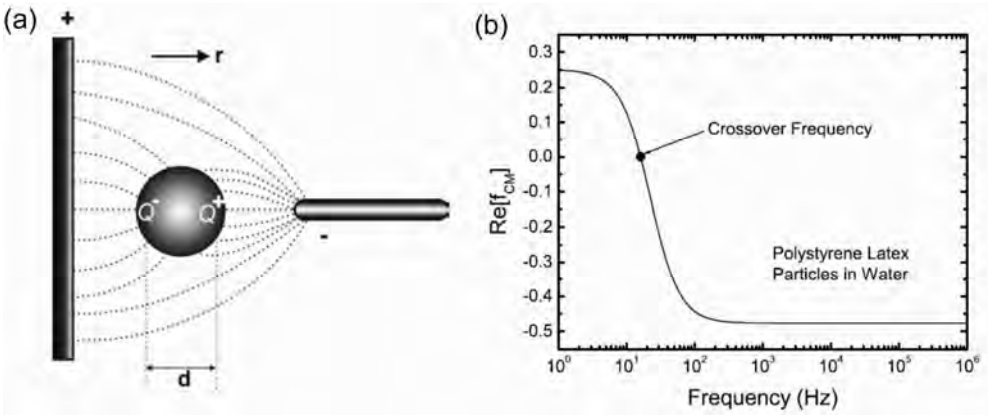

Fig. 40 A polarizable particle in non-uniform electric field: Columbic forces induced on the particle from both sides are non equal and as a result a net force is applied to the particle. (a) [28] Real part of the Clausius-Mossotti factor as a function of the frequency for a polystyrene particle in water. Two regimes of dielectrophoresis are marked with a 'crossover frequency' (c_{freq}): at higher frequencies than c_{freq} the system exhibit negative DEP force, whereas for a lower frequency system exhibits a positive DEP force. (b) [20]

It is important to mention that dielectrophoretic forces require enormous electric fields, usually in the range of 10^6 V m^{-1}. In macroscopic systems, to obtain such an intensity of electric field, we should apply a very large difference of potential to the electrodes. The typical distance over the electrodes in microsystems is tens or hundreds of micrometers. Thus, to generate useful DEP force, we can easily create big electric fields just by applying tens of volts.

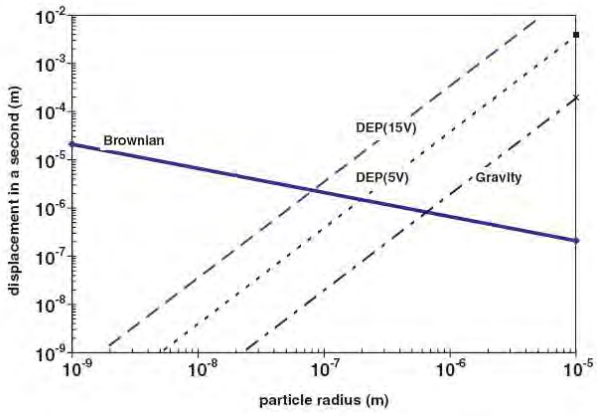

Fig. 41 Scaling relationship between gravity, Brownian motion and DEP. Plot shows particle displacement in 1 s versus particle radius (particle density is 1050 kg·m^{-3}). The characteristic length used in this plot is 25 µm. [32]

Another important issue of DEP is the scale of particles. Gravitational force and thermal effects, associated with Brownian motion, have influence on particles. If the particle has a nanometer dimensions (which is typical size for nano-particles, quantum dots etc.) Brownian motion is dominant, whereas for big particles (tens of hundreds of micrometers) gravity is dominant (see Fig. 41). Thus, for particles with a micron regime gravitational force can be overcome with a DEP force, and relatively low electric field.

2.4.6 ELECTRO-ROTATION

An external electric field applied to a polarizable object results in the formation of an induced dipole moment. External, uniform electric field acts on two charges which are at the end of the dipole and which experience equal and opposite forces (see Fig. 42a). These forces result in a torque around the center point of the dipole. As a result, the dipole is arranged parallelly to the electric field lines. A setup of four electrodes organized in a way to created electro-rotation is shown in Fig. 42b.

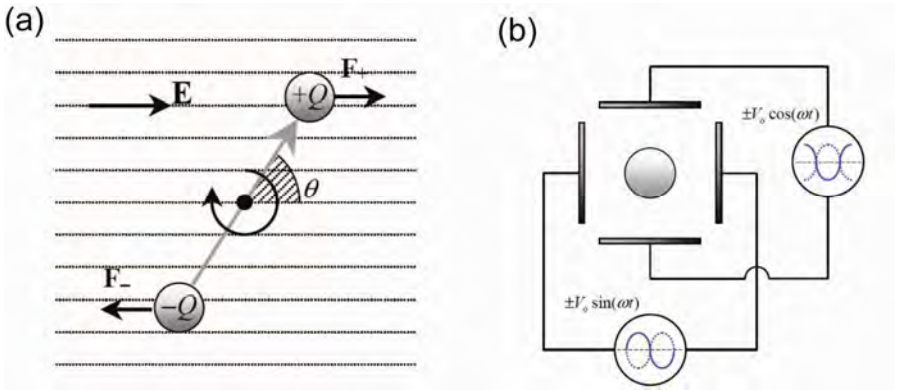

Fig. 42 In uniform electric field two equal forces try to align dipole with the lines of electric field (a). A setup for electro-rotation: two pairs of electrodes and four signals, successively 90° out of phase, are applied to them making the object rotating synchronously with the signal. (b) [28]

Rotating or circularly polarized electric field applied to the system induce a dipole which tries to align with the lines of electric field. The signal applied to the electrodes is phase-shifted, the particles experience a constant torque and rotate around their axis. The torque is zero when the phase angle between induced dipole and the applied field is zero, whereas torque has maximum value when the phase is ±90°. Electro-rotational torque can be given with equation:

$$\Gamma_{\mathrm{ROT}} = -4\pi\varepsilon_m a^3 \,\mathrm{Im}\left[\frac{\tilde{\varepsilon}_p - \tilde{\varepsilon}_m}{\tilde{\varepsilon}_p + 2\tilde{\varepsilon}_m}\right] \cdot \left|\vec{E}\right|^2 \tag{82}$$

where a^3 denotes the volume of the particle. [28]

2.4.7 TRAVELING-WAVE DIELECTROPHORESIS (TW-DEP)

The phenomenon of traveling-wave dielectrophoresis (tw-DEP) was discovered in the early eighties. Tw-DEP is similar to the electro-rotation effect, however in this case electric field is not rotating but changes linearly along the electrodes on the surface (see Fig. 43). An shifted-phase AC signal travels along the series of electrodes. This AC field induce a moving dipole. If the electric field is moving fast, the dipole is physically displaced from the electric field peak. The interaction between EF and induced dipole indicates a force which is the same as the direction of travel of EF.

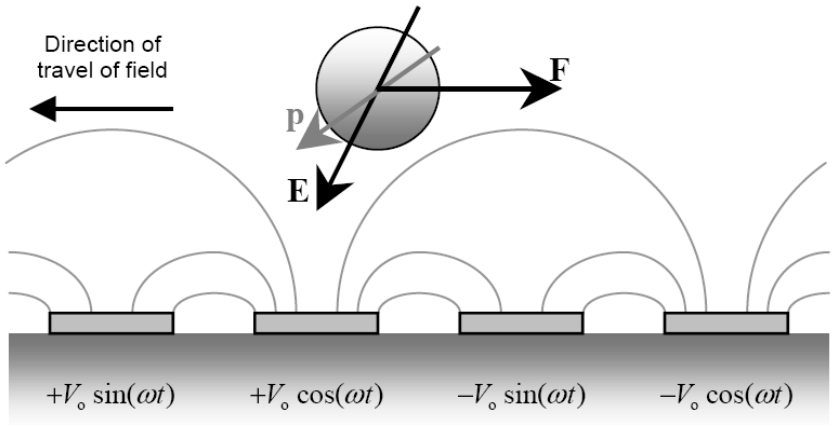

Fig. 43 A general view of particle over the series of electrodes array. A phase-shifted signals are applied to obtain a movement of the particle. [28] [31]

To effectively use tw-DEP in experiments we have to simultaneously fulfill two criteria of the frequency and conductivity:

i) the negative DEP force has to work on the particle in the electric field,

ii) the imaginary part of the Clausius-Mossotti factor has non-zero value, and as a result the particle can move above the electrodes

The plots of real and imaginary value of CM formula as a function of the frequency are shown in Fig. 44.

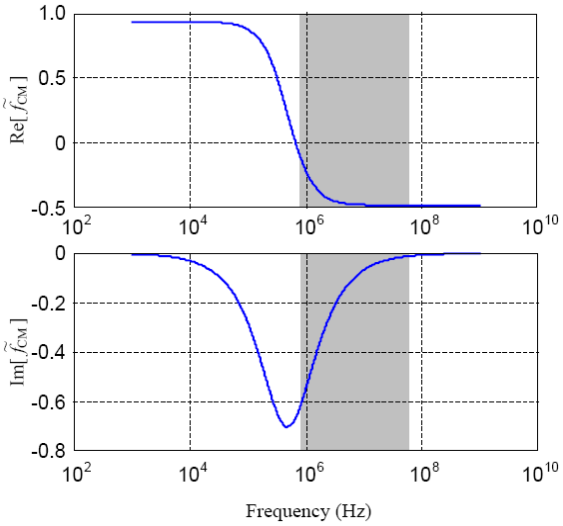

Fig. 44 Real (top) and imaginary (bottom) part of the Clausius-Mossotti (CM) factor as a function of frequency. Plots calculated for a solid state latex particles suspended in low conductivity liquid. Tw-DEP occurs only in grey region. [28]

2.4.8 Induced Charge Electro-Kinetics (ICEK)

An interesting example of ICEK is a phenomenon known as Induced Charge Electro-Osmotic (ICEO). It was discovered by Russian scientists in the sixties, yet it became unknown on the West till nineties, since all the papers were published only in Russian language.

A good example of ICEO is an uncharged, polarizable cylinder—in practice a piece of metal wire—placed in external electric field. As shown in Fig. 45a, shortly after applying EF, metal cylinder is polarized. Also, ionic current

$$\vec{J} = \sigma \cdot \vec{E} \tag{83}$$

affects the applied electric field. If there is no Faradaic reactions, ionic charge accumulate as the double layer around the wire. As shown in Fig. 45b, the EF lines become expelled and are parallel to the wire surface. The induced diffuse charge ζ is non-uniform. It is negative where the initial current leaves the surface of the wire, and the positive where it enters (see Fig. 45b). We can predict the ICEO flow around the wire; the fluid is drawn along the field axis and it is ejected radially. ICEO dominates if total Zeta potential is less than:

$$\xi \ll 2(\frac{kT}{e})\log(\frac{L}{\lambda_D}) \tag{84}$$

where total Zeta potential is defined as a sum of initial and induced potential. In a highly charged particles, this condition is violated and surface conduction lead to non-equilibrium electro-surface phenomena (NESP). For a very high voltages it may lead to second-kind electrostatic phenomena. [33] [34]

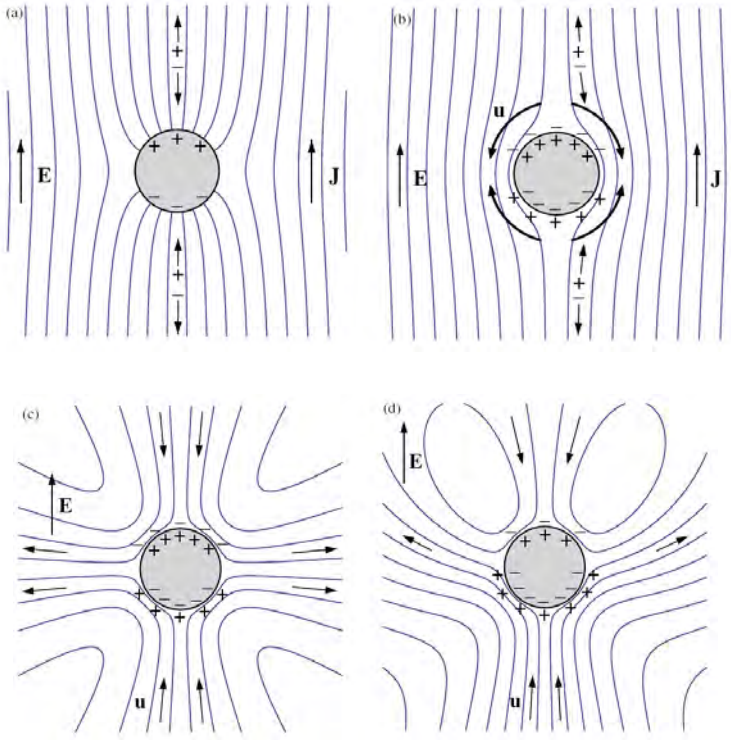

Fig. 45 Cylindrical metal wire is placed in external electric field in a solution of electrolyte (a) shortly after applying EF, (b) after applying EF, polarized wire attracts counterions from the solution, double layer on the interface is created, (c) resulting ICEO streamlines around the wire, (d) the flow around charged metal wire. [34]

2.4.9 APPLICATION OF ELECTROKINETIC PHENOMENA

Electrokinetic phenomena, very interesting from the academic point of view, are also widely used and applied in science and technology. Electrophoresis has been used for many years in biochemistry and molecular biology laboratories (see Fig. 46 for a CZE and gel electrophoresis setups). It is used to characterize and fractionate proteins and DNA fragments. This may be performed in solutions in a capillary and is also known as capillary electrophoresis (CE or CZE – Capillary Zone Electrophoresis). Instead of capillary poly(acryl amide) gel is used and this technique is known as gel electrophoresis. In gel electrophoresis a pH gradient can be used to improve separation. This is especially useful in separation of the proteins. Each fraction stops migrating at the pH where it has an isoelectric point, therefore this technique is known as isoelectric focusing.

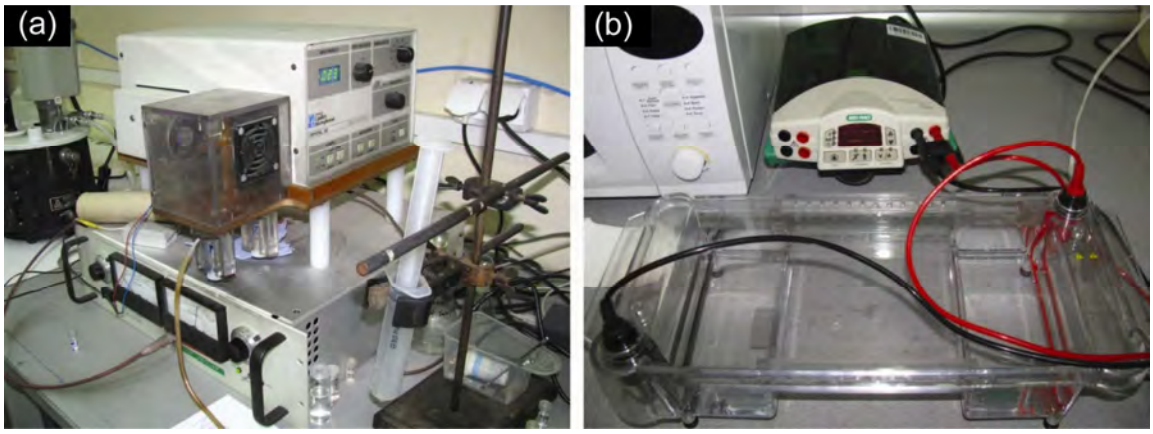

Fig. 46 Example of setups for capillary (a) and gel (b) electrophoresis.

Electro-osmosis may be used in environmental remediation, i.e. the removal of pollutants from contaminated soil. First step is placing electrodes in contaminated soil, and then applying a potential difference between them. As a result, injected water is forced to flow through the granular soil, taking along the contaminants. Another application of electro-osmosis is dewatering of porous solutions, such as soils or sludges. Electro-osmosis is used in electrodialysis. Under the influence of an electric field and aqueous electrolyte solution is transported across anion and cation exchange membranes. Ions are accumulated at the membrane that has the same charge sign. In this way the solution is separated in an electrolyte-freed and an electrolyte-enriched fraction. [35]

Industrial applications are electrophoretic coatings (e.g. coatings in car industry). This technique is also known as electrodeposition, the material to be coated on the electrode has opposite charge than electrode. Electrodeposition is successful in coating surfaces that are hardly accessible: image displays, light bulbs, the inner walls of cans for food and drinks, and bodies of the cars. Electrophoretic imaging in a liquid environment uses colloidal particles of pigments dispersed in a liquid to which dyes may be added to improve the contrast. It is used in flat-panel displays and in photocopying devices.

Electrokinetic phenomena are also used in transdermal administration of therapeutic agents and this method called iontophoresis. [36] Transdermal drug delivery is a very convenient way of drug administration, however its application is limited to molecules with a low molecular weight due to low permeability of human skin. In iontophoresis electric field impose a movement of ions: positive ions in the anodal compartment move towards the cathode and anions move in opposite direction (see Fig. 47).

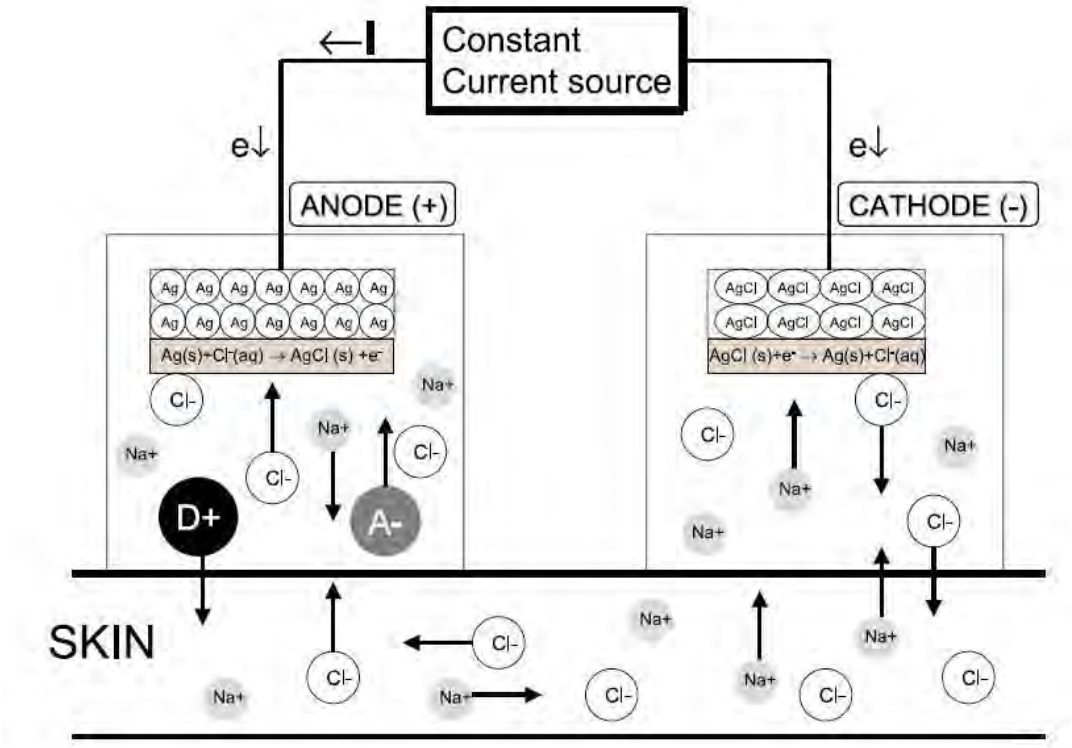

Fig. 47 Iontophoresis using Ag/AgCl electrode system. [37] Anode contains an ionizable active ingredient D^+ and its counter-ion A^- and NaCl. Application of an electric field causes a flow of current through the patient's skin. As the active ingredient is a cation it is transported from the anodal compartment into the skin.

Iontophoresis can provide an alternative for drugs with therapeutic agents which have a low oral bioavailability or have a short half-time life. [37]

2.5 REFERENCES FOR CHAPTER 2

[1] W. M. Gelbart and A. BenShaul, Journal of Physical Chemistry **100**, 13169-13189 (1996).

[2] C.N. Likos, Physics Reports-review Section of Physics Letters **348**, 267-439 (2001).

[3] R. A. L. Jones, *Soft Condensed Matter*, 1st ed. (Oxford University Press, USA, 2002).

[4] M. E. Cates and M.R Evans, *Soft and Fragile Matter: Nonequilibrium Dynamics, Metastability and Flow (PBK)*, 1st ed. (Taylor & Francis, 2000).

[5] T. J. Sluckin, D. A. Dunmur, and H. Stegemeyer, *Crystals That Flow: Classic Papers from the History of Liquid Crystals*, 1st ed. (CRC Press, 2004).

[6] J. W. Goodby, I. M. Saez, S. J Cowling, Verena Görtz, Michael Draper, A. W. Hall, S. Sia, G. Cosquer, S.-E. Lee, and E. P. Raynes, Angew. Chem. Int. Ed. Engl **47**, 2754-2787 (2008).

[7] D. J. R. Cristaldi, S. Pennisi, and F. Pulvirenti, *Liquid Crystal Display Drivers: Techniques and Circuits*, 1st ed. (Springer, 2009).

[8] S. Wu and D. Yang, *Fundamentals of Liquid Crystal Devices* (Wiley, 2006).

[9] A. A. Sonin, *Freely Suspended Liquid Crystalline Films* (Wiley, 1999).

[10] P. Oswald and P. Pieranski, *Smectic and Columnar Liquid Crystals: Concepts and Physical Properties Illustrated by Experiments*, 1st ed. (CRC Press, 2005).
[11] ed. M. Nič, J.Jirát, B. Košata, A. Jenkins, and A. McNaught, *IUPAC Compendium of Chemical Terminology*, 2.1.0 wyd. (IUPAC, Research Triagle Park, NC, 2009).
[12] Richard Pashley and Marilyn Karaman, *Applied Colloid and Surface Chemistry*, 1st .d. (Wiley, 2004).
[13] Maurice Kleman and Oleg D. Lavrentovich, *Soft Matter Physics: An Introduction*, 1st .d. (Springer, 2002).
[14] I. W. Hamley, *Introduction to Soft Matter: Synthetic and Biological Self-Assembling Materials*, Revised (Wiley, 2007).
[15] T. Cosgrove, *Colloid Science: Principles, Methods and Applications* (Wiley-Blackwell, 2005).
[16] R. A. Serway and J. W. Jewett, *Physics for Scientists and Engineers, Volume 2, Chapters 23-46*, 7th ed. (Brooks Cole, 2007).
[17] P. Lorrain and D. R. Corson, *Electromagnetism: Principles and Applications*, 2nd ed. (W. H. Freeman, 1990).
[18] Y. S. Lee, *Self-Assembly and Nanotechnology: A Force Balance Approach* (Wiley-Interscience, 2008).
[19] H.-J. Butt and M. Kappl, *Surface and Interfacial Forces* (Wiley-VCH, 2010).
[20] J. H. Masliyah and S. Bhattacharjee, *Electrokinetic and Colloid Transport Phenomena* (Wiley-Interscience, 2006).
[21] R. van Roij, Physica A: Statistical Mechanics and Its Applications **389**, 4317-4331 (2010).
[22] K. A. Dill and Sarina Bromberg, *Molecular Driving Forces: Statistical Thermodynamics in Chemistry & Biology*, 1st ed. (Garland Science, 2002).
[23] D. Andelman, Soft Condensed Matter Physics in Molecular and Cell Biology 97-122 (2006).
[24] J. Koetz, *Polyelectrolytes and Nanoparticles* (Springer Berlin Heidelberg, 2009).
[25] P. Bertrand, A. Jonas, A. Laschewsky, and R. Legras, Macromol. Rapid Commun. **21**, 319-348 (2000).
[26] B., M. Lodish, *Molecular Cell Biology Fifth Edition* (2004).
[27] P. Atkins and J. de Paula, *Physical Chemistry*, 8th ed. (W. H. Freeman, 2006).
[28] H. Morgan and N. G. Green, *AC Electrokinetic: Colloids and Nanoparticles*, 1st ed. (Research Studies Press Ltd, 2002).
[29] W. Norde, *Colloids and Interfaces in Life Sciences*, 1st ed. (CRC Press, 2003).
[30] N.-T. Nguyen, *Micromixers: Fundamentals, Design, and Fabrication* (William Andrew, 2008).
[31] M. P. Hughes, *Nanoelectromechanics in Engineering and Biology*, 1st ed. (CRC Press, 2002).
[32] A. Castellanos, A. Ramos, A. González, N. G. Green, and H Morgan, J. Phys. D: Appl. Phys. **36**, 2584-2597 (2003).
[33] M. Z. Bazant and T. M. Squires, Physical Review Letters **92**, (2004).
[34] T. M. Squires and M. Z. Bazant, Journal of Fluid Mechanics **509**, 217-252 (2004).
[35] J. D. Zahn, *Methods in Bioengineering: Biomicrofabrication and Biomicrofluidics*, 1st ed. (Artech House, 2009).
[36] A. K. Banga, *Electrically Assisted Transdermal and Topical Drug Delivery*, 1st ed. (CRC Press, 1998).
[37] Y. N. Kalia, A. Naik, J. Garrison, and R. H. Guy, Advanced Drug Delivery Reviews **56**, 619-658 (2004).

Chapter 3 Results and discussion

Chapter 3.1
Dynamic charge separation in a free standing smectic films

Liquid crystals in their smectic phases present the interesting feature that they can be spanned over an opening (e.g. a circular rim) forming a free-standing membrane (or film). We are using these free standing smectic films (FSSF) to study the transport of ions within their plane and to study the emergence of macroscopic separation of charge FSSF can have uniform thickness—a constant number of smectic layers within the whole film—or the can be non-uniform in their thickness. It is possible to create thinner and thicker areas - either using menisci or the—so called—free floating islands of thicker material. The change of thickness on the film is associated with the presence of dislocation lines and with a change of the conductivity in the plane of the film. I discovered that application of an oscillating electric field in the plane of a film of non-uniform thickness can accumulate free electrostatic charge in the viscinity of the dislocation lines. This accumulation of charge leads to an emergence of an electro-hydrodynamic instability, macroscopic motion of the 'islands' of thicker LC and macroscopic separation of electrostatic charge. We argue that the instabilities are generated by separation of charge via electrophoretic motion of ions in the film. Interestingly, the electrophoretic motion of ions couples with the macroscopic motion of the LC material that can be observed with the use of simple optical microscopy. Importantly, and in agreement with the thesis of this dissertation the instability ensues only at frequencies smaller than critical and is most pronounced at the threshold frequencies, while at frequencies larger than critical, the phenomenon disappears. The critical frequency is associated with the time that the ions require to translate over distances comparable to the Debye screening length.

3.1.1 INTRODUCTION

Membranes and films have inspired both non-scientists and researchers for hundreds of years. The most readily available films are soap membranes and soap bubbles. Many prominent scientists spent time discovering the static shapes and dynamics of soap bubbles. Leonardo da Vinci, Isaac Newton, Robert Hooke, Charles Boys, Michael Faraday and others employed soap bubbles and films to investigate the reflection and refraction of colors of light. [1] [2] [3] Research on soap bubbles were both experimental and theoretical. In 1918 Jean Perrin observed the stepwise thinning of soap films, and simultaneously he was already familiar with the discovery of liquid crystals by Reinitzer in 1888. He connected thinning of the film with its layered structure. He was also the first person who used optical interferential method to measure thickness of the soap film. [4]

Smectic liquid crystals are phases formed by rod or disc-shaped molecules organized into one-dimensionally periodic arrays of layers. Each layer is a two dimensional fluid on the order of a molecular length in thickness. Free-standing smectic films are thin objects, formed from molecules that self-organize into a periodic stackings of layers. FSSF are stable (in appropriate conditions – up to months) because of a lack of the solvent who can evaporate, low vapor pressure of the molecules creating film, high viscosity of the smectic phase and ability of molecules to self-organize to ordered, layered structures.

When a small amount of LC which posses a smectic phase—and the environment and the air has the temperature in which the Sm phase exists—is placed on a stiff frame it is possible to span this liquid crystal over the opening in the frame. FSSF are very thin (even 2-3 molecular layer thick) yet vide structures (openings in the frames can be as big as a few millimeters). For this reason FSSF are a two-dimensional systems; the aspect ratio between the thickness and the width is as high as 10^6, they also posses the highest surface-to-volume ratio.

First experimental observations of free standing smectic films were performed by Friedel in 1922. Friedel invented method of creating free-standing smectic films based on smearing of a small amount of liquid crystal over stiff frame. The interest in FSSF revived after over two decades, at the end of 1940s. In 1953 Russian scientists, Derjaguin and Titievskaya, and in 1957 Scheludko performed first experiments on FSSF with experimental setups allowing visual observation and simultaneous control of thermodynamic condition, i.e. film diameter, pressure inside the film. [4]

Free-standing smectic film are popular and interesting subject of research due to many reasons, e.g. enormously big aspect ratio (the relation of the diameter of the film to its thickness). Typical film can be spanned over the opening which is a few millimeters wide, whereas its thickness can be as low as a few nanometers. Therefore its aspect ratio is ca.

10^6. For this reason free-standing smectic films are great models for studying phenomena in two-dimensional system. Phase transitions, surface phenomena, hydrodynamic and electro-hydrodynamic instabilities can be studied under carefully controlled conditions. FSSF are also very stable if compared with lyotropic films or soap bubbles. FSSF are stable due to absence of the solvent and the low vapor pressure of smectic-forming compounds. FSSF can be pierced with a glass fiber or steel needle without breaking. Smectic films can also vibrate and therefore they behave like a drumhead (so called smectic drums). Structure of FSSF can be changed by environment, i.e. the temperature of the frame and the air around the film, humidity or the pressure of the air. Metallic (or generally conductive) frames allow also to apply an electric field in the plane of the smectic membrane. [5]

FSSF are interesting also from the practical point of view. Problems of stability of thin films, its thinning and rupture are important in many areas, e.g., oil industry, cosmetic and food industry. Moreover, problems of molecular organization, phase transitions in thin films and elasticity are crucial for better understanding of many biological systems, like bio-membranes. [4] Experiments on FSSF can lead to precise determination of physico-chemical parameters of liquid crystals (i.e. surface tension). It is important in electronic industry when working on new Liquid Crystal Display technologies.

3.1.1.1 Structure of a free-standing smectic film

A smectic phase consists of a number of layers. In each layer the major axes of the molecules forming the smectic phase fluctuates relative to a normal to these layers. The thickness of each layer is equal to the length of the molecule. The smectic layering allows only films that are an integral number layers thick. The non-uniformity in the structure of smectic phase (i.e. change in the thickness of the layer) results in creation of a dislocation line. A good example of such a change of thickness is a meniscus around a needle or a meniscus created when smectic phase is in a contact with a solid state wall.

The basic parameters and structure of FSSF is the same as of a smectic phase in bulk. In FSSF obtained in experiments there are two types of structures which are absent in the normal smectic phase. These structures are holes and islands (see Fig. 48).

Both holes and islands can form spontaneously or can be generated artificially in the FSSF. The hole is when a part of the film is thicker than the surrounding smectic phase. The difference can be as small as one molecular layer (see Fig. 48b) or higher. The difference in the thickness is related with the dislocation on the border of the film and the hole.

The island is a thicker part of smectic film (‘pencake-like’ stacks of extra layers of molecules). The picture of the island is shown in Fig. 48c while Fig. 48d illustrates a schematic representation of the smectic layers. Each change of thickness of the

membrane by one smectic layer is associated with one dislocation line running along the boundary between the thicker and thinner portions of the film. The dislocations lines can group together provide for an abrupt change of thickness by several smectic layers over a short in the plane of the film.

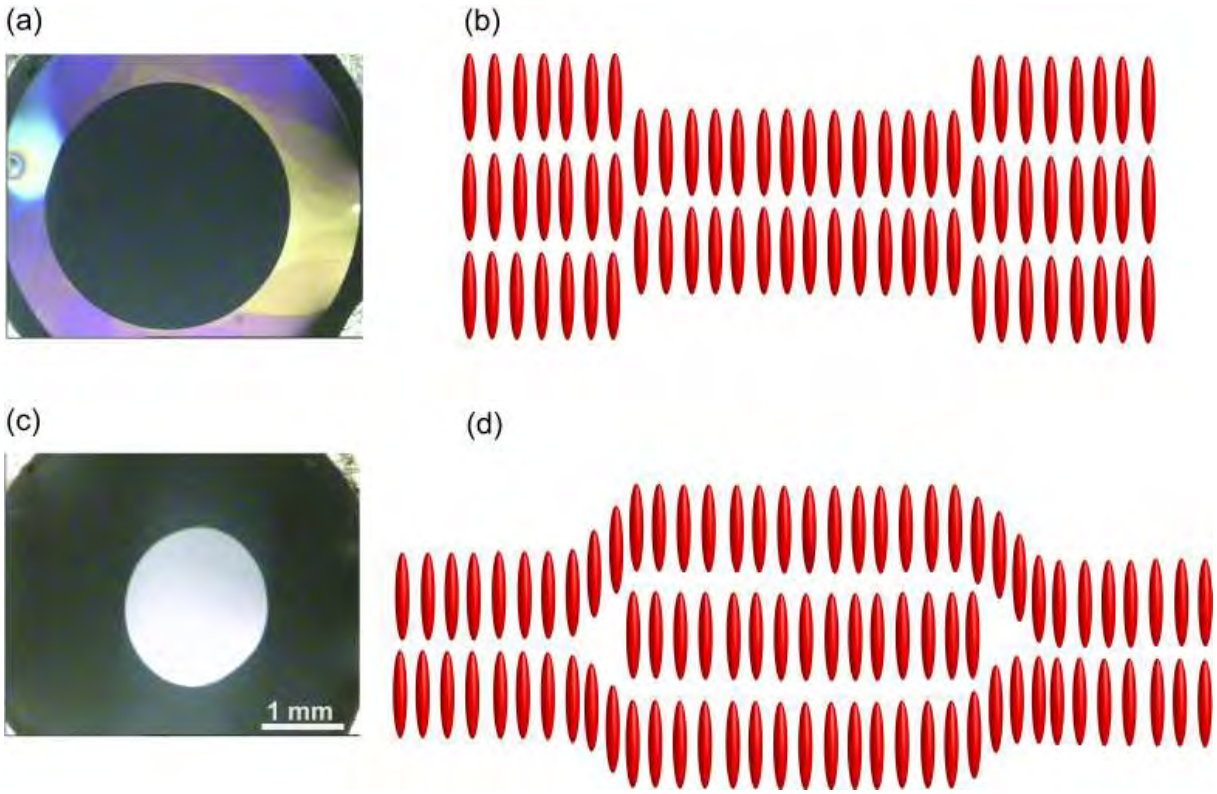

Fig. 48 Two types films of non-uniform thickness: a hole (a, b) and an island (c, d). A hole is a thinner part of a smectic film, (a) visible as a circular black shape in the center of the film. A schematic view of the smectic layers across the film is shown on figure (c). An island is a thicker part of the smectic film, in reflected light it is visible as a circular shape. In figure (d) is shown a schematic view across the film for the liquid crystal island.
Fig. 48a and Fig. 48c were taken for 8CB liquid crystal via optical microscope in reflected light.

Those two structures can form in the main area of the film. Every FSSF have to be stretched on some kind of a frame (made of metal or glass). Meniscus forms at the edge of the frame. A schematic view of a meniscus near a stiff wall is shown in Fig. 49.

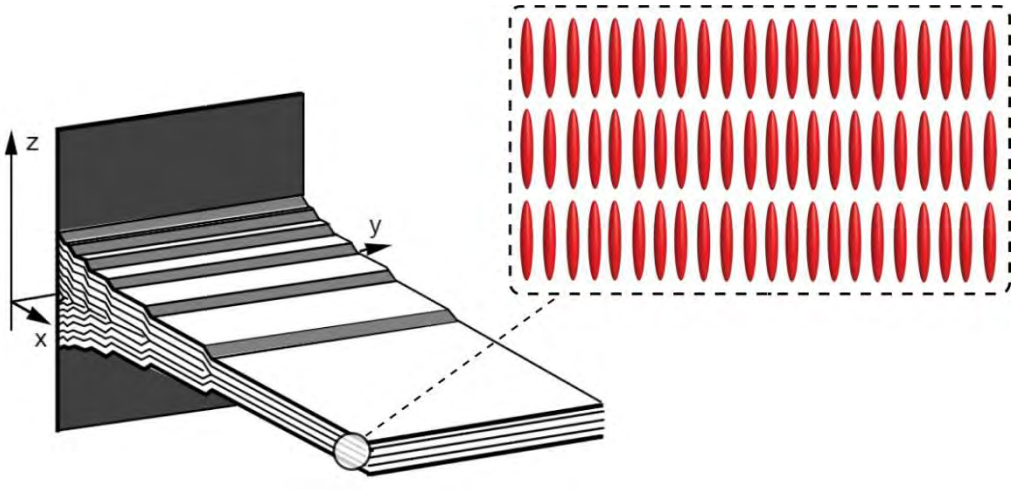

Fig. 49 A schematic picture of the meniscus in the free-standing smectic film close to the wall, i.e. a metal frame. [6]

FSSF can be pierced with a glass fiber or a steel needle, first coated with a small amount of liquid crystal. Upon piercing a meniscus forms around the needle. As the thickness of the meniscus can change with a discrete values of the molecular layer, it is obvious that every change of the thickness of the film results in dislocation line within the film. In contrary to a solid state, in FSSF dislocations are repelled from the surfaces. In meniscus and other structures (holes and islands) the dislocations are located in the middle of meniscus or the film. [6]

3.1.1.2 Ionic impurities in FSSF

Liquid crystals that are free from ionic impurities are good insulators. An electrostatic charge can be injected into LC samples e.g., by a high intensity laser field, chemical doping [7], rubbing or high electric field [8], or acquired from the surrounding atmosphere. Ionic impurities are unwanted in LC displays [9] because presence of charged impurities may lead to:

i) screening of the electrodes [10] ,
ii) decrease of the quality of images via long-term image retention [11],
iii) flickering at low frequency due to the local change of the electric field by moving ions [12], or
iv) retention of the boundary of the image due to the distortion of transmission at the edges of the pixels [13].

Long term, constant electric field applied to LC cells leads to the phenomenon of image

retention (see Fig. 50), caused by the leakage of current [14], which is also attributed to the presence of small concentrations of ionic impurities. The source of ions (or ionic impurities) in Liquid Crystal Displays are:

i) alignment layers,
ii) surrounding glue,
iii) UV glue polymerization,
iv) the filling process,
v) dissociation of LC molecules,
vi) residue of the organic synthesis process,

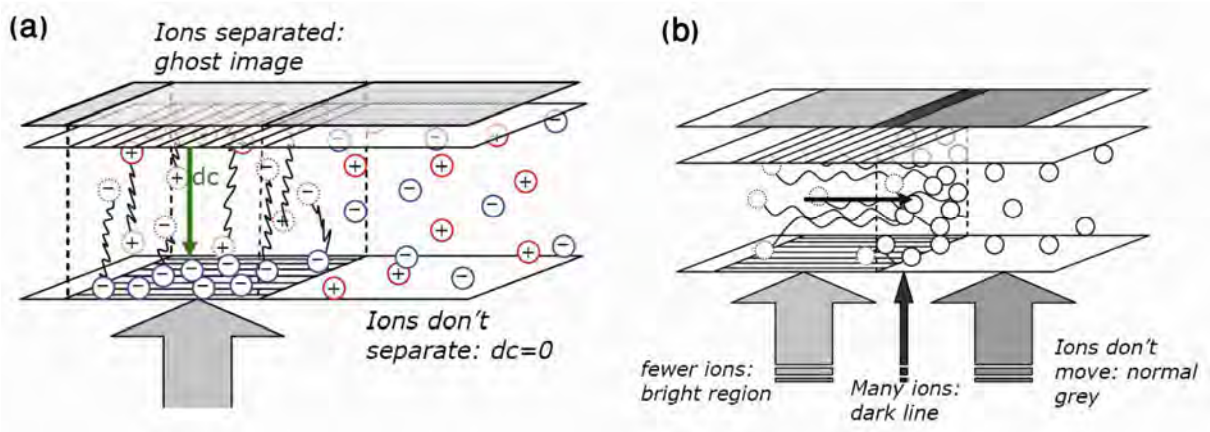

Fig. 50 Schematic illustration of different types of image retention caused by ionic impurities (a) image sticking, (b) boundary image retention.
(source: Goran Stojmenovik, Image sticking and burn-in in flat panel displays, white paper)

We can divide image retention phenomena into main three types:

1) image sticking – this is also known as ghost image phenomena or shortly, 'ghosting'. LCDs are controlled with changes of polarity. The driving signal posses a small DC component. If steady image is displayer for long time this constant component separate the ions in liquid crystal cell, negative ions migrate to positive electrode and positive ions migrate to negative electrode. Moreover, those separated ions can stick to the alignment layer. When steady image is removed and uniform background is displayed, the previously separated ions will remain in their positions, sticked to the alignment layer. Separated ions create electric field who interferes with applied electric field which controls LC cell. The regions of LCD where ions separate will posses different transmission than the rest of LCD where there is no ions. This is the reason of 'ghost images' (see Fig. 51). The simplest way to avoid ghosting is to eliminate a DC component from the electric signal switching the LC cell.

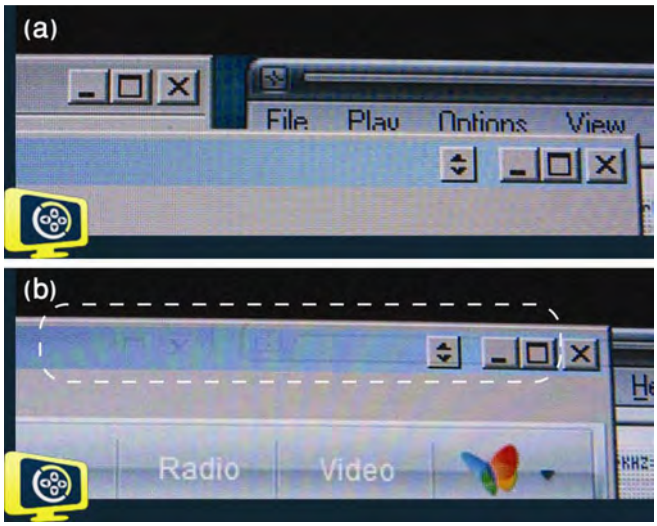

Fig. 51 Ghost images: (a) view of a part of the LCD with an image displayed for a long period of time, (b) after removing top windows there is still visible residue of them (marked with white lines)
(source: http://www.widescreengamer.com/articles/lcd_image_screen_burn_on_dell_2005fpw.html)

2) change in light transmission – when electric field is applied through a LC cell, the response is a certain level of transmission of the light. As the ions in the cell separate, they modify the internal electric field and as the result the light transmission through the cell is changing. This results in different grey level, which changes with the concentration of ionic impurities in the cell.

3) Boundary image retention – is related with increased concentration of the ions on the border of static image. When static image is displayed for a long time, ions move (diffuse) sideways—as the electric field is the same in the LC cell—to the border of the image. When they reach border of displayed image they stop and in this place the concentration of the ions will increase, and as a result the border of the image will become dark. After removing static image those dark lines still become visible. This is the worst case of image retention—it takes a lot of time to develop in on the LCD but also it takes long to dispose it due to facet that movement of ions in direction perpendicular to the lines of electric field base on diffusion.
(source: Goran Stojmenovik, Image sticking and burn-in in flat panel displays, white paper)

Even if the material is free from charged impurities, they inevitably appear during the use of the material: either via tribocharging due to the rubbing of the bounding surfaces, or via ionization due to high electric field or UV illumination, or by contamination from the environment.

The study of ion transport in LCs, and in particular, a design for a simple method

of visualization of the presence of ions in LC materials and of evaluation of their concentration is not only of basic interest but also of technological importance. In addition the movement of ions shed light on the local structure of the liquid crystal material [15] [16]. The transport of ions in ferroelectric smectic liquid crystals was studied from the point of view of their potential application in display technology with the emphasis on switching and bistability of smectic displays [17].

3.1.1.3 Electro-hydrodynamic instabilities in FSSF

The situation in FSSF under external electric field is quite similar in principle to a Rayleigh-Bérnard convection. Electro-convection can be observed in FSSFs driven out of equilibrium with the use of an external electric field. This field can be uniform in the plane of the film (Fig. 52a) or can be applied radially (Fig. 52b). Electro-convection in FSSF gained much attention and were extensively examined both experimentally [18] [19] [20] [21] and theoretically. [22]

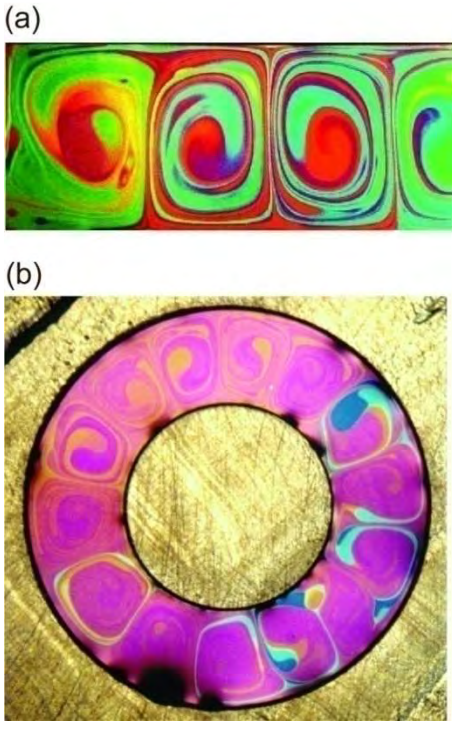

Fig. 52 Electrically driven convection in a free standing smectic film (8CB): (a) between two metal wires placed 2 mm apart, (b) electroconvection in an annular smectic film. The electric field is applied between inner electrode and external metal frame. Both pictures are recorded via CCD camera in reflected light. Different colors are a result of different thickness of the film.
(source: http://www.physics.utoronto.ca/~nonlin/index.html)

When electric field is applied to the electrodes there is a critical voltage above which convection ensues. Convection can present different patterns depending on the magnitude of the electric field—Fig. 52—as the applied voltage increases the flow within the film changes from steady to unsteady and turbulent. [23]

Electric field applied across the electrodes drives an electric current through the film. If the applied voltage is low, the current is flowing through the film. Pure LC are isolators, however they posses traces of ionic impurities. Additionally is such experiments LC are doped with organic compound which is a good acceptor of electrons. Above critical voltage, the electrical forces lead to an instability in the film. As a result, vortices appear as shown in Fig. 52.

All experiments on electro-convection were performed for a uniform smectic films whereas in my experiments there is always an abrupt change in the thickness. The change is a result of piercing the film with the needle and thus creating a meniscus around the needle. The change is a result of creating an island in the very center of the film. The experiments were performed for a few liquid crystals, both ferroelectric and non-ferroelectric, in a wide span of temperatures.

3.1.2 MATERIALS AND METHODS

3.1.2.1 Experimental setup

The simplified view of experimental setup that we used is illustrated in Fig. 53.

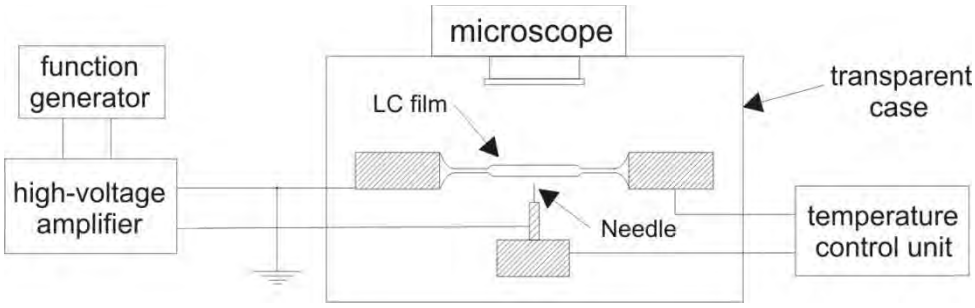

Fig. 53 A schematic illustration of our experimental setup. The metal frame on which we span the LC films was enclosed in a transparent screen-box to isolate the setup thermally and to reduce contamination from the air. I observed the film with a microscope in reflected light. The frame and the needle were both equipped with temperature control units and with connections to the high voltage amplifier.

A circular metal rim with an opening of a diameter of 5 mm was embedded in a hot stage. Both the rim and the stage were made of brass. The stage was mounted on an XYZ micromanipulator (Leica (XY) and ThorLabs (Z)).

To control the temperature of the stage, a PID temperature controller (type 650, Unipan, Poland) was used, allowing the control of the temperature of the stage in the range from 0 to 99 ℃ with an accuracy of 0.1 ℃. T he temperature was monitored independently with two PT100 (Elfa, Poland) sensors. The first sensor was connected to the PID controller, and the second to a digital multimeter (196 System DMM, Keithley, USA).

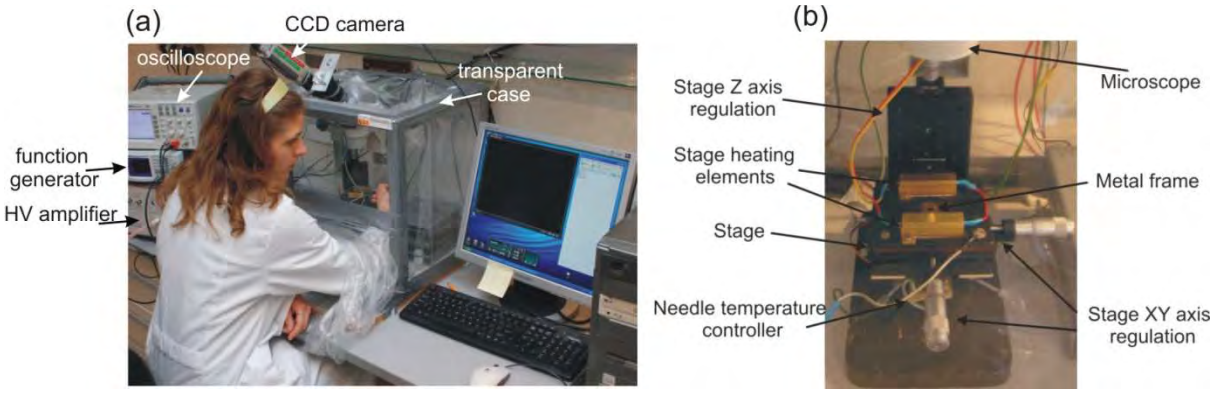

Fig. 54 Picture of (a) experimental setup used in experiments. (b) detailed view of the metal stage with circular opening and corresponding micromanipulators.

Below the circular opening a stainless steel needle (diameter ca. 400 μm, with the tip sharpened to a radius of curvature of approximately 25 μm) was placed. The needle was mounted on its own heat stage and an XYZ micromanipulator (Leica). The temperature of the steel needle was controlled with a home-made electronic device, allowing the control with an accuracy of 0.01 ℃. A multimeter connected to the PT100 temperature sensor mounted on the needle stage was employed to monitor the temperature of the needle.

A radial electric field between the needle and the circular rim was applied. The circular rim and the needle were connected to a high voltage amplifier (10/10B, Trek Inc.) controlled with a function generator (5062, Tabor Electronics Ltd.). Square wave functions with duty cycle 50 % were applied. Frequency (f) varied from single Hz's to few kHz, while the peak-to-peak potential difference (U) from tens of volts to 1 kV. Frequency and potential difference were monitored with a digital oscilloscope (54504A, Hewlett-Packard).

The liquid crystalline film was observed using a Nikon MSZ645 stereoscope equipped with a colour CCD camera (Vido, AU-CC882SF) mounted on one of the eyepieces and connected to a PC via an analogue video card, and an LED light source, positioned in the second eyepiece. Both the camera and the LED were aligned with the optical axes with the use of home-made manipulators. All observations were carried out in reflected light: the light from the LED travelled through the stereoscope from one of the eyepieces onto the film; reflected from the film and came back through the stereoscope to the second eyepiece and the CCD chip.

The stereoscope and the stage was placed in a transparent box in order to isolate the experimental setup thermally, to avoid the motion of the air above the film, and to prevent the film from absorbing impurities from the air. The box was equipped with a polyethylene sleeve to allow for manipulation of the samples (see Fig. 54a for details).

3.1.2.2 Materials

I investigated four different liquid crystalline materials:

i) 4-octyl-4'-cyanobiphenyl (**8CB**),
ii) 4'-nitrophenyl-4-octyloxybenzoate (**NPOB**),
iii) methylbutyl 4-n-nonanoyloxy-biphenyl-4'-carboxylate (**MBOBC**), and
iv) 4-[4-(1-methylheptyloxycarbonyl)phenyl]-4'-[6-(propanoyloxy)hexyloxy]biphenyl-4-carboxylate (**MHPPHBC**).

The chemical structures of these compounds are shown in Fig. 55. For sequence of phase transitions see Table 3.

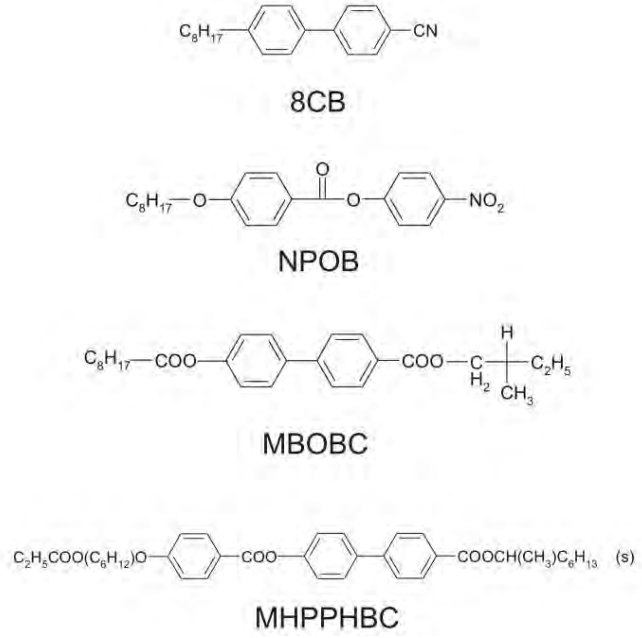

Fig. 55 The chemical structure of liquid crystals used in experiments.

Importantly, two of the LC materials (MBOBC and MHPPHBC) possess SmA* and SmC* ferroelectric phase in which the material exhibits a non-zero spontaneous polarization due to the dipole moment and a chiral structure of the LC molecule. The remaining two compounds (8CB and NPOB) do not exhibit ferroelectric ordering and were examined in their SmA phases. All compounds were purchased from the Military University of Technology (Warsaw, Poland) and used as delivered.

Table 3. Phase transition of the liquid crystals used in our experiments (where C, SmA, SmC, N and I stand for Crystalline, Smectic A, Smectic C, Nematic and Isotropic phase respectively).

Compound	Phase	T_{TR}	Phase	T_{TR}	Phase	T_{TR}	Phase
8CB	C	21.25 ℃	SmA	33.85 ℃	N	40.85 ℃	I
NPOB	C	50 ℃	SmA	61.2 ℃	N	67.9 ℃	I
MBOBC	C	39 ℃	SmC*	41.5 ℃	SmA*	59.5 ℃	I
MHPPHBC	C	54.1 ℃	SmC*	74.4 ℃	SmA*	95.8 ℃	I

3.1.2.3 Experiments

Liquid crystalline films were prepared in the following way: first, the temperature of the stage and the rim was set to a few degrees above the melting point of the liquid crystal (the temperature of the needle was always set to the same value as the temperature of the stage). Then, a few milligrams of LC was placed on the metal rim. After the material has melted we span the film on the rim by sliding a metal spatula over the rim (see Fig. 56). The film was allowed to equilibrate for ca. 5 minutes.

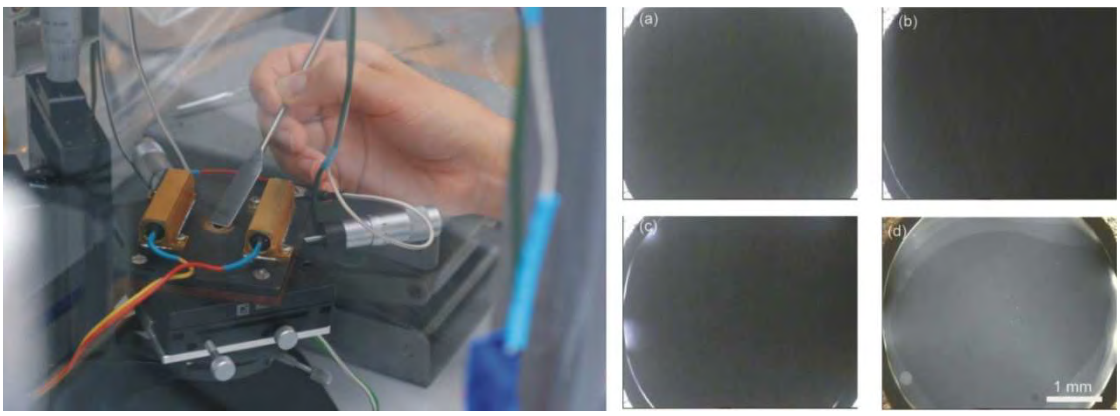

Fig. 56 Spanning free-standing smectic film of 8CB liquid crystal with a use of a metal spatula (left). A detailed spanning process (right): a small amount of 8CB liquid crystal was placed on the left side of the frame (a). A metal spatula was placed on the frame and moved over the opening (b & c) until the smectic film was created (d).
Source of the left picture: Stefan Ciechan

I used two variations of the experimental setup:

i) one in which the film was pierced by the steel needle, and

ii) the second in which the tip of the needle was placed slightly (250 μm) below the film.

The general scheme of smectic film and the needle and corresponding view from optical microscope is shown in Fig. 57.

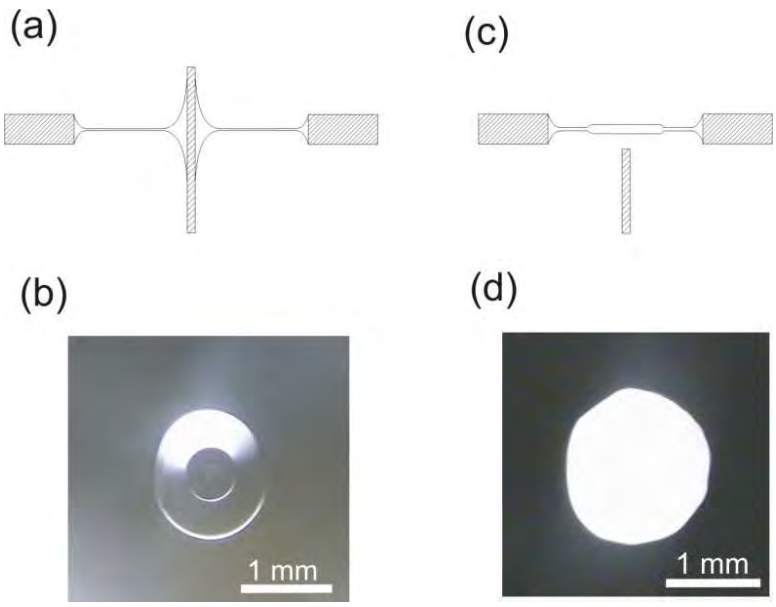

Fig. 57 Schematic illustrations of the types of conducted experiments: (a) needle pierced through the film, (b) pictures of the meniscus around the needle pierced through 8CB film, (c) schematic illustrations of needle under LC film, (d) liquid crystalline island of freely suspended MHPPHBC film.

In the first case, the needle was wetted with a minute amount of the LC material, and the meniscus around the needle was formed spontaneously at the instant of piercing the film. In the second case, a freely floating island was created above the needle (see Fig. 58 for detailed view of LC island above the needle).

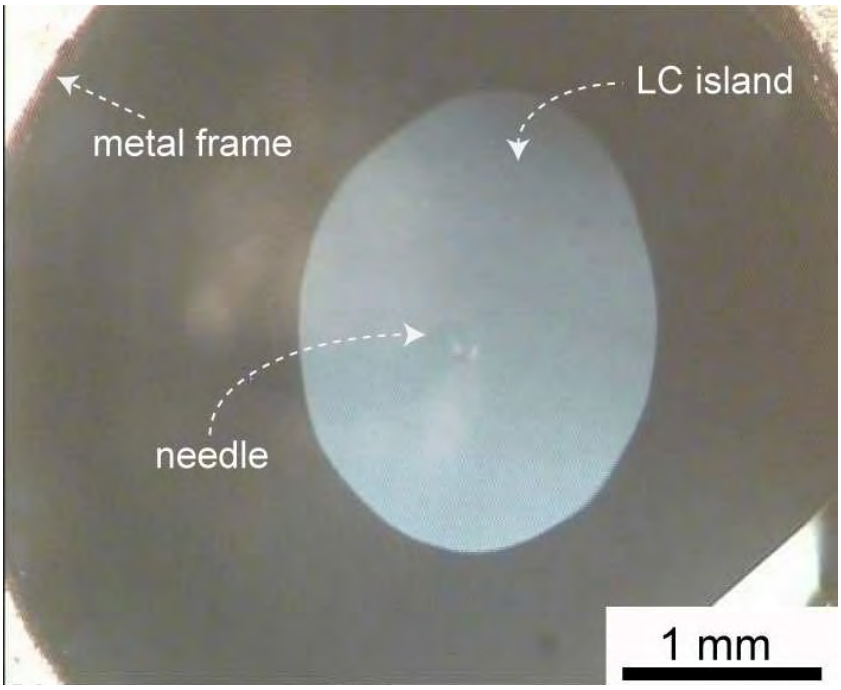

Fig. 58 Free-standing smectic film with a freely floating island of 8CB liquid crystal. The tip of the needle is placed ca. 250 µm below the level of the film. (note: the film in reflected light is black, not transparent. To visualize the needle under the film I used an additional source of light).

Usually, the islands did not form spontaneously. In order to create an island, a low frequency (few Hz) and high amplitude (hundreds of Volts) electric field was applied. It caused a disruption of the LC meniscus formed initially in the rim into many small islands. Then, either a DC or a high frequency ($f \geq 100$ Hz) electric field was applied to make the small islands merge into a single one. The single LC island formed above the needle because of dielectrophoresis: since LC material has a higher dielectric constant than the air, it is pulled into the regions of higher intensity of the field – into the center of the rim.

For each series of measurements, I typically set the potential difference to a constant value and slowly decreased the frequency, starting from a value of f ~1 kHz, until the instability ensued. The shapes of the menisci (islands) were recorded using the CCD camera and analyzed.

3.1.3 PHENOMENA IN FSSF IN EXTERNAL ELECTRIC FIELD

3.1.3.1 Dielectrophoresis

The importance of the dielectrophoretic (DEP) effect was mentioned earlier in Chapter 3.1.2. I used DEP force to create a single, big LC island. The process of creating LC island with DEP force is shown in Fig. 59. As the DEP effect was explained in detail in theoretical part of this thesis (see Chapter 2.4), the most important thing in DEP phenomena in non-uniform electric field, the influence if frequency and the difference of the electric permittivity.

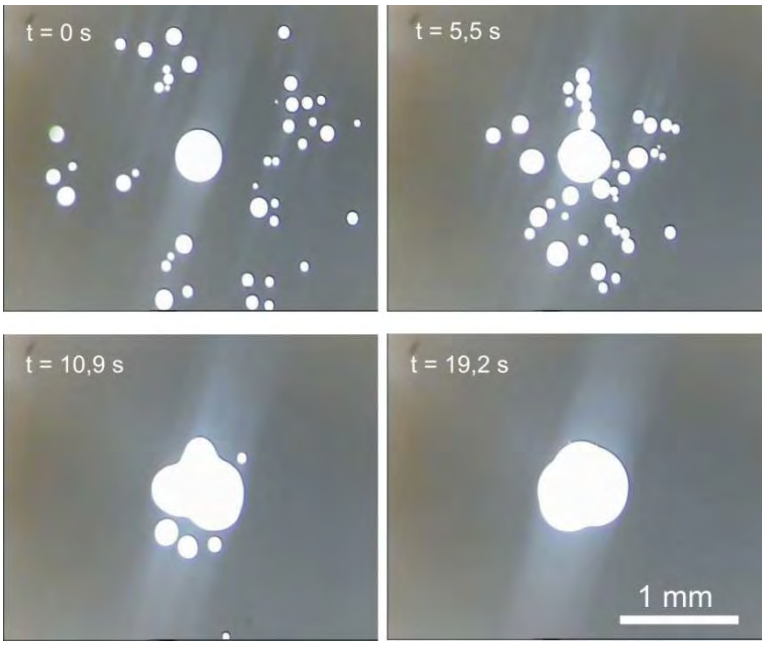

Fig. 59 Consecutive micrographs depicting the procedure of merging numerous small islands into a single one with the use of dielectrophoretic (DEP) forces (f = 100 Hz, U = 300 V). Pictures taken for the MHPPHBC liquid crystal.

In this case, non-uniform electric field is generated by geometry of two electrodes: grounded external electrode (metal frame on which I span the film) and the internal electrode: a sharp, long steel needle placed in the very center of the frame. Liquid crystals used in experiments have bigger dielectric permittivity than the air and as a result LC islands are drag into the area where intensity of electric field is highest, i.e. the center of the frame. During that dragging they collide and merge together into a single, big LC island.

3.1.3.2 Electroconvection

Another phenomena found in the experiments is electroconvection in smectic films. When the steel needle is piercing the film we observed that applying a constant electric field (U = const.) there is a persistent whirling motion of the LC material.

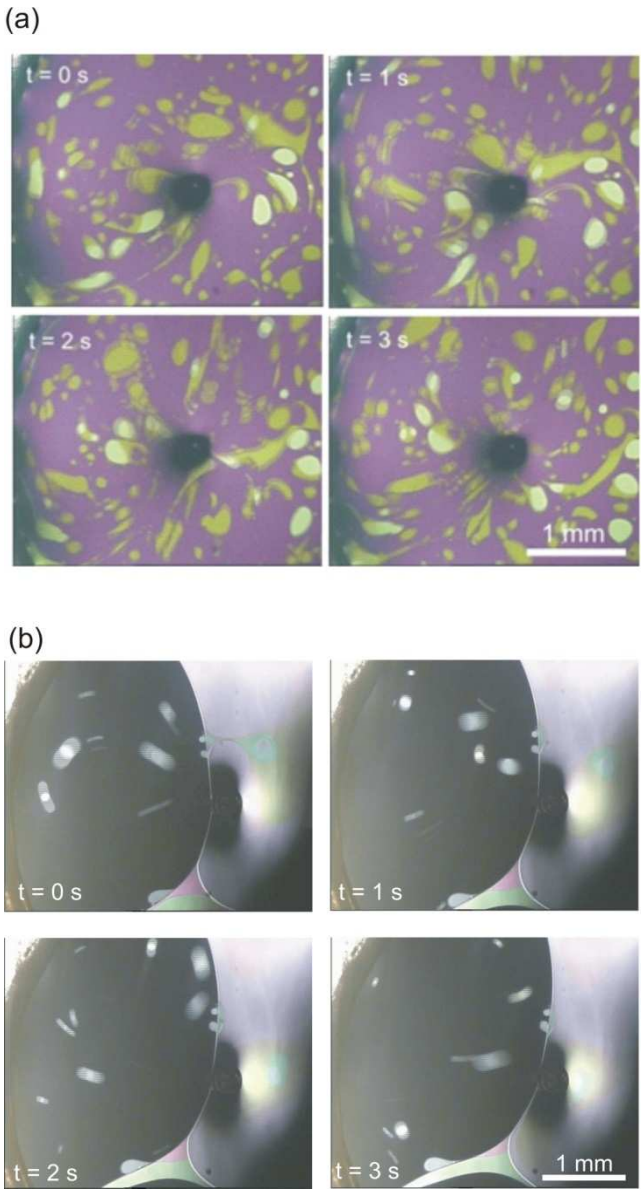

Fig. 60 Consecutive micrographs depicting the electroconvection in the plane of the film: (a) electroconvection of the 8CB liquid crystal, (b) electroconvection of NPOB liquid crystal. The dark spot in the middle is the tip of the needle that pierces the LC film.

The circular area of the rim divided into a small number of “convective cells” within which the LC material flew in a continuous circling motion (see Fig. 60). Although I did not measure the

electrical current, I attribute this observation to electro-convection and to leakage or conduction of current through the LC film. When I withdrew the needle from the film (thus breaking the electrical circuit) and left it tens of microns below the LC material, with the field switched on, the convection stopped.

3.1.4 RESULTS

3.1.4.1 Quantitative analysis of the instability

3.1.4.1.1 Steel needle in contact with the film

In the first type of experimental setup (the inner electrode piercing the film) I examined the behaviour of two liquid crystals: 8CB forming SmA phase (at 30 ℃) and MHPPHBC forming SmA* phase (at 85 ℃). I prepared the LC films and menisci as described in the previous section. Then, I applied the electric field of varying amplitude from 75 to 300 V per radius of the rim (2.5 mm) and of varying frequency (from 100 Hz to single Hz). For each set of parameters (f and U) I recorded the deformations of the LC film and later analyzed the micrographs.

My first observation is that for a given amplitude of the applied alternating electric field, the meniscus is stable for all frequencies higher than the critical frequency, f_{CR}. For frequencies above f_{CR} I did not observe any noticeable deformation of the boundary of the meniscus – it remained circular, as depicted in Fig. 61a, d and g.

For $f \approx f_{CR}$ the meniscus became unstable and its boundary began to deform periodically and followed the oscillations of the electric field (Fig. 61 b, c, e, f, h, and i). These deformations had the form of tips (or “fingers”) growing radially outwards from the boundary of the meniscus. As I decreased f further below f_{CR} the amplitude of the deformations (the length of the fingers) grew (Fig. 62).

At very low frequencies (few Hz with the exact value of f depending on the magnitude of the electric field) the length of the fingers became comparable to, or as long as the radius of the rim. When the fingers reached the rim, the meniscus typically broke, and the whole system became disordered: small islands of thicker LC material were created and floated on the LC film.

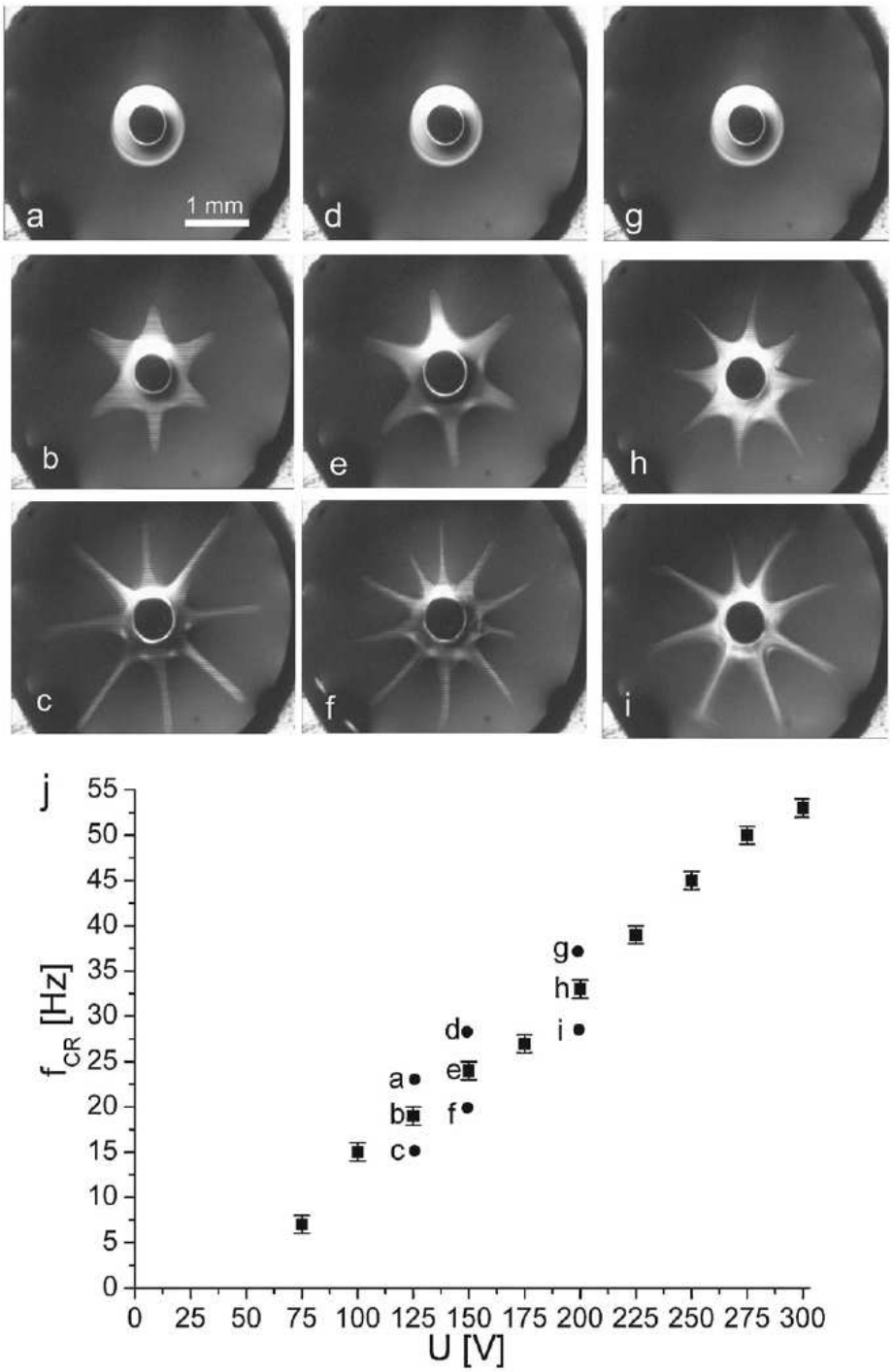

Fig. 61 The qualitative behaviour of the 8CB thick film subjected to an oscillating electric field is shown in parts (a) to (i). For a fixed potential difference *U*, there is a critical value of frequency above which the meniscus is stable (parts a, d and g). Below that frequency I observed instabilities (b, c, e, f, h, and i). Due to the sharp transition between the stable and unstable meniscus I was able to estimate the dependence of the value of the critical frequency on the applied voltage via a direct observation of the meniscus; I present this graph in part (j).

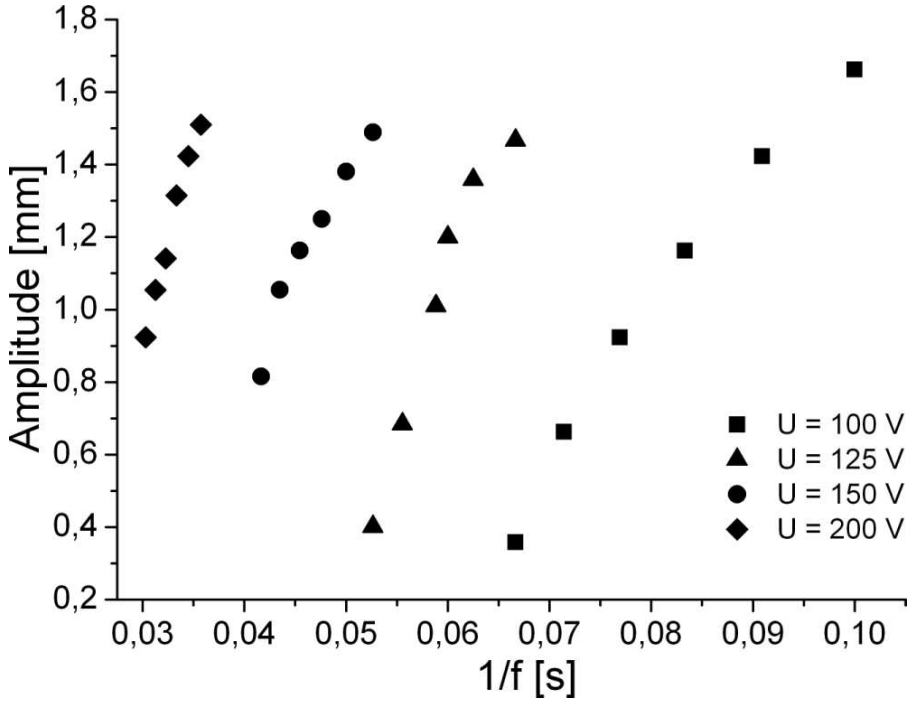

Fig. 62 Amplitude of the deformations of the boundary of meniscus as a function of the interval between switches of the polarization of the electric field for 8CB liquid crystal for different values of potential difference.

3.1.4.1.2 Inner electrode not in contact with the film

In order to avoid the problems associated with the leakage of current at low frequencies and electro-convection, I performed experiments with the needle positioned below, that is not in contact with the film. In these experiments I used MHPPHBC liquid crystal due to fact that MHPPHBC easily and reproducibly formed freely floating LC 'islands' – circular regions of thicker film.

I created single large (ca. 1 mm in diameter) islands in steps. I first spanned the film that typically did not posses any islands. Then I pulled LC material from the meniscus on the rim by applying a low frequency (~3 Hz) and high amplitude (~200 V) electric field. After few cycles there were typically about ten small islands on the film. Then I applied a high frequency (f~100 Hz) and high amplitude (U~300 V) electric field to make the islands merge into a single one by dielectrophoretic forces.

Qualitatively, the behaviour of this system was similar to that when the needle was in contact with the film. The shape of the islands depend on the applied voltage and frequency as shown in Fig. 63.

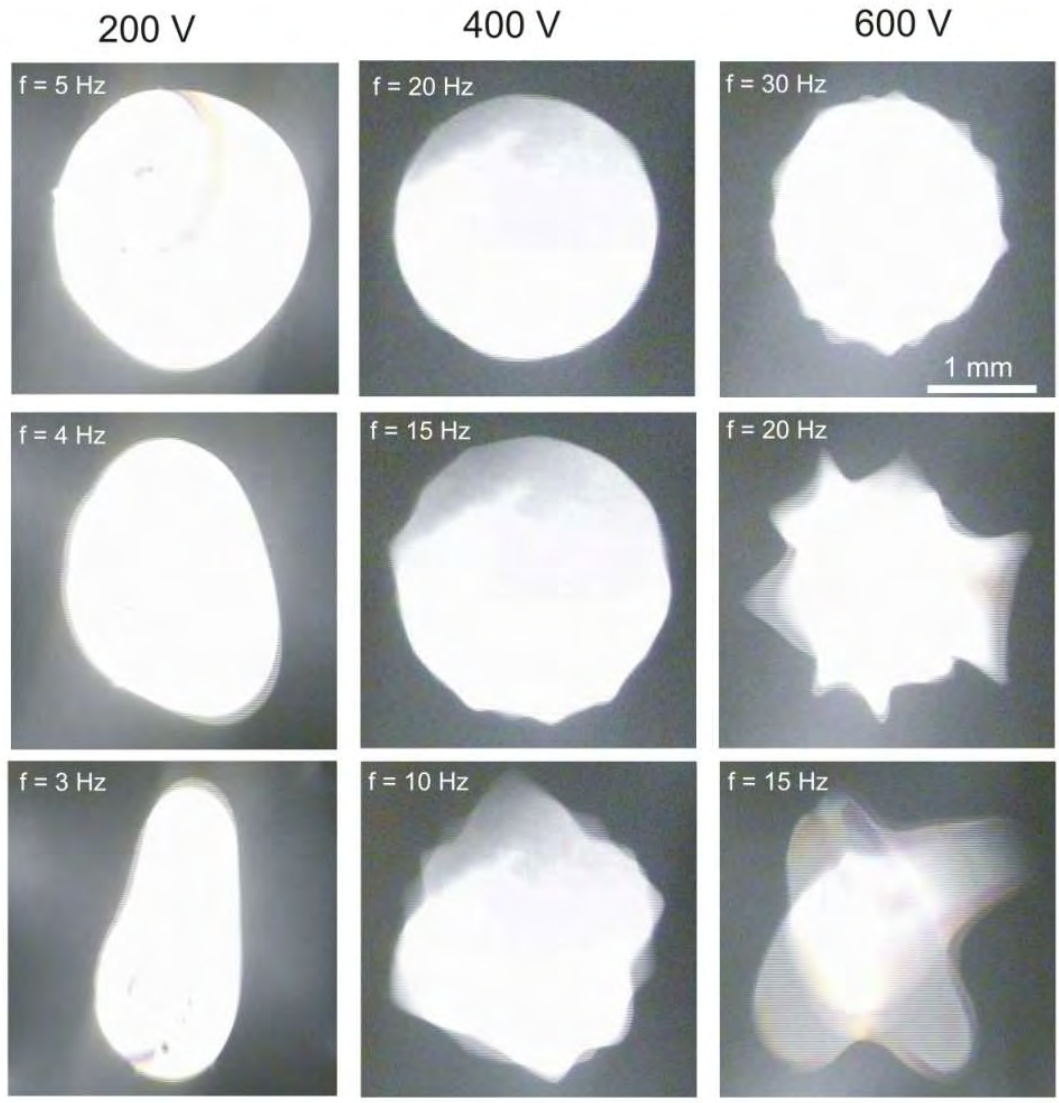

Fig. 63 Deformation of the MHPPHBC (SmA* phase) liquid crystalline island. For lower voltage oscillation frequency is present at f = 5 Hz, whereas oscillation for U = 600 V are present at f = 30 Hz. Oscillations for higher voltage have higher amplitude thus are clearly visible. For low frequencies, in both cases, we see deformation of the whole island.

For example, for U = 200 V, the island was stable for all frequencies above f_{CR} = 5 Hz. For $f < f_{CR}$ the island became unstable and deformed in synchrony with the applied electric field. For U = 600 V, f_{CR} = 30 Hz, and, for smaller frequencies, multiple 'fingers' showed. The amplitude of the deformations increased with increasing U and with decreasing f. Like in the case of the films pierced by the needle, the critical frequency increased linearly with the amplitude of the applied electric field (Fig. 15b).

3.1.4.1.3 Critical frequency f_{CR}

The transition between a stable (immobile) meniscus (Fig. 61a, d and g) and an oscillating one (Fig. 61b, e, and h) was so sharp that the critical frequency could be easily determined by visual observation of the film while lowering the frequency by a single Hz at a time. I present the relation between such determined f_{CR} and U in Figure 61j.

In order to introduce a more quantitative method of determination of f_{CR} for the various LC materials that we used, and to measure how f_{CR} depends on the difference, U, of the electrostatic potential between the electrodes, for each pair of values of f and U we recorded a video depicting the evolution of the shape of the meniscus. Then, by inspecting individual frames, we measured the minimum (D_{MIN}) and the maximum (D_{MAX}) distance between two points on the boundary of the meniscus located on the opposite sides of the centre of the rim. We defined the amplitude, A, of the deformation as:

$$A = \frac{D_{MAX} - D_{MIN}}{2} \tag{85}$$

The amplitude grew monotonically—and roughly linearly—with the reciprocal of the frequency

$$A \propto \frac{1}{f} \tag{86}$$

as shown in Fig. 64a. In order to determine the critical frequency f_{CR} for each value of U, I plotted A as a function of $1/f$, then fitted a linear relation:

$$A_{FIT}\left(\frac{1}{f}\right) = A_0 + \alpha\left(\frac{1}{f}\right) \tag{87}$$

to the experimental points with A_0 and α being the fitting parameters. Then I calculated the critical frequency as

$$f_{CR} = -\frac{\alpha}{A_0} \tag{88}$$

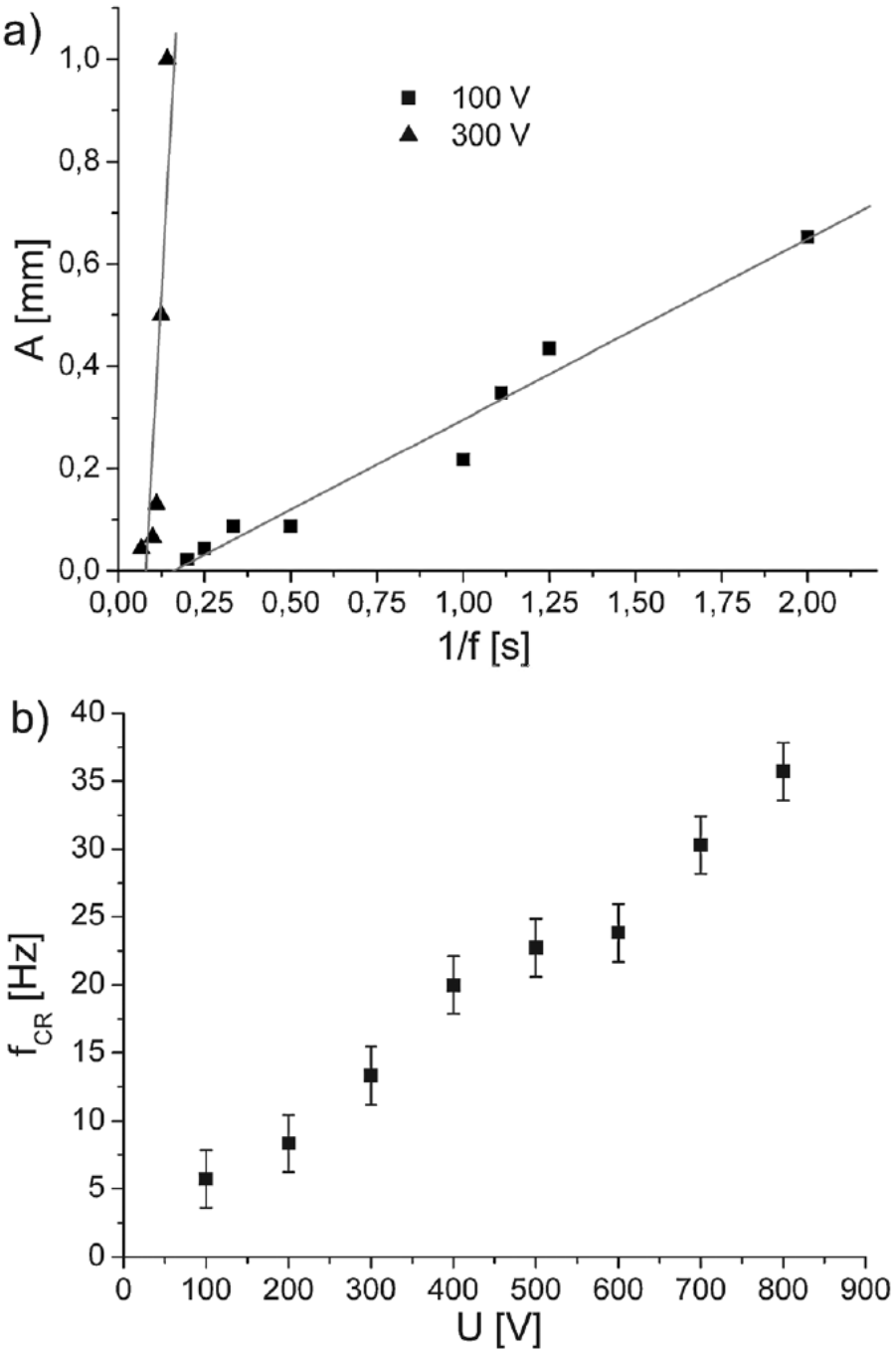

Fig. 64 Method of estimating the critical frequency for MHPPHBC liquid crystal (a). The graph shows the experimentally measured dependence of the amplitude of deformation of the LC island on the frequency of the applied electric field (plotted as a function of the reciprocal of the frequency). A linear fit allows us to determine the value of the critical frequency for the particular value of the electric field. Critical frequency plotted as a function of applied voltage for constant island diameter (ca. 2 mm) for MHPPHBC liquid crystals (SmA* phase) (b). Measurements were performed for the needle not in contact with the film.

3.1.4.1.4 Meniscus in a DC field

In the experiments I also checked LC meniscus both in the DC and AC (oscillating) fields. The results are shown in Fig. 65, both for AC (left) and DC (right).

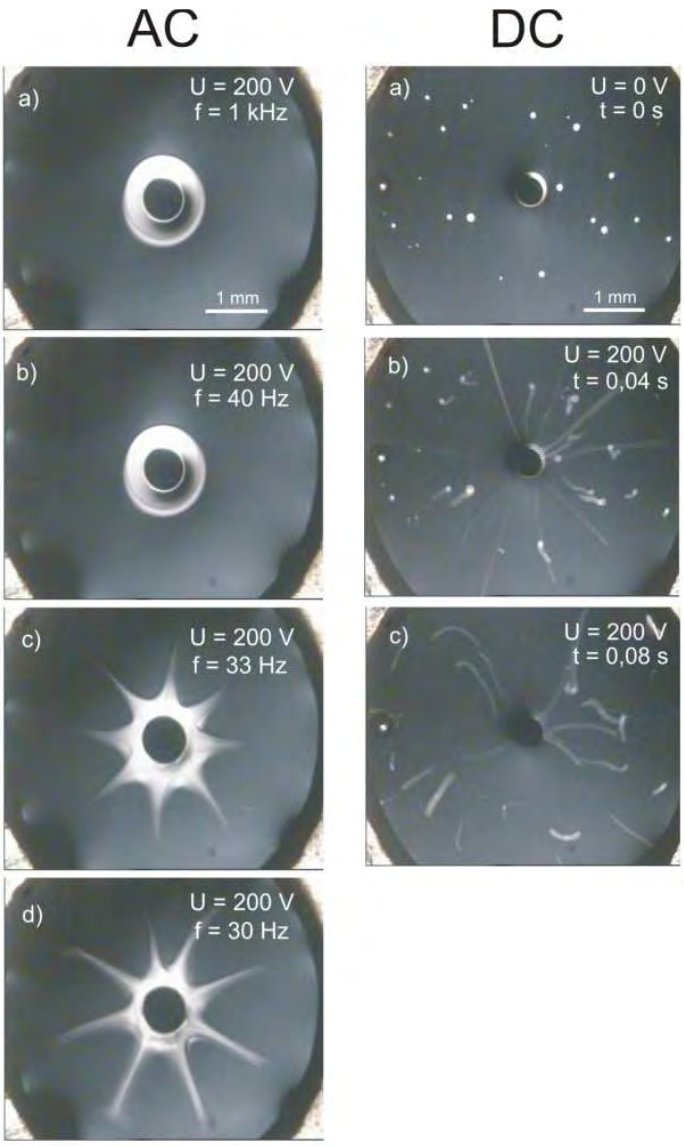

Fig. 65 LC menisci in AC electric field (left) and DC (right) electric field.

(left) Views of meniscus under high and low frequency AC electric field. For very large (a) and large (b) frequencies meniscus is stable and no change is visible whereas for critical frequency (f_{CR}) meniscus becomes unstable (c and d).
(right) Electrophoretic motion of ions in DC electric field cause damaging of the meniscus (a) metal needle with meniscus in the centre of the picture, no EF is applied (b) and (c) after applying DC electric field (U = 200 V) ions move from meniscus to metal frame, drag material with them and as a result destroy meniscus. White dots visible on film are small LC islands (thicker part of film).

Without electric field I observed no motion of meniscus (Fig. 65a). After applying DC signal, electrophoretic force was applied on ions in Liquid Crystal film. They start moving toward metal frame and drag material. As a result they caused damaging of the meniscus (Fig. 65 b and c for DC signal). In this experiment I demonstrated a clear evidence of the coupling between the motion of ions and macroscopic transport of mass in thin films of smectic LC. The transport of mass manifests itself by deformations of the circular dislocation lines into "flower-like" shapes in an oscillating EF.

3.1.4.2 Qualitative analysis of the instability and discussion of other possible mechanisms of instability

I observed similar phenomena in all the LCs that I tested (8CB, NPOB, MBOBC and MHPPHBC) and both in the smectic SmA and in the ferroelectric SmA* phases. In all these systems the menisci and islands were stable for frequencies larger than a critical frequency, and unstable below it (Fig. 61, 63, and 66).

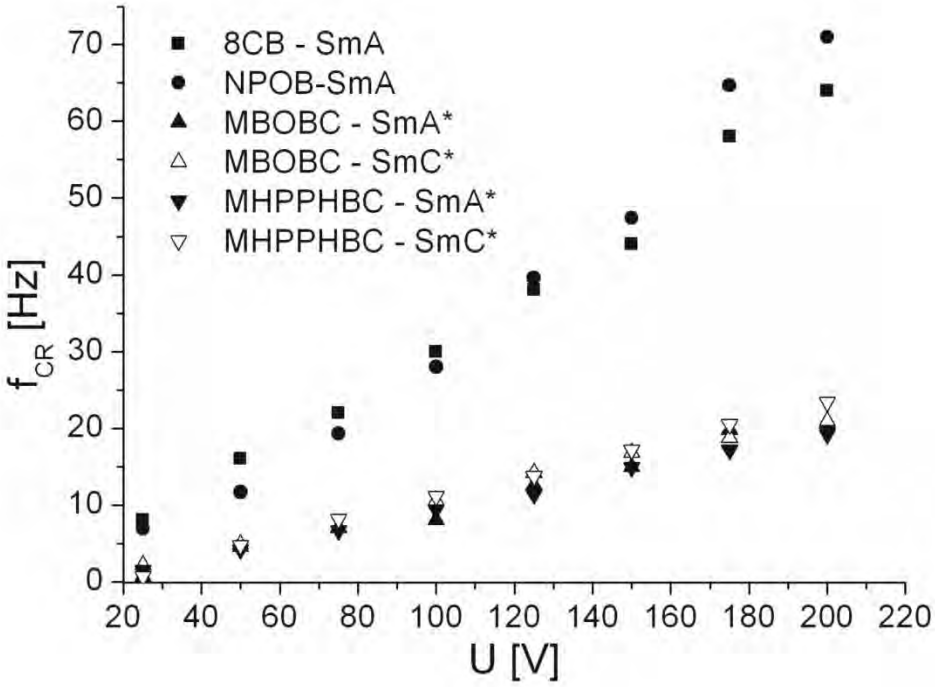

Fig. 66 Values of the critical frequencies, f_{CR}, as a function of applied voltage, U, for the four different liquid crystals used in experiments. Measurements performed for the needle in contact with the film.

A study of a system similar to the one we study here (with a [4-(3-methyl-2-chloropentanoyloxy)-40-heptyloxybiphenyl ferroelectric LC) [24] suggested that a low frequency electric field can be used to partially lift the efficiency of screening imposed by the presence of ions in a ferroelectric LC material. In the absence of impurities a ferroelectric LC phase possesses a spatially uniform ground state with all the molecular dipoles aligned along a common direction, resulting in a macroscopic net polarization of the material. The presence of ions hinders the long-range order—the ions migrate to the boundaries of the unidirectional, polarized domains where they screen the charge that arises from the non-zero divergence of the polarization field at the grain boundaries.

In [24] the authors showed the effect of coupling between the direction of polarization of the ferroelectric LC and the direction of the dislocation vectors at a boundary of a meniscus or of an island. The film polarizes locally along the dislocation line. Application of a radial electric field (perpendicular to the direction of the dislocation, which is circular around the needle) applies a torque on the molecular dipoles, and—through the said coupling—a torque to the dislocation line. The expectation is thus that the field should destabilize the circular dislocation line into a flower-like pattern with extended segments of the dislocation lines oriented radially (along the direction of the electric field). However, due to the screening of the polarization grains, and the—resulting—short-range character of the dipolar order in the LC material, the interaction of the dislocation line with the radial electric field is too weak to overcome the line tension and to destabilize the circular shape of the dislocation. As the instability occurs only at low frequencies (few Hz) of the electric field, it was suggested [24] that for a short interval after the event of switching the polarization of the electric field, the ionic impurities, resting at the boundaries of the grains of polarization, migrate to new positions of equilibrium, and, during this short interval the screening is partially lifted. Decreased efficiency of screening leads to a transient long-range ferroelectric ordering. As a consequence, during these short transients, the electric field acts with a torque on substantially large regions of the LC material polarized along the dislocation line, which leads to the observed instability of the shape of the meniscus.

As I describe below, some of observations are different from those reported in the paper of Hołyst et al. [24] As was suggested by the authors of the work cited, in LC samples containing ionic impurities the deformations of the film can be observed only at the moment of switching of the polarization of the applied electric field when the ions move and the efficiency of screening of the polarization field is partially lifted. However two of observations suggest an alternative explanation. First, the fingering instability both in the ferroelectric and in the common smectic phases. Second, as I lower the frequency below the critical value the fingers continue to grow in length throughout the whole period of constant polarization of the electric field, rather than showing only for a short, and roughly constant in length, transient

and then decaying. For very low frequencies (i.e. 1 Hz or lower), for the mechanism described in [24] we would expect that after the reorganization of the ionic clouds in the LC material, the boundaries of the uniform polarization of the LC should again be screened and the fingers should shorten, leading to a circular meniscus. In fact, in [24] the authors reported no instability in a constant electric field, while we do observe that in a DC electric field the meniscus is unstable. Further, the observation when the needle is in contact with the film the consistent whirling motion suggests that ionic impurities are constantly being created and transported between the electrodes.

There are two other—than the torque on a polarization field—electric forces that can play a role in our system:

(i) dielectrophoresis (DEP), and

(ii) electrostatic force on the meniscus that is charged via an electrophoretic motion (and separation) of ionic impurities.

Dielectrophoresis is expected to pull the liquid crystalline material towards the center of the rim, where the intensity of the electric field is greatest, and we use this effect to create single large islands of the LC material. This effect cannot be, however, attributed to the emergence of the flower instability.

A consistent explanation of all observations is based on the hypothesis that under the action of the oscillating electric field, at least a portion of the electrostatic charge present in the sample undergoes a microscopic separation which subsequently leads to dyCHASE and macroscopic patterns that are observed. Below I propose a simple model of this behavior and compare it with the results of our experiments.

3.1.4.2.1 Dynamic separation of charges

We do not know the chemical nature of the ions present in our samples. I start with an estimation of the electrophoretic mobility of hypothetical ions of different charge q = 1, 2 and $3e^{\pm}$ (e = 1.60217×10^{-19} C) and of different hydrodynamic radii r = 1, 5 and 10 Å respectively. The mobility μ is given by

$$\mu = \frac{q}{6\pi r\eta} \tag{89}$$

where η is the coefficient of viscosity of the medium.

Because the coefficients of viscosity for the isotropic phases of the MHPPHBC, MBOB and NPOB liquid crystals are not available in the literature, in estimates I assumed the value of

the coefficient of viscosity for the isotropic phases of all our compounds as the same as of 8CB, η =25.84 mPa s at 314.1 K [25]. Table 4 summarizes the results of this estimate.

Table 4. Electrophoretic mobility for different ion diameter and charge

q (e)	R (Å)	μ ($m^2 V^{-1} s^{-1}$)
1	1	$3.29 \cdot 10^{-10}$
2	5	$1.32 \cdot 10^{-10}$
3	10	$0.98 \cdot 10^{-10}$

The values that I obtained compare well to the values reported in the literature [13] [17] [26] [27] for electrophoretic mobility of ions in LC ($\mu \approx 10^{-10}$ m^2 V^{-1} s^{-1}).

We now estimate the distance d_{ions} travelled by the ions within half the period of the oscillations of the electric field at the critical frequency. This distance is:

$$d_{ions} = \mu \cdot \frac{1}{2 f_{CR}} \cdot E_{||} \tag{90}$$

where:

$$E_{||} = \frac{U}{R_{rim}} \tag{91}$$

This is a crude approximation for the purpose of the order of magnitude estimate.

Because f_{CR} was found to be linearly dependent on E, we can put:

$$f_{CR} = \left(\frac{df_{CR}}{dU} \right) \cdot \left(\frac{U}{R_{rim}} \right) \cdot R_{rim} \tag{92}$$

and obtain

$$d_{ions} = \left(\frac{\mu}{2R_{rim}} \right) \cdot \left(\frac{df_{CR}}{dU} \right)^{-1} \tag{93}$$

with the value of the derivative $\left(\frac{df_{CR}}{dU}\right)$ extracted from the linear fit to the experimentally determined relations of $f_{CR}(U)$.

Table 5 contains the results of the calculation of the d_{ions} for all the series of experiments that we performed and all three estimated values of the electrophoretic mobility. In summary, for $\mu = 1 \cdot 10^{-10}$ m^2 V^{-1} s^{-1}, d_{ions} ranged from d_{ions} = 50 nm for NPOB in the SmA phase (Fig. 19) to d_{ions} = 460 nm for MHPPHBC in the SmA* phase (Fig. 17b).
The results of this estimation are similar in magnitude to the reported value of the Debye screening length (examined in free standing film prepared with a mixture of liquid crystals—CS1015), 0.7 mm. CS1015 is ferroelectric liquid crystal commercially available from Chisso Co. with SmC* phase in room temperature. [28]

Table 5. Estimated electrophoretic mobility and distance traveled by the ions within half the period of the oscillations of the EF at the critical frequency for different types of liquid crystals used in our experiments.

Liquid Crystal	μ ($m^2 \cdot V^{-1} \cdot s^{-1}$)	d_{ion} (µm)
8CB – SmA	$3{,}29 \cdot 10^{-10}$	0,32
Fig. 61	$1{,}32 \cdot 10^{-10}$	0,13
	$0{,}98 \cdot 10^{-10}$	0,096
MHPPOBC – SmA*	$3{,}29 \cdot 10^{-10}$	1,56
Fig. 64b	$1{,}32 \cdot 10^{-10}$	0,63
	$0{,}98 \cdot 10^{-10}$	0,46
8CB – SmA	$3{,}29 \cdot 10^{-10}$	0,204
Fig. 66	$1{,}32 \cdot 10^{-10}$	0,082
	$0{,}98 \cdot 10^{-10}$	0,061
NPOB – SmA	$3{,}29 \cdot 10^{-10}$	0,17
Fig. 66	$1{,}32 \cdot 10^{-10}$	0,068
	$0{,}98 \cdot 10^{-10}$	0,051
MBOBC – SmA*	$3{,}29 \cdot 10^{-10}$	0,57
Fig. 66	$1{,}32 \cdot 10^{-10}$	0,23
	$0{,}98 \cdot 10^{-10}$	0,17
MBOBC – SmC*	$3{,}29 \cdot 10^{-10}$	0,57
Fig. 66	$1{,}32 \cdot 10^{-10}$	0,23
	$0{,}98 \cdot 10^{-10}$	0,17
MHPPOBC – SmA*	$3{,}29 \cdot 10^{-10}$	0,64
Fig. 66	$1{,}32 \cdot 10^{-10}$	0,26
	$0{,}98 \cdot 10^{-10}$	0,2
MHPPOBC – SmC*	$3{,}29 \cdot 10^{-10}$	0,52
Fig. 66	$1{,}32 \cdot 10^{-10}$	0,21
	$0{,}98 \cdot 10^{-10}$	0,15

3.1.4.2.2 Critical frequency versus diameter of the island

The postulate that the distance over which the oppositely charged ions separate is related to the properties of the LC material (such as the Debye screening length), and not the geometry of the system, is supported by the observation that the value of the critical frequency does not depend on the diameter of the meniscus, *d*.

In Fig. 67 I demonstrate the critical frequency measured for the system with the needle in contact with the film of 8CB LC. Measurements were performed in the SmA phase for four different diameters of the meniscus (from 1.19 mm to 1.85 mm).

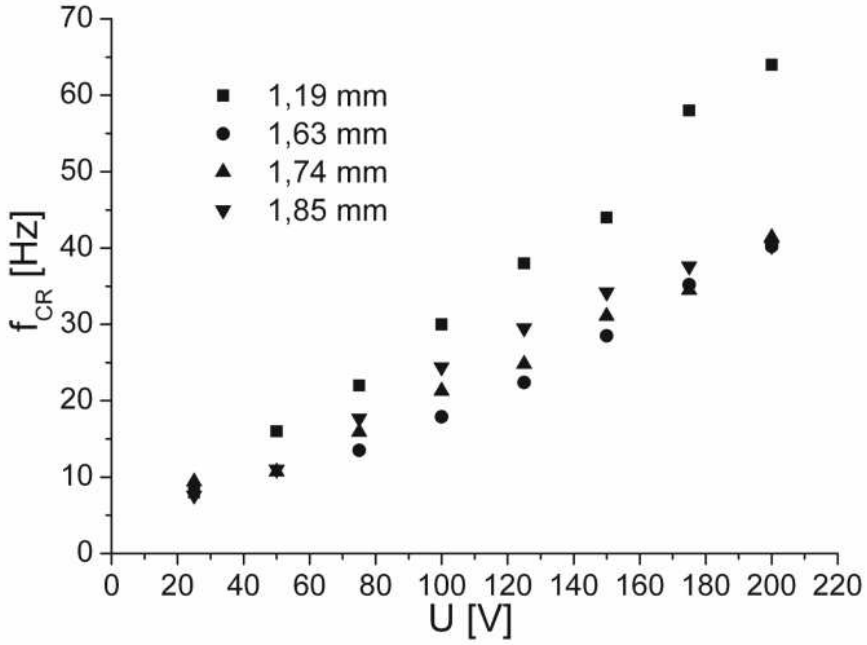

Fig. 67 Critical frequency as a function of applied voltage for 8CB (SmA phase) liquid crystal. Series were performed for several LC island (island diameter from 1.19 mm to 1.74 mm) for the needle in contact with the film.

The critical frequency shows a monotonic— and approximately linear in *U*—increase for all series, and the slope of the experimental functions of $f_{CR}(U)$ does not depend systematically on the diameter of the meniscus.

Fig. 68 shows the critical interval of time, i.e., the interval needed for the ions to separate:

$$\tau_0 = \frac{1}{2} \cdot \frac{1}{f_{CR}} \tag{94}$$

as a function of the diameter of the island. The measurements were performed with the needle not in contact with the film, and for different islands of diameters ranging from d = 1.04 to 2.65 mm. The data presented in Fig. 68 suggests that τ_0 = (1/2f_{CR}) is constant within the approximation that the magnitude of the electric field does not depend appreciably on the radial position r (or the diameter d of the meniscus).

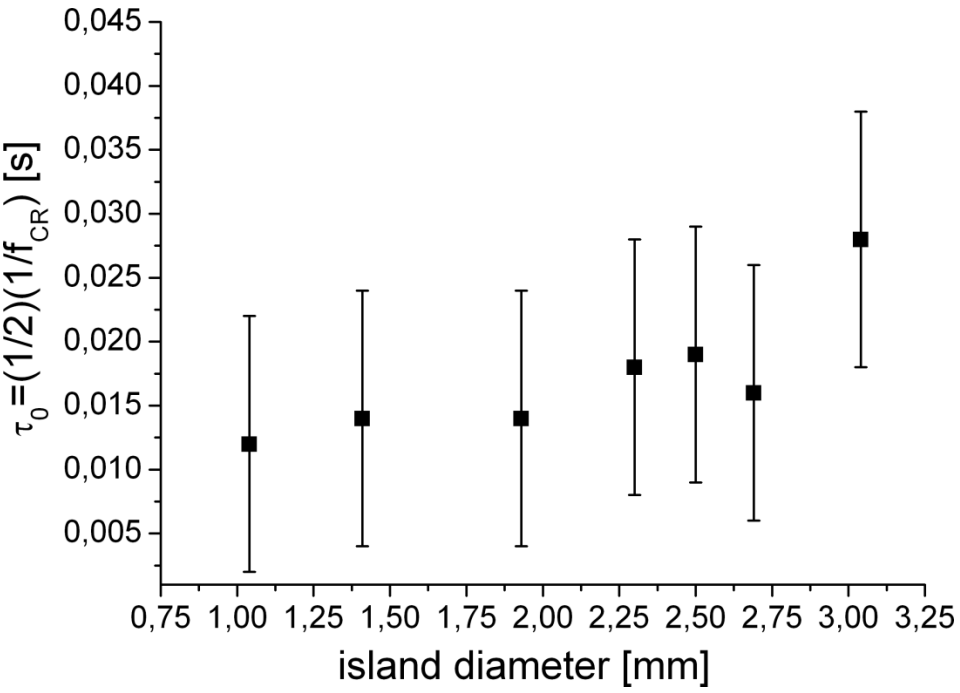

Fig. 68 Critical interval of time τ_0 plotted as a function of the diameter of the island for MHPPHBC (SmA* phase). Measurements performed for the needle not in contact with the film for *U* = 600 V.

As seen, except for the biggest diameter, the differences between τ_0 for different island sizes are within the statistical errors. The slight increase in τ_D observed with increasing diameter of the island can be attributed to the decrease in the amplitude of the radial component of the electric field with increasing r.

Table 6 demonstrate estimated values of the distance d_{ion} traveled by the ions under the influence of external electric field within the time τ_0.

Table 6. The table below depicts the estimated values of the distance d_{ion} traveled by the ions within the critical interval $\tau_0 = 1/2f_{CR}$.

Island diameter	μ ($m^2 \cdot V^{-1} \cdot s^{-1}$)	d_{ion} (μm)
d = 1,19 mm	$3.29 \cdot 10^{-10}$	0.204
	$1.32 \cdot 10^{-10}$	0.082
	$0.98 \cdot 10^{-10}$	0.061
d = 1,63 mm	$3.29 \cdot 10^{-10}$	0.3
	$1.32 \cdot 10^{-10}$	0.12
	$0.98 \cdot 10^{-10}$	0.089
d = 1,74 mm	$3.29 \cdot 10^{-10}$	0.35
	$1.32 \cdot 10^{-10}$	0.14
	$0.98 \cdot 10^{-10}$	0.1
d = 1,85 mm	$3.29 \cdot 10^{-10}$	0.33
	$1.32 \cdot 10^{-10}$	0.13
	$0.98 \cdot 10^{-10}$	0.1

Within the approximations adopted in the estimate I do not find a significant dependence of d_{ion} on the diameter of the LC island.

3.1.4.2.3 Rate of growth of the finger

At frequencies lower than critical, we divide the interval

$$\tau = \frac{1}{2f} \tag{95}$$

between the switches of the polarization of the electric field into

$$\tau = \tau_0 + \tau_D \tag{96}$$

where

$$\tau_0 = \frac{1}{2 f_{CR}} \tag{97}$$

is the time needed for separation of the charges and for charging of the boundary of the meniscus, and

$$\tau_D = \frac{1}{2} \cdot \left(\frac{1}{f} - \frac{1}{f_{CR}} \right) \tag{98}$$

is the interval during which the (electrostatically charged) boundary of the meniscus deforms. In Fig. 69 I demonstrate the amplitude of the deformation of the island versus τ_D for ferroelectric liquid crystal MHPPHBC in SmA* phase.

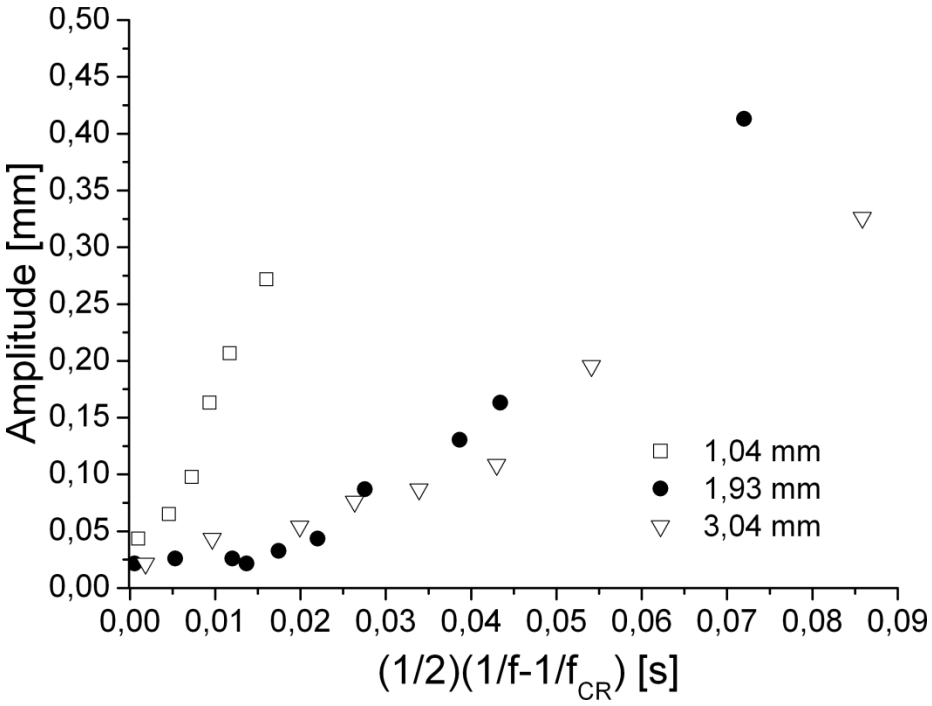

Fig. 69 Amplitude of the deformation of the boundary of the meniscus vs. the interval between the switches of polarization minus the time needed for the ions to separate, $\left(\frac{1}{2}\right) \cdot \left(\frac{1}{f} - \frac{1}{f_{CR}} \right)$ for MHPPHBC liquid crystal (SmA* phase). Series of experiments were performed for different island diameters ranging from 1.04 mm to 3.04 mm. The needle was not in contact with the film and the applied voltage was U = 600 V. As seen, the amplitude of the deformation increases with $\left(\frac{1}{2}\right) \cdot \left(\frac{1}{f} - \frac{1}{f_{CR}} \right)$.

I performed the measurements with the needle not in contact with the film and for liquid crystal islands of different diameters, from d = 1.04 to 3.04 mm. Amplitude (A) of the deformation exhibits a monotonic increase as a function of τ_D. That is, the deformation never decreases as time progresses (with increasing τ_D). I note the apparent difference in the growth rate of the deformations for different diameters of the islands.

Fig. 70 demonstrate a plot of the amplitude of deformation versus τ_D for a selected diameter of the island (d = 1.93 mm), for the same compound but for different values of U.

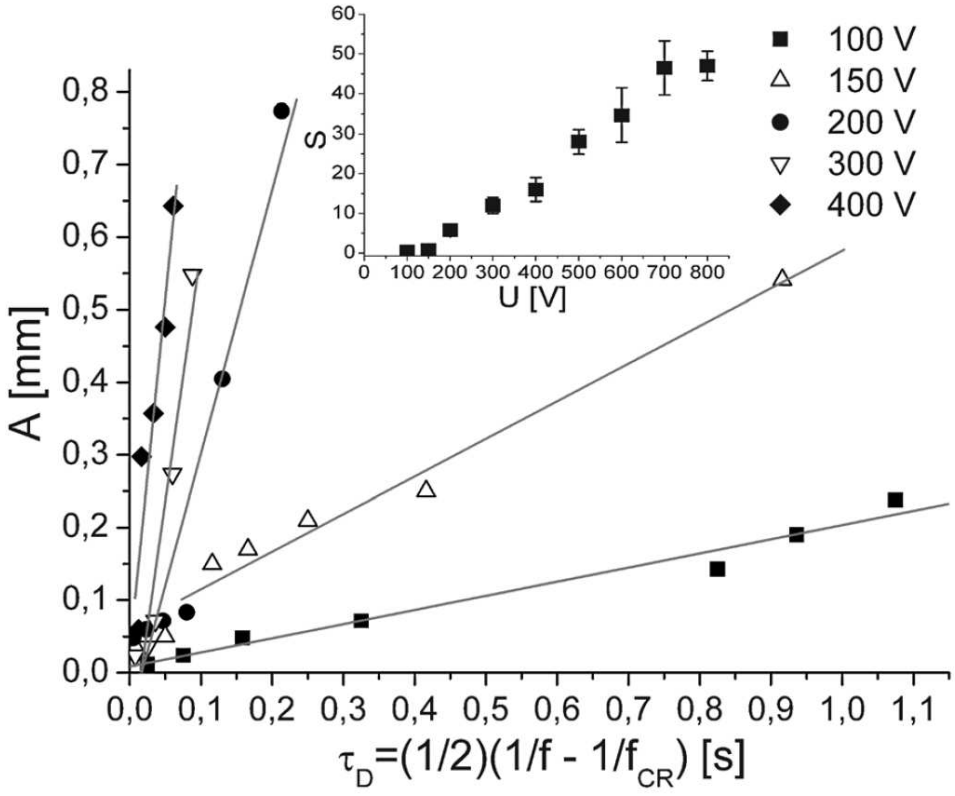

Fig. 70 Amplitude of the deformation of the boundary of the meniscus vs. the interval between the switches of polarization minus the time needed for the ions to separate. Experiments with MHPPHBC liquid crystal (SmA* phase). The needle was not in contact with the film. The applied voltage ranged from *U* = 100 V to *U* = 800 V. For clarity, I have plot only five selected series of data. The inset shows the dependence of the rate of growth (S) on the amplitude of deformation as a function of the applied voltage (obtained by linear regression of series A(τ_D)).

As before, the dependence of the amplitude of deformation, A, on τ_D shows a monotonic increase in τ_D and, with a good approximation, can be described by the relation

$$A(\tau_D) = A_0 + S \cdot \tau_D \tag{99}$$

where S is the rate of growth and A_0 is a constant.

For each value of voltage applied we calculated the quantity S from the linear fit to the data. As seen, the rate of growth is a linear function of the applied voltage U.

3.1.5 NUMERICAL CALCULATIONS OF THE ELECTRIC FIELD

Numerical calculations of electric field between the needle and the frame were performed by prof. Marcin Fiałkowski and are available in publication [29].

3.1.6 DISCUSSION

The results presented in this thesis form the first experimental evidence of macroscopic separation of electrostatic charge induced by an oscillating electric field. I refer to this phenomenon as the dynamic charge separation (dyCHASE). Importantly, dyCHASE is sensitive both to the frequency and to the amplitude of the electric field. The feature that the transition from a relaxed distribution of charges to dyCHASE is sharp in frequency allows for an easy dynamic control of the phenomenon, and consequently to a control over—at least important characteristics of—charge distribution and over macroscopic behavior of our system.

dyCHASE can be explained with a model based on the electrophoretic motion of ions. I demonstrated that there exists a sharp frequency threshold ("critical frequency"—f_{CR}) below which the meniscus (or the island boundary) becomes unstable. This critical frequency is associated with the time that it takes for the ions to move (separate) electrophoretically over the Debye screening length. The above model finds confirmation in experimental results: the critical frequency f_{CR} is a linear function of the voltage applied to the film, and it does not depend on the diameter of the meniscus or the island. Although findings are different than the ones reported in [24] I suppose that the effects of coupling between the directions of dislocations and polarization in ferroelectric smectic LCs exist and require further investigation.

In my experiments I did not monitor the thickness of the LC islands (or menisci). It can be argued that the thickness should not affect neither the qualitative nor the quantitative

behavior because the forces that determine the motion (deformation) of the meniscus are both proportional to its thickness:

(i) I can assume that the density of charge on the boundary is proportional to the content of the ionic impurities in the LC material, and, assuming a constant density of ionic impurities in the LC, the charge on the boundary should be proportional to the thickness of the meniscus, and
(ii) the elastic forces (arising from the line tension of the dislocation lines) are also proportional to this thickness, as the number of dislocations at the boundary is.

Also the viscous forces that oppose the motion of the boundary are proportional to the amount of LC material that is subject to motion (shear). The fact that I did not observed significant scatter in the values of critical frequency and the rate of growth of the fingers in repeated experiments with the same control parameters suggest that indeed the behavior of the system does not depend appreciably on the thickness of the film.

I was not able to discriminate the critical frequencies for the motion of cations and anions separately. If these differed substantially in their electrophoretic mobility the system could show substantial asymmetry between the positively and negatively charged 'fingers' and perhaps display a difference in the critical intervals for the positive and negative ions to reach the boundary of the meniscus and to deform it in the electric field.

My observations raise an important question about the microscopic details of the non-equilibrium distribution of charge for frequencies equal to and lower than the critical value that corresponds to oscillations of ions over the Debye length.

i) why do the charges macroscopically separate when the oscillations of ions exceed the threshold of the screening length?

ii) can the observed behavior shed light on the relation between ionic strength, screening lengths and relaxation time-scales for fluctuations in the local density of electrostatic charge?

Finally a similar methodology applied to heterogeneous systems characterized by a set of characteristic length- and time-scales (e.g. corresponding to different sizes of macro-ions present in the system) could exhibit selective, frequency modulated dyCHASE and allow independent control of the electrostatic interactions between the different charged components of the system.

3.1.7 REFERENCES FOR CHAPTER 3.1

[1] Lovett, Demonstrating Science with Soap Films (Taylor & Francis, 1994).
[2] C. V. Boys, Soap Bubbles: Their Colors and Forces Which Mold Them (Dover Publications, 1958).
[3] Cyril Isenberg, The Science of Soap Films and Soap Bubbles (Dover Publications, 1992).
[4] A. A. Sonin, Freely Suspended Liquid Crystalline Films (Wiley, 1999).
[5] P. Oswald and P. Pierański, Smectic and Columnar Liquid Crystals: Concepts and Physical Properties Illustrated by Experiments, 1st ed. (CRC Press, 2005).
[6] J. C. Géminard, R. Hołyst, and P. Oswald, Acta Physica Polonica B **29**, 1737-1747 (1998).
[7] M. Funahashi and J. Hanna, Chemical Physics Letters **397**, 319-323 (2004).
[8] R. J. Bushby and O.R. Lozman, Current Opinion in Solid State & Materials Science **6**, 569-578 (2002).
[9] K. Neyts, S. Vermael, C. Desimpel, G. Stojmenovik, A.R.M. Verschueren, D.K.G. de Boer, R. Snijkers, P. Machiels, and A. van Brandenburg, Journal of Applied Physics **94**, 3891-3896 (2003).
[10] R. S. Zola, L.R. Evangelista, and G. Barbero, Journal of Physical Chemistry B **110**, 10186-10189 (2006).
[11] G. Stojmenovik, S. Vermael, K. Neyts, R. van Asselt, and A. R. M. Verschueren, Journal of Applied Physics **96**, 3601-3608 (2004).
[12] K. H. Yang, Journal of Applied Physics **67**, 36-39 (1990).
[13] G. Stojmenovik, K. Neyts, S. Vermael, A. R. M. Verschueren, and R. Van Asselt, Japanese Journal of Applied Physics Part 1-regular Papers Brief **44**, 6190-6195 (2005).
[14] S. Takahashi, Journal of Applied Physics **70**, 5346-5350 (1991).
[15] D. Adam, F. Closs, T. Frey, D. Funhoff, D. Haarer, H. Ringsdorf, P. Schumhmacher, and K. Siemensmeyer, Physical Review Letters **70**, 457-460 (1993).
[16] M. Funahashi and J. Hanna, Physical Review Letters **78**, 2184-2187 (1997).
[17] K. Neyts and F. Beunis, Ferroelectrics **344**, 499-510 (2006).
[18] P. Tsai, S. W. Morris, and Z. A. Daya, EPL **84**, (2008).
[19] P. Tsai, Z. A. Daya, and S. W. Morris, Physical Review E **72**, (2005).
[20] P. Tsai, Z. A. Daya, and S. W. Morris, Physical Review Letters **92**, (2004).
[21] Z. A. Daya, V. B. Deyirmenjian, and S. W. Morris, Physical Review E **64**, (2001).
[22] P. Tsai, Z. A. Daya, V. B. Deyirmenjian, and S. W. Morris, Physical Review E **76**, (2007).
[23] Peichun Tsai, The Route to Chaos and Turbulence in Annular Electroconvection, Ph.D. thesis, 2007.
[24] R. Hołyst, A. Poniewierski, P. Fortmeier, and H. Stegemeyer, Physical Review Letters **81**, 5848-5851 (1998).
[25] J. Jadzyn, R. Dabrowski, T. Lech, and G. Czechowski, Journal of Chemical and Engineering Data **46**, 110-112 (2001).
[26] H. De Vleeschouwer, A. Verschueren, F. Bougrioua, R. van Asselt, E. Alexander, S. Vermael, K. Neyts, and H. Pauwels, Japanese Journal of Applied Physics Part 1-regular Papers Short Notes & **40**, 3272-3276 (2001).
[27] L. O. Palomares, J. A. Reyes, and G. Barbero, Physics Letters A **333**, 157-163 (2004).
[28] J. B. Lee, R. A. Pelcovits, and R.B. Meyer, Physical Review E **75**, (2007).
[29] T. Szymborski, O. Cybulski, I. Bownik, A. Żywociński, S.A. Wieczorek, M. Fiałkowski, R. Hołyst, and P. Garstecki, Soft Matter **5**, 2352-2360 (2009).

Chapter 3.2
Dynamics of a liquid crystalline meniscus in external AC field

In this chapter I present detailed analysis of a the electro-hydrodynamic instability that I observed in 8CB FSSF together with a electro-hydrodynamical model and calculations of the estimated induced charge and of the value of the line tension.

The experiments were performed for 8CB and 8CB doped with an organic salt – BDTC. A fast camera (PHOTRON) was used to record videos with high temporal resolution, and MatLab scripts to analyze and visualize the data. The fast camera observations revealed the dynamics of the oscillation of the island. The island has a circular shape for frequencies larger than critical, and for frequencies lower the island it deforms: the circular shape becomes irregular. In the shape of the island we can distinguish "arms" which increase their length in synchrony with the applied electric field. When the polarization is opposite the arm decrease its length.

Further, the electro-hydrodynamic (EHD) model was created to define the forces responsible for deformation of the island in an externally applied electric field. I used the model to calculate:

i) induced charge Q at the edge of the island,

ii) the line tension, which is an equivalent of the surface tension in a 2D systems.

The results shows that the induced charge Q is bigger for doped 8CB liquid crystal compared to pure 8CB. The magnitude of the line tension obtained from our experiments agrees to within an order of magnitude to the values from published previously in the literature. The line tension for a single experiment is decreasing during the growth of the arm. The driving force for the instability is the force generated by the electric field and the process is therefore far from equilibrium. The quantitative results presented in this chapter support the heuristic picture presented in the dyCHASE mechanism. The results provide also a new vista for measuring the magnitude of the line tension in systems that are far from equilibrium.

3.2.1 INTRODUCTION

As was described in Chapter 3.1 the free-standing smectic films (FSSF) consists of layers of LC molecules oriented parallel to the free surfaces. However if the number of layers in two parts of the film is different a step is formed between them and as a result an edge dislocation is created [1] (Fig. 71).

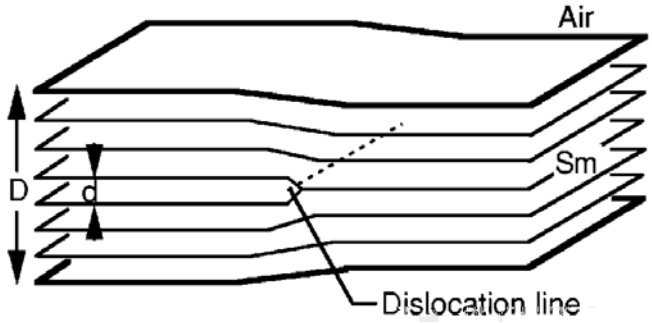

Fig. 71 Edge dislocation in a free-standing smectic film. Edge-dislocation line is defined to be the defect line that bounds two domains of the film that have different thicknesses *D*. The Burger vector *b* is defined to be the thickness difference and *b* is an integer multiple of the layer thickness *d*. [2]

The interaction of a dislocation line with a free surface—of surface tension γ—is described by the equation:

$$\gamma > \sqrt{K \cdot B} \tag{100}$$

K – curvature of the surface,

B – compressibility module.

If the surface tension is bigger than $\sqrt{K \cdot B}$, edge dislocation is repelled from the surface, therefore dislocation must locate in the midplane of the free-standing film [2].

The existence of the dislocation at the edge of the island (a spherical—at least one—additional layer of smectic molecules on the FSSF) or the hole (a lack of at least one layer of smectic molecules in the FSSF which has a spherical shape) costs energy to the system. This energy is in fact a one-dimensional analog of surface tension. Energy expressed per unit length is called a *line tension*. [3]

There are typically two ways of measuring the line tension. First, suggested by Geminard et al. [4] is to determine the critical radius R_c of a dislocation loop in a horizontal film. Depending on its initial value the radius of the loop will increase or decrease in time. Two main forces are acting on the loop. The line tension tends to minimalize size of the loop.

The pressure difference tends to increase the radius of the loop. The interplay between line tension and difference of the pressure can be used to calculate the critical radius R_c. In a thick film where the interactions between the dislocation and the free surfaces can be omitted, thus R_c is given by:

$$R_c = \frac{E}{b \cdot \Delta P} \tag{101}$$

where:

E – line tension,

B – Burgers vector,

$\Delta P = P_{air} - P_{smectic}$ – the hydrostatic pressure drop between the air and the smectic phase, that is imposed by meniscus [5]

This method requires the nucleation of different-sized loops (by placing a heating wire under the smectic film), and observing their growth ($R>R_c$) or collapse ($R<R_c$). After a number of experiments in which critical radius R_C is determined, the line tension E is calculated using the equation (101). [3]

In the second method one also nucleates a dislocation loop (also with use of a heating wire) in a vertical film and measures the anisotropy of the shape of the loop when it is in contact with the top edge of the frame. The shape of the loop depends on the gravitational constant *g*:

$$E \cdot \kappa = b\left(\Delta P_0 + \rho g z\right) \tag{102}$$

where:

κ – the local curvature of the dislocation,

ρ – the density of liquid crystal,

z – the vertical coordinate,

P_0 – constant equal to the pressure difference at z = 0 (for thick films)

P_0 constant in thin films also include a term coming from the interaction between the free surfaces (disjoining pressure). [3]

Fitting the experimental data with eq. (103) allows to obtain the line tension value and ΔP_0 value. Using the second method, Geminard at al. [2] measured the line tension in a vertical Sm-A free-standing film. The dependence of the value of the line tension on the number of smectic layers of the line tension of an elementary dislocation is given in Fig. 72. The line tension T is shown as a function of the number of smectic layers N:

$$N = \frac{D}{d} \tag{103}$$

where *D* is a thickness of the island and *d* is a thickness of a single layer.

The value of the line tension increases by 20% when the film thickness decreases from 25 to 2 layers. This increase results from the interaction of the dislocation with the two free surfaces. For a thick islands the value of the line tension, for a single dislocation line, is constant and equal $T \approx 8 \cdot 10^{-12}$ N.

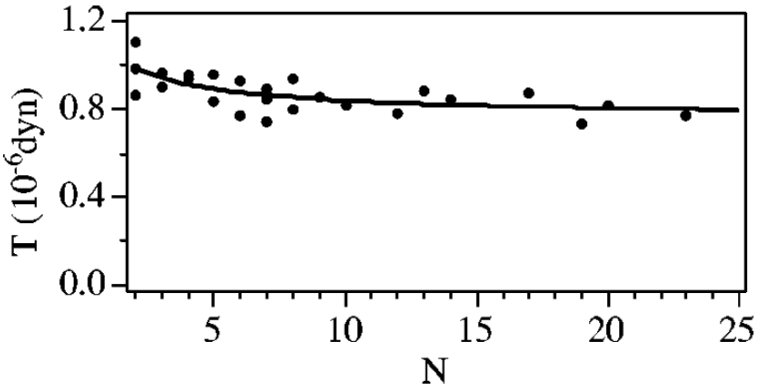

Fig. 72 Line tension T as a function of the film thickness N [2]. The line tension $T \approx 0.8 \cdot 10^{-6}$ dyn is equal to $T \approx 8 \cdot 10^{-12}$ N.

Gemianard at al. [4] measured the value of the line tension in a horizontally placed 8CB free-standing film and obtained the value of $T \approx 8 \cdot 10^{-7}$ dyn, i.e. $T \approx 8 \cdot 10^{-12}$ N for elementary edge dislocation.

Recently, the line tension of liquid crystal multilayer has been studied experimentally with the Langmuir technique. The 8CB liquid crystal was placed on the water. The authors performed experiments both on single molecular layer and multilayer domains. The domains of 8CB (so called rafts) have a circular shape, in order to minimalize the line tension. When two islands (rafts) merged, the shape changed to circular. Analysis of the relaxation rate led to the calculation of the line tension. The line tension of monolayer domains of 8CB on water is $1.2 \cdot 10^{-12}$ N [6], the same order of magnitude as for other monolayer systems.

3.2.2 MATERIALS AND METHODS

The experimental setup was described in detail in Chapter 3.1. I used a flat, metal plate with a circular opening. The plate was mounted on the XYZ micromanipulators. Under the opening, I placed a steel needle. The metal stage and the needle were connected to the high voltage amplifier (TREK 10/10B) and function generator (Tabor Electronics Ltd., type 5062). The signal from the function generator was amplified *x*1000 by the HV amplifier and applied between the stage and the needle. The smectic film was observed via a stereoscope and a camera placed on the stereoscope. All experiments were performed for a square-wave signal with duty cycle equal to 50 %.

In these experiments, I used a super-fast camera PHOTRON (FastCam 1024PCI), to record videos at a rate of 2000 fps (frames-per-second), instead of 30 fps in previous experiments. The use of the PHOTRON camera gave me insight into the dynamics of deformations of the shape of the island.

All experiments were performed with the 8CB liquid crystal. The detailed information about its phase transitions was placed in the Chapter 3.1. To examine influence of ions on hydrodynamic instability of the LC island I doped 8CB with organic salt: benzyltetradecyldimethylammonium chloride (BDTC) from Sigma Aldrich (Fig. 73).

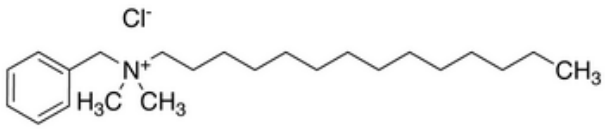

Fig. 73 Organic salt, benzyltetradecyldimethylammonium chloride (BDTC) used for doping of 8CB liquid crystal.

The process of preparation of a free-standing smectic film and LC ‘island’ was described in details in the Chapter 3.1. A small amount of 8CB was placed on the edge of the metal frame and then spanned with a metal spatula in a single, smooth move. To obtain a liquid crystalline island a low-frequency high-intensity electric field was applied, and a certain amount of liquid crystal was pulled off from the meniscus to the center of the film. Next step was applying a high-frequency high-intensity electric field. A dielectrophoresis (DEP) force acted on small islands; the force was directed into a center of the film and LC islands when are very close to each other merge into a big, single island.

All experiments were performed for geometry with a steel needle placed ca. 250 µm under the FSSF. Additionally I demonstrate an experiment with a steel needle piercing 8CB film to analyze a dynamics of LC meniscus around the needle. Previous analysis, performed with a movies recorded with 30 fps, did not allowed to obtain insight into any details about this phenomena.

For each measurement of the dynamics of deformations of the LC island I have set the voltage and the frequency to constant values. When the system fell into periodic oscillations I recorded (at a rate of 2000 frames per second) the motion of the meniscus over an interval comprising at least five cycles of the periodic transformations.

In order to analyze the dynamics quantitatively I used a MatLab® software with an Image Analysis Toolbox. As a result of extensive image processing I analysed the geometric parameters describing temporal changes of the boundary of the LC island. In particular, for each video frame (see Fig. 74), the angular profile of the length of the radius vector, $R(\varphi)$, indicating the island borderline was determined. Besides, I estimated: the number of the arms N, the temporal profiles of the length (circumference) of the borderline $O(t)$, the temporal profiles of the lengths of the arms $A(t)$, and the values of their maximum lengths A_{max}.

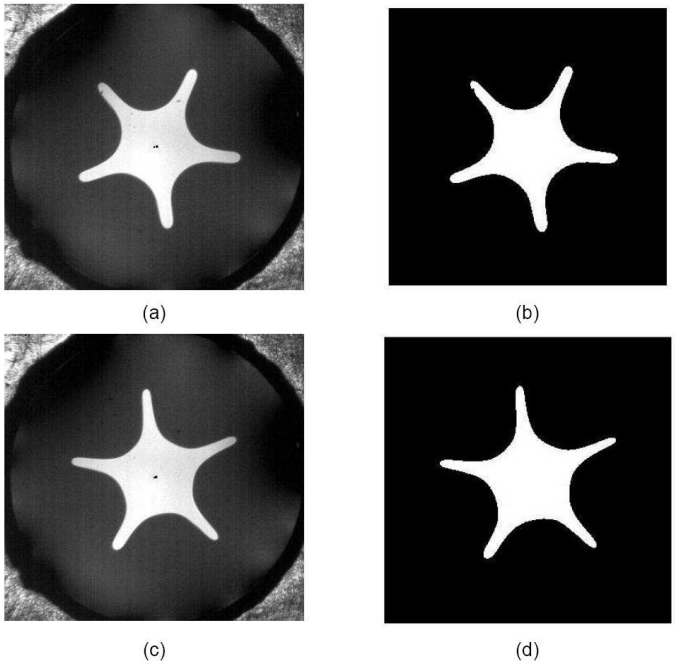

Fig. 74 An example of digital analysis of the single frame from a movie recorded with a fast-camera. (a, c) Two frames were taken for a different position of the arms of the island, and corresponding binarized pictures (b, d). The black dots in the very center of the island are the position of the steel needle and the center of mass of the island.

3.2.3 QUALITATIVE ANALYSIS OF DEFORMATION OF THE ISLANDS

The first step in the analysis of the deformation of the LC island is a qualitative description of the dynamics. In Fig. 75 I show a typical deformation of a stable island, above f_{CR}, (a). Below critical frequency island show different types of instabilities (b-g). It can be stretched in an ellipse-like way (b), which is characteristic for low voltage. At higher voltage the number of arms is increasing. In (c) is shown an island with a three arms, and correspond with four (d), five (e), six (f) and seven (g). The higher number of arms were observed during experiments, however for a single, long experiment (i.e. for a wide range of the voltages and frequencies), I recorded maximally six arms.

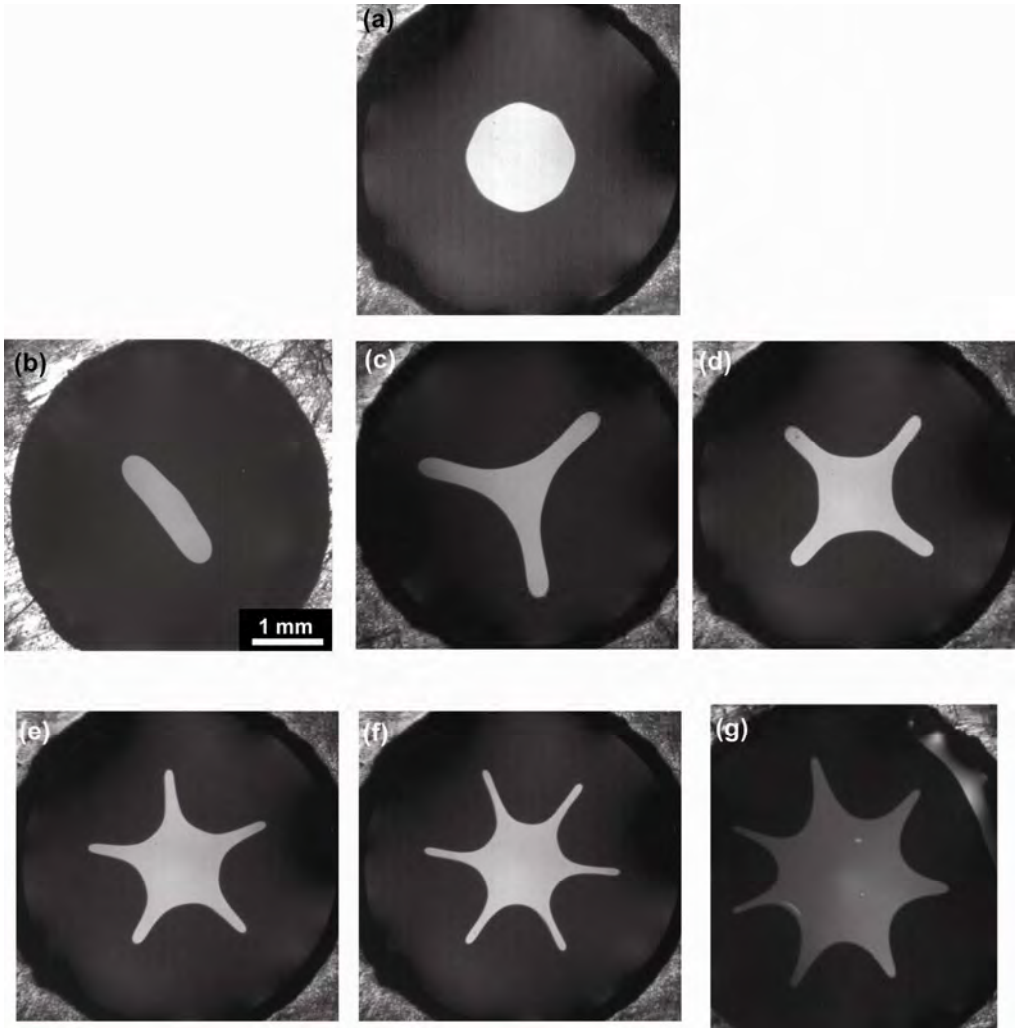

Fig. 75 A stable island made of 8CB liquid crystal (a), which is observed above critical frequency ($f>f_{CR}$). Deformed island for frequencies below critical frequency ($f<f_{CR}$) and different applied voltages (b-g). These pictures are only an examples of deformation of the islands observed during the experiments.

3.2.3.1 Changes of the island for a set of frequencies below critical frequency (f_{CR})

In the Fig. 76 and Fig. 77 I present the changes of the shape of the LC island below the critical frequency. These figures demonstrate, in a qualitative way, how the amplitude of the deformation changes with the frequency. The lower the frequency, the higher time of acting of the electric field on the island:

$$t \propto \frac{1}{2f} \tag{104}$$

Thus, the lower frequency the higher time of working of electric field on a LC island and therefore, the higher the amplitude of the deformation of the island.

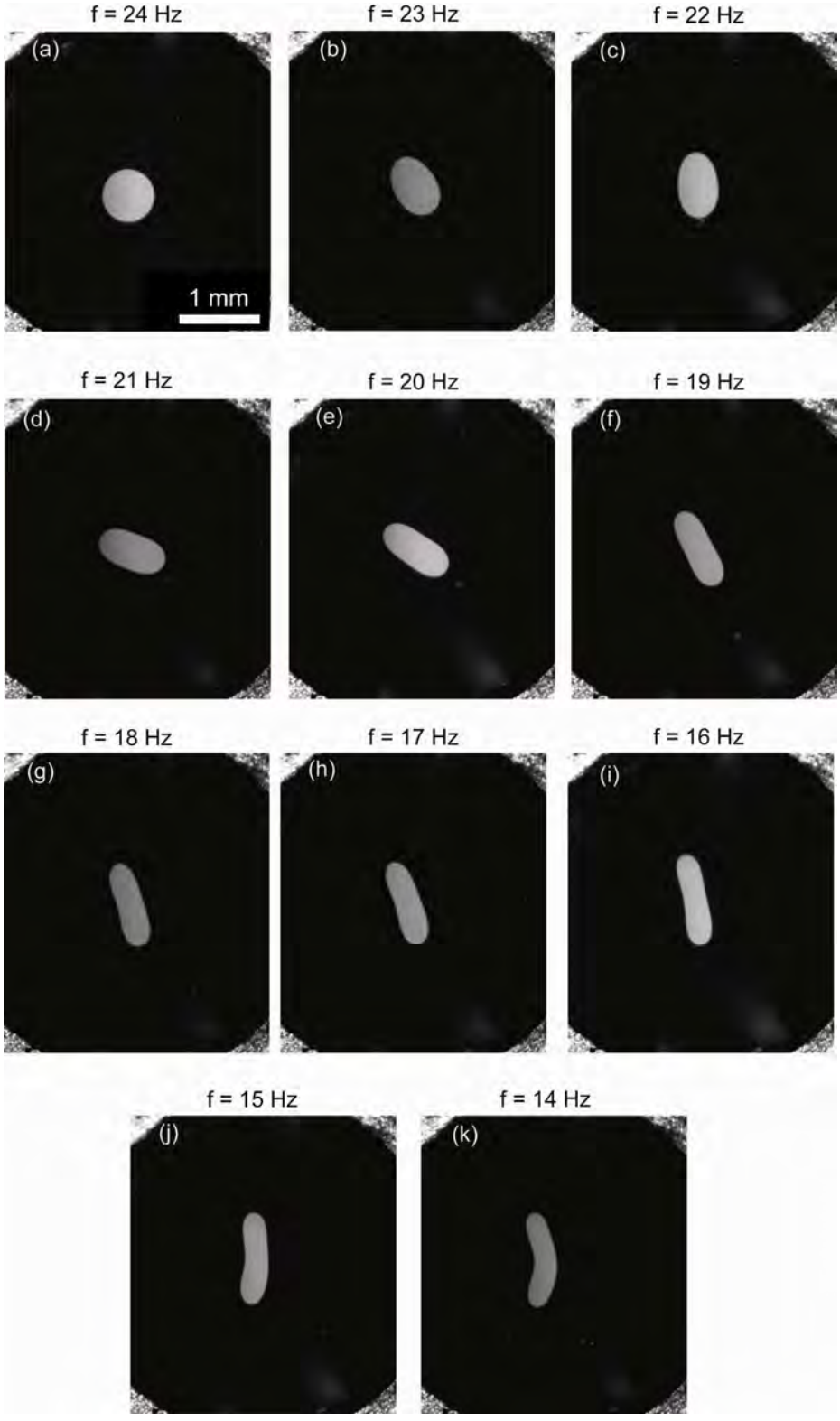

Fig. 76 Deformation of the 8CB island for U = 400 V. The critical frequency is f_{CR}=24 Hz (a) and pictures depicts change of amplitude below the critical frequency (b-k). The amplitude of deformation is higher as the frequency in decreasing. There is visible shift in position of the island, yet the island is in the center of the metal rim for all frequencies.

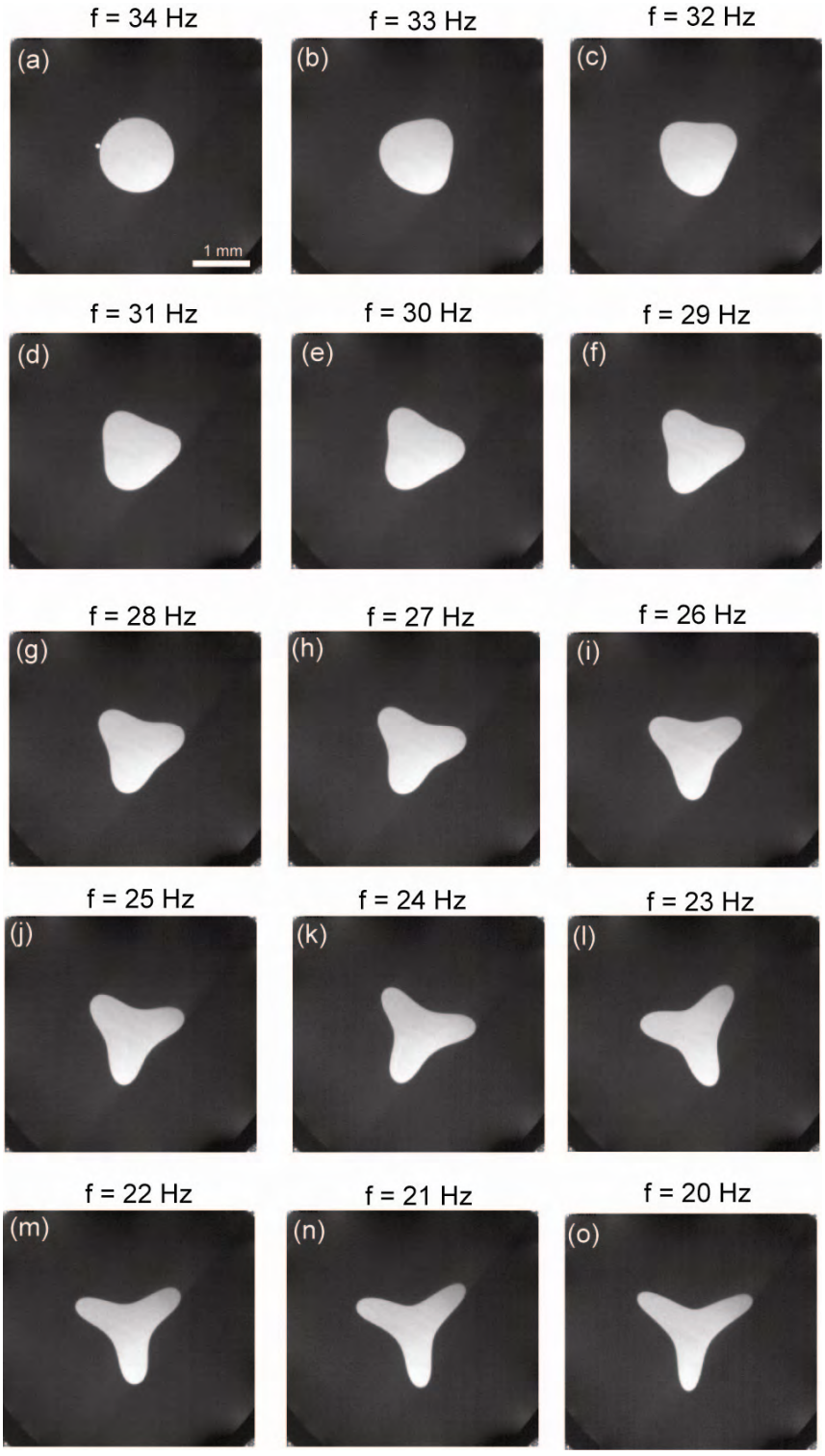

Fig. 77 Deformation of the 8CB island for U = 650 V and for a set of frequencies, starting from the critical frequency f = 34 Hz (a) and below (b-o).

3.2.3.2 Temporal changes of the island for constant voltage and frequency below f_{CR}

Herein I show examples of temporal changes of the shape of the LC island for a constant voltage and a frequency lower than the critical value.

For $f < f_{CR}$ the island is unstable and oscillates periodically in synchrony with the applied voltage. In the figures below I present how the shape of the island changes within an entire period of changes of the electric field.

The simplest example is shown in Fig. 78, where the deformed island is very similar to an ellipse for both polarizations of the needle. The axes of the ellipses are perpendicular for both polarizations. At the beginning the island elongates (b) and as the electric force is acting on it, it stretches out till maximum value (e). At that point the electric field changes polarization (for instance, if the needle was polarized with positive potential, it changes to negative) and the fingers start to shrink, till the island assumes the initial circular shape (i). The electric force continues to act on the island and it starts to deform in a perpendicular axis to the previous deformation, till the maximum value (l). at that point the polarization changes again and the island starts to shrink again, to obtain the initial shape (o). The whole process of deformation of the island started (a) and ended (o) with a non-deformed island (e.g. between the deformation of the island due to change of polarization of the electric field the island retains its spherical shape).

More complicated deformations are shown in Fig. 79 and Fig. 80, where the island has three and seven arms. The analysis of the deformation is the similar as in a case of two arms (or an ellipse-like case). The island starts to deform and the length of the arms is growing till a maximum value, then it shrinks and the island has an initial, round shape. In this case, both for three and seven arm, the next arms are pulled-out from an area of the island which is shifted in phase. In this chapter I show only a three different cases: ellipse, three arm and seven arms case (see Fig. 81).

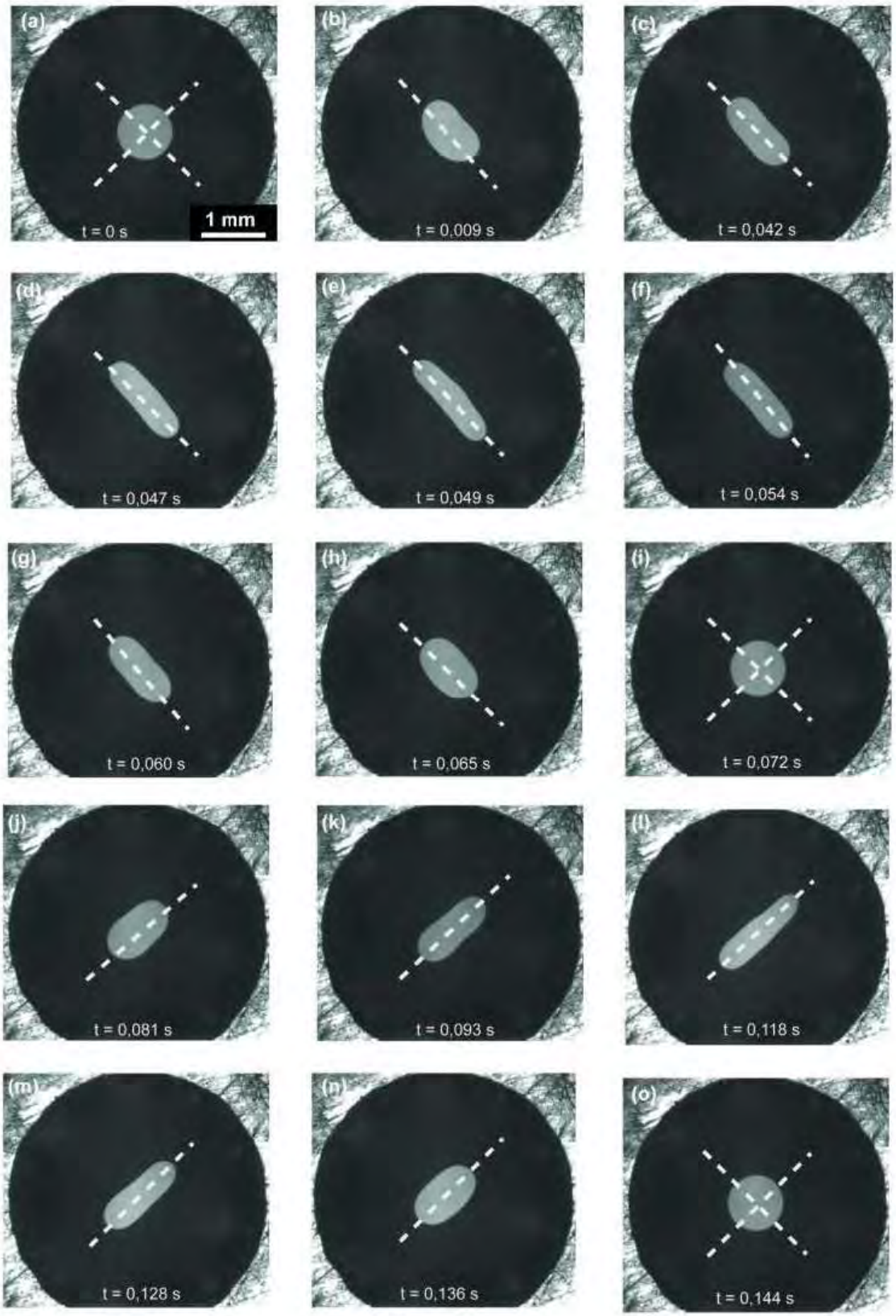

Fig. 78 Changes of 8CB liquid crystal island for U = 200 V and f = 7 Hz. Movie recorded with 1000 fps. The dotted line indicates axis of deformation.

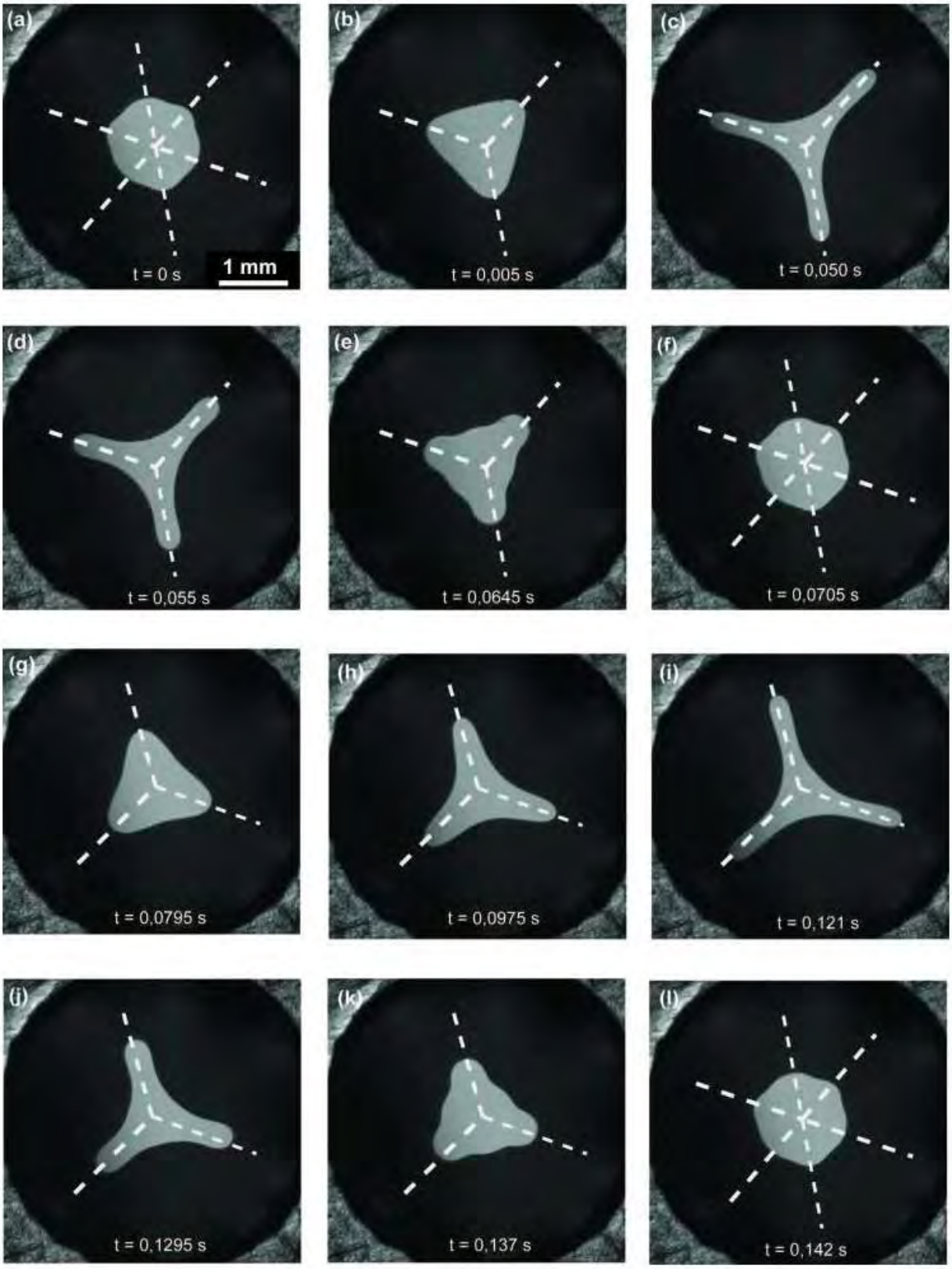

Fig. 79 Changes of 8CB liquid crystal island for U = 200 V and f = 7 Hz. Movie recorded with a 2000 fps. The dotted line indicates axis of deformation.

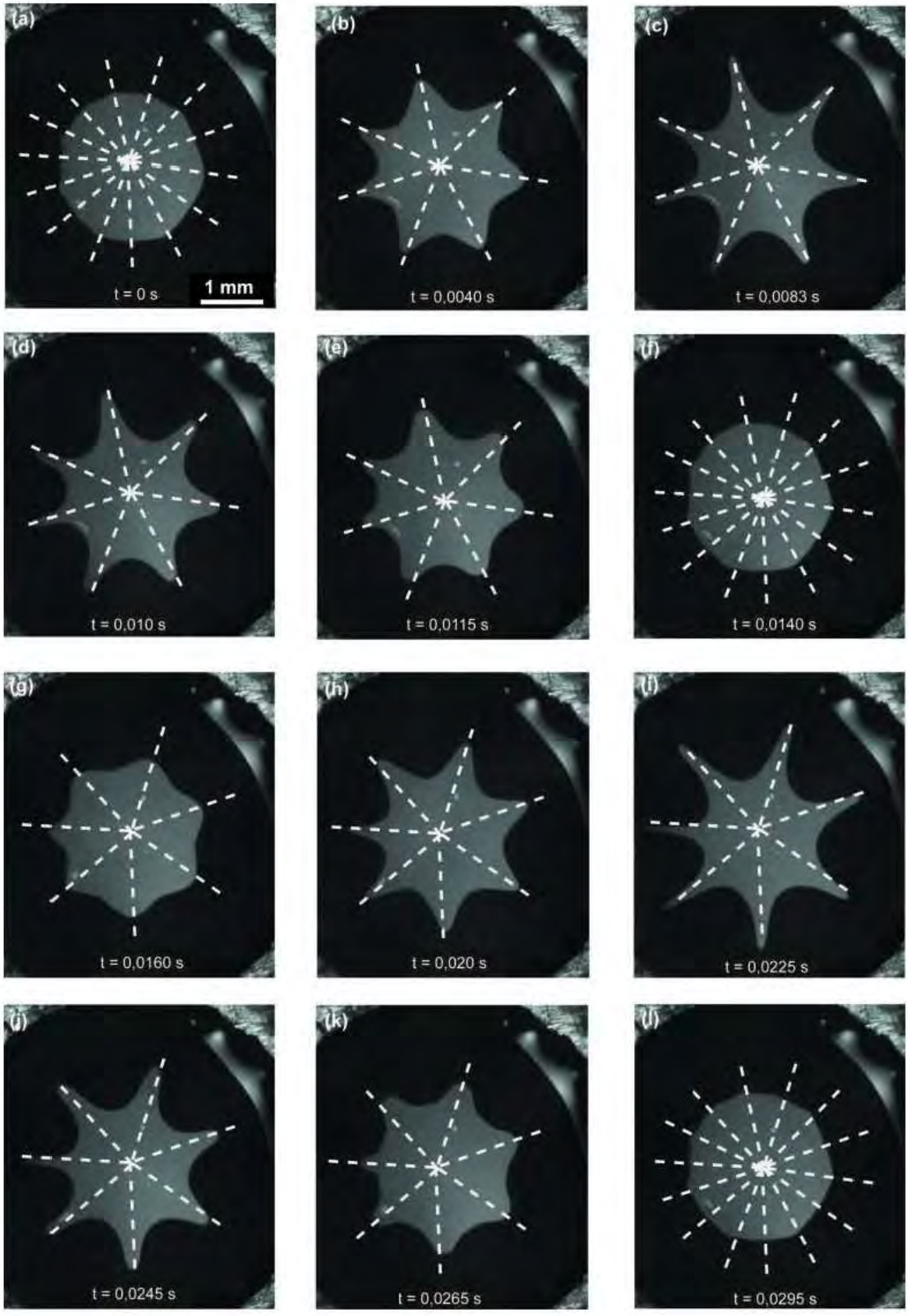

Fig. 80 Changes of 8CB liquid crystal island for U = 800 V and f = 35 Hz. Movie recorded with a 2000 fps. The dotted line indicates axis of deformation.

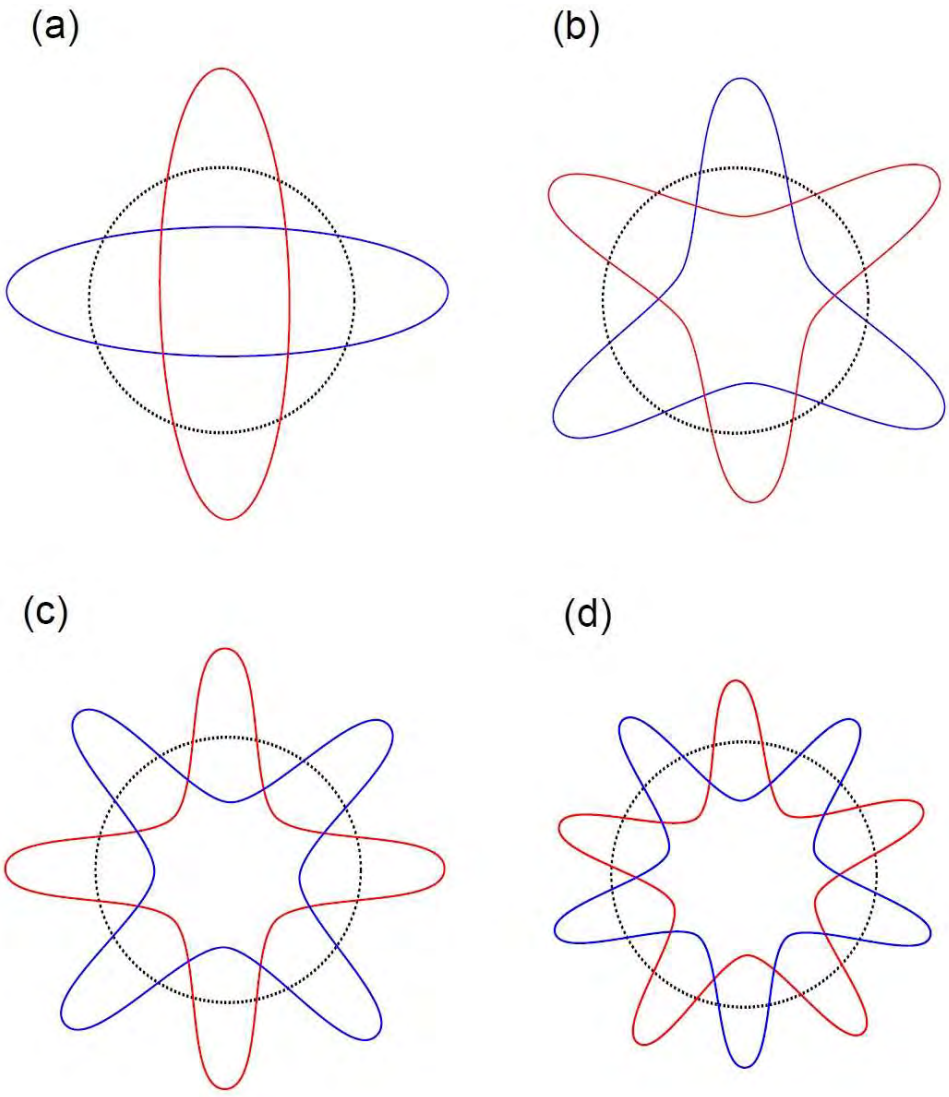

Fig. 81 Examples of the deformations of the liquid crystalline islands. The dotted line present initial, non-deformed island. The red and blue lines present deformed islands (to be more specific, their edges). The line and blue lines are showing deformations for both polarizations of the needle: positive and negative. As it can be see, the shape of the island's edge are complementary for both polarizations. When one type of arm, i.e. for positive polarization, is growing the second type is at its minimal position. When I changed the polarization the second type arm is growing (increasing its length) and previous is shrinking (decreasing its length).
The surface of the non-deformed island and the deformed island is constant during the time and for different frequencies (the surface of dotted circle and red and blue shape is the same for each case).

3.2.3.3 Temporal changes of the meniscus around needle at constant voltage and frequency below f_{CR}

In previous sub-chapters I presented the temporal changes of the LC island. Herein, I present how LC meniscus behaves in AC electric field, recorded with a fast camera PHOTRON. The videos were recorded at 1000 frames-per-second to visualize precisely how the meniscus behave under the action of an oscillating electric field.

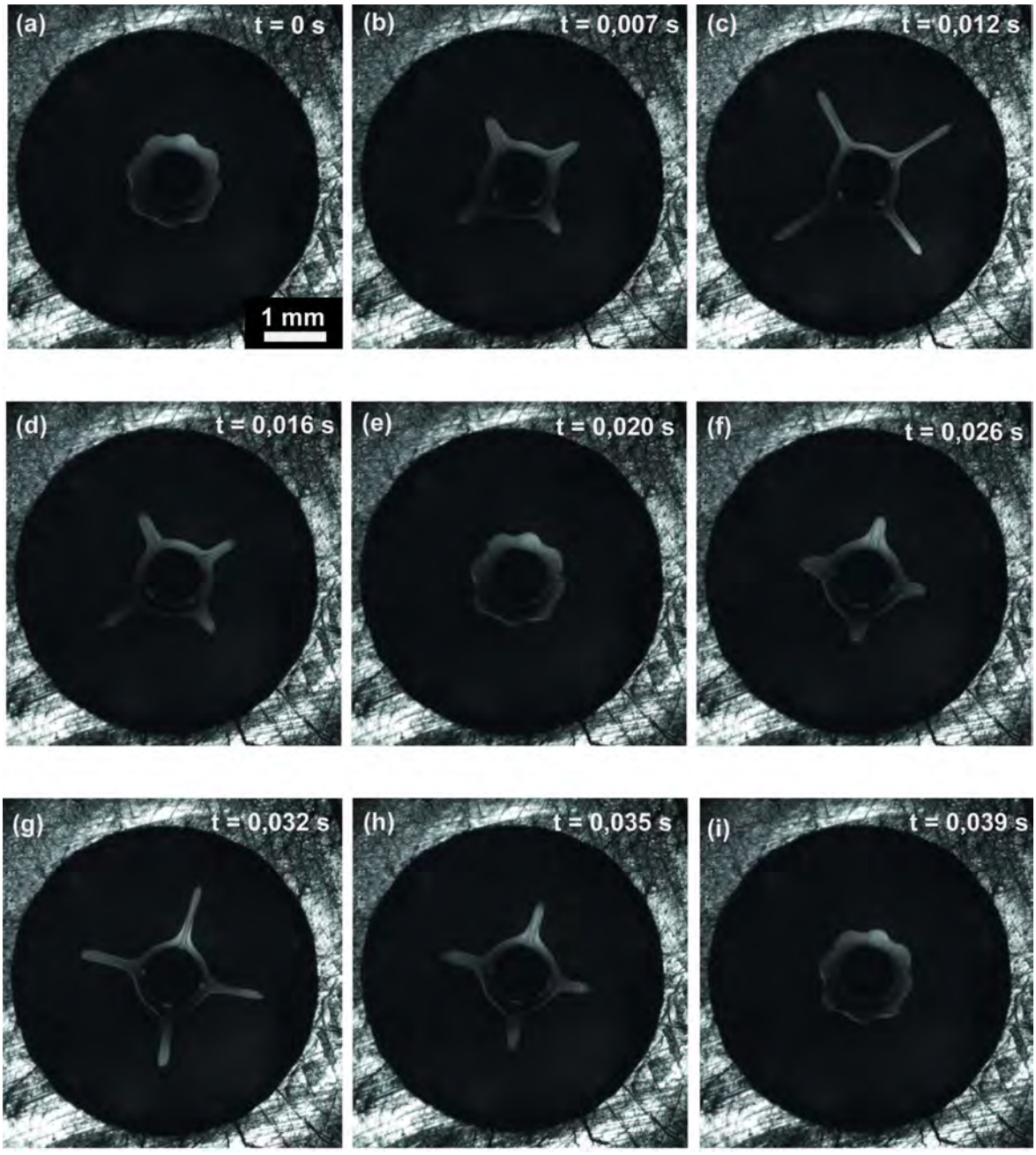

Fig. 82 The 8CB free-standing smectic film pierced with a steel needle (a black dot in a very center of the picture). The movie was recorded for U = 200 V and f = 25 Hz, the free-standing smectic film and the needle were set for the temperature T = 26 ℃.

The results presented in the Fig. 82 were performed for a 8CB free-standing smectic film pierced with the steel needle. The experiment was performed in a way previously described in Chapter 3.1. After spanning the film a small amount of liquid crystal was placed on the steel needle, and the film was carefully pierced with the needle, to obtain a LC meniscus around it. To avoid a thermal convection the temperature of the metal stage and the needle was set-up to T = 26 ℃.

The critical frequency for this experiment was established for f_{CR} = 26 Hz. The movie presented in Fig. 82 was recorded for frequency f = 25 Hz. The meniscus for this frequency destabilizes in a way similar to the LC island described in Fig. 81c.

The meniscus above f_{CR} is circular in shape, below critical frequency it destabilizes to a four-arm shape. The amplitude of the arms is growing in time, till its maximal value (Fig. 82c). Then the polarization of the needle changes to opposite and the amplitude of the arms is decreasing until the meniscus become again circular in shape (Fig. 82e) and the process is repeated for the another polarization of the needle (Fig. 82f-i).

The scheme of the deformation (the increase and decrease of the amplitude of the arm, and the complementary position for the positive and negative polarization) is the same as for the deformation of the LC island.

3.2.4 QUANTITATIVE ANALYSIS OF DEFORMATION OF THE ISLANDS: NUMERICAL ANALYSIS OF FLUCTUATIONS OF EDGE OF THE ISLAND

3.2.4.1 Geometrical parameters of the LC island

The oscillations of the LC islands were recorded for different parameters of the process (i.e., *U*, *f*, island diameter, and organic salt concentration) and analyzed afterwards—for each frame—with the use of the custom written procedures in the MatLab environment. As a result, I obtained a numerical description of the periodical changes of the island's edge in alternating electric field. The parameterisation of the non-deformed and deformed island is shown in Fig. 83.

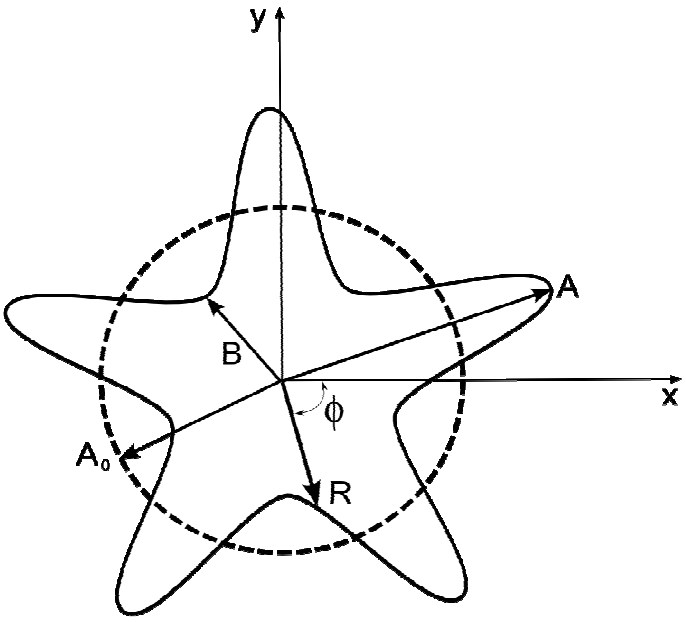

Fig. 83 Numerical parameterization of the non-deformed and deformed liquid crystalline island. The dotted line is a non-deformed LC island, whereas a continuous line is a deformed island, i.e. an island below critical frequency f_{CR}.

The next step is to characterize the changes of the shape of the island with parameters depicted in Fig. 83, i.e.:

A_0 – the radius of non-deformed island,

N – the number of the arms of deformed island,

R – a vector with beginning in the center of the island and the end at its edge,

ϕ – the angle between x axis and vector R,

A – the length of the A arm,

B – the length of the B arm.

3.2.4.2 Number of arms N of deformed island

The LC island in an oscillating electric field performs a flower-like shape with a number of arms. The pictures of these instabilities were shown in Fig. 75. The dependency of the number of the arms as a function of the applied voltage is shown in Fig. 84.

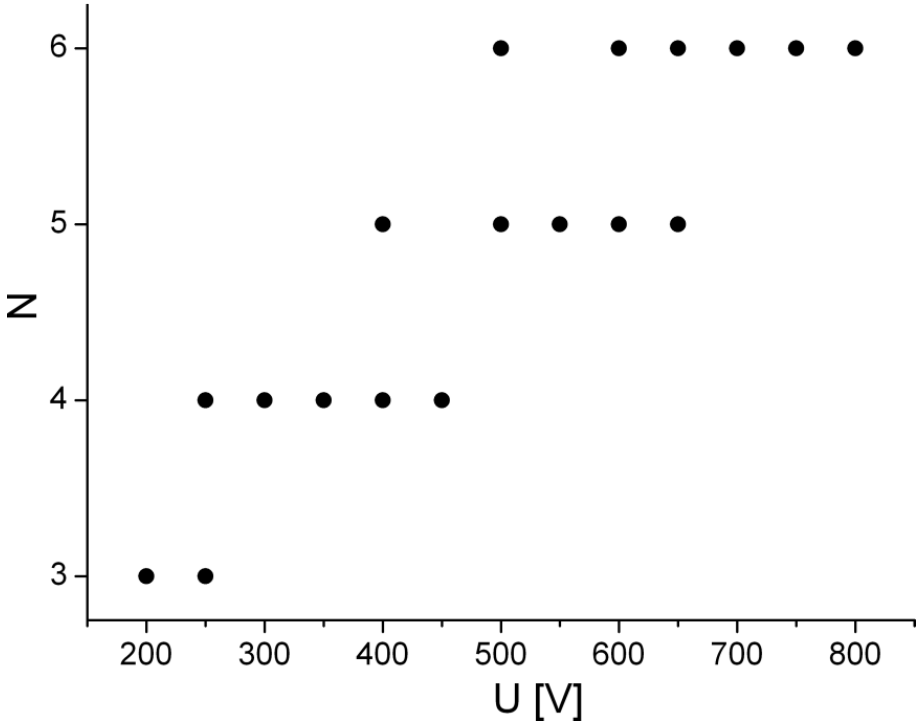

Fig. 84 Number of arms (*N*) of deformed LC island as a function of applied voltage (*U*). The results were obtained for a single island of 8CB liquid crystal with addition of BDTC 10^{-3} M/M. Each point represents a set of experiments (videos) thus each point is a range of frequencies where a certain number of arms occur, i.e. for voltage U=800 V six arms (N=6) occurs for frequencies from *f*=69 Hz up to *f*=82 Hz.

The results are shown for a single LC island made of 8CB doped with BDTC organic salt. In this series of experiments an island presented between 3 and 6 arms. In a few cases, the different number of the arms can be obtained for the same voltage (yet for different frequencies), i.e. for 250 V an island can destabilize into a 3 or 4 arm island and for 400 V I could obtain an island with 4 or 5 arms etc. An example (recorded for 8CB with 10^{-6} M/M BDTC) shown in the Fig. 85 presents different number of the arms for identical *U* and *f*. An island for *U* = 400 V and $f > f_{CR}$ is shown in Fig. 85a. For *f* = 18 Hz I observed four arms (Fig. 85b and c). Increasing frequency above critical and again lowering to *f* = 18 Hz gave a three arms island (Fig. 85d and e).

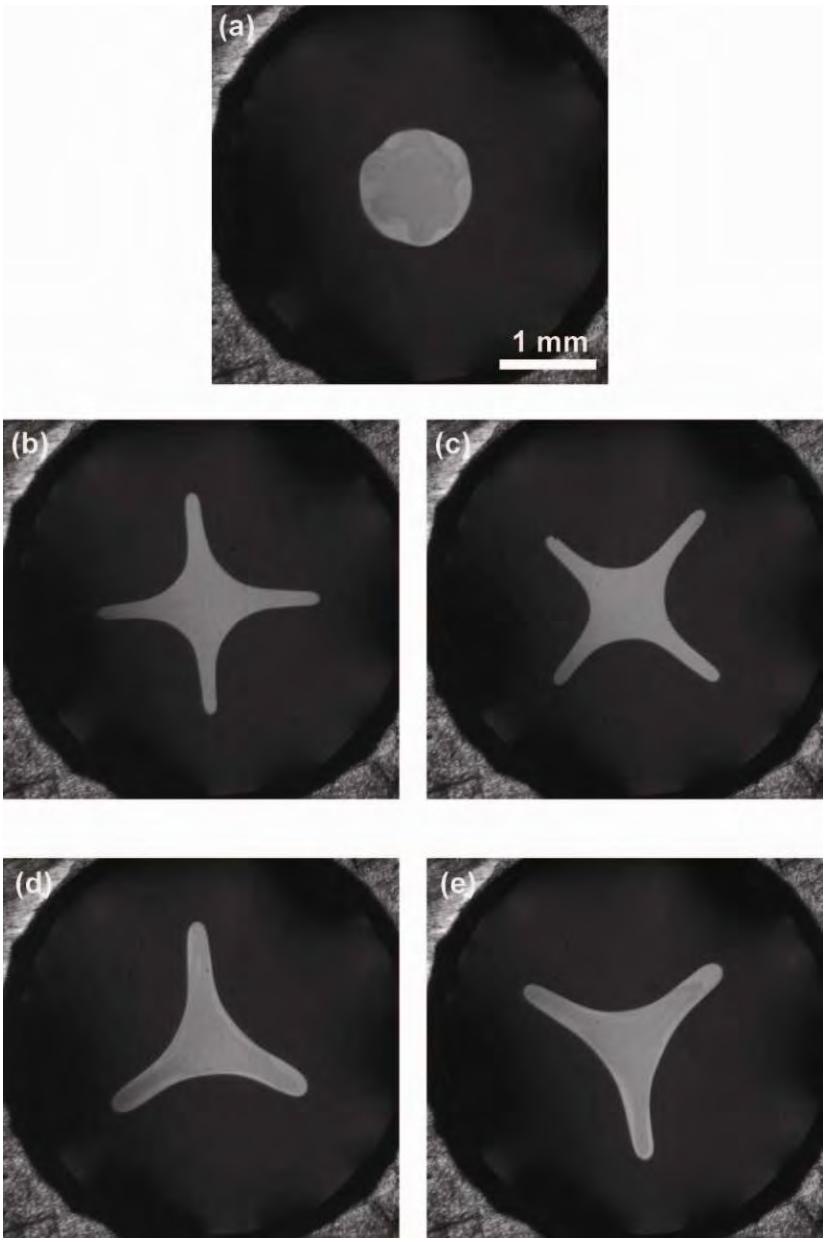

Fig. 85 For the same pair of parameters (U, f) I observed different number of arms. An island for U = 400 V and $f > f_{CR}$ (a). Deformations of the island for U = 400 V and f = 18 Hz ($f < f_{CR}$) (b-e). Four arms (b and c) or three arms (d and e) were observed.
Experiments performed for LC island of 8CB with 10^{-6} M/M BDTC organic salt. Movies were recorded with 2000 fps.

3.2.4.3 The shape of the deformed island

Fig. 86 presents examples of the *R* vector (in the cylindrical coordinates) as a function of ϕ angle for different types of deformed islands. Dependencies R=f(ϕ) were used to calculate the mean length of the arm A.

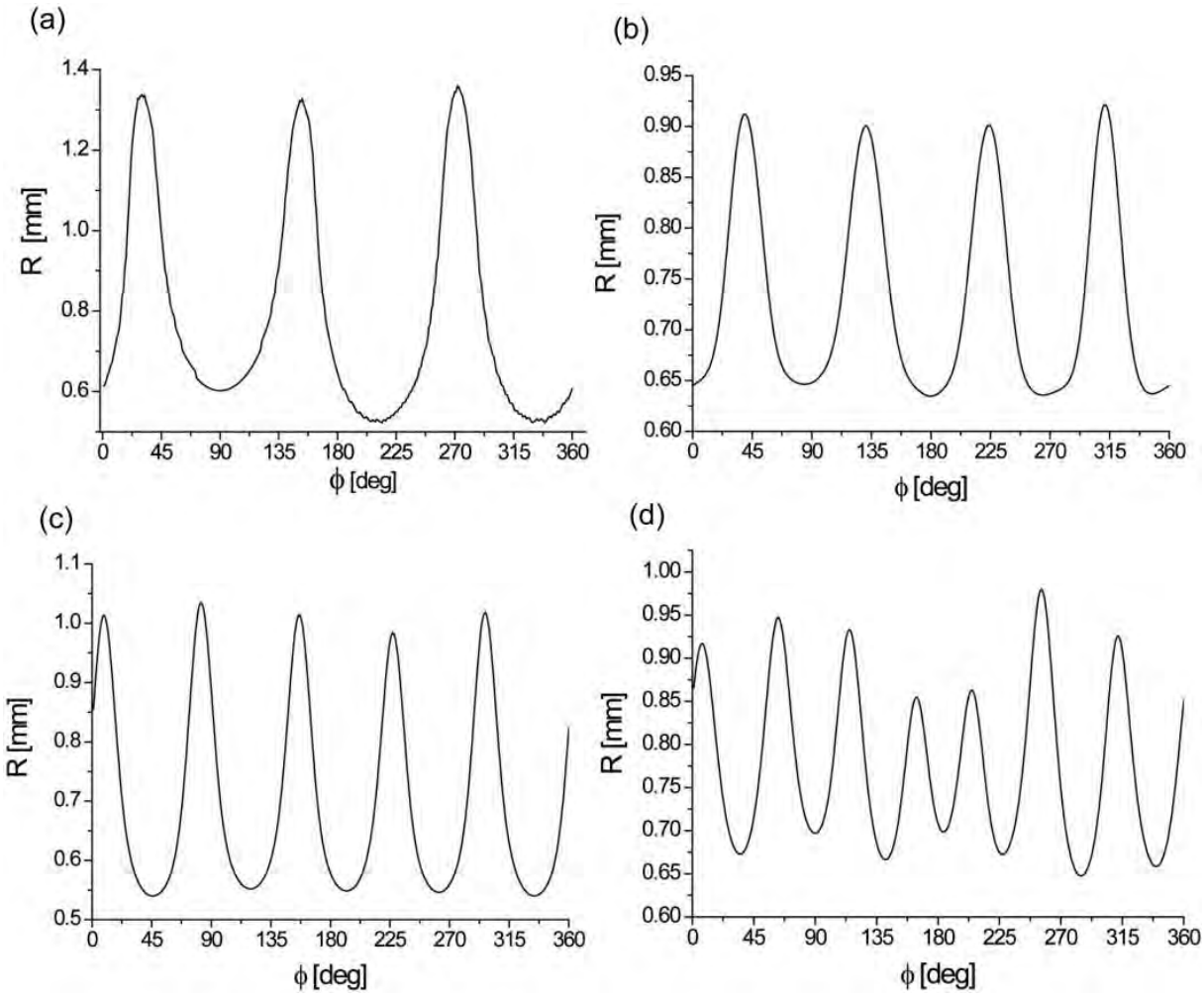

Fig. 86 Position vector of the edge of the island *R* as a function of the angle for island with: (a) N = 3 arms, (b) N=4 arms, (c) N=5 arms, and (d) N=6 arms. The results were obtained for 8CB liquid crystal with 10^{-3} BDTC.

3.2.4.4 Temporal changes of the length of the arms

The changes of length of both arms as a function of time are shown in the Fig. 87. Because in each tact of a different polarization of the electric field different spots on the boundary of the island grow into fingers the arms form two separate groups. Because we anticipate that one group has an accumulated positive electrostatic charge at the tips of the fingers, and the other groups has a negative charge at these apexes, we call one group ‘P-fingers’ (drawn from Plus) and the other one ‘M-fingers’ (drawn from Minus).

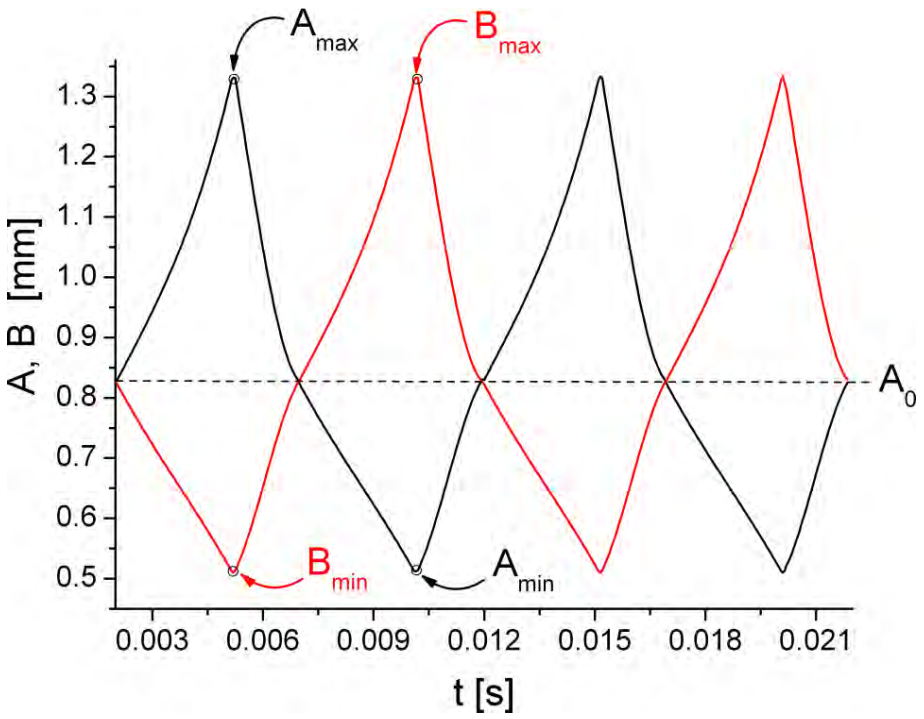

Fig. 87 Temporal changes of the length of the arm A (red line) and B (black line) (compare the Fig. 82 to localize the A and B arms). A_{max} and A_{min} is a maximal and minimal value of the amplitude of the A arm, whereas B_{max} and B_{min} is a maximal and minimal value of the amplitude of the B arm. Herein I demonstrate amplitude versus time for two changes of polarization. The changes of the amplitude are in the synchrony with the changes of polarization.
The results for 8CB liquid crystal with 10^{-3} BDTC, U=200 V, f = 11 Hz.

The amplitude of the deformation for arms A (P-fingers) and B (M-fingers) are shifted in phase. When the arm A is in its maximal value, the arm B is in a minimal position. As was previously stated, the amplitude changes in synchrony with applied electric field, so in Fig. 87 I presented two periods of polarization.

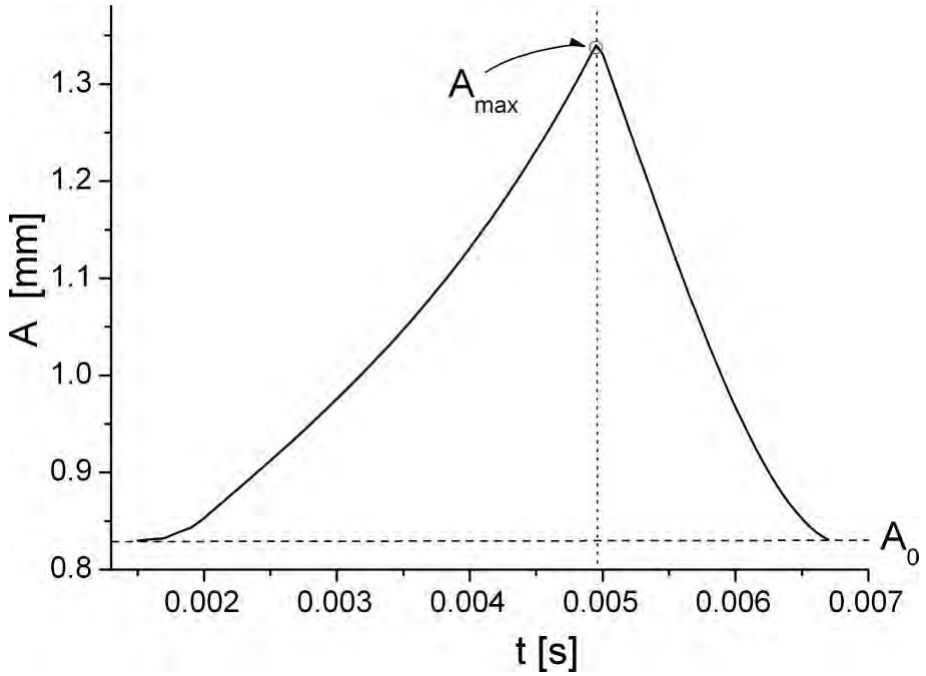

Fig. 88 Detailed view of the time evolution of the island's arm. The clear asymmetry is visible for both sides of the plot. The results for 8CB liquid crystal with 10^{-3} BDTC, *U*=200 V, *f* = 11 Hz.

Precise analysis of the data presented in Fig. 87 shows that the profile of growth of the length of the arm is not symmetrical with respect to the change of the arrow of time. A profile for a single event of growth and decrease of a finger is shown in Fig. 88. The growth starts from the A_0, which is the radius of a non-deformed island. The length is growing till the value of A_{max}, then it starts to decrease till it achieves the initial value A_0. The time of obtaining A_{max} ($t_{A0\text{-}Amax}$) and again obtaining A_0 ($t_{Amax\text{-}A0}$) are not equal. Thus, the rates of the growth and of the decrease of length of the finger are different: when arm is growing the time is longer and the velocity of the arm is lower comparing to the second stage, when the arm is shrinking: the time is shorter and the velocity is larger. This observation holds for all cases, i.e. for all islands, both for pure 8CB and 8CB doped with organic salts.

3.2.4.5 Normalized perimeter of the island

In the Fig. 89 is presented the perimeter of the deformed island as a function of time. For non-deformed island the perimeter is equal to:

$$P = 2\pi A_0 \tag{105}$$

where A_0 is the radius of the non-deformed island.

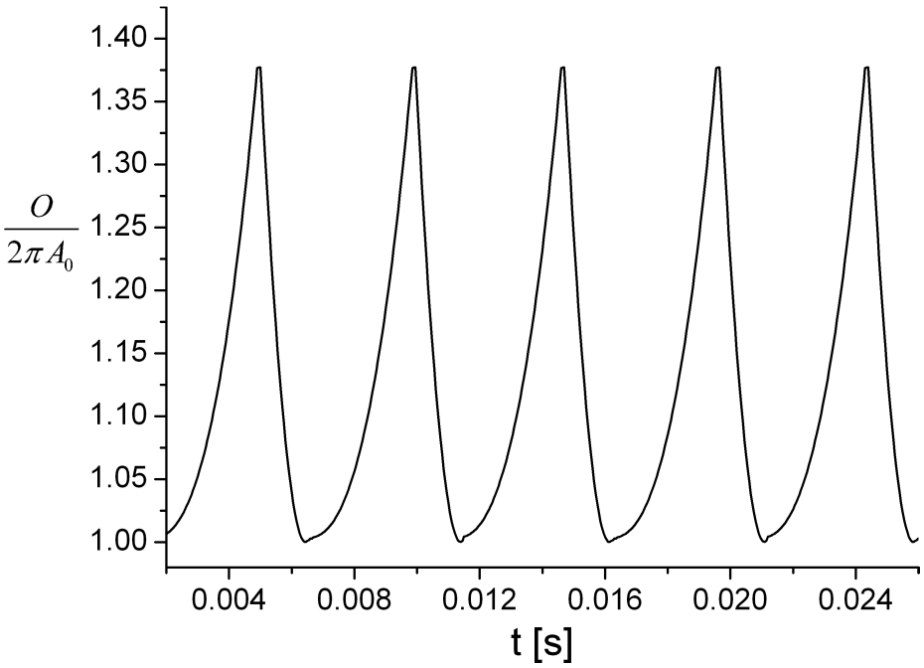

Fig. 89 Temporal changes of the measured perimeter (labeled as *O*) normalized by the calculated perimeter *P* of the island. Analysis performed for the 8CB with 10^{-3} BDTC organic salt, *U* = 200 V, *f* = 11 Hz.

At frequencies higher than the critical value the island is non-deformed, thus the perimeter is equal to $2\pi A_0$ and therefore after normalization is equal 1. For $f < f_{CR}$, the island start to deform and thus the perimeter will change in time. In Fig. 89 is presented a typical plot of normalized perimeter as a function of time. This region on the plot can be identified in the movie, as a growing of the arms from the island to its maximal value.

The maximal values of the perimeter in the Fig. 89 are maximal deformations of the arm A and B, i.e. A_{max} and B_{max}. As the arms are decreasing, the perimeter of the island is also decreasing, and at the end the ratio of circumference to the circumference of non-deformed island ($2\pi A_0$) is equal to one.

3.2.4.6 Maximum length of the arms as a function of the frequency

I denote the maximum value of the deformation of the island's arm as A_{max}. Fig. 90 shows an example of linear regression of A_{max} and the time t defined as:

$$t = \frac{1}{f} \tag{106}$$

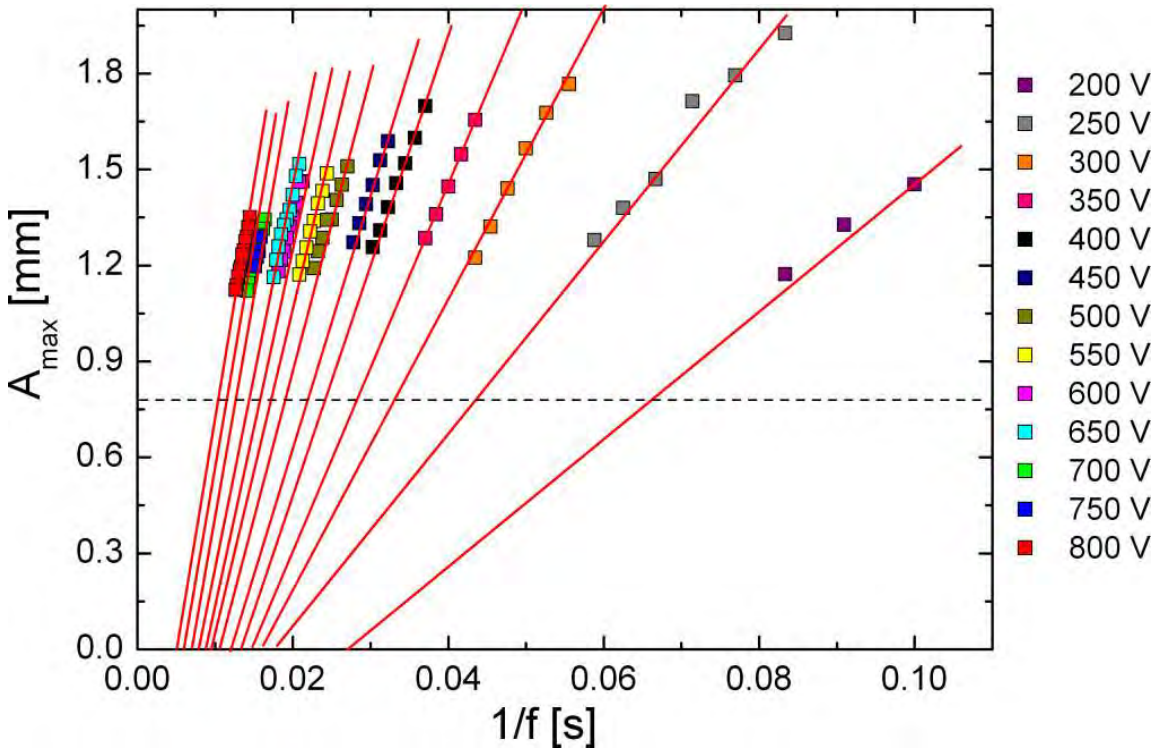

Fig. 90 The value of maximal deformation of the island, A_{max}, versus the time on acting of the electric field on the LC island. (a) The linear regression for each set of points cut the value of non-deformed island (dotted line), thus give us the critical frequency f_{CR}.
The results obtained for a single LC island made of 8CB with 10^{-3} M/M BDTC organic salt.

The points in a single series (i.e. for an applied voltage) shows a linear dependency between the A_{max} and the time. Knowing the radius of the non-deformed island (A_0) I could calculate the critical frequency f_{CR} from the point of intersection of A_0 and the linear fit. The f_{CR} is given by:

$$f_{CR} = \frac{1}{t_{CR}} \tag{107}$$

The dependency of f_{CR} and U is shown in Fig. 91.

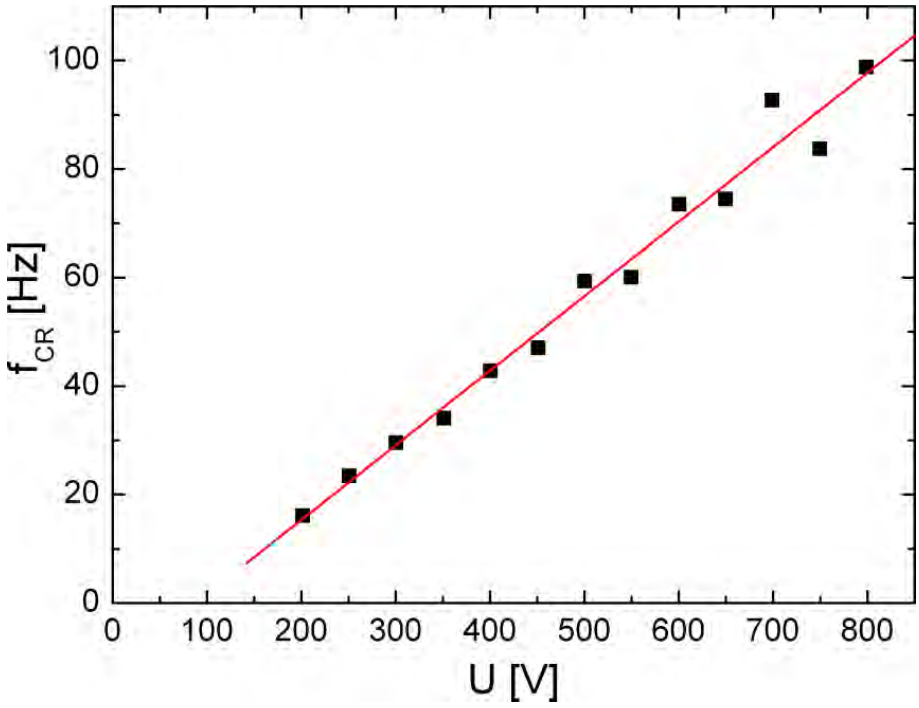

Fig. 91 Critical frequency (f_{CR}) as a function of the voltage (U). The results obtained for a single LC island made of 8CB with 10^{-3} M/M BDTC organic salt.

The numerical analysis gave the same result (linear dependency of f_{CR}=f(U)) like our previous asses of f_{CR} by a 'naked eye' (see Chapter 3.1).

The slope of every linear regression from Fig. 90 as a function of voltage is given in Fig. 92. The slope is defined as:

$$\kappa = \frac{dA_{\max}}{d\left(\frac{1}{f}\right)} \tag{108}$$

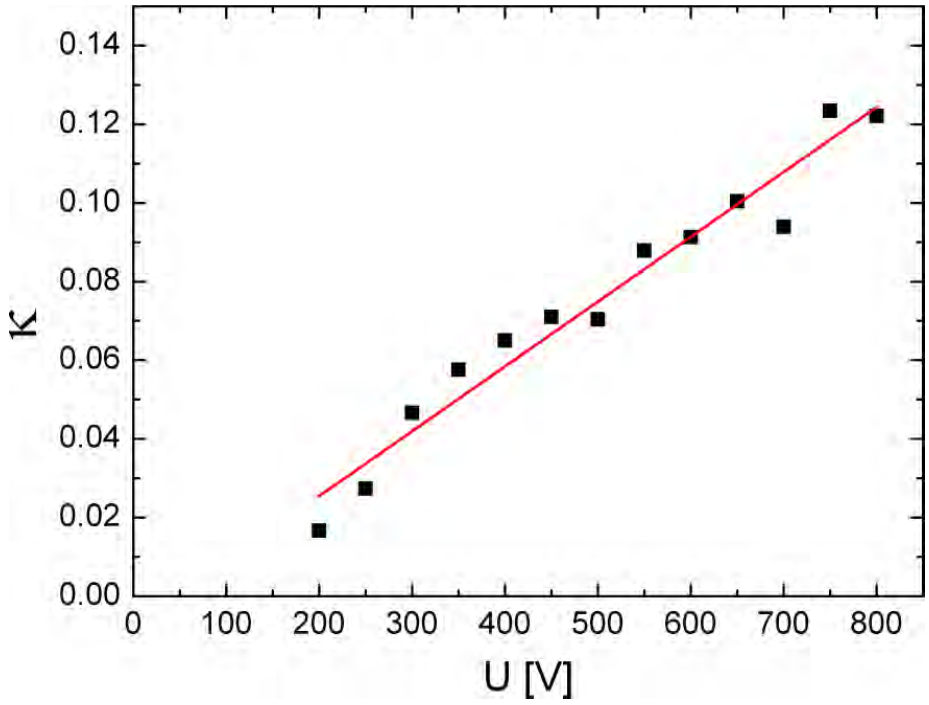

Fig. 92 The κ coefficient (slope) of the linear regression plots from Fig. 90, as a function of the voltage.

The κ and f_{CR} coefficients depends also on other properties of the system, i.e. the diameter of the island, the number of the arms etc. For each set of experiments (i.e. *U* and *f*) value of A_{max} was approximated with a correlation:

$$A_{\max} = \kappa \cdot \left(\frac{1}{f} - \frac{1}{f_{CR}} \right) + A_0 \tag{109}$$

where κ and f_{CR} are functions of *U*.

Fig. 93 compares experimental results and A_{max} calculated with equation (109). The points are on the diagonal line, which mean that the theoretical and experimental values are in good agreement.

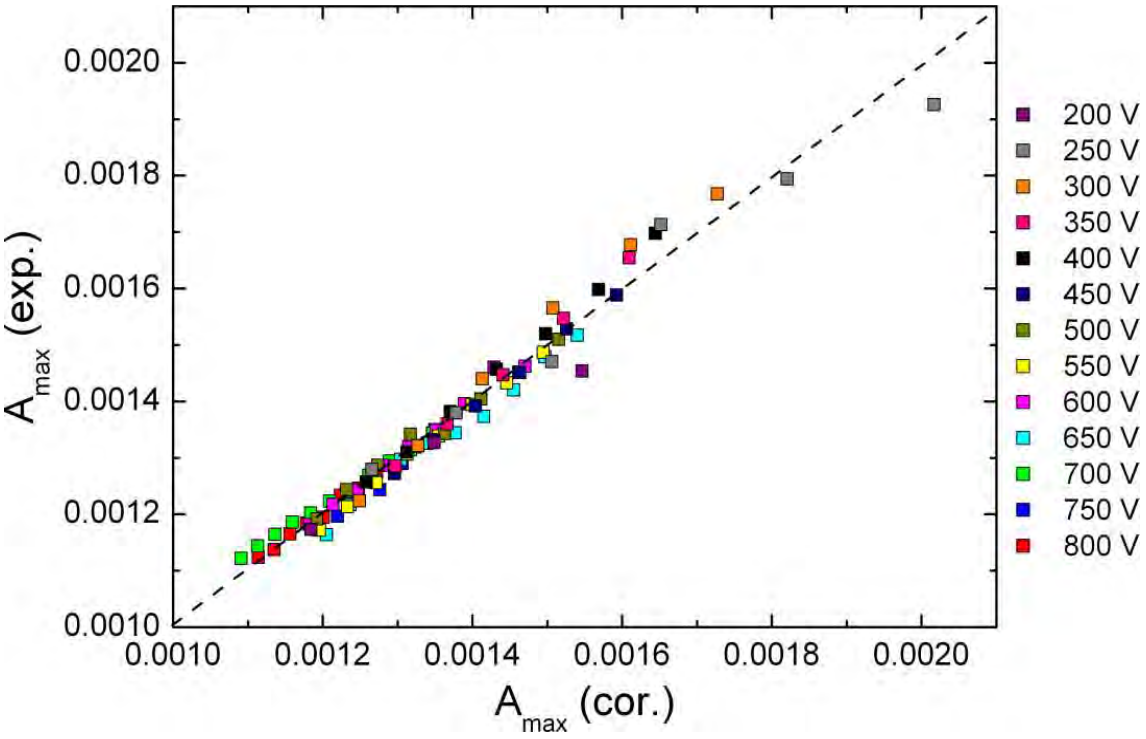

Fig. 93 Parity plot – experimental value of A_{max} as a function of the A_{max} re-calculated from correlation.

3.2.5 ELECTRO-HYDRODYNAMIC (EHD) MODEL

3.2.5.1 Assumptions of the EHD model

The LC islands oscillate periodically in synchrony with the changes of polarization of the electric field. The main goal of the EHD model is to:

i) describe the forces acting on the LC island,

ii) assess the order of magnitude of these forces,

iii) check the influence of the ion concentration on the induced charge on the border of the LC island.

The aim of developing the EHD model was to:

i) describe the forces acting on the LC island,

ii) assess the order of the magnitude of these forces,

iii) calculate the value of line tension F_σ and induced charge Q,

iv) verify the influence of organic salt on induced charge Q.

The EHD model was developed using the balance of the transformation of different form of energy in the system:

$$P_e = D_\mu \pm M_{kin} \pm P_\sigma \tag{110}$$

In the balance (110) I took into account the following energies:

P_e – energy of the electric field, E_e

M_{kin} – kinetic energy of the LC island, E_{kin}

D_μ – energy E_μ dissipated into a heat,

P_σ – energy E_σ correlated with a length of the dislocation line at the edge of the LC island.

Rate of change of each energy ($\frac{dE}{dt}$) can be approximately written as the product of a substituent force acting on the arm at the point A (i.e. at the top of the arm) and the velocity of the arm A, i.e. u_A:

$$P_i = \frac{dE_i}{dt} = F_i \cdot u_A \tag{111}$$

After dividing (111) by the velocity of the arm A, the eq. (110) can be rewritten as a balance of the forces:

$$F_e = F_\mu \pm F_{kin} \pm F_\sigma \tag{112}$$

In the balance of the forces from (112) each constituents are:

F_e – force of the electric field acting on the LC island,

F_μ – force of hydrodynamic resistance,

F_k – inertial force,

F_σ – force of the dislocation line at the edge of the LC island.

The LC island has axes of symmetry (i.e. the simplest deformation, an ellipse, has two exes of symmetry) thus all balances and calculation will be performed for one smectic layer inside a single arm.

In our model we assume that all forces taken into account are proportional to the thickness of the LC island. The force acting on the induced charge Q is proportional to the volume of the island. The line tension force is proportional to the single smectic layer (or more specific, to the dislocation line in the one smectic layer). The viscous dissipation occurs in the volume of the LC island. And finally, the change of kinetic energy is related to the mass of the island, thus is proportional to the thickness of the LC island.

To assess the force of hydrodynamic resistance and inertial force it is necessary to know the velocity field inside the LC island. The forces at the right side of the equation (112) must be related with the experimental parameters: radial coordinate of the point A and its velocity u_A.

3.2.5.2 Modeling of the velocity field inside the island

In order to explain the construction of the model of the velocity field inside the LC island we use the simplest case of an approximately ellipsoidal island (with two pertrusions). We note that the evolution of the boundary of the island resembles an ellipsoid that can be obtained from a circle by a non-Euclidean, anisotropic scaling transformation, in which one direction is dilated (enlarged) while the second is contracted (shortened) in such a way as to preserve the surface area of the object. Fig. 94 demonstrates such a transformation on the example of a rectangle. In the experiments the surface area of the island is indeed preserved, so one can write a scaling for the x and y:

$$y \to y^* \tag{113}$$

where

$$y^* = \alpha_y^* \cdot y \tag{114}$$

and

$$\alpha_y = \frac{A(t)}{A_0} \tag{115}$$

And in the same way:

$$x \to x^* \tag{116}$$

$$x^* = \alpha_x^* \cdot x \tag{117}$$

$$\alpha_x = \frac{A(t)}{A_0} \tag{118}$$

Then the velocity field (u_x(x,y) and u_y(x,y)) inside the island can be written as:

$$u_y = \frac{y}{A} u_A \tag{119}$$

$$u_x = \frac{x}{B}(-u_B) \tag{120}$$

Where u_A and u_B are the rates of change of the length of the P-finger and M-finger. As a result, local constituents of shear inside the island can be related with the velocity of the points A and B and the edge of the island:

$$\frac{\partial u_y}{\partial y} = \frac{u_A}{A} \tag{121}$$

$$\frac{\partial u_x}{\partial x} = -\frac{u_B}{B} \tag{122}$$

Shape of the deformed island is similar to the ellipse, therefore coordinates of the circumference in Cartesian coordinates can be described as:

$$\left(\frac{Y}{A}\right)^2 + \left(\frac{X}{B}\right)^2 = 1 \tag{123}$$

or the equivalent equation in cylindrical coordinates:

$$R(\varphi) = A\left[\alpha^4 - (\alpha^4 - 1)\cos^2(\varphi)\right]^{-1/2} \tag{124}$$

where α is a ratio of deformation of the arm to the radius of non-deformed island:

$$\alpha = \frac{A}{A_0} \tag{125}$$

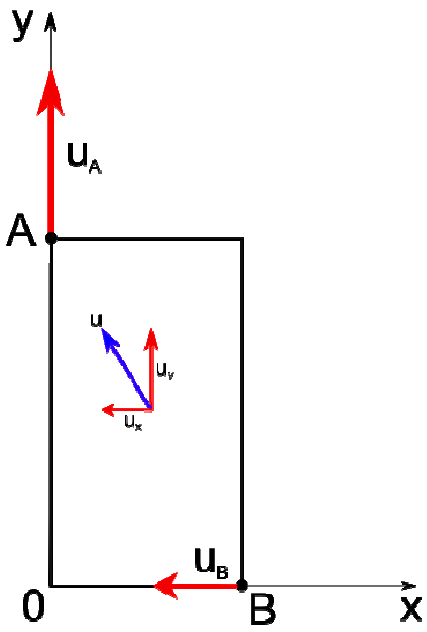

Fig. 94 The velocity field inside the arm of LC island can be approximated with evenly stretched rectangle. Vectors u_A and u_B shows a direction and magnitude of velocity vector A and B at the edge of the island. Partial constituent of the velocity profile u_x and u_y are defining a velocity field in every point inside the island.

In order to take into consideration all axes of symmetry of the system, especially for islands with number of arms N > 2, it is possible to transform the angular coordinate φ:

$$\varphi' = \left(\frac{N}{2}\varphi\right) \tag{126}$$

What gives an equation (127) describing vector *R*, in a form which approximate the shape of the island with arbitrary number of arms:

$$R(\varphi) = A\left[\alpha^4 - (\alpha^4 - 1)\cos^2\left(\frac{N}{2}\varphi\right)\right]^{-1/2} \tag{127}$$

where $\alpha = \frac{A}{A_0}$ (ratio of deformation of the arm to the radius of non-deformed island)

In any coordinate system the surface of the island can be determined with equation:

$$S(t) = \pi A(t)B(t) \tag{128}$$

The surface does not depend on the length of the arms and their number *N*:

$$S = \int_0^{2\pi} d\phi \int_0^R r\, dr = \pi A_o^2 \tag{129}$$

Therefore its time derivative is equal to

$$\begin{aligned} &\frac{dS}{dt} \equiv 0 \\ &\frac{dS}{dt} = \pi A\left(\frac{dB}{dt}\right) + \pi B\left(\frac{dA}{dt}\right) = \pi A\, u_B + \pi B u_A \end{aligned} \tag{130}$$

where:

$$\begin{aligned} \frac{dA}{dt} &= u_A \\ \frac{dB}{dt} &= u_B \end{aligned} \tag{131}$$

Using the eq. (130) it is possible to write a dependency between velocity u_A and u_B (i.e. velocities of the peaks of arm A and B):

$$\frac{u_A}{A} = -\frac{u_B}{B} \tag{132}$$

and using eq. (125):

$$u_B = \left(\frac{B}{A}\right) u_A = \left(\frac{1}{\alpha^2}\right) u_A \tag{133}$$

Partial constituent of the velocity profile (119 and 120) in a new, cylindrical coordinate are given by:

$$\begin{cases} u_r = r\left(\frac{u_A}{A}\right)\cos(N\phi) \\ u_\phi = -\left(\frac{2}{N}\right)\left(\frac{u_A}{A}\right)\sin(N\phi) \end{cases} \tag{134}$$

and using eq. (125):

$$\begin{cases} u_r = \frac{r}{\alpha}\left(\frac{d\alpha}{dt}\right)\cos(N\phi) \\ u_\phi = -\left(\frac{2}{N\alpha}\right)\left(\frac{d\alpha}{dt}\right)\sin(N\phi) \end{cases} \tag{135}$$

Eq. (135) fulfill continuity equation (differential balance of mass) inside the island:

$$\frac{\partial(ru_{\phi})}{\partial\phi}+\frac{\partial(ru_{r})}{\partial r}=0 \tag{136}$$

Velocity field defined by eq. (135) was used to calculate hydrodynamic resistance and inertial forces inside the island.

3.2.5.3 Modeling of the forces from the balance equation

3.2.5.3.1 The rate of dissipation energy and hydrodynamic resistance

Having these velocity field it is possible to discuss the viscous dissipation. The flow and deformation of viscous material require energy. This mechanical energy, during the flow of the liquid, is dissipated or converted into a heat. The smectic A film is a highly anisotropic material. However, in the plane of the layers it behaves like the Newtonian fluid. Thus, the rate of viscous dissipation per unit volume within the island body obeys a general relationship [7]:

$$\varepsilon=\tau:\nabla\vec{u}=\mu\,\nabla\vec{u}\,:\nabla\vec{u} \tag{137}$$

The rate of the dissipation energy inside a differential volume in cylindrical coordinates:

$$\varepsilon=\mu u_{A}^{2}\left(\frac{4+\left(N^{2}-4\right)\sin^{2}\left(N\phi\right)}{A_{o}^{2}\,\alpha^{2}}\right) \tag{138}$$

Integrating the eq. (137) over the island's edge given by eq. (127) it is possible to obtain the rate of viscous dissipation for a single 8CB layer for a one arm:

$$D_{\mu}=h\int_{0}^{2\pi}d\varphi\int_{0}^{R}\varepsilon\,r\,dr \tag{139}$$

where h is a height of the single layer of the 8CB liquid crystal. Analytical form of this integral is shown as a correlation:

$$D_{\mu}=\mu\cdot\phi_{\mu}\cdot u_{A}^{2}\cdot h \tag{140}$$

where ϕ_{μ} is a shape factor.

The shape factor depends only on the geometry of the island:

$$\phi_\mu = \phi_\mu\left(\frac{A}{A_0}, N, A_0, h\right) \tag{141}$$

where:

A – length of the arm (P-finger or M-finger),

A_0 – diameter of the non-deformed island,

N – number of arms for deformed island,

h – thickness of the LC island.

For constant value of A_0 (the same LC island for a set of experiments), h (the thickness of island do not change during the experiments) and N (the number of deformed arms is constant for a single experiment), the shape factor is a function of relative arm lengths $\frac{A}{A_0}$.

The value of Φ_μ as a function of α for island with a different number of the arms is presented in Fig. 95.

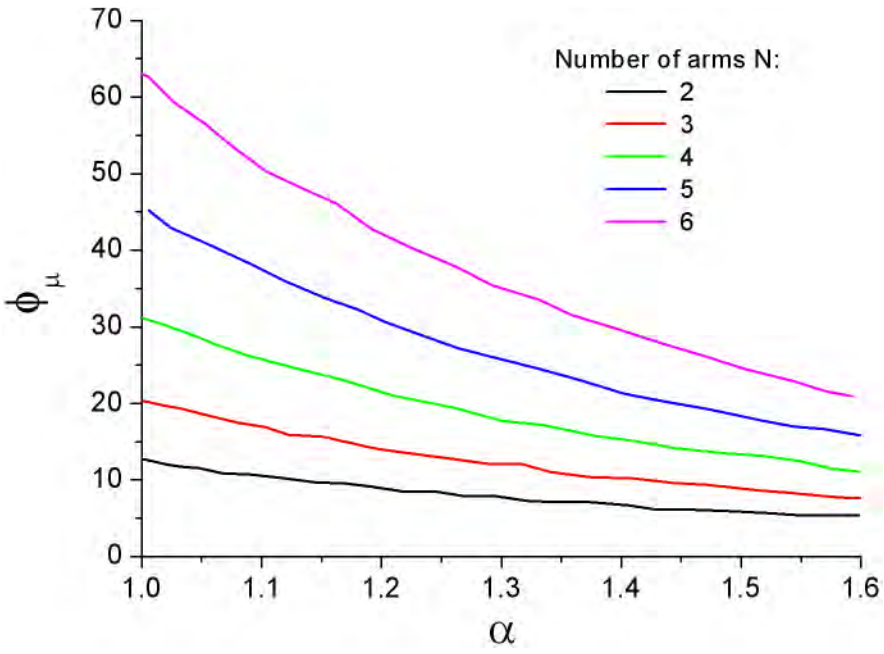

Fig. 95 Shape factor ϕ_μ as a function of $\alpha = \frac{A}{A_0}$ and the number of the arms N.

The rate of the viscous dissipation was used to calculate the hydrodynamic resistance F_μ. For the laminar flow and for A_0 = const. and N = const. the hydrodynamic viscous resistance to the deformation depends linearly on the velocity u_A.

The force F_μ can be calculated by dividing the rate of the viscous dissipation by the velocity of the arm u_A:

$$F_\mu = \frac{D_\mu}{u_A} = \mu \cdot \phi_\mu \cdot u_A \cdot h \tag{142}$$

where:

μ – viscosity of the 8CB liquid crystal,

u_A – velocity of the arm A (defined as $\frac{dA}{dt}$),

ϕ_μ – shape factor,

3.2.5.3.2 The rate of change of kinetic energy and inertia force

In cylindrical coordinates the kinetic energy of the differential element of the fluid is given by equation:

$$e_k = \frac{1}{2}\rho\left|\vec{u}\right|^2 = \frac{1}{2}\rho\left(u_\varphi^2 + u_r^2\right) \tag{143}$$

Kinetic energy of one smectic layer is given by equation:

$$E_{kin} = h\int_0^{2\pi} d\varphi \int_0^R e_k \, r \, dr \tag{144}$$

Knowing the rate of change of kinetic energy in our system one can calculate the substituent inertia force acting on the tip of the arm (i.e. point A):

$$\begin{aligned} M_k &\equiv \left(\frac{dE_{kin}}{dt}\right) \\ M_k &= \left(\frac{dE_{kin}}{dA}\right)\left(\frac{dA}{dt}\right) = F_\rho \cdot u_A \end{aligned} \tag{145}$$

Thus it is possible to express that force in a differential form as below:

$$F_\rho = \frac{dE}{dA} \tag{146}$$

Fig. 96 shows comparison of inertia force and the dissipative force (hydrodynamic resistance). Inertia force is usually no bigger than 10% of hydrodynamic force.

The balance of the forces can be done for any time of the arm evolution, i.e. during increasing of the arm length or decreasing of the length of the arm. However, for the sake of numeric analysis and the accuracy of the image analysis the best point is defined as 'optimal point'. For this optimal point (A_{opt}) the inertia force is about 3%. Optimal point is defined as:

$$A_{opt} = 0.4(A_{\max} - A_0) + A_0 \tag{147}$$

Therefore, in the rest of calculations inertia force was abandoned and all measurements were performed for A_{opt} defined as above.

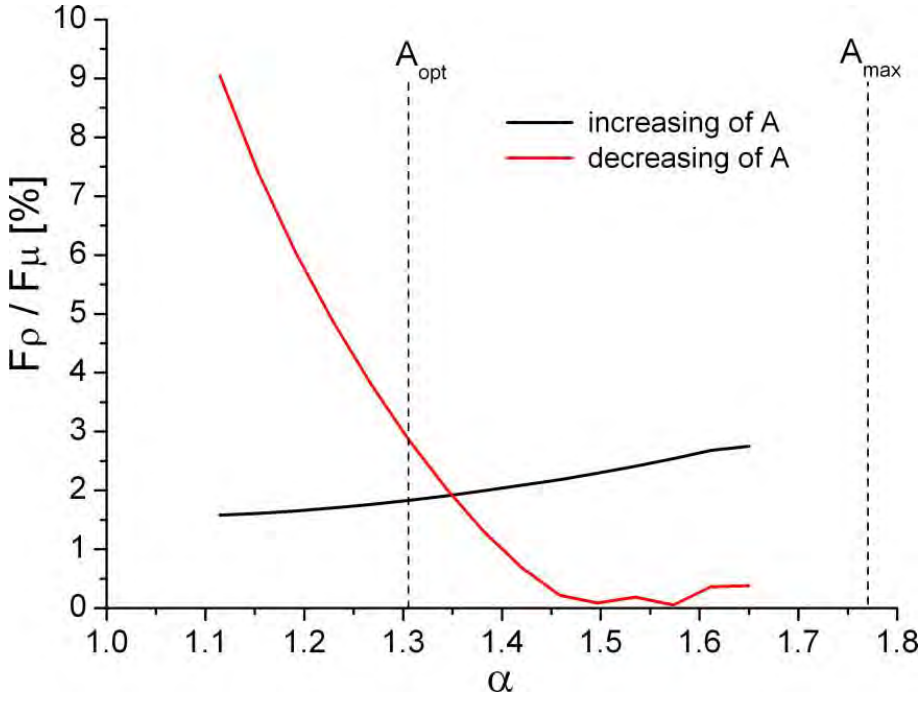

Fig. 96 Comparison of two forces: inertia (F_ρ) and dissipative (F_μ) during growing (black line) and shrinking (red line) of the arm. In optimal point (A_{opt}) their relation is equal to 3%, therefore the rest of calculation was performed for that A_{opt}, and inertia force was no considered in equations.

3.2.5.3.3 Line tension force at the border of the island

All liquid crystal islands or menisci has a dislocation line at its edge. Increasing the length of the dislocation line is possible when energy E_σ is delivered to the system. The length of the dislocation line is symbolized as O. Herein, I assume that E_σ and O are scalars so I assume that the force F_o is a proportionality factor between them, and is pointed radially from the tip of the finger. In equation (148) I also analyze the energy E_σ and its changes in time:

$$P_\sigma \equiv \left(\frac{dE_\sigma}{dt} \right) = F_o \left(\frac{dO}{dt} \right) \quad = F_o \left(\frac{dO}{dA} \right) u_A \tag{148}$$

Moreover O is a function of R, and R is a function of A, therefore derivative $\frac{dO}{dA}$ is a function of the length of the arm A.

This problem can also be analyzed for a single dislocation and a force acting perpendicular to the dislocation line:

$$P_\sigma = F_\sigma \cdot u_A \tag{149}$$

The force is acting in every point of the arm, it has the same magnitude but opposite sense thus effectively it works only at the end of the arm. Comparing the equations (148) and (149) the equation appears:

$$F_\sigma = F_o \left(\frac{dO}{dA} \right) \tag{150}$$

Equation (150) give a relationship between F_o and F_σ.

The F_o force has the same direction as u_A but opposite sense: the F_o is acting to the center of the island whereas u_A to the edge of metal rim.

3.2.5.3.4 Power of the electric field

The next step is to assume that the driving force of the instability of the LC island in AC electric field is an interaction of the electric field with the induced charges Q on the edge of the island (or LC meniscus in a case of a film pierced with a needle). I assume, that the

induced charges Q are located in the very top of the arms A and B as schematically is shown in the Fig. 97. Moreover, I assume that the induced charges are so small that they do not change the electric field acting on the LC island.

The driving force of deformation of the island is interaction of the external electric field ψ with charges Q_A and Q_B, located at the top of arms A and B. Potential V will fulfill the Laplace equation

$$\nabla^2 V = 0 \tag{151}$$

for boundary conditions determined by geometrical properties of the metal rim and difference of potential ΔV between the rim and the needle. Intensity of the electric field $\psi(r)$ can be calculated as:

$$\psi_A = \left(\frac{\partial V}{\partial r} \right)_A \tag{152}$$

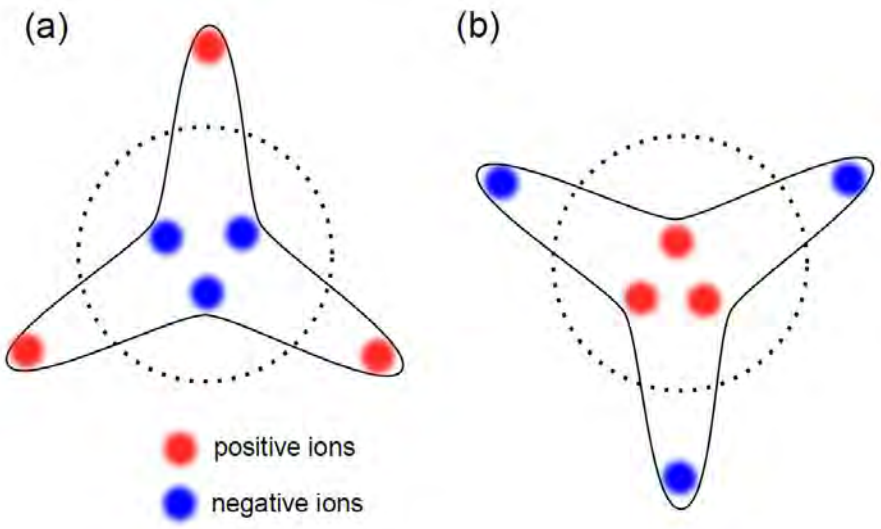

Fig. 97 Proposed mechanism of separation of the ions in destabilized island. The red and blue dots are the regions of big concentration of the ions (anions and cations).When the needle is polarized with positive potential (a), the negative ions are located close to the center of the island, and the positive are expelled from the center. In the second case (b), the needle is polarized with negative potential thus the positive ions gather in the center of the island, whereas the negative ions are located at the end of the tips.

For this conditions the constituent power of the electric field P_e, which describes interaction of electric field ψ with the induced charges Q_A and Q_B can be written as follows:

$$P_e \equiv \left(\frac{dE_q}{dt} \right) = \left[Q_A \psi_A u_A + Q_B \psi_B u_B \right] = F_e u_A \tag{153}$$

Substituent electric force F_e can be approximated with equation:

$$F_e = Q_A \overline{\Psi}_A \tag{154}$$

if substituent electric field $\overline{\Psi}_A$ (which take into account ψ_A and ψ_B) is a function of the length of the arm A.

$$\overline{\Psi_A} = \psi_A + \left(\frac{u_B}{u_A} \right) \left(\frac{Q_B}{Q_A} \right) \psi_B \tag{155}$$

This condition is fulfilled for constant value of the charge, i.e. $Q_A = Q_B = const$. Then, the substituent value of electric field can be calculated as:

$$\overline{\Psi_A} = \psi_A + \left(\frac{A_0}{A} \right)^2 \psi \left(\frac{A_0^2}{A} \right) \tag{156}$$

And using eq. (1.43) calculate the electric force, and—at the end—the induced charge Q.

3.2.6 BALANCE OF CONSTITUENT FORCES AT THE TOP OF THE ARM

The time evolution of the arm of LC island is shown in Fig. 98. As was mentioned earlier, the difference in the shape of this profile is related with the interaction of the force generated by electric field on the induced charge, viscous dissipation and the edge tension.

Herein, I will give quantitative analysis of this relation.

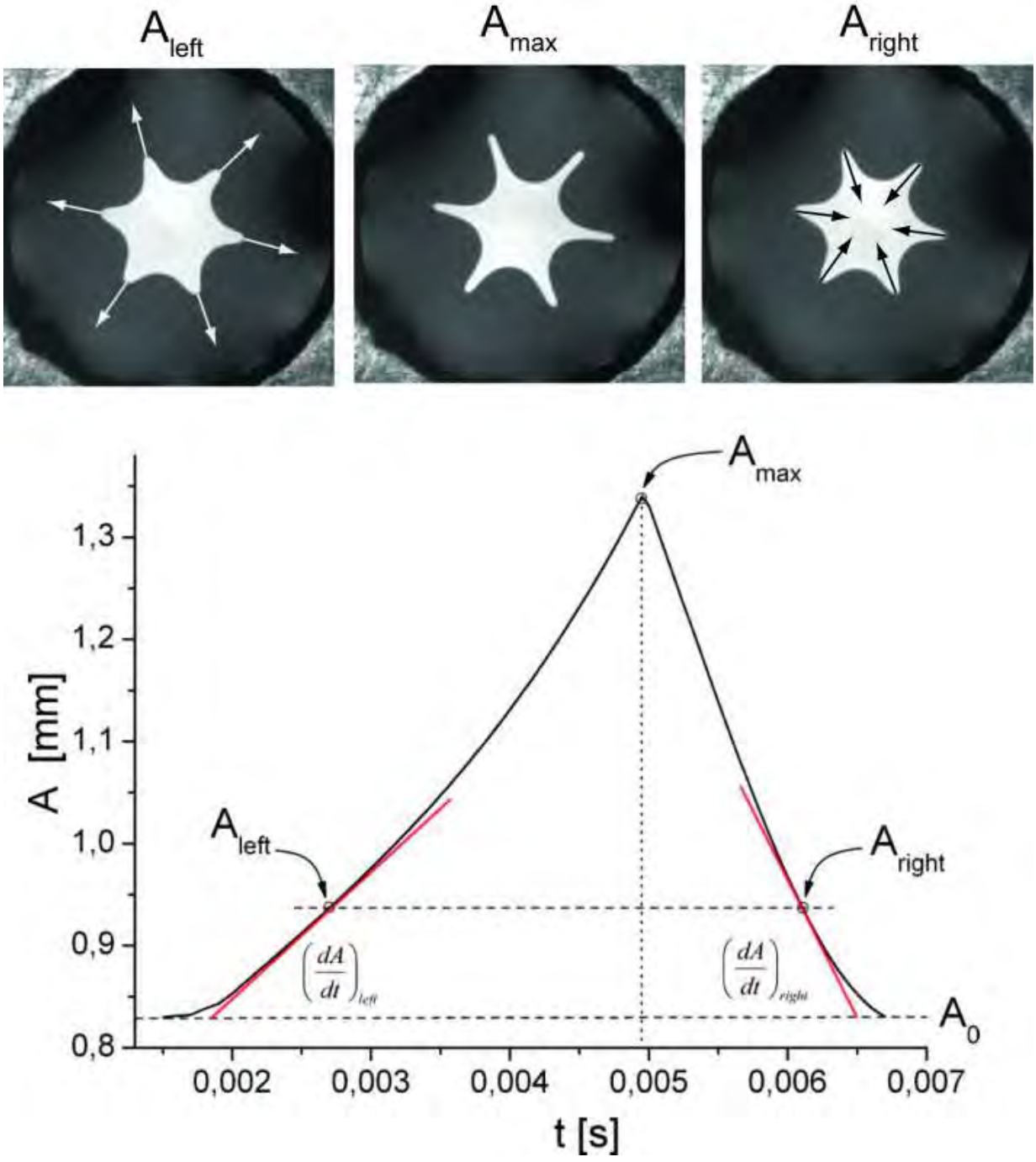

Fig. 98 The amplitude of the arm as a function of time, this profile was averaged for a couple of other profiles. The time of arm growing is longer than the time of shrinking due to interaction of force from electric field with the edge tension.

The balance of forces acting on the tip of the arm is given by equation:

$$F_e \pm F_\sigma = F_\mu \pm F_k \tag{157}$$

The sum (with the sign depending on the direction of motion) of the force acting on the induced charge and the force coming from the edge tension is equal the force of generated

by viscous dissipation and by the inertial force. However, both forces F_μ and F_k are a function of α and the calculations showed that F_k is less than 10% of F_μ. For that reason, we neglect the inertial force in further considerations. The force balance will be given as:

$$F_e = F_\mu \pm F_\sigma \tag{158}$$

The edge tension is acting against the electric force when the arm is growing (left side of the plot shown in Fig. 98) and acting synergistically on the right side, where it is shrinking. The force balance can be fully shown as:

$$\begin{cases} F_e = F_{\mu\_Left} - F_\sigma \\ F_e = F_{\mu\_Right} + F_\sigma \end{cases} \tag{159}$$

I already presented that:

$$F_\mu = \mu \cdot \phi_\mu \cdot u_A \tag{160}$$

Therefore, force balance equations for each side are:

$$\begin{cases} F_e = \mu \cdot \phi_\mu \cdot u_{A\_Left} - F_\sigma \\ F_e = \mu \cdot \phi_\mu \cdot u_{A\_Right} + F_\sigma \end{cases} \tag{161}$$

The force F_e which is acting on the induced charges is:

$$F_e = Q \cdot \phi_e \tag{162}$$

And the force F_σ can be calculated as:

$$F_\sigma = \frac{P_\sigma}{u_A} = F_o \left(\frac{dO}{dA} \right) \tag{163}$$

And finally, the eq. 159 are:

$$\begin{cases} Q\phi_e = \mu\phi_\mu u_{A\_Left} - F_\sigma \left(\frac{dO}{dA} \right) \\ Q\phi_e = \mu\phi_\mu u_{A\_Right} + F_\sigma \left(\frac{dO}{dA} \right) \end{cases} \tag{164}$$

where u_{A_Left} and u_{A_Right} are the velocities of the arm A during rising (left) and shrinking (right). Finally, adding up the sides of the eq. 164 it is possible to calculate the unknown induced charge Q:

$$Q = \mu\left(\frac{\phi_\mu}{\phi_e}\right)\frac{\left(u_{A\_Right} + u_{A\_Left}\right)}{2} \tag{165}$$

At the same time, subtracting the sides of the eq. 164 it is possible to calculate the edge tension force F_σ:

$$F_\sigma = \mu\phi_\mu\left(\frac{dA}{dO}\right)\frac{\left(u_{A\_Right} - u_{A\_Left}\right)}{2} \tag{166}$$

The example of results for the induced charge Q is given in Fig. 99. The charge is plotted as a function of α (ratio of deformation of the arm to the radius of non-deformed island).

The results are given for two cases: pure 8CB and 8CB doped with organic salt BDTC. To compare induced charge in each case the parameters for the experiments were very similar: for 8CB *U* = 150 V and *f* = 9 Hz, whereas for 8CB doped with BDTC *U* = 200 V and *f* = 10 Hz.

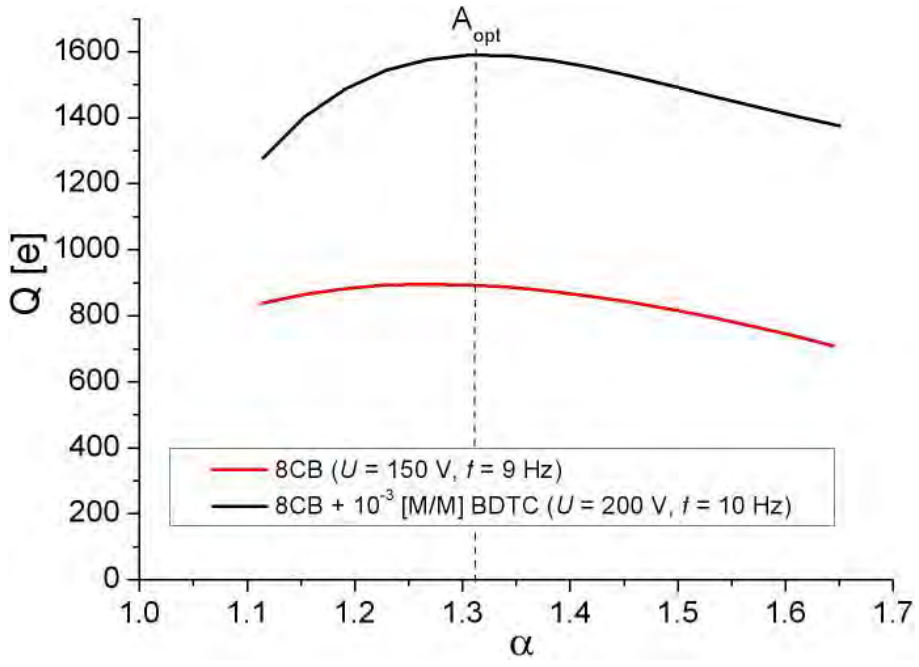

Fig. 99 Averaged induced charge Q in a single arm calculated for a single smectic layer.

Fig. 99 demonstrates that:

i) The value of induced charge for 8CB is lower (for A_{opt} it is ca. 1.8 times lower) than for 8CB doped with organic salt. This difference can be explained in terms of additional charged species, i.e. ions I introduced artificially to 8CB, and which have influence on the charge.

ii) The shape of the $Q(\alpha)$ for 8CB is more flat that for 8CB with organic salt. For doped 8CB it rise till A_{opt} to a Q_{max}, and afterwards the charge Q is decreasing its value. The flat shape of the dependency for pure 8CB might be related with small amount of ionic species in the island, which can charge the boundary at the beginning of the process. For doped 8CB this time apparently is longer.

The results for line tension force F_σ is given in the Fig. 100. The red line shows dependency of calculated line tension as a functi$_{\text{i}}$on of α. Black line for $8 \cdot 10^{-12}$ N is a constant value of the line tension taken from the literature (Geminard et al. [2] [4]).

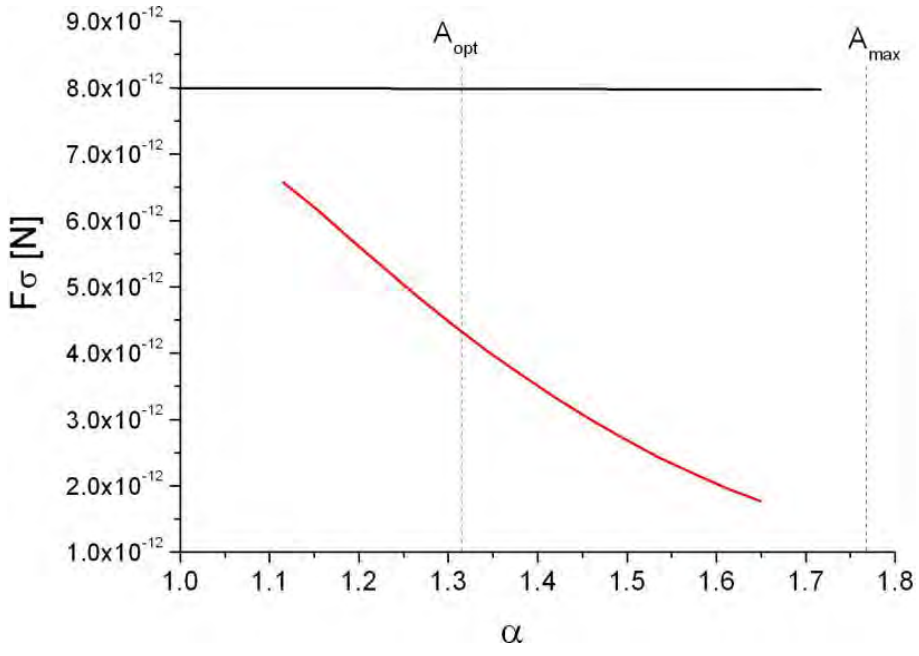

Fig. 100 An example of edge tension F_σ as a function of α. The black line at $8 \cdot 10^{-12}$ N is a value of line tension taken from [8] Result for 8CB + 10^{-3} BDTC (U = 200 V, f = 10 Hz).

The estimated line tension force is a monotonically decreasing function of α. The values are slightly lower than the line tension proposed by Geminard et al. To compare F_σ from different experiments (i.e. from videos recorded for different *U* and *f*) the value of F_σ for A_{opt} was calculated. The results are given in the Fig. 101.

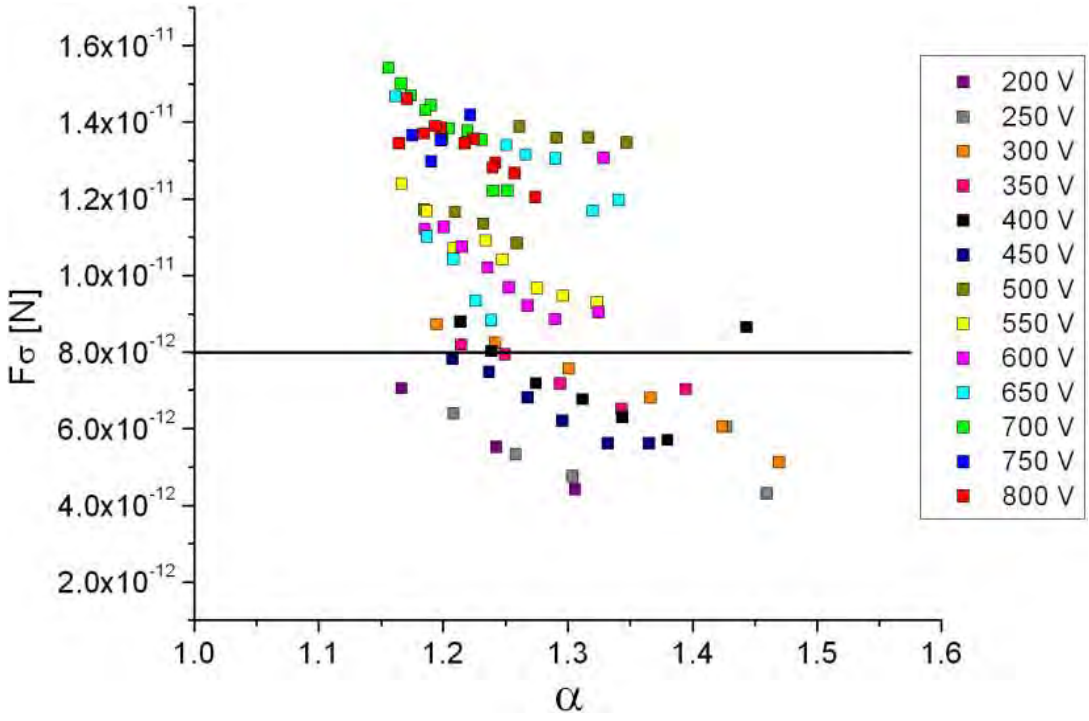

Fig. 101 Line tension force as a function of α for a 8CB + 10^{-3} BDTC. Each point represent a frequency for a given voltage. Line tension was calculated for every recorded movie for the A_{opt} value (see Fig. 100 for details).

The results are given for a different *U* and *f*, yet performed for a single LC island, with a constant diameter. The tendency of line tension on the graph is to decrease with increasing α (ratio of deformation of the arm to the radius of non-deformed island, i.e. $\frac{A}{A_0}$)

Like for a case for single experiment, here the value of line tension is in the order of magnitude of value suggested by Geminard et al. [2] [4] The difference between results presented in Fig. 25 and Fig. 26 and data from literature might be explained as follows. First of all, in all these experiments conditions (mainly time of periodic oscillations) are far from equilibrium. That might explain decreasing the line tension for a single movie or decreasing tendency in Fig. 26. The second aspect is the dissipation of the energy of the dislocation.

The higher is the length of the arm (i.e. the higher $\frac{dO}{dA}$) the higher tension of the dislocation line. Higher tension is correlated with a higher dissipation of the energy of the dislocation, what as a result the value of line tension is decreasing.

3.2.7 INFLUENCE OF ORGANIC SALTS ON INDUCED CHARGE

Fig. 99 show a change of induced charge Q as a function of α for a single experiment. Fig. 102 show induced charge Q for one arm and single smectic layer and a parabolic fit of these points. Each point is a one series of videos (for a single LC island, i.e. A_0=const. and different parameters *U* and *f*).

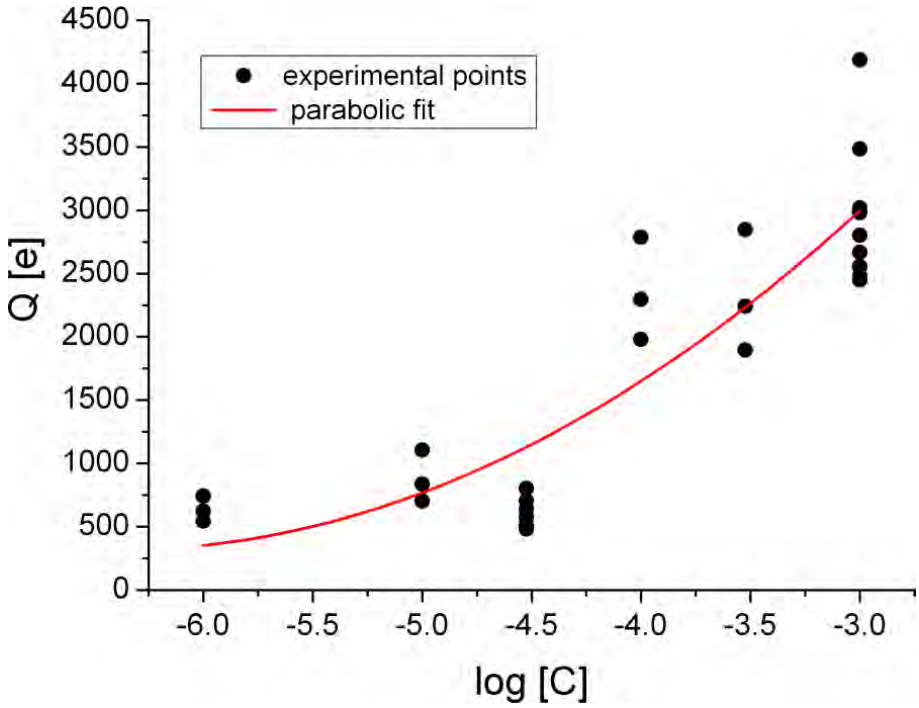

Fig. 102 Induced charge Q for a single arm and single smectic layer, for different BDTC salt concentrations (from 10^{-3} to 10^{-6} M/M). Induced charge Q for a set of experiments for different concentrations. A parabolic fit showing the increasing charge Q with increasing salt concentration.

The charge Q was calculated in every experiment for the A_{opt} point. As seen on Fig. 102 the higher concentration of the organic salt the higher induced charge. The results were fitted

with a parabolic fit, however it is visible that between 10^{-6} and $5{\cdot}10^{-4}$ the induced charge is constant, and increasing for higher concentrations (10^{-4} to 10^{-3} [M/M] BDTC).

3.2.8 CONCLUSIONS

Periodic oscillations of the LC island in external electric field exhibit an electro-hydrodynamic (EHD) instability. To quantitatively describe the behavior of the system image analysis was used. To describe the phenomenon a EHD model was created. As a result, the following conclusions can be made:

i) In EHD model four forces (or energies) play role: force of electric field, inertia force, hydrodynamic resistance force and force related with dislocation line. The inertia force can be neglected, therefore in the model three major forces are responsible for oscillations.

ii) The line tension is acting against the electric field during the growth of the arm, and with the electric field when the arm is shrinking. As a result, the asymmetry of that process is visible: the time for growing is longer than the time of shrinking of the arm.

iii) Balance of the forces and results from the experiments allowed to calculate the line tension force. The line tension value (for experiments with pure 8CB and 8CB doped with organic salt) is below the value of line tension obtained by Geminard et al. [4] within the same order of magnitude.

iv) For a single experiment we systematically observe a decrease of the estimated value of the line tension with increasing length of the arm. It might by caused by dissipation of the dislocation energy—as the arm is growing the energy dissipates.

v) The induced charge depends on the amount of ionic species in the sample: LC doped with organic salt shows a higher value of induced charge Q than a pure 8CB.

vi) Introducing ions to the 8CB liquid crystal influence the induced charge Q. Concentration at the level from 10^{-6} to $5{\cdot}10^{-4}$ [M/M] BDTC do not influence Q in a noticeable way. The concentration above 10^{-4} [M/M] BDTC increase induced charge.

3.2.9 REFERENCES FOR CHAPTER 3.2

[1] L. Lejcek and P. Oswald, Journal De Physique II **1**, 931-937 (1991).
[2] J. C. Geminard, C. Laroche, and P. Oswald, Physical Review E **58**, 5923-5925 (1998).
[3] A. Żywociński, F. Picano, P. Oswald, and J.C. Géminard, Physical Review E **62**, 8133-8140 (2000).
[4] J. C. Géminard, R. Hołyst, and P. Oswald, Phys. Rev. Lett. **78**, 1924 (1997).
[5] F. Picano, R. Hołyst, and P. Oswald, Physical Review E **62**, 3747-3757 (2000).
[6] J. Lauger, C.R. Robertson, C.W. Frank, and G.G. Fuller, Langmuir **12**, 5630-5635 (1996).
[7] H. Winter, in (American Institute of Chemical Engineers, 1987).

Chapter 3.3
Acceleration of phase separation in a liquid crystal/polymer mixture by application of an external, oscillating electric field

Part of my work within the PhD studies involved the studies of the influence of an oscillating electric field on the rate of phase separation processes. This project was lead by Natalia Zębacz and the experiments were performed with optical microscope and static light scattering (SLS). Herein I will describe only SLS method and results. I will analyze the results obtained by Natalia Zębacz and explain the mechanism – I will demonstrate that mechanism responsible for accelerating the phase separation is dyCHASE.

Application of a high frequency (i.e. 1 kHz) electric field did not affected the phase separation process of liquid crystalline domains in a polymer matrix. However, application a low frequency electric field (i.e. < 50 Hz) accelerated the process even 1000 times.

There is a sharp transition frequency, which can be referred as critical frequency (f_{CR}). The critical frequency is in order of magnitude of frequencies we observed in our previous experiments with free-standing smectic films. The experiments were performed for 5CB liquid but also for 8CB liquid crystal, so for a liquid crystal used as a material for preparing free-standing smectic film.

After doping liquid crystal with an organic salt Natalia Zębacz observed further acceleration of phase separation. Thus, we believe that the mechanism of accelerating phase separation is in fact a dyCHASE mechanism. Ions in liquid crystalline domains move when sample is placed in external AC electric field. At large frequencies these ions are effectively immobile, but at low frequencies they separate on the interface between liquid crystal domain and the polymer matrix. This polarizes the interfaces of the domains and accelerates their coalescence, speeding up the phase separation process.

3.3.1 INTRODUCTION

3.3.1.1 Mixtures of polymer and liquid crystals

To describe a mixture of two different polymers or a polymer/liquid crystal a Flory-Huggins mean field theory can be used. The mean field theory for the polymer and solution mixture compares free-energy for two states: one before mixing and second after mixing. The same theory can be used for analysis binary polymer blends. The Helmholtz free energy of mixing for a mixture of two polymers, A and B, is given by:

$$\frac{\Delta F_{mix}}{n_{site} \cdot k_B T} = \frac{\phi_A}{N_A} \ln \phi_A + \frac{\phi_B}{N_B} \ln \phi_B + \chi \phi_A \phi_B \tag{167}$$

where:

$N_A, N_B -$ degrees of polymerization of polymer A and B,

$\phi_A, \phi_B -$ volume fractions of polymer A and B defined as below:

$$\phi_A = \frac{V_A}{V},\ \phi_B = \frac{V_B}{V} \tag{168}$$

and

$$\phi_A + \phi_B = 1 \tag{169}$$

$$V_A + V_B = V \tag{170}$$

The equation (167) can be used for a prediction of a phase diagram of binary mixture (the superscripts ‘ and ‘’ refers to separate phases):

$$\frac{\partial \Delta F_{mix}(\phi'_A)}{\partial \phi_A} = \frac{\partial \Delta F mix(\phi''_A)}{\partial \phi_A} \tag{171}$$

- for the system in equilibrium, and

$$\frac{\partial^2 \Delta F_{mix}}{\partial \phi_A^2} = 0 \tag{172}$$

- for the instability (the mixture separated into two phases),

and for the system in the critical point: [1]

$$\frac{\partial^3 \Delta F_{mix}}{\partial \phi_A^3} = 0 \tag{173}$$

3.3.1.2 Applications of mixtures of polymer/liquid crystals

The most known applications of mixtures of polymer and liquid crystals are Polymer Dispersed Liquid Crystals (PDLC) and Polymer Stabilized Liquid Crystals (PSLC). PDLC, were discovered in the eighties at the Kent University, USA. As the name suggest, PDLC is a polymer matrix with a dispersed small (from tens of nanometers up to a dozen of micrometers) domains of liquid crystal (see Fig. 103).

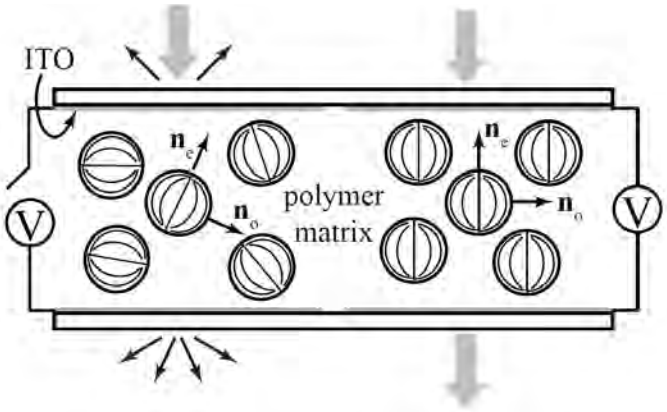

Fig. 103 Polymer Dispersed Liquid Crystal (PDLC) device. It consists of a two layers of glass covered with ITO and a polymer matrix with liquid crystals domains. When the electric field is in OFF state the multiple scattering occurs and the sample is 'opaque', whereas in the ON state all molecules of liquid crystal align parallel to the lines of electric field and the sample is transparent. [2]

There are multiple methods of fabrication of PDLC systems. The most common is to mix monomer and LC and then polymerize the monomer with UV light or temperature. Formation of the polymer matrix forces liquid crystal to merge into droplets, which are uniformly distributed across the sample. PDLC have already found application as displays [3] and a 'smart windows' (or 'smart glasses') [4] [5]. Due to mismatch between index of refraction of liquid crystal and polymer matrix, the light is scattered. When an external electric field is applied to the sample, the molecules of liquid crystal re-orient themselves to the line of electric field. If ordinary index of refraction n_o of LC matches index of refraction of the polymer matrix n_p, such obtained composite if optically homogenous and transparent.

In PSLC only a small concentration of polymer is added to a liquid crystal. The polymer forms a network structure across the mixture of polymer and LC. To use PSLC as a display, in a reverse mode, the substrate is treated with polyimide and then rubbed.

The liquid crystal molecules arrange themselves on the substrate very similar to a twisted nematic structure. Then, the LC is mixed with a monomer and subjected to a UV radiation, which polymerize monomer and stabilize the arrangement of LC molecules. When there is no applied electric field the device is transparent. When EF is applied to the substrate the planar texture changes to focal conic texture and the material is opaque. For a display working in a normal mode, no previous preparation of the substrate is needed.

Recently a new kind of dispersion gained attention – holographic polymer dispersed liquid crystals (H-PDLC) [6]. The preparation of the H-PDLC is as follows: the mixture of monomer, liquid crystal and curing agent is subjected to a two or more coherent laser beams. Laser beams interfere and create a pattern inside the sample. As a result, in the bright places—where a constructive interference takes place—polymerization of the monomer occurs faster than in dark places where a destructive interference takes place. Sample consists two regions: in bright areas polymer-rich phase whereas in dark areas liquid crystal-rich phase. H-PDLC already found use as a electrically switched diffraction grafting [7] [8], photonic crystals [9] and switchable mirrors .

3.3.1.3 Spinodal decomposition

A typical phase diagram of a binary system is shown in Fig. 104. One can distinguish a metastable region between two curves: a binodal curve and a spinodal curve. A binodal curve separate one-phase region from a metastable region, whereas a spinodal curve separate metastable region from the two-phase region (unstable region). Both curves intersect together in a single point, called a critical point. Above binodal curve exists a stable region with only one phase (or a region with a perfect mixing).

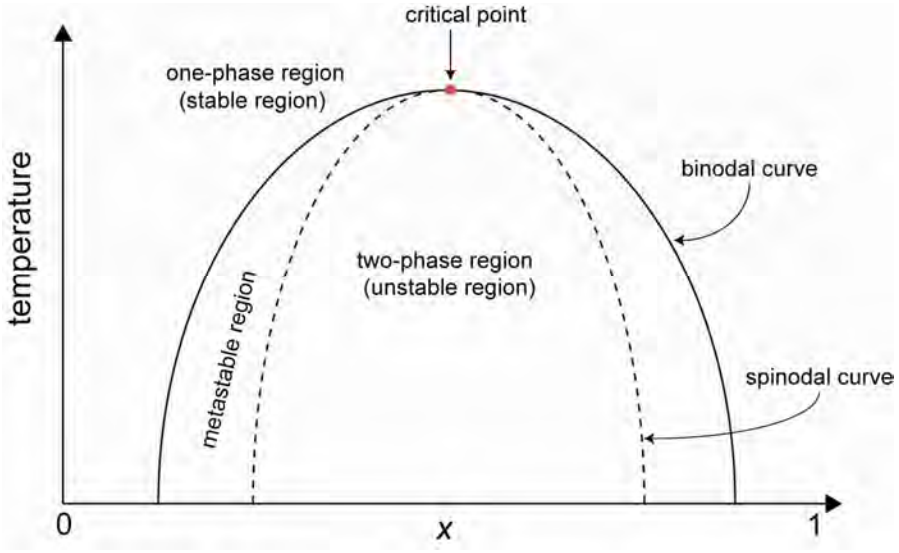

Fig. 104 The typical phase diagram of a binary system, i.e. temperature versus concentration of one of the component. Phase diagram consists two curves: binodal and spinodal. The binodal cure is plotted as a solid line whereas spinodal curve as a dashed line, they join in a one point called critical point. Above critical point a stable region exists with a one phase. Between binodal and spinodal lines exists a metastable region. Below spinodal curve exist a highly unstable, two-phase region.

In the metastable region the system can be a single phase or a two phase. If the external perturbations are small the system in that region becomes a single phase. However, when perturbations become large, this region become unstable, demixes and became a two-phase. In the center of phase diagram (between two spinodal curves) exist an unstable region. In that area the system become unstable when all perturbations, both small and large, are influence the system. For this reason mixture always separates into two phases.

When mixture of two compounds is the temperature above the binodal curve and is quenched to metastable phase, the separation process occurs by a nucleation and growth mechanism. The difference between typical phase separation (i.e. nucleation and growth-NG), Fig. 105a, and spinodal decomposition, Fig. 105b, is shown below.

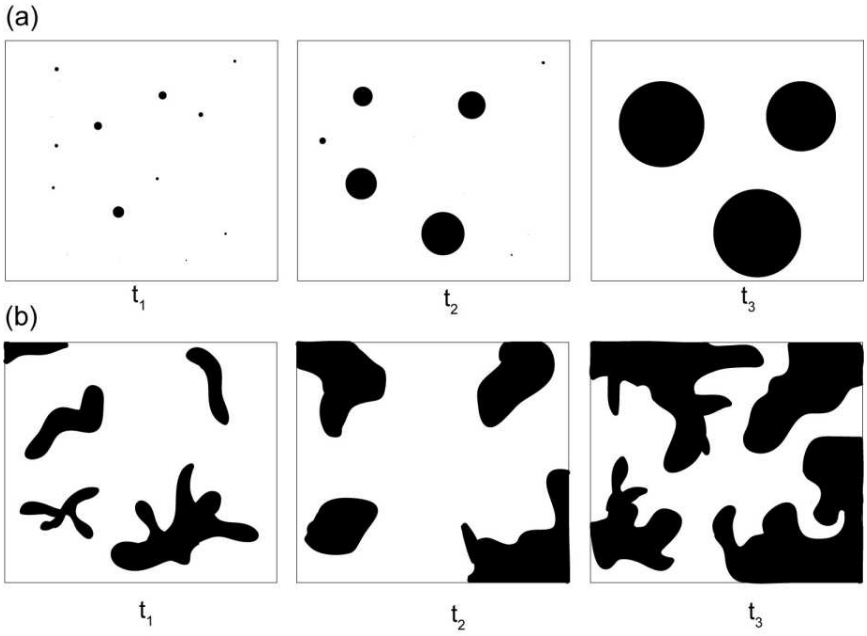

Fig. 105 Phase separation for a binary mixture for a two cases: a) nucleation and growth, and b) spinodal decomposition, both shown as a function of time (t_1=0 s).

Nucleation-and-growth mechanism is well known due to its importance in metallurgy and materials science [10] [11]. The process starts with creating a small clusters of minority atoms/molecules in the mixture (Fig. 105a at t_1). Next, droplets are growing due to diffusion process from oversaturated matrix, the growing droplets are colliding and merging together during that process (coalescence process) (Fig. 105a at t_2 and t_3). Sometimes the Ostwald ripening is the main mechanism in nucleation-and-growth process. [1]

3.3.1.4 Investigation of phase separation

To evaluate phase transition, especially spinodal decomposition, various experimental techniques are used. One of the simplest and effective is optical microscopy. The mixture of two compounds (polymer/polymer, polymer/liquid crystal etc.) is placed between two glass substrates. The sample is placed on a heating stage and visualized with microscope and usually recorded with a CCD camera. Recorded movie is analyzed afterwards frame-by-frame with a dedicated software. With the use of optical microscope one can gain information—usually by applying an image analysis techniques—about shape of domains (circular, prolate), its area (and thus the radius and diameter), mean values of area, as well as distribution of the domains across the sample.

Static light scattering (SLS) is a widely used technique to investigate a spinodal decomposition. In SLS experiment a laser beam passes through the collimator and impinge

on the sample. The incident beam is scattered on the sample and is collected by a paraboloidal mirror. The mirror reflects scattered light towards a photodiode detector and the data is collected by a computer.

In homogenous mixtures (e.g. above critical temperature for a binary mixtures), if the fluctuations are neglected, there is no scattering of the light. If the phase transition occurs, the mixture separates onto two (or more) phases, and it is no longer homogenous. Laser beam is scattered on different domain, which differs in index of refraction. Analysis of the scattering vector give information about size of the domain in the sample, thus insight into a kinetics of phase separation.

Also other techniques can be applied to investigate phase transitions in polymer systems, i.e. optical microscopy combined with rheological measurements [12], light scattering techniques combined with rheology [13], resonance light scattering (RLS) spectroscopy [14], X-ray photoelectron spectroscopy (XPS) [15] and small- and wide-angle X-ray scattering (SAXS and WAXS) combined with differential scanning calorimetry (DSC) [16].

3.3.1.5 Soft matter mixtures in electric field

The influence of the electric field on different types of systems is a subject of intense research in past years. For instance, electric field was used to achieve a long-ranged ordering in block-copolymer systems. The aligning affect is a result of a difference between dielectric constants ε of each blocks. To lower the free energy of the system, the domains in block-copolymer align parallel to the lines of electric field. [17] [18] [19] [20] [21] A good understanding of mechanisms in aligning is important to use this method to produce a new class of materials for applications in nanotechnology.

Another example is electro-hydrodynamic (EHD) patterning process, also known as electro-hydrodynamic lithography (EHL) process. EHL is a method of contactless patterning of a thin polymer layer with use of electric field. In EHL process a thin layer of polymer is placed on a conductive substrate, and the second electrode in placed parallel to the first one above the polymer layer, so between polymer and second electrode is a free space. When electric field is applied EHD surface instability occurs making a regular pattern on the surface of film. It can be treated as a capacitor with an air gap between electrodes. The dielectric discontinuity at the polymer film and air interface gives rise to the displacement charges. Those charges couple with the electric field causing destabilizing electrostatic pressure, and thus creating instability. [22] [23]

3.3.2 MATERIALS AND METHODS

3.3.2.1 Experimental setup

To perform experiments with Static Light Scattering (SLS) Natalia Ziębacz used a standard He-Ne laser with power 5 mW and which radiates wavelength λ = 632.8 μm. The scattering of light was monitored on a linear array of 512 photodiodes, and the scattering intensity *S(q,t)* was determined as a function of the scattering wavevector *q* and time *t*. The scattering angles, *θ*, in this experiment were between *θ* = 0.5°–25° and the corresponding wavevectors were between *q* = 0.2–6.9 μm^{-1}. In real space it is possible in principle observe the domains of size:

$$L = \frac{2\pi}{q} \tag{174}$$

which gives diameter 1÷31 μm. In practice, the first few photodiodes are too close to the main beam to give reliable results, therefore in practice the range of *L* that could be observed in our apparatus was between 1÷5 μm. The values of scattered light intensity *S(q,t)* as a function of time *t* were registered every 5 seconds at the beginning of the experiment, and with a lapse of time, this interval time was adjusted between 5 and 180 seconds depending on how fast the process was going. The position of the peak in *S(q,t)* was monitored as a function of the scattering wavevector.

For experiments with alternating electric field she connected the source of alternating electric field to the conductive spacers, which were in touch with ITO plates. She used a function generator (TABOR) connected with high-voltage amplifier (TREK, model 10/10B). The square wave with modulation 50% was used in all experiments. Oscilloscope (RIGOL) was used to monitor applied signal. The voltage used in experiments was between 0÷200 V and the frequency was from single Hz up to 1 kHz.

3.3.2.2 Materials

Materials used in experiments::

- Polymer: polystyrene (PS), from Fluca Chemicals Co., with properties as below: index of refraction n_{PS} = 1.589, molecular weight M_w = 74500 and the polydispersity index M_w/M_n = 1.03.
- Liquid crystals: 4-cyano-4'-n-pentylbiphenyl (5CB) and 4-cyano-4'-n-octylbiphenyl (8CB). Both were obtained from the Military University of Technology, Warsaw, Poland. The precise temperature of the phase transitions for the 5CB and 8CB are shown in the Table 7.

Table 7. The phase transitions for 5CB and 8CB liquid crystals used in experiments.

Compound	Phase	T_{TR}	Phase	T_{TR}	Phase	T_{TR}	Phase
5CB	C	24 ℃	N	35 ℃	I	—	—
8CB	C	21.25 ℃	SmA	33.85 ℃	N	40.85 ℃	I

In the isotropic phase, the 5CB index of refraction is n_{5CB} = 1.5878, so the difference between polystyrene and 5CB is:

$$\Delta n_1 = n_{PS} - n_{5CB} = 0.0012$$

In the isotropic phase the refractive index of 8CB is n_{8CB} = 1.566, so for polystyrene and 8CB the difference is:

$$\Delta n_2 = n_{PS} - n_{8CB} = 0.023$$

Due to small difference between index of refraction of the polystyrene and the liquid crystals, (Δn_1 and Δn_2) the multiple scattering of light in these mixtures can be neglected for small sizes of the studied system. It has been previously estimated by Graca et al. [24] that for such small differences in the refractive indices the mean free path of light in the sample consisting of the polymer-rich domains and the LC-rich domains (in the isotropic phase) is $l_i \sim 10^3$ μm. Therefore in order to avoid multiple scattering of light the samples were of thickness less than 100 μm.

3.3.2.3 Experiments

In experiments Natalia Ziębacz used two different types of samples. The first sample to examine phase separation without electric field and the second sample to measure separation with the use of alternating electric field.

To prepare samples for experiments without electric field (both for optical microscopy experiments and static light scattering), the liquid crystals (5CB or 8CB) and polystyrene were dissolved in toluene and stirred mechanically for 48 h at 65 ℃ (slightly above the cloud point temperature). The mixtures containing 40% of toluene, were afterwards placed on a glass slide (10 mm in diameter), cut from microscope cover glass. The films were dried and annealed for 36÷48 h at temperature of 65 ℃. After the evaporation of toluene the films were covered with the second glass plate, and the home-made copper spacers (60 µm) were used to distance both plates.

The experiments with electric field required transparent and conductive glass slides, therefore in such experiments she used microscope slides covered with Indium-Tin Oxide (ITO) (see Fig. 106 for details). The slides were etched with one side, so she could use copper spacers both to distance ITO plates from each other and as a conductive wire to apply electric field to the electrodes.

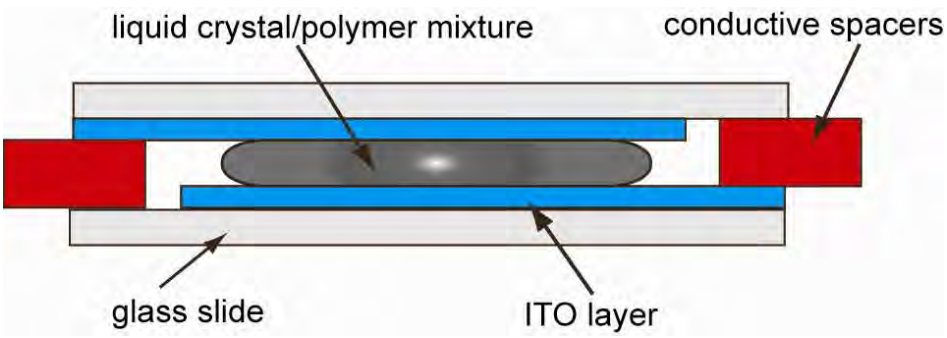

Fig. 106 A schematic representation of the sample used for experiments with electric field. The sample (liquid crystal/polymer mixture) was placed between two—covered with ITO—glass slides and the electric field was applied to the conductive spacers. The picture is not with the scale of real sample.

3.3.3 RESULTS

3.3.3.1 Static Light Scattering

3.3.3.1.1 AC electric field

The results for static light scattering (SLS) without electric field are shown in Fig. 107

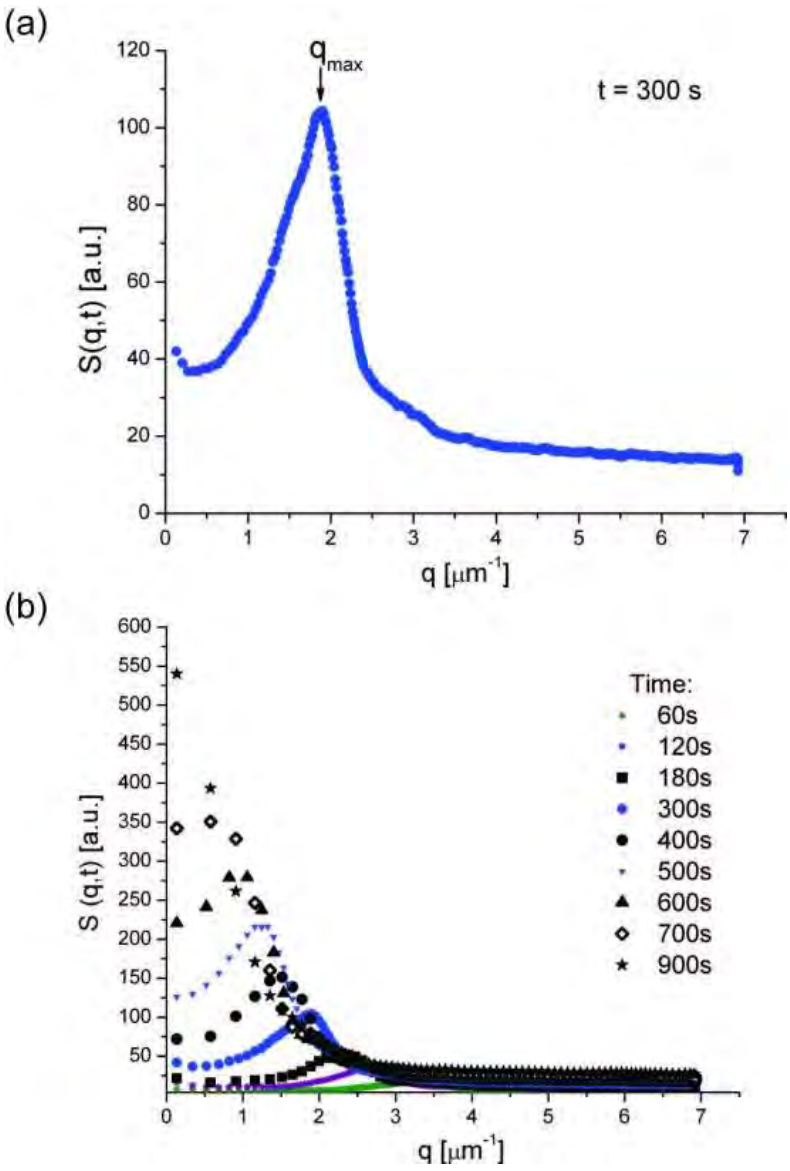

Fig. 107 Static light scattering for the 5CB/PS mixture (84/16 % by weight). Mixture was cooled from 55 ℃ to 35.5 ℃, into the I+I regi on. (a) Scattering intensity S(q,t) as a function of the wave vector (q) for the time of phase separation equal to t = 300 s, whereas q_{max} is the dominating wavevector component. (b) The time evolution of scattering intensity versus wavevector for a different times.
Figure taken from [25] and Ph.D. thesis of Natalia Ziębacz.

In each plot of scattering intensity versus wavevector one can distinguish a maximum value q_{max}, which is the dominating wavevector component. The position of the q_{max} is inversely proportional to the size of the domain:

$$L(t) \propto \frac{1}{q_{\max}(t)} \tag{175}$$

The average size of the domains of polymer in the I+I and N+I region changes in time and is given by:

$$L(t) \propto \frac{1}{q_{\max}(t)} \propto \frac{1}{t^{a}} \tag{176}$$

with the a=-0.3±0.04. The *a* parameter is constant both for mixture 5CB/PS and 8CB/PS. The similar results were obtained for mixture of 8CB/PS for different polymer mass. [24] [26] [27]

Next, Natalia Ziębacz performed experiments with and without electric field. The results are shown in Fig. 108. Plots presents time evolution of the intensity of light scattering S(q,t) for a mixture of 5CB/PS (72/28 wt%). The results were obtained in the N+I region.

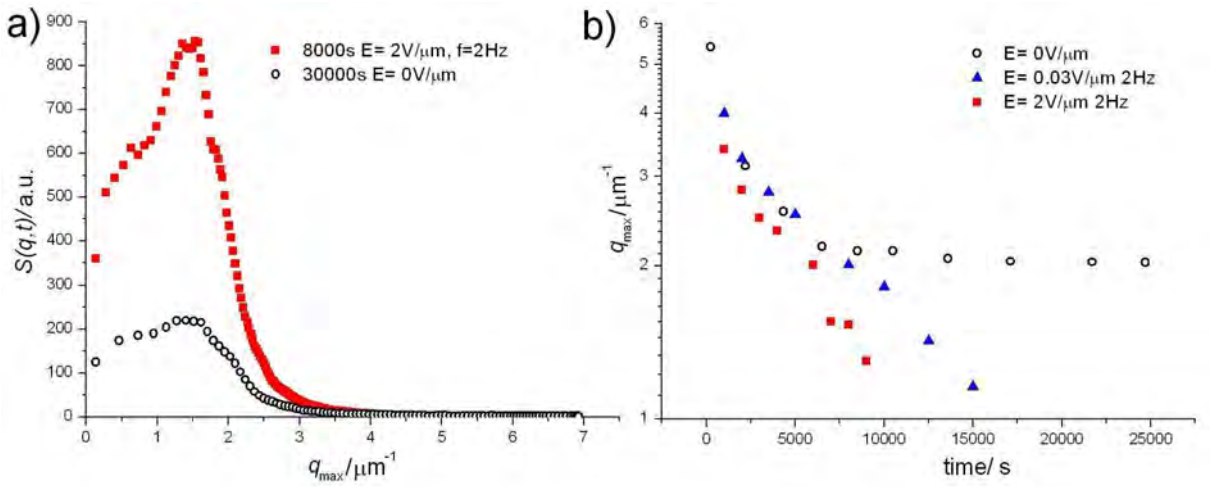

Fig. 108 The results of light scattering experiments for a phase separation with and without electric field. The measurements obtained for a mixture of 5CB/PS (72/28 wt%), the sample was cooled down to temperature 33.8 °C in the N+I region. (a) The results for experiments with electric field are shown with a red squares (***E*** = 2 V μm^{-1} and *f* = 2 Hz). (b) Single log plot of the time evolution of the vector q_{max}. The results for phase separation without electric field are represented by circles, results for electric field of frequency *f* = 2 Hz are represented by a triangle (***E***=0.03 V μm^{-1}) and a square (***E***=2 V μm^{-1}).
Figure taken from Ph.D. thesis of N. Ziębacz and [25].

Fig. 108a presents a light scattering intensity as a function q_{max} wavevector. For a different times the same q_{max} was achieved, however measurements with electric field lasted ca. four time shorter than experiments without electric field.

The acceleration of the phase separation with the use of external electric field is clearly visible in the Fig. 108b. This is a single logarithmic plot of the q_{max} wavevector as a function of time. Without electric field the separation process is fast, until it achieves ca. q_{max}=2 μm^{-1}. For that value there exists a plateau and the growth of domain is stopped, whereas for phase separation with the use of electric field Natalia Ziębacz measured a growth process. Also, the influence of the value of electric field is visible: higher value of electric field results in the acceleration of the separation process.

The more precise results are shown in the Fig. 109. A set of experiments were performed for a 5CB/PS mixture (72/28 wt%). An experiment without electric field show that time to obtain the domains of average diameter d = 6.36 µm is *ca.* 91 000 seconds. The experiments with electric field were performed for different intensity (***E*** = 1, 2, 3 and 5 $V\mu m^{-1}$) and constant frequency *f* = 2 Hz. A domains with diameter d = 6.36 µm, with use of electric field ***E*** = 5 $V\mu m^{-1}$, grows for ca. 123 seconds. It means that use of high intensity EF accelerate phase separation ca. 740 times.

The higher the electric field applied to the system, the larger the slope of the linear fit to the experimental points (Fig. 109a).

To show qualitatively the influence of electric field on the time of phase separation, I plotted the time when the domains achieve diameter of *d*=6.36 µm versus electric field. The higher the electric field applied to the system, the lower time needed to obtain diameter equal to *d*. (see Fig. 109b)

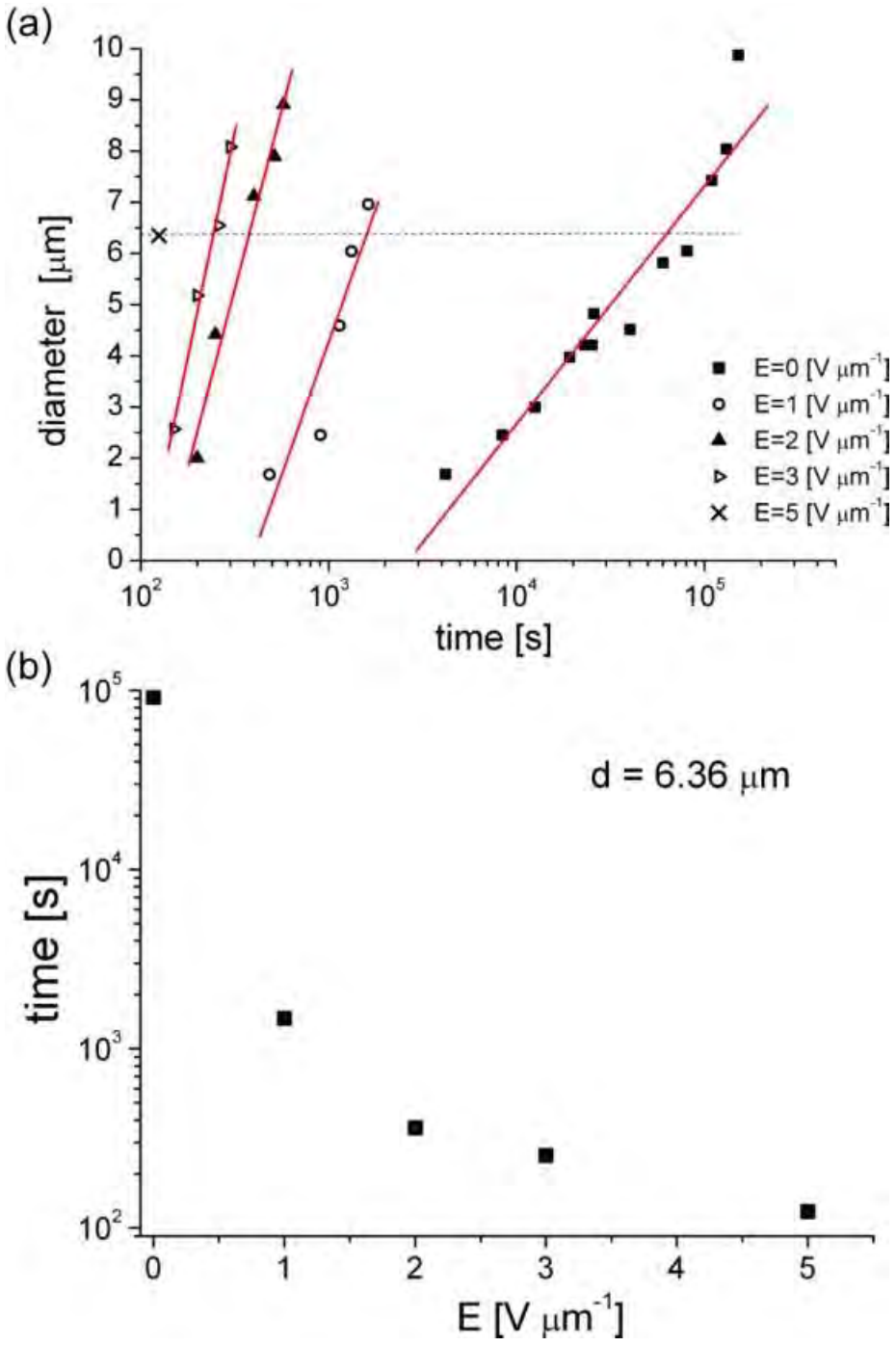

Fig. 109 Diameter of the domain versus time for different intensity of the electric field. (a) Results obtained for experiment without electric field (***E***=0 V μm^{-1}) and with electric field. The frequency for all experiments with EF was set to *f*=2 Hz. (b) Time of domain growth till the diameter achieves *d*=6.36 μm, as a function of the electric field ***E*** applied to the system. Results for samples of 5CB/PS (72/28 wt%), cooled down to 35.5 ℃ into the I+I region.
Fig. 109a was taken from [25].

Previous experiments were performed for a 5CB liquid crystal in nematic phase. However, the experiments performed for free-standing smectic films were done for a 8CB liquid crystal. In next experiments Natalia Ziębacz compared mixture of 8CB/PS and 5CB/PS with and without electric field. We didn't observed any quantitative difference between separation of those mixtures. In Fig. 110 we show the dependence of q_{max} wavevector versus time for two different liquid crystals: 5CB and 8CB. 5CB/PS mixture (72/28 wt%) was cooled down to 35.5 °C into the I+I region, whereas 8CB/PS (72/28 wt%) was cooled down to 44.9 °C also into the I+I region.

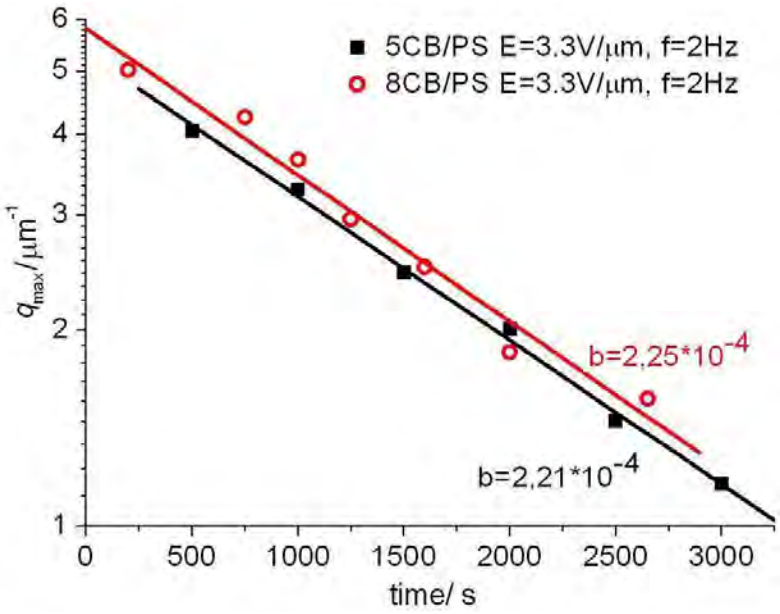

Fig. 110 Wavevector q_{max} as a function of time for a samples of liquid crystal: 5CB and 8CB and a polystyrene (PS). Both experiments were performed with external electric field: $\boldsymbol{E}$ = 3.3 Vμm^{-1} and frequency f = 2 Hz.
Figure taken from [25].

The results could be fit to the function:

$$L(t) \propto exp(bt) \tag{177}$$

The b coefficient in expression (177) for the 5CB and 8CB experiments were almost the same: $2.25 \cdot 10^{-4}$ for 8CB/PS and $2.21 \cdot 10^{-4}$ for 5CB/PS.

3.3.3.1.2 Influence of frequency

In the next part of experiments Natalia Ziębacz evaluated influence of frequency of the AC electric field on the phase separation process. The results are presented in the Fig. 111.

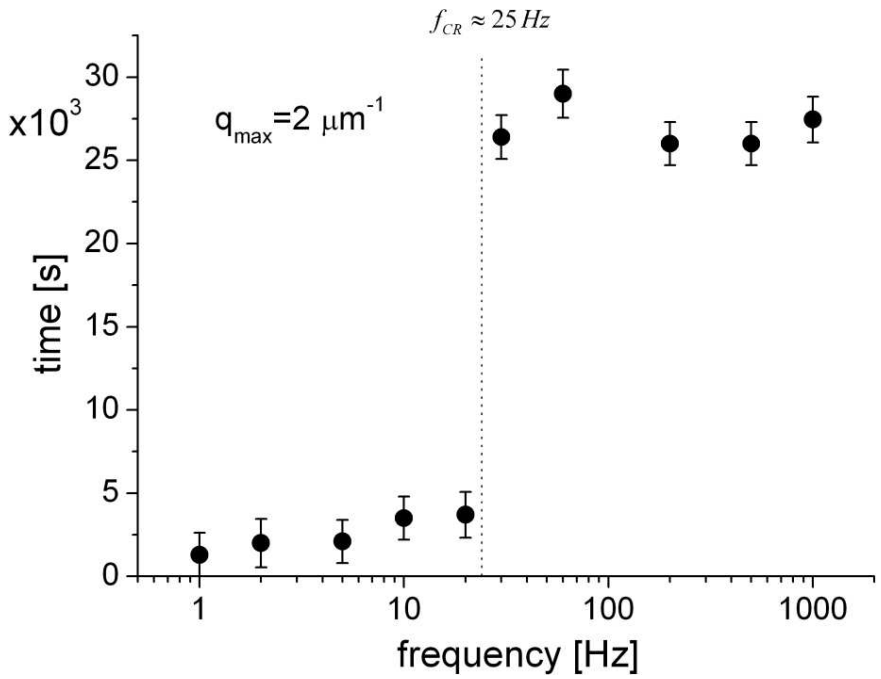

Fig. 111 Time versus frequency of the AC electric field. The time on the Y axis means the time which the domain achieve wave vector q_{max} equal to 2 μm^{-1}. Results were obtained for mixture of 5CB/PS (72/28 wt%) cooled down to 35.5 °C (I+I region). At the frequency f_{CR}≈25 Hz there is a clear threshold in acceleration of the phase separation—below the f_{CR} the time to obtain domain with a wave vector 2 μm^{-1} is shorter than for frequencies higher than critical. All experiments were performed for electric field ***E***=3.3 Vμm^{-1}.
Figure taken from [25].

Fig. 111 presents dependence of the time as a function of frequency of the electric field. The time of which wave vector attains a value of 2 μm^{-1}. The domain size is a reciprocal of wave vector, thus it means, that the domain size is ca. 0.5 µm.

For frequencies higher than critical (f_{CR}) Natalia Ziębacz did not observed any acceleration of the phase separation. For frequencies lower than critical, i.e., between 1 Hz and 20 Hz, the time of separation was accelerated approximately 10 times.

3.3.3.1.3 DC electric field

In previous subchapters it was shown that AC electric field with frequency lower than critical can accelerate phase separation. Fig. 112 shows also that high frequencies, (i.e. 1 kHz), do not accelerate this process. Herein, the influence of DC electric field on the separation process is presented.

Fig. 112 compare two experiments. In Fig. 112a is shown an experiment without electric field, intensity of light scattering intensity S(q,t) versus wave vector q. For different time (from 10 seconds up to 84 000 seconds) one can precisely show the maximum wave vector q_{max}. In Fig. 112b is shown an experiment with a DC electric field. At the very beginning the phase separation occurred without the use of electric field. When the q_{max} peak appeared the DC electric was applied to the sample. Instead of single peak, like in phase separation without electric field, there is a plateau. The interpretation may be as follows: the domains of liquid crystal in DC electric field were destroyed and many smaller, quasi-circular, domains was created in the sample, therefore there is no single peak from a one diameter of the domain.

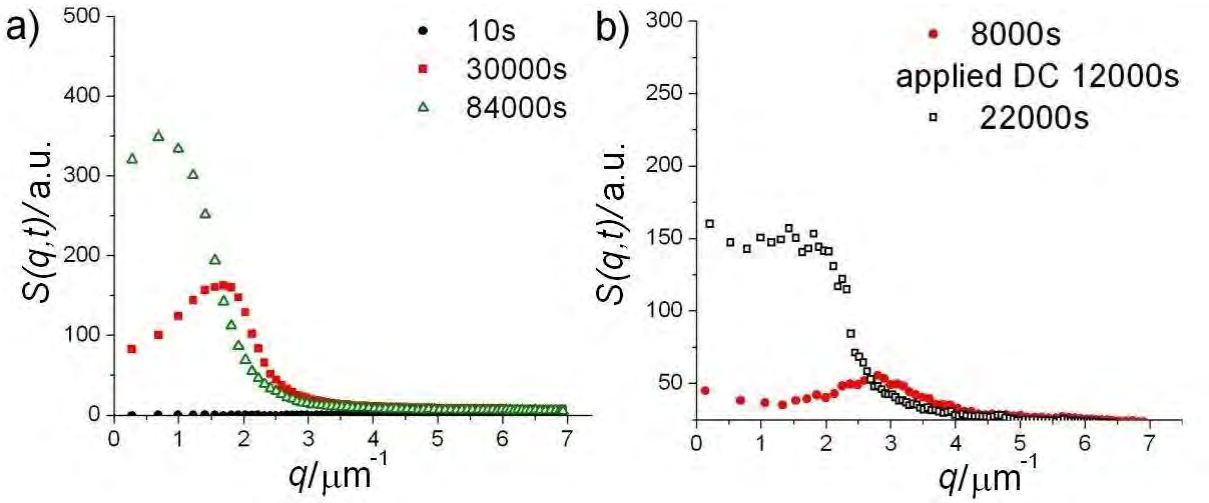

Fig. 112 Light scattering intensity as a function of a wave vector q. (a) Experiments without applying external electric field, we can distinguish a q_{max} wave vector for each case. (b) Phase separation process with the use of electric field, $\boldsymbol{E}$=0.03 Vμm^{-1}.
All experiments were performed for 5CB/PS (72/27 wt%). Mixture of liquid crystal and polymer was cooled down from 55 °C to 35.5 °C into the I+I region. Thickness of the samples was 10 μm. Figures were taken from [25].

3.3.3.1.4 Influence of ions on acceleration of phase separation

Since the external electric field accelerates the phase separation Natalia Ziębacz checked how addition of organic salts (e.g. additional species with electric charge) will influence the process. The system studied in this case was a mixture of poly(methylphenylsiloxane) (PMPS) from Sigma Aldrich Co. (with parameters: M_W=2274 and M_W/M_N=1.35) and polystyrene (PS) from Fluka Chemical Co. (with parameters: M_W=10700 and M_W/M_N=1.03). To change its conductivity the mixture was doped with benzyltetradecyldimethylammonium chloride (BDTC) from Sigma Aldrich.

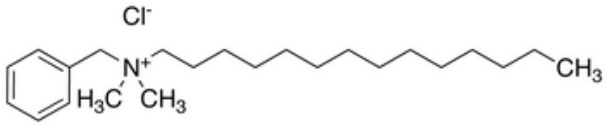

Fig. 113 Organic salt, benzyltetradecyldimethylammonium chloride (BDTC) used in doping polymer blends.

The BDTC was added to polymer blend in quantity 0.3 %wt. The phase diagram of PS/PMPS was shown elsewhere [25]. The experiments with electric field and addition of BDTC organic salt are shown in Fig. 114.

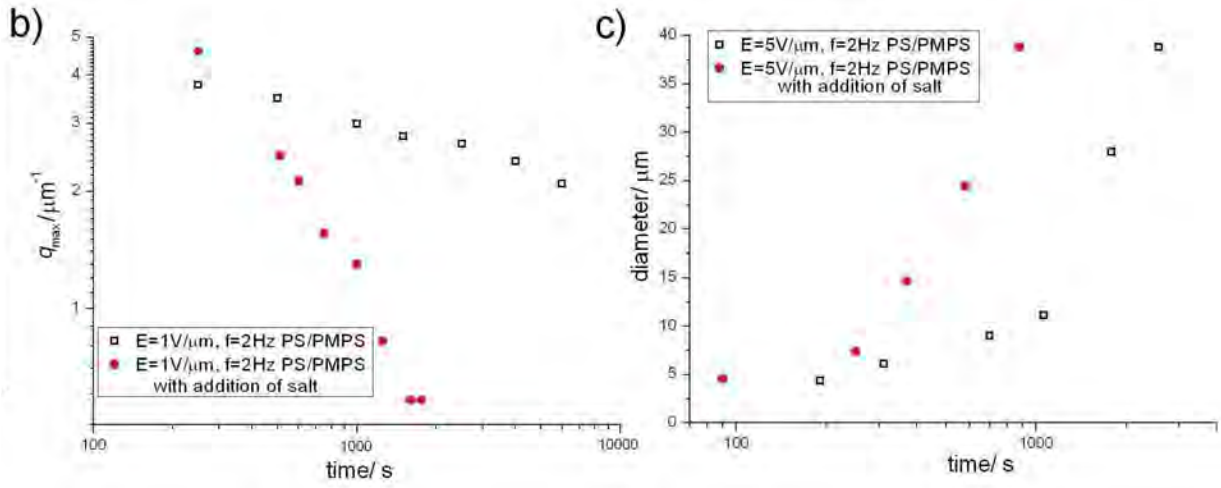

Fig. 114 The wave vector q_{max} as a function of time (a) and mean diameter of the domain as a function of time (b) for PS/PMPS mixtures in electric field. The used mixture was PS/PMPS (30/70 %wt) cooled down to 105 °C, with 0.3 %wt of BDTC organic salt.
Figure taken from [25].

The addition of organic salt (e.g. the increase of free ions in the sample) cause the acceleration of the phase separation (Fig. 114a). The addition of ions causes that the q_{max} wave vector can be obtained one order of magnitude faster than a pure sample.

In Fig. 114b is presented dependency of diameter of the domain as a function of time. Comparing certain diameter for samples with additional salt and pure shows that organic salt accelerated 2-3 times process of phase separation.

3.3.4 MECHANISM OF PHASE SEPARATION

Herein, I will summarize the results obtained by Natalia Ziębacz in her experiments:

1. Natalia Ziębacz determined a critical frequency (f_{CR}) of alternating electric field above she did not observed the acceleration of the phase transition. Below the critical frequency she did observed the acceleration of phase separation. The value of this critical frequency is relatively small, e.g. $f_{CR} < 50$ Hz in the experiments.

2. There is no acceleration of the process when she applied a direct current (DC) electric field. She observed, via SLS, a destruction of the previously separated LC domains into a smaller ones.

3. Artificially doped samples (both polymer/LC and polymer/polymer) with organic salt separate faster (in AC electric field with $f<f_{CR}$) than samples with natural concentration of ions.

For this reason, the mechanism of acceleration of phase separation in external electric field is related to the dynamic charge separation (dyCHASE) process, described previously in Chapter 3.1 and 3.2 where the model system was a free-standing smectic film.

In a system with a free-standing smectic film (both, in a geometry when the needle pierce the film or is under the LC island), the boundary of the meniscus becomes charged when the frequency of the oscillating electric field is lower than f_{CR}. The f_{CR} is that system is related with electrophoretic mobility and the Debye screening length with relation:

$$f_{CR} \propto \frac{\mu \cdot E}{\lambda} \tag{178}$$

For $f<f_{CR}$ ions separate over the Debye length and electrically charge the boundary of the meniscus. In Chapter 3.1 I discussed this phenomena and state that two conditions must be fulfill to observe instability of the charged meniscus:

i) frequency of the oscillating electric field has to be lower than critical (f_{CR}), to separate ions over the Debye length,

ii) discontinuity at the boundary of the meniscus (in the case of free-standing smectic films it was a conductivity of the liquid crystal and the surrounding air, since the LC island is a thicker than the LC film).

In the case of phase separations Natalia Ziębacz did not observed any acceleration for a frequencies higher than critical. Using the dyCHASE mechanism it can be explained as an immobility of the ions: the frequency of electric field changes so fast, that ions cannot move themselves over the Debye length and for very high frequencies they oscillate around their position.

For a frequencies smaller than critical, ions separate over the Debye length, and on the interface liquid crystal/polymer they charge the LC domain. It means that LC domains are macroscopically charged, and can attract themselves due to strong, electrostatic interactions. The domains becomes close to each other and finally, the thin layer of the polymer between them breaks and the domains merge into a single one. (see Fig. 115)

The second important condition is the discontinuity rule. For many conventional electrolytes, the ionic mobility is approximately inversely proportional to the macroscopic viscosity of the solution. This relationship:

$$\mu \propto \frac{1}{\eta} \tag{179}$$

was suggested by P. Walden in 1906. The Walden's rule is very useful from practical point of view, because it allows us connect mobility of the objects in nanoscale with macroscopic properties of the system, which can be easily measured.

In mixtures, that was studies in experiments performed by Natalia Ziębacz, there is a big difference in the macroscopic viscosity – the polystyrene has a much bigger viscosity than used liquid crystals (5CB or 8CB). Applying the Walden's rule to these experiments, one see that conductivity of the liquid crystal is bigger than polymer (see eq. 180).

$$\frac{1}{\eta_{LC}} \gg \frac{1}{\eta_{polymer}} \tag{180}$$

Due to the fact that the ions separate over the Debye length and cannot move to the polymer matrix they accumulate on the interface and macroscopically polarize the LC domain.

In a DC electric field the ions move due to electrophoretic force and accumulate on the interface of LC/polymer. As the electric field do not change its polarity the force is constant. The ions act on the border of LC domain, and after certain time the stresses acting on the domain overcome the surface tension of the domain. As a result domains breaks into a number of smaller domain (see Fig. 116)

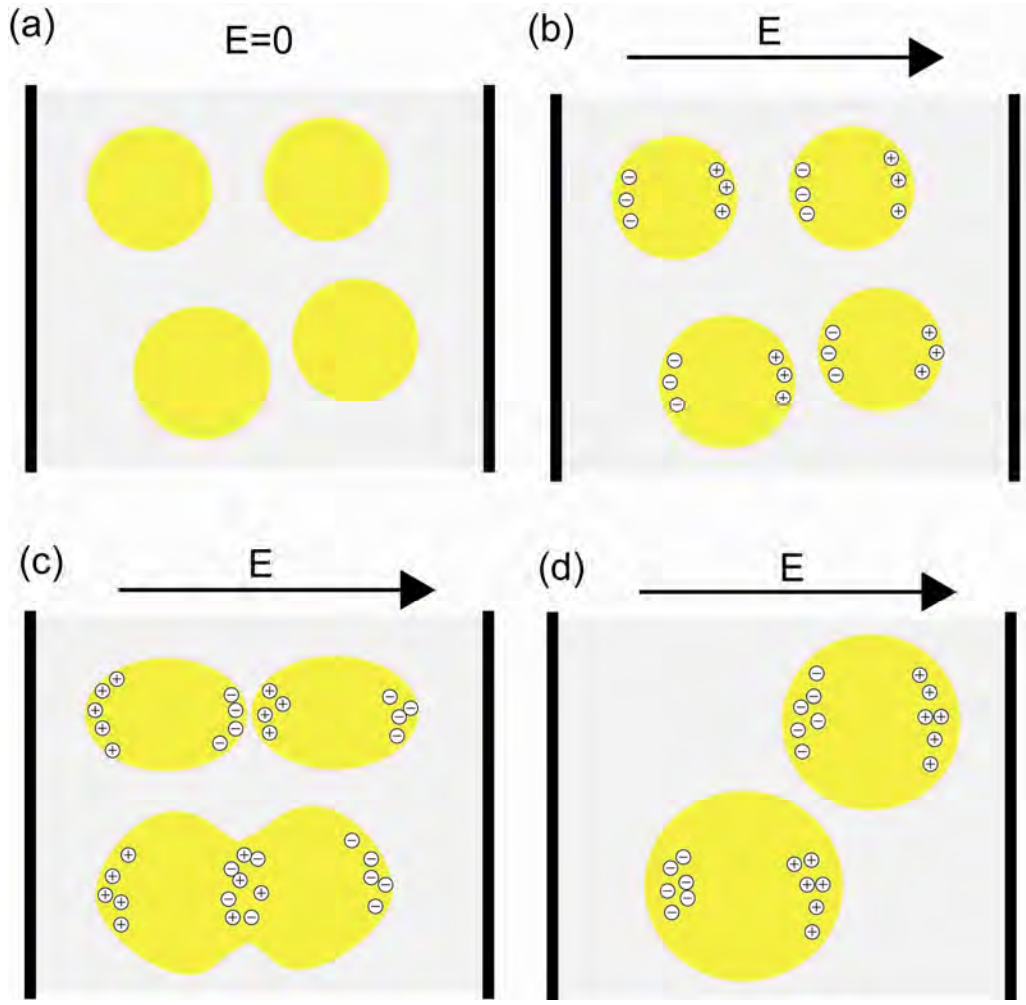

Fig. 115 The mechanism of phase separation. LC domain (yellow circles) are under application of AC electric field obtain a macroscopic charge due to dyCHASE mechanism (a, b). Charged domain attract each other, the thin polymer film between them breaks (c) and domains merge into a big one (d). The black lines are electrodes.
Note: the ions are not in scale with the size of domains.

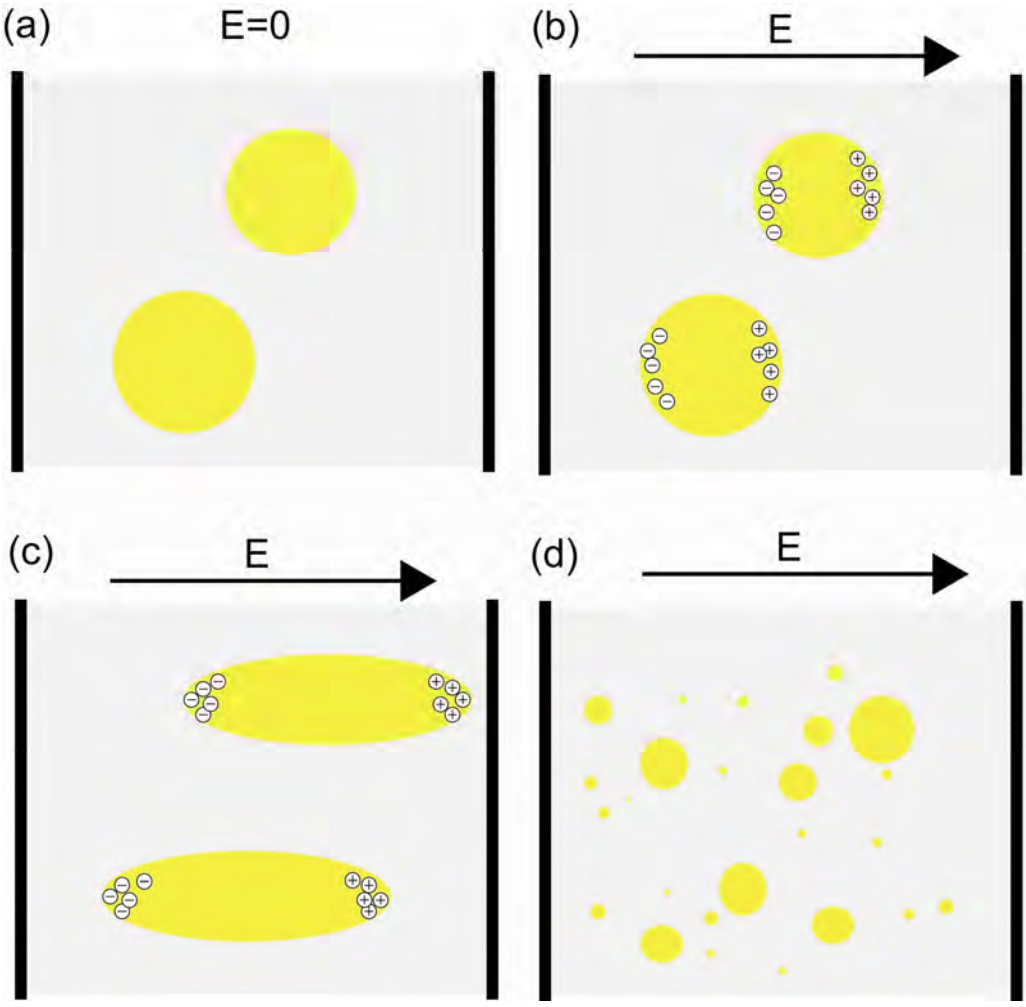

Fig. 116 The mechanism of stability of LC domains under the DC electric field. In DC electric field LC domains obtain a charge due to a dyCHASE mechanism (a, b). As the EF is acting on the domains, the accumulated ions act on the domain and elongate it. (c) When the stresses on the end of the domain overcome the surface tension the domain breaks into a small domains (d).
Note: the ions are not in scale with the size of domains.

Analyzing the mechanism of phase separation we have to discuss the other forces which may affects this process. One of those is dielectrophoretic (DEP) force. In our analysis we can neglect this force, because DEP is strongest in frequencies in range of MHz, whereas we are using a tens of Hz.

Moreover, it is hard to connect our observations and conclusion to the Tsori et al. [28] According to him electric field of intensity above 2 V μm^{-1} is able to induce a phase separation process. In the experiments we did not noticed any shift in phase transition temperatures in the samples both with the external electric field, or without electric field. It did not depend on the value of electric field and its frequency.

3.3.5 SUMMARY

Herein, I described a mechanism of acceleration of the phase separation in a polymer/liquid crystal and polymer/polymer mixture. The mechanism can be related to the electrophoretic movement of charged species, i.e. ions present in the sample. Ions are impurities or can be introduced artificially as a doping of organic or inorganic salts.

As the same mechanism works for different liquid crystals (5CB and 8CB) and polymer/polymer mixture. We state that this is a general mechanism for systems with even small amount of ions.

As the frequencies needed to electrophoretically move ions are relatively small (f < 50 Hz), it can be used in industrial application to accelerate phase separation, e.g. cosmetic and food industry.

Absence of this phenomenon for large frequencies, sharp threshold frequency and influence of doping indicate that we can relate this phenomenon to previously observer dyCHASE effect.

3.3.6 REFERENCES FOR CHAPTER 3.3

[1] I. Demyanchuk, Mixing/Demixing in Polymer Blends (2006).

[2] S. J. Woltman, G. D. Jay, and G. P. Crawford, *Liquid Crystals: Frontiers in Biomedical Applications*, 1st ed. (World Scientific Publishing Company, 2007).

[3] J. W. Doane, A. Golemme, J.L. West, J.B. Whitehead, and B.G. Wu, Molecular Crystals and Liquid Crystals **165**, 511-532 (1988).

[4] C. M. Lampert, Solar Energy Materials and Solar Cells **76**, 489-499 (2003).

[5] S. Park and J. W. Hong, Thin Solid Films **517**, 3183-3186 (2009).

[6] T.J. Bunning, L.V. Natarajan, V.P. Tondiglia, and R.L. Sutherland, Annual Review of Materials Science **30**, 83-115 (2000).

[7] K. Pavani, I. Naydenova, J. Raghavendra, S. Martin, and V. Toal, J. Opt. A: Pure Appl. Opt. **11**, 024023 (2009).

[8] YanJun Liu, Bin Zhang, Yu Jia, and KeShu Xu, Optics Communications **218**, 27-32 (2003).

[9] X. Sun, X. Tao, T. Ye, P. Xue, and Y.-S. Szeto, Appl. Phys. B **87**, 267-271 (2007).

[10] Dimo Kashchiev, *Nucleation* (Butterworth-Heinemann, 2000).

[11] J. W. P. Schmelzer, *Nucleation Theory and Applications*, 1st ed. (Wiley-VCH, 2005).

[12] Yanhua Niu, Liang Yang, Katsumi Shimizu, Jai A. Pathak, Howard Wang, and Zhigang Wang, The Journal of Physical Chemistry B **113**, 8820-8827 (2009).

[13] RunMing Li, Wei Yu, and ChiXing Zhou, Journal of Macromolecular Science, Part B: Physics **46**, 1051 (2007).

[14] J Yang, XD Chen, RW Fu, WA Luo, YB Li, i MQ Zhang, Physical Chemistry Chemical Physics **12**, 2238-2245 (2010).

[15] JX Yu, CM Mahoney, AJ Fahey, WL Hicks, R Hard, FV Bright, and JA Gardella, Langmuir **25**, 11467-11471 (2009).

[16] N.S. Murthy, W. Wang, and J. Kohn, Polymer **51**, 3978-3988 (2010).

[17] K. Amundson, E. Helfand, X. Quan, and S. D. Smith, Macromolecules **26**, 2698-2703 (1993).

[18] A. Böker, A. Knoll, H. Elbs, V. Abetz, A. H. E. Müller, and G. Krausch, Macromolecules **35**, 1319-1325 (2002).

[19] A. Böker, H. Elbs, H. Hänsel, A. Knoll, S. Ludwigs, H. Zettl, V. Urban, V. Abetz, A. H. E. Müller, and G. Krausch, Phys. Rev. Lett. **89**, 135502 (2002).

[20] T. Thurn-Albrecht, J. DeRouchey, T. P. Russell, and H. M. Jaeger, Macromolecules **33**, 3250-3253 (2000).

[21] T. Thurn-Albrecht, J. DeRouchey, T. P. Russell, and R. Kolb, Macromolecules **35**, 8106-8110 (2002).

[22] Yoav Tsori, *Polymers, Liquids And Colloids In Electric Fields* (World Scientific Publishing Company, 2009).

[23] P. Goldberg-Oppenheimer and U. Steiner, Small **6**, 1248-1254 (2010).

[24] M. Graca, S.A. Wieczorek, and R. Hołyst, Macromolecules **36**, 6903-6913 (2003).

[25] N. Ziębacz, S. A. Wieczorek, T. Szymborski, P. Garstecki, and R. Hołyst, Chemphyschem **10**, 2620-2622 (2009).

[26] M. Graca, S. A. Wieczorek, and R. Hołyst, Physical Review Letters **90**, (2003).

[27] I. Demyanchuk, S.A. Wieczorek, and R. Hołyst, Journal of Physical Chemistry B **110**, 9869-9875 (2006).

[28] Y. Tsori, F. Tournilhac, and L. Leibler, Nature **430**, 544-547 (2004).

Chapter 3.4
Polarization of the water/oil interface in external electric field

Microfluidics is a relatively new area of science and technology. It deals with designing and manufacturing devices where fluid flows at microscale length scales.

In this chapter I will describe the background information about microfluidics, with special attention to the methods of creating droplets at the microscale: flow-focusing (FF) and T-junction systems. Microfluidics offers rapid and efficient methods for creating emulsions. The only disadvantage—low efficiency of creating droplets—can be overcome by creating a multiple generators in a single chip. I will describe a multiple Flow-Focusing device in this chapter.

The main part of this chapter describes my results of studies of the electrocoalescence process. Coalescence is a process where two droplets merge together into a larger single droplet with the use of electric field. This process in typical emulsion is very slow, because droplets are stabilized with surfactants. To overcome that stabilization it is possible to apply AC electric field and polarize the droplets. They become macroscopically polarized, thus start to attract each other and accelerate coalescence process. I conducted experiments to evaluate the influence of the applied voltage and the frequency on the rate of the electrocoalescence process. The experiments were performed for ultra-pure water and NaCl electrolyte solution. The results show that the rate of electrocoalescence changes monotonically with increasing voltage. Moreover, I found that the rate of electrocoalescence is increasing to critical frequency, correlated with time of ion separation of the oil/water interface. Above this frequency the intensity of coalescence due to ion separation decreases.

These results show that electrocoalescence process at the microscale can be controlled with the voltage and frequency of the applied electric field, and depends strongly on the conductivity of the dispersed phase.

3.4.1 GENERATING EMULSIONS IN MICROFLUIDIC DEVICES

3.4.1.1 Introduction

One of the main factors of the evolution of modern technology is miniaturization. The most known example is computer industry: at the end of the WWII ENIAC computer was a huge machine whereas a microprocessor nowadays is a tiny device that can be placed in a hand. The fast progress in the 80-ties in the MEMS technology was a catalyst for the new-born microfluidics, however the first “microfluidic” device was a miniaturized gas chromatography system developed in 1975.

Microfluidics that is an idea of science and technology of creating complex systems of microchannels which conduct liquids and gases. The channels are usually of widths of tens of hundreds of micrometers. A sub-group of techniques known as droplet microfluidics was also developed: it is a science and engineering of creating and controlling droplets of liquids and gasses in microscale.

In the late 1990s George Whitesides used an elastomer, PDMS, for fast and cheap prototyping of the devices. [1] [2] The device could be produced within a single day, from the technical draw in CAD software to working device. The result was an increase in research over the microfluidics and the number of papers published on this subject increased as well. The applications of microfluidics and so called, lab-on-a-chip (LoC) systems are:

i) Electrophoretic separation systems, [3]

ii) Micromixers, [4]

iii) PCR devices, [5]

iv) Cytometers, [6]

v) Chemical micro-reactors, [7]

vi) Bio-applications (protein manipulation and analysis, pathogen detection etc.) [8]

Microfluidics found another interesting applications: it can be used as a fast and efficient method of creating emulsions. The droplet-microfluidics technology allows creating droplets with average diameter from 10 µm to 100 µm. The advantage of this process is excellent monodispersity and wide branch of possible emulsion can be created: direct, reverse and multiple.

3.4.1.2 Fluid mechanics in microscale

The typical size of the channels: depth and width of tens of micrometers and total length of channels of a single millimeters cause the viscous forces dominate over the inertial ones, thus the describing equations of the flow are linear. The size of the channel results in the type of the flow: in this scale it is laminar.

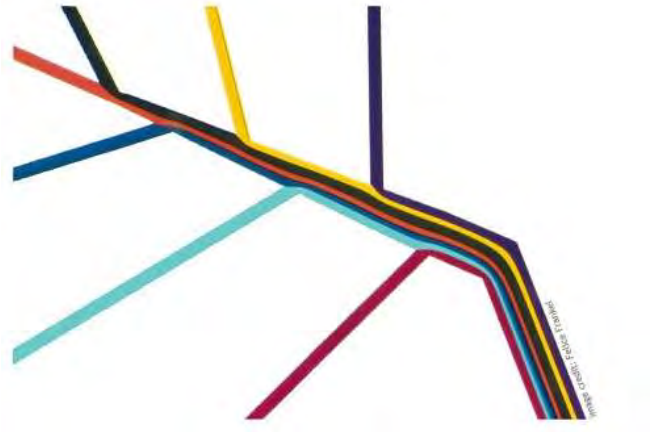

Fig. 117 The laminar flow in the microfluidic channels. Six channel merge into a single one: in each of the there is a flow a water with a dye. Streams merge into single one, yet do not mix and flow together. (source: George Whitesides group, Harvard)

The flow inside the channel obeys the Hagen-Poiseuille equation which relates the speed linearly to the pressure drop through the channel and to hydraulic resistance:

$$\Delta p = QR \tag{181}$$

$$R = \frac{8\mu L}{\pi r^4} \tag{182}$$

where:

Δp – the pressure drop within the channel,
Q – the volumetric rate of flow,
R – the hydraulic resistance of the given channel, which depends on:
μ – the dynamic viscosity,
L – the length of the channel,
r – the inner radius of the channel,

The laminar flow in the microfluidic channel is connected with the Reynolds number, Re:

$$\mathrm{Re} = \frac{vL\rho}{\mu} \tag{183}$$

v – the average flow speed,
L – characteristic length scale of the channel,
ρ – the density of the fluid,
μ – the dynamic viscosity,

For Re << 2000 viscous forces dominate and the flow is laminar. For Re > 2000 the inertial forces start to dominate, which produce instability and, in the end, a turbulent flow. Due to small dimensions' of the channels the Reynolds numbers are usually Re < 10 therefore in microscale the flow is laminar. A spectacular example of laminar flow is presented in Fig. 117, where a flow of six different streams of solutions of dye is presented. The mixing is such system occurs only via diffusion. The mixing via diffusion is related with a Peclet number, Pe:

$$Pe = \frac{vw}{D} \tag{184}$$

v – the velocity of fluid,
w – the width of the channel,
D – diffusion coefficient,

The Peclet number compares the typical time scale for diffusive transport to that for convective transport. Transverse diffusion of solutes broadens the laminar interface, flattens the concentration gradient across the streams and homogenize the liquids. For flows in microsystems the Peclet numbers are usually large (ca. 1000)

3.4.1.3 Microfabrication

There exist a wide list of techniques used nowadays to create microfluidic devices. To name the most important one:

i) soft photolithography,

ii) additive techniques (i.e., CVD, PVD, sol-gel deposition),

iii) subtractive techniques (i.e., wet etching, dry etching, physical-chemical etching),

iv) pattern transfer techniques (i.e., subtractive transfer, additive transfer),

v) silicon bulk micromachining,

vi) microstereo lithography. [9]

3.4.1.4 Preparing of microfluidic device with soft lithography

Soft photolithography process was developed for the microelectronic industry. It was however, applied to create a microstructured device. The basic concept of making these devices is shown in Fig. 118.

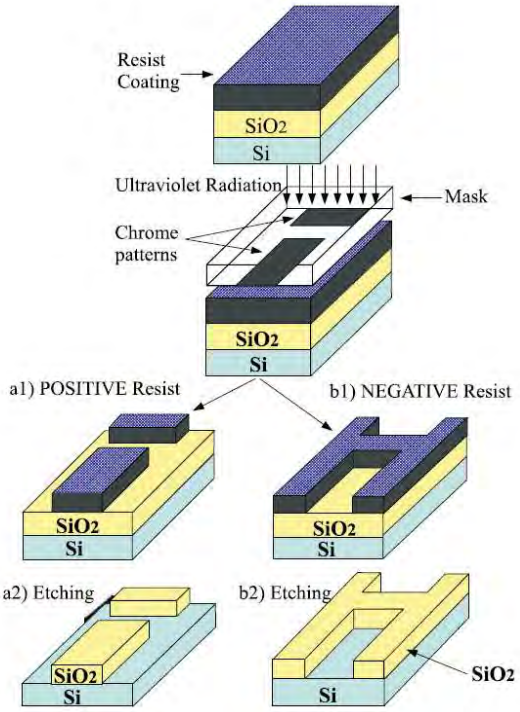

Fig. 118 Schematic illustration of the soft photolithography process with a main steps: resist coating and ultraviolet radiation, etching of the positive (a1) and negative (b1) resist. The last step of the process is etching of SiO_2 (a2 and b2). At the end of the process one obtain a piece of Si wafer with the negative of the channels (so called 'master'). [10]

The first step in preparing a 'master' is a spinning of a thin layer of a photoresist. The photoresist can be a positive or negative, i.e. after curing and etching one can remove the cured or non-cured regions. After preparing thin layer of photoresist it is necessary to expose it to a UV radiation through a mask, thus developing a special patter of the channels. Next step is removing the non-cured or cured resin (depending on the resin used in previous step). Typical process stop in this place: the pattern of the channels is already developed and the 'master' is ready. The last step can remove resist and the SiO_2, however it is not necessary. Having a 'master' one can prepare the device and method known as 'replica molding' can be used to prepare it (Fig. 119). The first step is to mix a pre-polymer and the curing agent with weight ratio 10:1. Next step is de-gassing under vacuum and pouring a thin layer (usually few mm) of PDMS over the Si wafer with channels on top. After curing in temperature 80 °C for a 6 to 8 hours, the PDMS is cut and peel off. Last stage it making the holes for the tubes and bonding the top and the bottom of the device. To bond them, one modify the surface with nitrogen plasma for 1 minute, put them together and place in the oven for 12 hours. After that the device is ready to use.

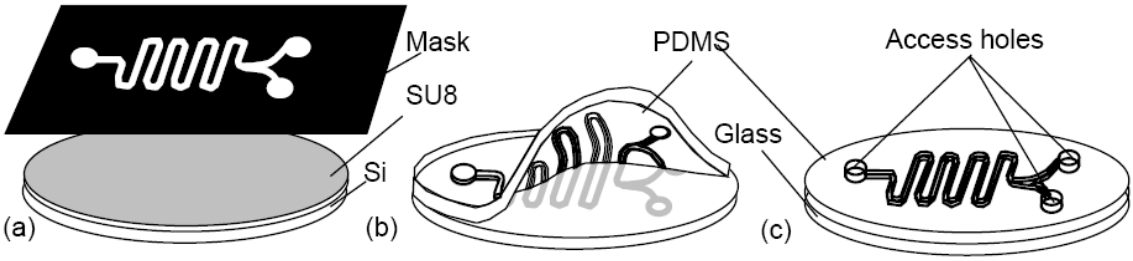

Fig. 119 Fabricating of microfluidic device with the use of soft lithography: (a) preparing a 'master' which was described in details in Fig. 118, (b) pouring, curing and cutting a PDMS layer, (c) after surface treatment the two pieces of PDMS are bonded together, making a microfluidic device. [9]

The most popular material for making microfluidic devices is poly(dimethylsiloxane) or PDMS. PDMS has an inorganic siloxane backbone with methyl groups attached to silicon (see Fig. 120). PDMS exhibits several unique properties: the prepolymers and curing agents are commercially available, it is stable against temperature and humidity and transparent. Transparency is an important advantage of PDMS: it allows to observe flow of the liquids inside the channels. PDMS is an elastomer and can be attached to a non-planar surfaces. The surface of PDMS can be easily modified with nitrogen plasma and therefore two pieces of PDMS can be easily bonded together after this treatment.

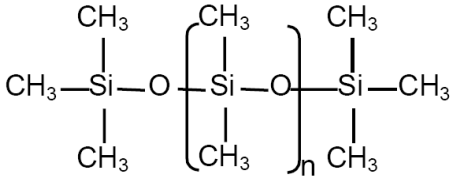

Fig. 120 Chemical structure of poly(dimethylsiloxane) (PDMS), an elastomer used as a substrate for making microfluidic devices.

3.4.1.5 Preparing of microfluidic device via micromachining

The other popular method of preparing microfluidic devices in micromachining. CNC (Computer Numerical Control) milling machines are used to create device and polymers like PMMA, PC or PEEK are used as the material. The CNC machine and the device is shown in Fig. 121

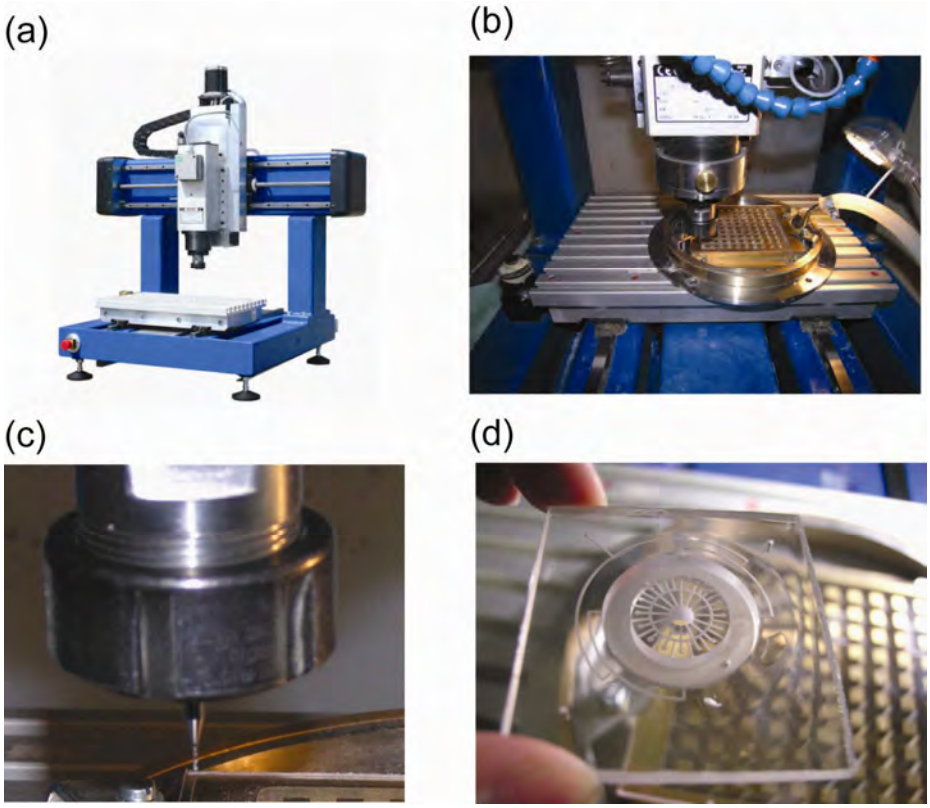

Fig. 121 (a) The CNC milling machine (ErgWind), (b) milling machine at work, preparing device in polycarbonate, (c) to prepare microfluidic channels a mill with a diameter 100 µm used, (d) microfluidic device milled in polycarbonate.

The first step is to design shape of the channels in any CAD software. The file with a project is opened in a specialized CAM software. This software can calculate the route for the mill, the time needed to create project etc. This same software can control the milling machine. After cutting polycarbonate and placing it in a special holder (visible on Fig. 121b) the computer automatically remove material from the shape, thus creating the device.

Appropriate methods of bonding of polycarbonate plates was developed. One of these is method developed by Ogończyk et al. [11]. The first step is to place two PC plates (top and bottom) in vapor of methylene chloride. Then the device is placed between two steel plates in temperature around T_g and with appropriate pressure. This procedure results in a good mechanical properties and non-deformed shape of the channel.

Jankowski et al. [12] and Derzsi et al. [13] proposed method for modification of the surface of the channel with polyelectrolytes to obtain hydrophobic and hydrophilic properties. The method can give both hydrophilic and hydrophobic surface within a single device, thus allowing to produce a multiple emulsions.

3.4.1.6 Methods of making droplets in microsystems

There are two main methods of creating droplets (both for the liquid and gas) in microscale:

i) T-junction,

ii) Flow-focusing (FF) systems

The T-junction was the oldest method of creating bubbles, developed by Thorsten. The T-junction depicted in Fig. 122 has a very simple design: there is a main straight channel, that carried the continuous fluid and is joined from the side by a second channel, which supplies the fluid that must be dispersed. The angle between these two channels is usually 90 degrees.

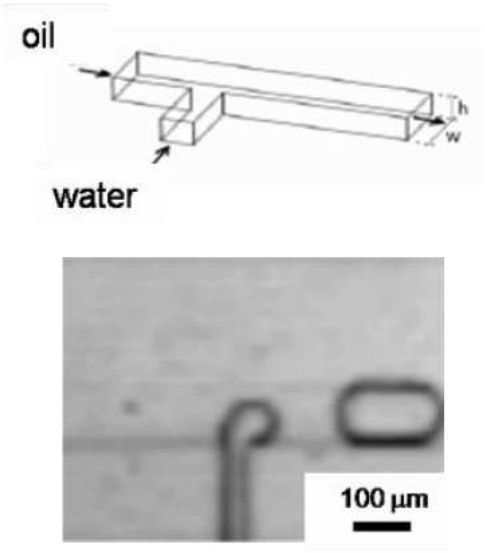

Fig. 122 The T-junction is a setup of two channel oriented perpendicular (top). Process of creating a droplet or a bubble in such a geometry (bottom). Pictures taken from [14]

The operation of the T-junction depends on the values of the speeds of flow of the two phases. It can be however parameterized by the value of the capillary number Ca. At low values of capillary numbers, which is $<10^{-2}$, formation of the droplets obeys 'squeezing model'. For the intermediate values of Ca number, where the viscous effects are noticeable, it can be described by dripping model. At highest rates of flow, i.e. for highest Ca number, the system develops a long jet before the droplets are created. [14]

The flow-focusing (FF) system was first demonstrated by A. Ganan-Calvo in his work on axisymmetric systems operating at high Reynolds, Weber and capillary numbers [15]. Afterwards, S. Anna and collaborators [16] showed that this concept can be applied to a planar geometry in typical microfluidic device. The application of creating a nitrogen bubbles and water droplets via FF system in shown in Fig. 123

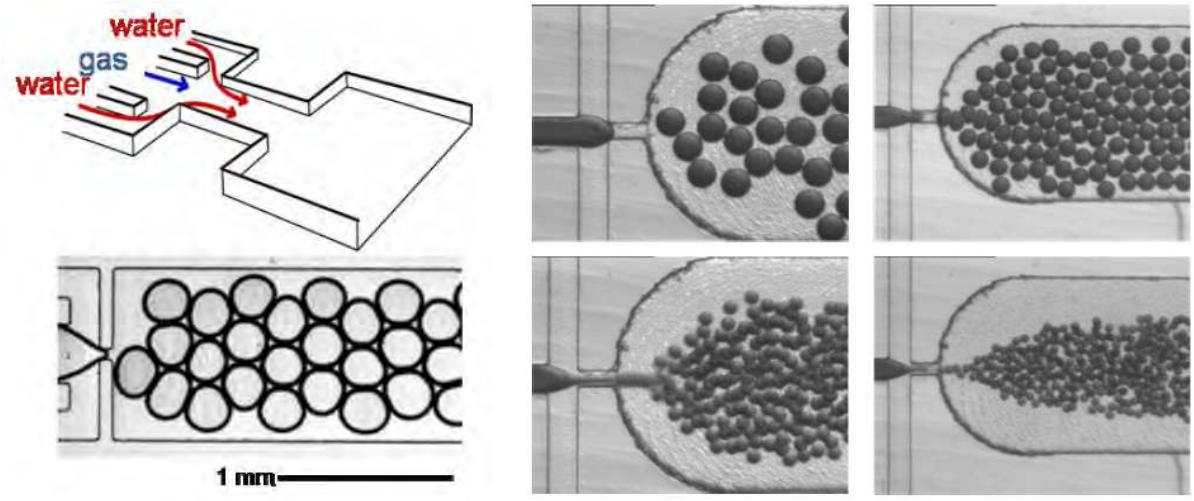

Fig. 123 The flow-focusing device for generation of a bubbles in a water (left), and FF system used for generation of an emulsion of water droplets (with small addition of a dye) in an oil. Different velocities indicate the different size of the water droplets. [14]

The idea of FF is as follows: two immiscible phases (e.g. water and oil or nitrogen and oil/water) are delivered to the microfluidic chip (see Fig. 123). In FF junction central inlet channel delivers fluid which will be dispersed. From the sides of the main channel two additional terminate upstream of the orifice. These side channel deliver a continuous stream of fluid which disrupts the main stream of the fluid and thus creating droplets or bubbles in the device. (see Fig. 124)

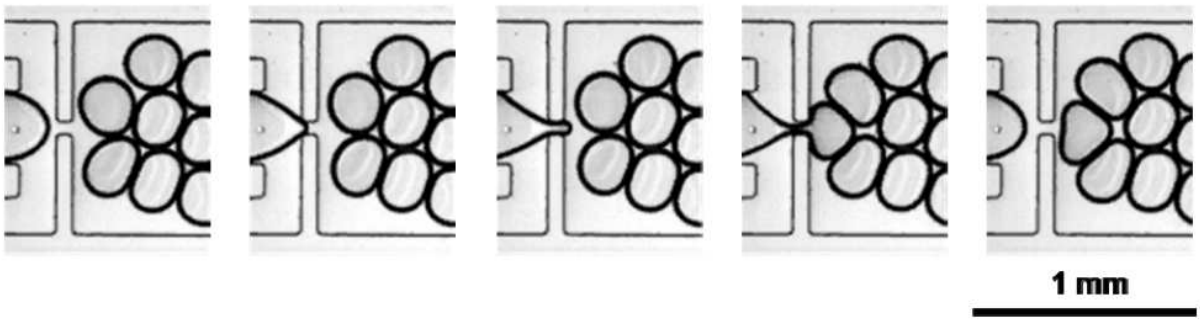

Fig. 124 A single cycle of creating a single bubble in a FF system. The continuous phase is water whereas the dispersed phase is nitrogen. Picture taken from: [14]

The continuous fluid has to wets the channels of the microfluidic device, whereas the dispersed fluid do not wet. Otherwise forming droplets or bubbles in a reproducible and controllable process is almost impossible.

3.4.1.6.1 Single and coupled generators

As was mentioned earlier the microfluidic devices are ideal for creating emulsions. Apart from the advantages of using it for this purpose the one big disadvantage is important: a single microfluidic generator is not a high-throughput method of preparing of large amount of emulsions. To overcome this problem we placed a set of couplet flow-focusing devices on a single microfluidic chip.

We examined single and coupled FF generators: two and four generators in a single chip, we used nitrogen and water as a dispersed phase to check their influence on preparing emulsions.

3.4.1.7 MATERIALS AND METHODS

To study the formation of gas bubble we sealed PDMS against glass slides, whereas for studying the formation of water droplets in hexadecane we sealed them against PDMS. The device was placed in oven overnight at 150 ℃ to ensure the hydrophobic character of the device. To create the gas bubbles we used deionized water (Millipore) as a continuous phase with Tween20, 2% w/w (Polysorbate 80, Aldrich) as surfactant to stabilize the bubbles. The dispersed phase was ultrapure nitrogen (Airgas).

To study the formation of water droplets in oil we used hexadecane (Sigma) as a continuous phase with Span80, 3% w/w (Sorbitian monooleate, Aldrich) as surfactant to stabilize generated water droplets. The dispersed water was deionized, ultrapure water (Millipore).

We used syringe pumps (Harvard Apparatus, model PhD2000) to controll the delivery of the fluids to the microfluidic chips. Nitrogen was regulated via valve connected to a gas cylinder. We used an upright microscope (Leica DMRX), a set of still- (Nicon Digital Camera DXM 1200), and fast-video camera (Phantom V7) to visualize and record movies of creating gas bubbles in water. Stereoscope and microscope (Nikon) together with fast camera (PHOTRON Fastcam 1024PCI) was used to visualize and record movies or creating water droplets in hexadecane. We studied the dependency or independency of parameters as follows:

i) influence of the geometry of the devices,

ii) the nature of fluids (e.g. the dispersed phase was water or nitrogen),

iii) flow parameters.

3.4.1.8 RESULTS

A picture describing the single FF device, and coupled devices (two and four FF generators) is shown in Fig. 125. We studied formation of nitrogen bubbles and water droplets, however herein I will show only results for single and coupled generators for preparing water droplets in hexadecane.

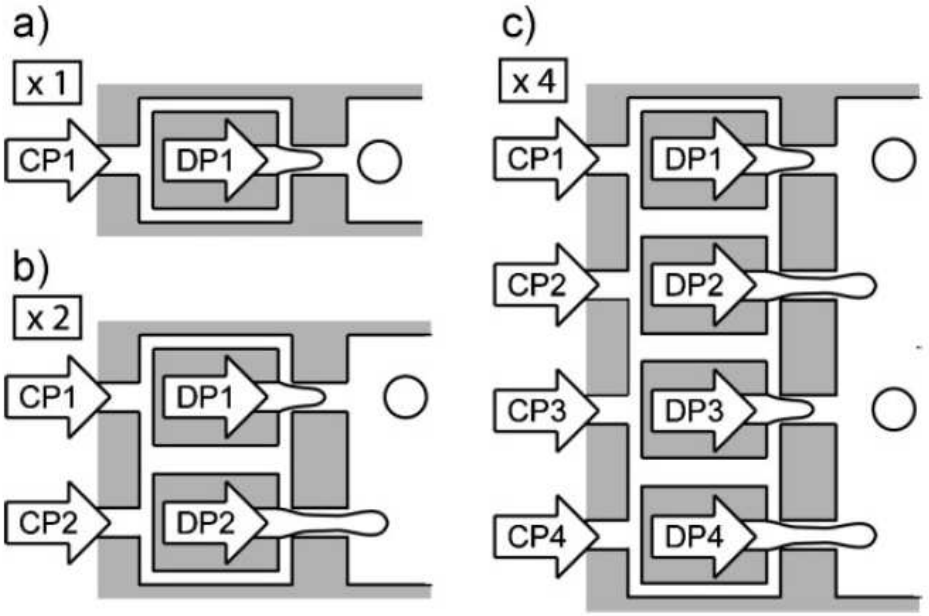

Fig. 125 Schematic illustration of the single (a) and coupled generators (b and c). The generators and feed with continuous phase (CP) and dispersed phase (DP), which was water or hexadecane and water or nitrogen. [17]

We studied formation of water droplets in the oil for one, two and four coupled generators for rate of flow as follows: Q_c=0.1, 0.3, 0.9 and 2.7 mL·h^{-1}. For each Q_c we adjusted the rate of flow of dispersed phase, i.e. water (Q_d) from the minimum value at which the formation of the droplets were possible, to a value at which the stream of water ceased to break-up in the orifice. Above the threshold value of Q_d the flow of water and hexadecane was laminar and droplets were no produced.

We observed that for a given value of Q_c the threshold value of Q_d was higher for a multi-orifice device than for a single-orifice device, e.g. for Q_c=0.3 mL·h^{-1} the threshold value Q_d≈0.32 mL·h^{-1} for a one-orifice system, whereas for a two-orifice system Q_d≈1.2 mL·h^{-1} and for four-orifice system Q_d≈2.4 mL h^{-1}.

The system with one generator gave droplets with diameter from 50 µm to several hundreds of micrometers. The sizes of droplets formed in this device increased with the increase of Q_d and decreased with increase of Q_c.

The system with two generators was similar to one-generator-system. The droplets were monodisperse and followed the same dependence of the rates of flow (i.e. Q_c and Q_d) as the single FF generator. There was no difference in the sizes of the droplets between these two systems.

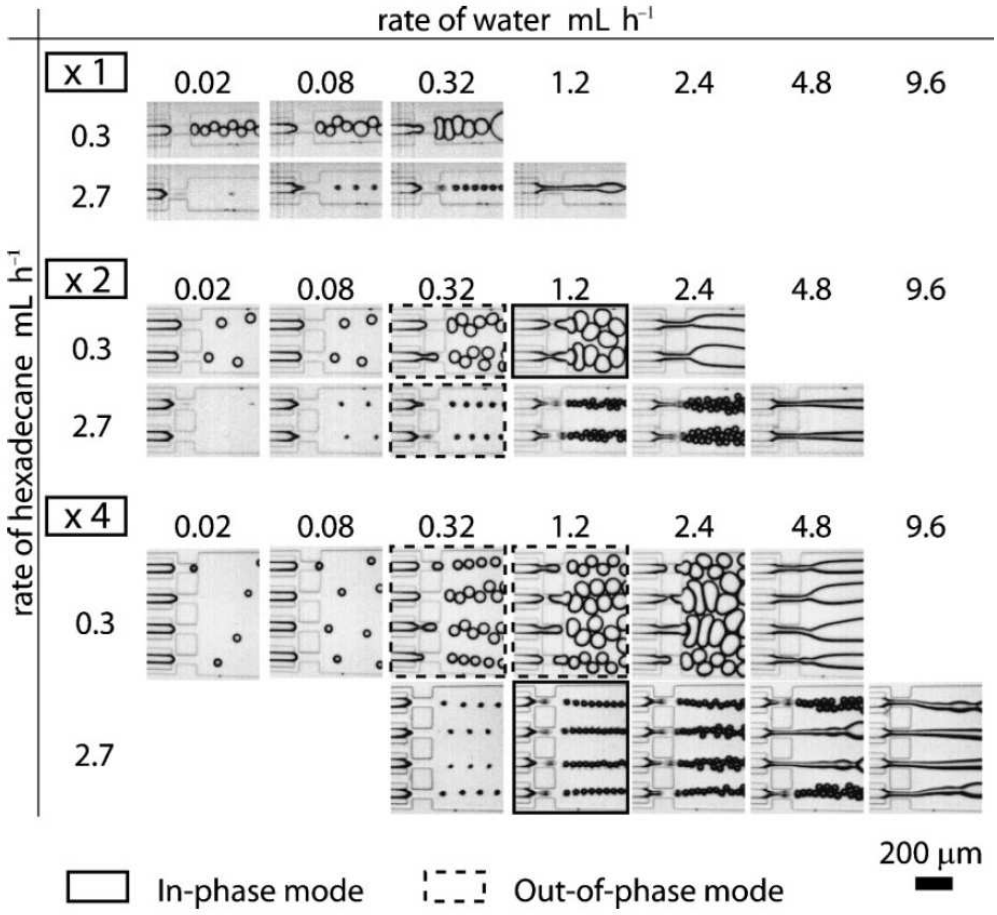

Fig. 126 Creating a water droplets in hexadecane in coupled FF generators. Pictures marked with solid rectangles represent a in-phase mode of operation of generators whereas a dashed rectangles represent an out-of-phase mode of generating of droplets. [17]

We observed a weak hydrodynamic coupling in system with two FF generators. It manifested in in-phase or out-of-phase generating of the droplets (see Fig. 126). In the in-phase mode the droplets were generated simultaneously, whereas in the out-of-phase mode they were created alternatively (see Fig. 126 for a rectangle with solid and dashed lines).

In the four FF generators system the inner orifices produced larger droplets than the outer orifices. The droplets produced in the four-orifice system were monodisperse as they were produced in inner or outer orifices. They showed a similar dependence of the size of

the droplets on the rates of the flow (Q_c and Q_d) for the single and two FF generator. In the four FF generators system we observed also in-phase and out-of-phase modes of operation. In the in-phase mode all orifices produce droplets simultaneously, whereas in the out-of-phase mode, the first and third orifice formed droplets simultaneously followed by the formation of droplets in the second and fourth orifice, followed by a repetition of this cycle (see Fig. 126, system x4, Q_c=0.3 and Q_d=1.2 mL h^{-1}).

3.4.1.9 CONCLUSIONS

Using the both liquid/gas and liquid/liquid systems we performed detailed experiments on single and coupled FF generators. We discovered that for fixed rates of flow the multi-orifice systems (two and four FF generators) can generate gas bubbles or water droplets in a wider range of the flow parameters, compared to the single-orifice system. The upper limit of the rate of flow of the dispersed phase—gas or liquid—was higher for coupled generators.

The formation of gas bubbles and tater droplets—coupled via the inlets of continuous fluid and common outlet—demonstrated a wide range of complex dynamics. For a gas/liquid system (not presented here yet described in details in [17]) each FF generator produced monodisperse or bidisperse bubbles. At high pressures all FF generators produced monodisperse bubbles. For a wide range of pressures the timing of breakup of bubbles in adjacent FF generators alternated. In contrary, for the liquid/liquid system each generator produced only monodisperse droplets over the entire range of rates of flow of liquids.

Our observations suggest that all the difference in the dynamics of formation droplets and bubbles in both systems is a result of the compressibility of the dispersed fluid (i.e. nitrogen and water).

In summary, it is possible to design and prepare a system with a multiple flow-focusing generators that are linked together via inlets or outlets, without considering the occurrence of unexpected dynamics, i.e. a case in which we observe an unstable formation of the droplets. Placement of a multiple FF generators in a single microfluidic chip can offer convenient means of constructing a microfluidic device with high throughput, e.g. for fast and efficient creating of emulsions.

3.4.2 ELECTROCOALESCENCE IN MICROSCALE: INFLUENCE OF VOLTAGE AND FREQUENCY

3.4.2.1 Introduction

Electrocoalescence (EC) is known for over 100 years: first patent for using EC in industry is dated back to 1908. [18] Since then EC is used for demulsification of crude oil [19] [20]. Applying high intensity electric field (EF) across electrodes immersed in a pipe or tank causes small droplets of water to merge due to polarization effects. Larger droplets sediment faster and settle down at the bottom of the tank. Electrocoalescence is an inexpensive, well known and efficient method and is thus widely used.

Electrocoalescence as a phenomenon is a process of merging water droplets by applying external electric field to a system with such an emulsion. Water molecule is in fact a dipole (see Fig. 127), thus is electric field will be aligned with electric field. Water droplet as a body, will be electrically charged, and surfaces of the droplets start to attract themselves. The forces are big to overcome the stabilization of the interface. The stabilization can be done by applying surfactants (i.e. during preparing emulsion) or in a natural way with amphiphilic molecules (i.e. during oil recovery). The precise mechanism and application of electrocoalescence is described below.

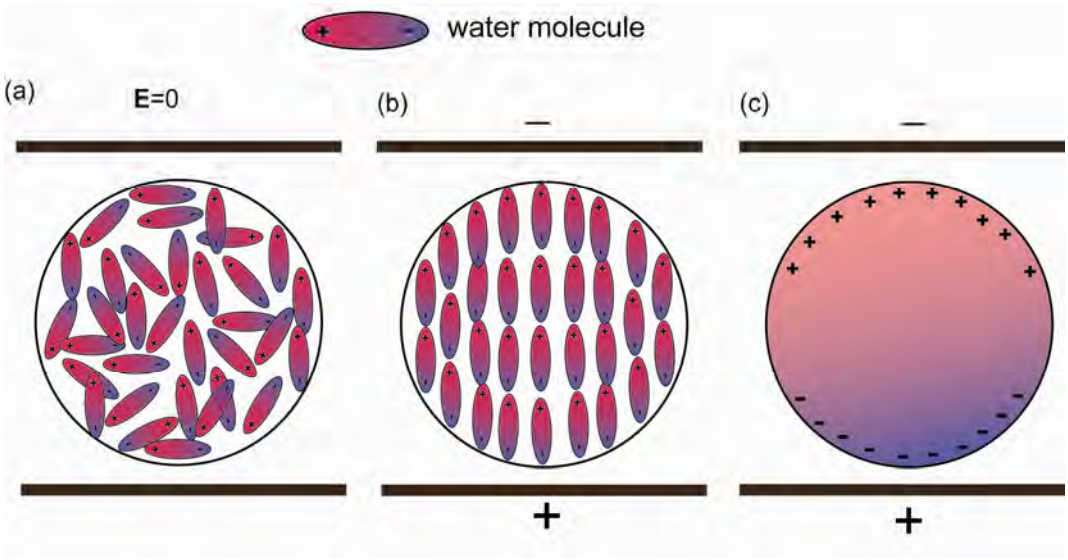

Fig. 127 Water droplet between electrodes without electric field (a) and between electrodes in external electric field (b, c). Water droplet placed between electrodes, but without electric field (a) shows no internal organization due to lack of the electric field. The molecules are arranged in a random way. Aligned molecules of water inside the droplet (b): the + and – inside the droplet attract themselves and neutralize each other. Non-neutralized charges are located at the interface. Effective bound charges at the surface (c).
These are only illustrative picture, there is no scale between the length of molecule of water and the diameter of water droplet.

3.4.2.2 Mechanism of coalescence

The coalescence between two water droplets immersed in an oil phase can be divided into three steps:

(i) approach of droplets,

(ii) draining of a thin film of the interfaces and

(iii) creation of a capillary bridge and merging of the two droplets.

Schematically these steps are shown in Fig. 128.

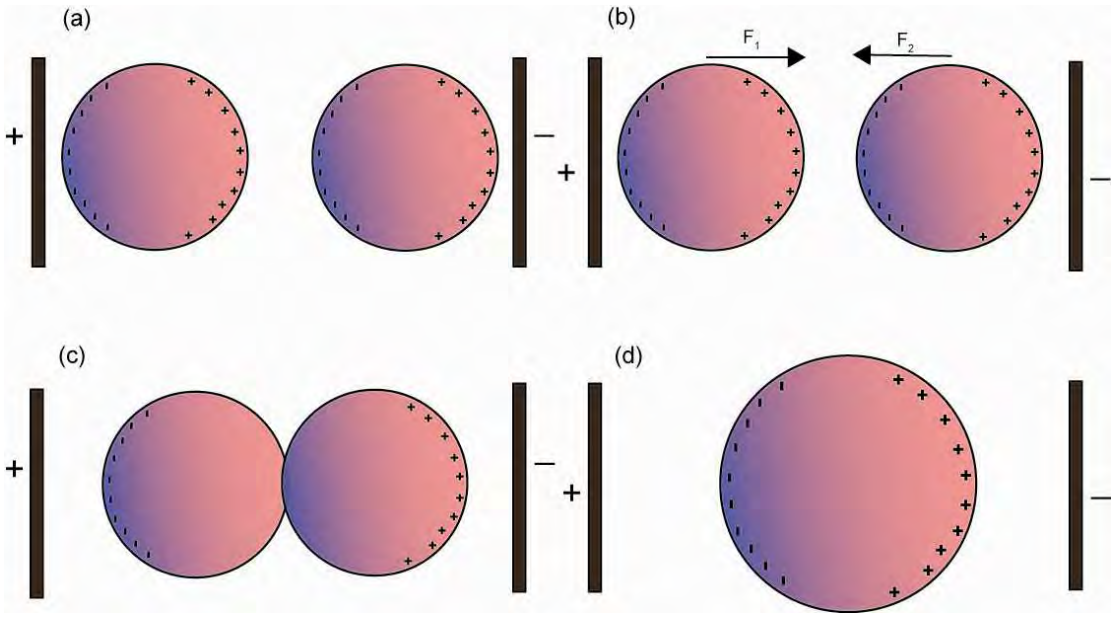

Fig. 128 Electrocoalescence of two water droplets in oil. (a) Two water droplets in external electric field become polarized and obtain a macroscopic charge, (b) positive and negative semi-spheres start to attract with the force $\vec{F}_1$ and $\vec{F}_2$, (c) at very small distance (a single nanometers) an instability occurs (i.e. mechanical or thermal), the thin oil film between water droplets breaks and the droplets start to merge, (d) the new, big droplet which is still in external electric field, is polarized and can attract another water droplet.

The first step is a hydrodynamicaly-driven slow process which ends with two separate droplets separated by thin oil film. After applying electric field the second step occurs. The droplets are getting close together due to different forces: it can be typical electrophoresis, but also dielectrophoresis (in a case when the electric field is disturbed and thus non-uniform) and different types of mechanical forces, i.e. due to stirring.

The result of getting closer is thinning of the oil film between the droplets. Capillary pressure and disjoining pressure are driving forces for this step, however it can be slowed down by the Marangoni effect is surfactant is present at the surface of the droplets.

The last step step of creation of a capillary bridge is controlled by thermal fluctuactions or mechanical disturbances (i.e. vibrations). As a result a new, big droplet is created. As it stays in electric field it is polarized as the smaller ones and the process of attracting and merging can be repeated.

3.4.2.3 Mechanism of electrocoalescence: types of polarization

All three steps can be accelerated by application of an EF that polarizes the droplets. Two interfaces when oppositely charged attract each other. This attraction provides additional force to drive the flow in the first two steps – in addition oppositely charged interfaces present a small energy to rupturing of the nanoscopic film of oil between them and to merging of the interfaces, even if there are protected with a surface active agents.

There are four basic molecular polarization mechanisms that can occur when electric field is applied to a dielectric:

i) electronic,
ii) atomic,
iii) orientational and
iv) interfacial polarization [21].

3.4.2.4 Mechanism of electrocoalescence: ionic polarizibility in water droplets

Apart from polarization described above, the water droplet can gain a charge from ions. When a drop of water containing ions is subjected to EF, at the poles of the droplet an induced charge occurs due to ions separation. Negative and positive ions separate due to their electrophoretic motion. To obtain macroscopic charge on the poles ions must separate to the Debye screening length (λ_D) or higher, which can be regulated by applying electric field of frequency lower than critical. Ions separate through electrophoretic motion where distance (d) scales linerly with time (t). As a result of this critical frquency f_{CR}—which is, in fact, a reciprocal of critical time—ions need to move over Debye screening length.

For frequencies higher than critical ions have no time to electrophoretically move over the Debye length and water droplet do not charge. In contrary, when frequency is lower than critical, electrostatically charged droplets start to attract each other and as a result accelerate EC process. Every critical frequency can be also corelated with a critical voltage (U_{CR}). Below that U_{CR} electric field is to small to electrophoretically move ions over to Debye length, i.e. polarise water droplet.

3.4.2.5 Influence of frequency on electrocoalescence process

Influence of AC frequency on EC process in microfluidic devices was recently examined by M. Zagnoni et al. [22] [23]. According to [22] there is general trend: the lower frequency is applied the lower is the critical voltage above EC occurs. In [23] authors showed that for frequencies between 10 Hz and 100 kHz no coalescence was observed below certain critical value of EF whereas for higher potentials EC occurred for frequencies up to 1 kHz. Authors in [24] did not observed any EC for frequencies higher than 100÷500 kHz.

Influence of the frequency on the efficiency process of the electrocoalescence was a subject of research in industry, where optimum frequencies have been reported [19] [20]. However, there is no agreement whether the existence of this optimal frequency is due to the limitation of power supply or is a result of the electromechanical relaxation (water droplet in strong oscillating EF elongate and contract as EF oscillates) of the droplet in EF.

According to review of J. Eow et al. [19] [20] magnitude of optimal frequency in one system range from 60 – 10 000 Hz, whereas in another it was 60 – 1000 Hz. When authors used pulsed DC electric field optimal frequency was less than 1 Hz and 15 Hz in a gas bubble-insulated electrode system. Optimal frequency in electro-coalescer with rotating cylindrical geometry was 25 Hz.

Apparently, there is no common value of optimal frequency for all that different systems: the magnitude of frequency depends on the type of electric field, arrangement of the electrodes, thickness and the type of insulation material [19] [20]. There is no agreement about origins of optimal frequency and its values. Yet, all authors show that optimal frequency has rather a low value and no one gave explanation about the mechanism of EC at this frequency.

3.4.2.6 Application of electrocoalescence in microfluidics

New interest in EC recently arose with the development of droplet microfluidics. Precise dosage and mixing of reagents is one of the prerequisites of Lab-on-a-Chip (LOC) technologies. Merging of droplets—in contrast to merging of continous streams—to combine reagents in situ on-chip is an attractive technology for avoidance of cross-contamination, thus electrocoalescence may be useful in systems applied to analytical chemistry, drug screening, protein crystallization and microbiology. Recent applications shows that EC can be used for incorporation of water droplets into continuous water stream [25], merging two water droplets [20] [25] [26] [27] [28] [29] [24], performing Polymerase Chain Reaction

(PCR) on-chip [30], studying bionetworks [31],studying breaking of emulsions [32] or using electrocoalescence as a tool for extraction at the microscale [33].

EC is convenient mechanism; it does not introduce chemical contaminations and can be easily controlled by the type (DC or AC) and value of applied voltage and frequency of the EF.

3.4.2.7 MATERIALS AND METHODS

I performed experiments on electrocoalescence in a stop-flow microfluidic device. This device comprises a flow-focusing junction for generation of monodisperse droplets and a Hele-Shaw-like outlet channel characterized by a large aspect ratio of width (5 mm) to height (100 µm). In order to ensure uniform height of the outlet channel, I used a bonding system that does not require intensive heating nor chemical modification of PC. Microfluidic device was micromachinned with a computer numerical controlled (CNC) milling machine (ErgWind, type MFG4025P) in 5 mm polycarbonate (PC). To join PC plates together I used 'press-lock' system: a shape around channels which was positive on the upper plate and negative on the bottom PC plate. After joining together and applying pressure both sides created microfluidic device.

Height and width of the channels in FFD was 100 µm, except the main channel—where electrocoalescence occurred—which was 5 mm wide. Two rows were milled—parallel to the main channel—to place two steel needles ca. 0.7 mm in diameter. They served as electrodes. The distance between the electrodes was set to 25 mm. These needles were co-planar and parallel with the outlet channel. To apply AC voltage I connected the system to a high voltage amplifier (Trek Inc., type 10/10B) controlled with a function generator (Tabor Electronics, type 5062) (see Fig. 129a). In every experiment I used square wave functions with duty cycle 50 %. Frequency (f) varied from single Hz to a 20 kHz (maximum value for a Trek amplifier), while the peak-to-peak voltage ($V_{p\text{-}p}$) varied from tens of volts to a 1 kV. I present the microfluidic device in Fig. 129b.

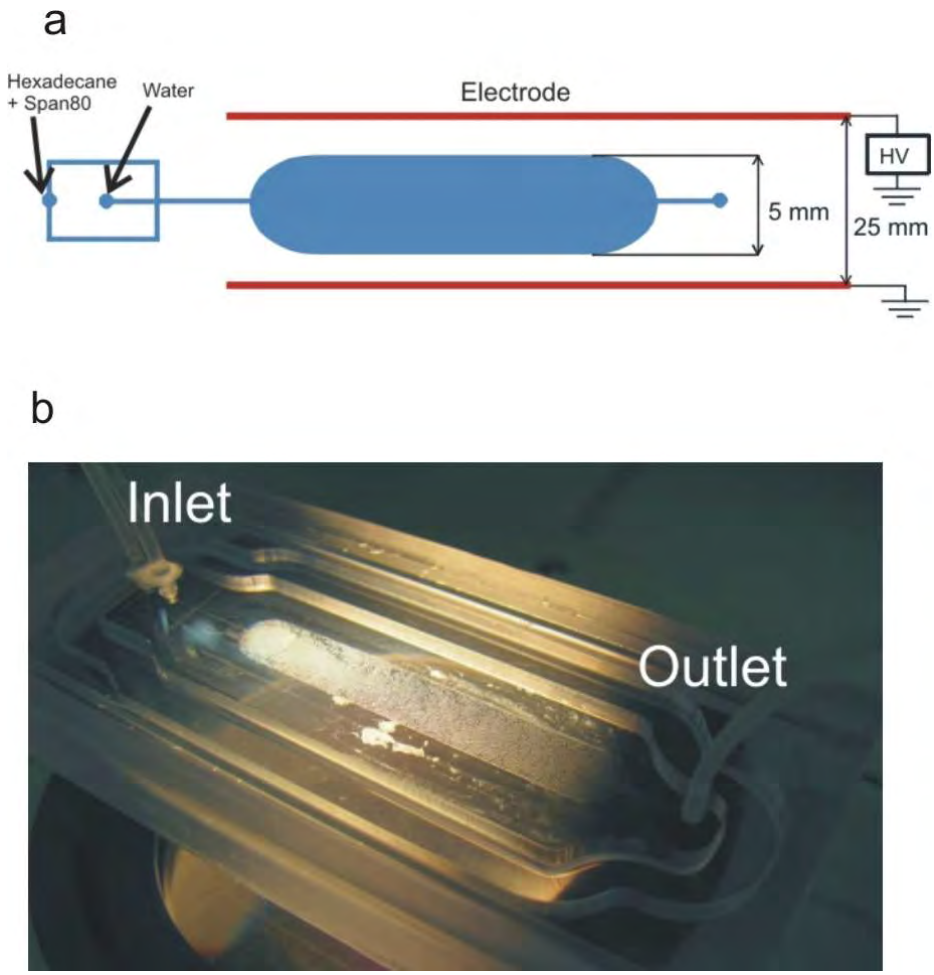

Fig. 129 The microfluidic system used in the experiments. (a) General scheme of the device. A Flow-focusing system was used to create a number of water droplets in the main channel. After filling the channel electric field was applied between two electrodes. One electrode is grounded whereas the second is connected to the HV amplifier. (b) A photo of the device. On the left two inlets are visible and on right one outlet. The main channel is filled with water droplets.

For the fluids I used hexadecane (Sigma, 99%) with 2 wt% Span 80 (Fluka) as the continuous phase and deionizer water (Millipore, 18 MΩ) as the dispersed phase. I used the same constant flow rate Q_{hex} = 0.6 ml·h^{-1} and Q_w = 1 ml·h^{-1} for hexadecane and water in all the experiments. These rates of the flow gave droplets with mean diameter 77 µm. In experiments with electrolyte solutions I added NaCl (Chempur, Poland) to the Millipore water. Programmable syringe pumps (Harvard Apparatus, type PHD2000) forced the flow of both fluids. I used fast camera (PHOTRON Fastcam 1024PCI, type 100k) mounted in stereoscope's port (NIKON, type SMZ1500) to record movies with a rate of 125 to 500 frames-per-second.

I monitored coalescence when the flow was stopped. To this end, I first allowed the microfluidic flow-focusing system to operate for 5 minutes to fill the outlet channel uniformly with an W/O emulsion (Fig. 130a). Then I stopped the flow, clamped the outlet and inlet and turned on the electric field. Afterwards I analyzed the movies frame-by-frame with MatLab & Image Analysis package. The scripts detected circular shape (water droplets) on the movies and irregular shapes after electrocoalescence process (see Fig. 130b).

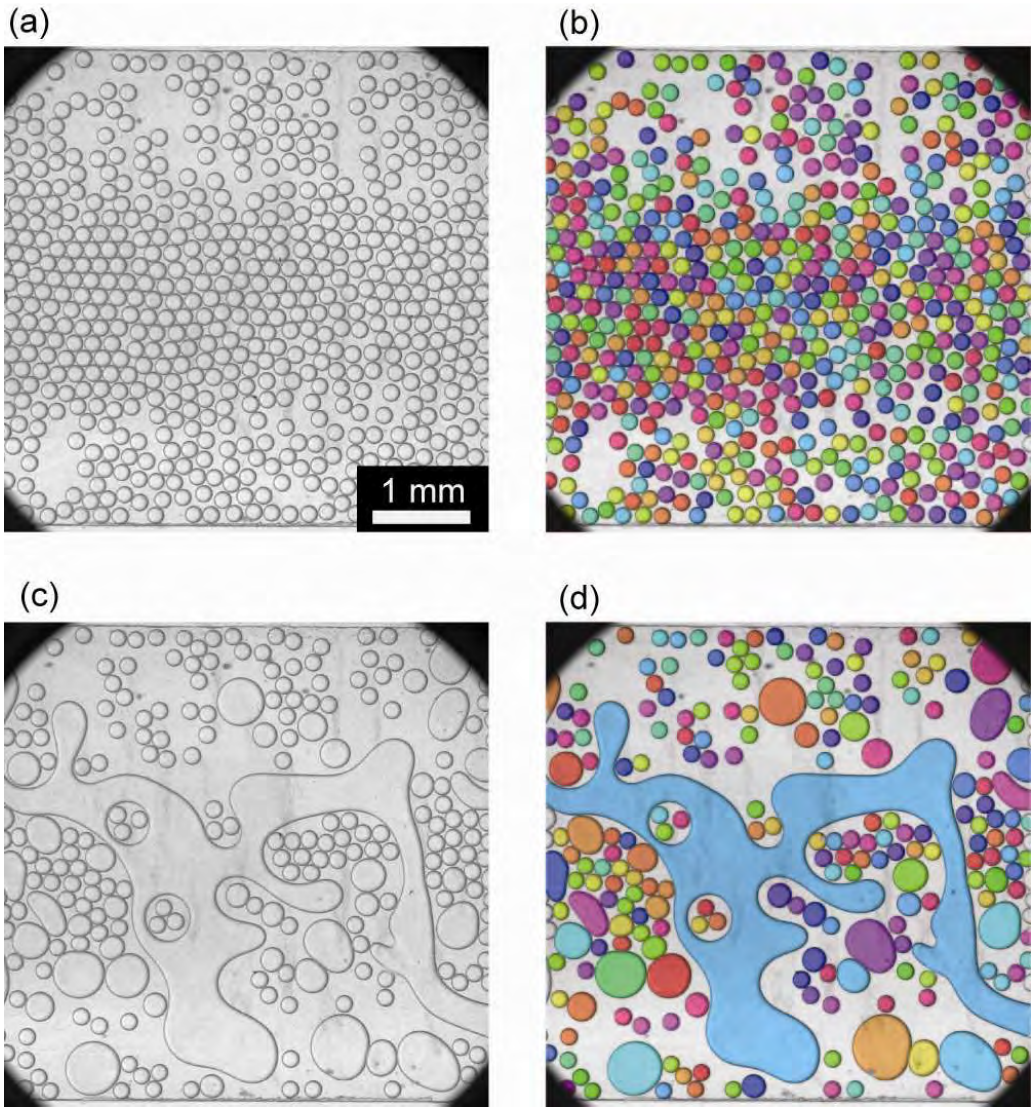

Fig. 130 Image analysis performed with MatLab software and Image Analysis package.
(a) raw picture made with Photron fast camera, without applied voltage and $t_0 = 0$ s,
(b) picture after image analysis, the contours of the droplets were detected and recognized object was filled in with a color,
(c) a raw picture for applied voltage and $t > t_0$ s,
(d) picture (c) after contour detection. Merged droplets are detected and filled in with colors.

3.4.2.8 RESULTS

3.4.2.8.1 Qualitative results

To obtain qualitative results I recorded videos with a fast camera and applied a MatLab software to analyze it frame-by-frame. I performed the experiments for two kinds of dispersed phases: a ultrapure Millipore water and ultrapure water with 10^{-4} M NaCl.

After applying EF to the system it is possible to distinguish three main behaviors:

i) no electrocoalescence (NEC),

ii) slow electrocoalescence (SEC) and

iii) fast electrocoalescence (FEC).

When there is no EF or its value is lower than critical U_{CR} there is no coalescence and we are in the NEC region. The droplets inside the channel are stable and I do not see—by naked eye or during MatLab analysis—any coalescence. Above the critical value there is SEC region. In that region the EC occurs slowly, i.e. I can see with a naked eye that single water droplets merge. When EF is gradually increased the parameters are proper for the FEC region. In that region EC is fast; with a naked eye I cannot distinguish how droplets merge. Only with the use of fast camera and high frames-per-second recording it is possible to analyze whole mechanism – two droplets merge together like in SEC region but the EC process propagate to next water droplets in the channel. For the highest value of EF almost all water droplets in the channel merge.

For qualitative analysis I conducted several experiments to asses voltage (U_{CR}) and frequency (f_{CR}) above which coalescence occurs, i.e. the water-in-oil emulsion (W/O) is not stable.

I conducted the experiment as follows: after I filled in channel with water droplets, I clamped the outlet and inlet to avoid movement inside the channel. Afterwards I applied electric field of constant frequency to the electrodes – I increased the electric field from tens of volts until coalescence of the droplets was visible. These observations I performed via stereoscope with naked eye. This method of assessing critical voltage is very simple, yet it gave insight in general influence of applied voltage, frequency and conductivity of the water on EC process. I conducted experiments for deionized water (Millipore) and different NaCl water solutions, concentrations ranged from 10^{-1} M to 10^{-6} M.

Herein, I present results from the experiments in Fig. 131. As a first (Fig. 131a) I demonstrate critical voltage as a function of the frequency with linear approximation to fit our data points and slop of each is plotted as a NaCl concentration in Fig. 131b. In Fig. 131a the

critical voltage grows monotonically with the critical frequency. The slope of the function (d*U*/d*f*) is plotted as a function of NaCl concentration and is presented in Fig. 131b.

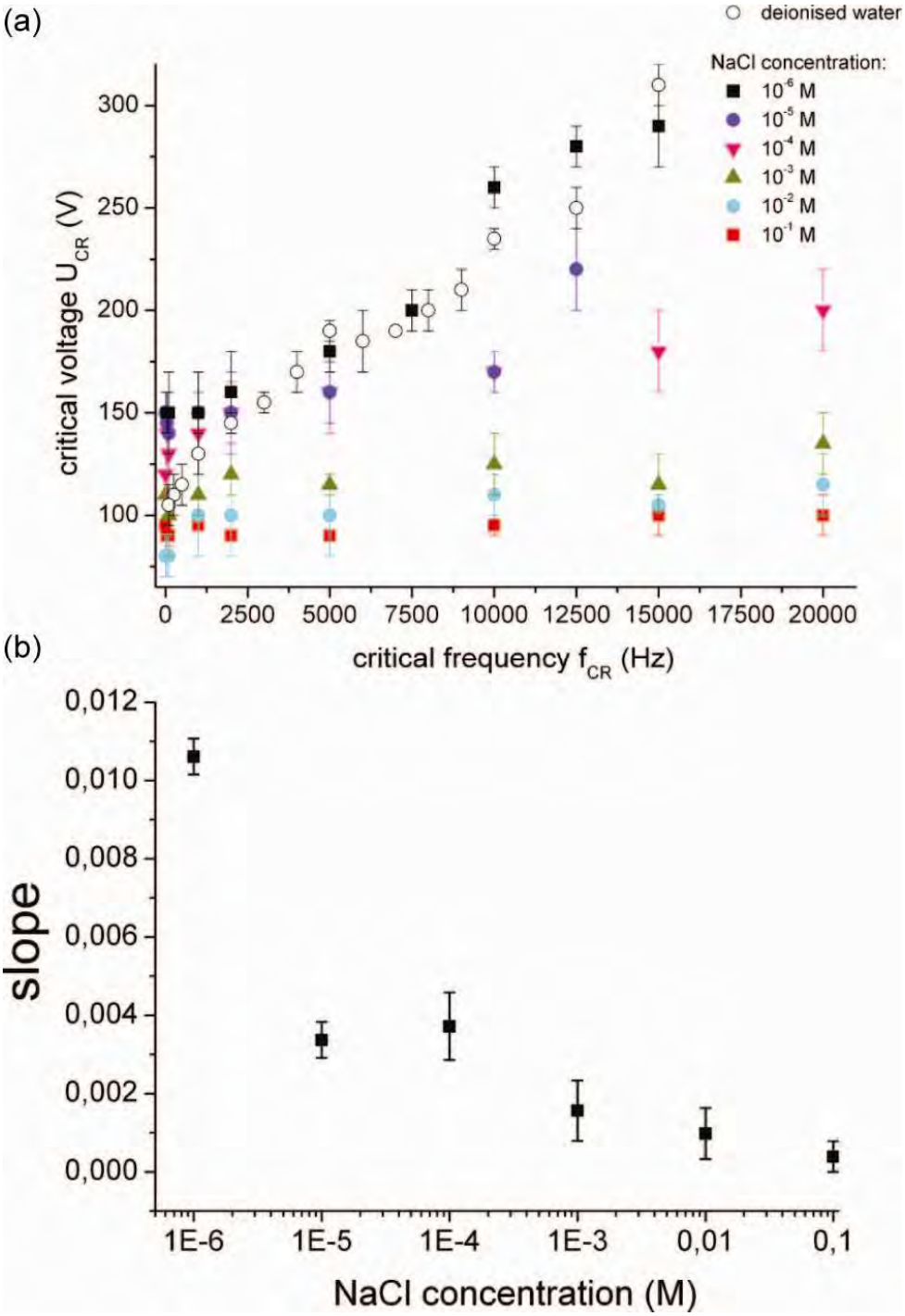

Fig. 131 Qualitative results for electrocoalescence process. (a) critical voltage (U_{CR}) as a function of frequency of electric field for ultra-pure water (Millipore) and electrolyte solution (10^{-4} M NaCl), (b) slope (dU_{CR}/df_{CR}) of the linear regression for critical voltage as a function of NaCl concentration.

The slope decrease with increasing NaCl concentration. The highest ion concentration—and as a result conductivity of the solution—the lowest electric field I applied to initiate coalescence process.

3.4.2.8.2 Quantitative results

To obtain quantitative results I used PHOTRON fast camera and MatLab Image Analysis toolbox. As in previous experiments I filled in microfluidic channel with water droplets, but instead of naked eye, I recorded movies for series of *U* and *f* for further analysis.

I performed experiments for ultrapure water (Millipore). I also chose 10^{-4} M NaCl concentration as a solution to asses influence of ions on the efficiency of the electrocoalescence process. MatLab scripts analyzed movies frame-by-frame afterwards. The routines detected and counted objects on every frame and colorized them as was presented in Fig. 130. I performed two experiments:

(i) for constant frequency and different voltage,

(ii) for constant voltage and different frequencies

3.4.2.8.3 Results for ultrapure Millipore water

The influence of frequency on a rate of electrocoalescence is presented in Fig. 132. Pictures present normalized number of the droplets as a function of time for constant voltage. Fig. 132a depicts 'low' frequencies: 1 Hz, 2 Hz, 5 Hz and 100 Hz. For *f*=1 Hz and *f*=2 Hz it is clearly visible that decreasing of the number of objects occurs when the polarization of the voltage is switched. Therefore *f*=5 Hz is a relatively high frequency (5 cycles in a second) so distinguishing the single changes of the objects is impossible. The highest frequency, *f*=100 Hz, gives the highest level of electrocoalescence.

For every frequency there is a final level of the coalesced objects, in Fig. 132 a 'plateau' region is existing. It is interesting that this 'plateau' level never reach zero, in the channel are always available (for *f*=100 Hz approx. 15%) water droplets who did not merge. The 'plateau' region on the plots and free water droplets are probably a result of screening of external electric field by a big water objects (a tens of droplets who merged into a single, big object). As water droplets merge and become bigger, they occupy a big part of the channel and as a result start to screen small droplets behind them.

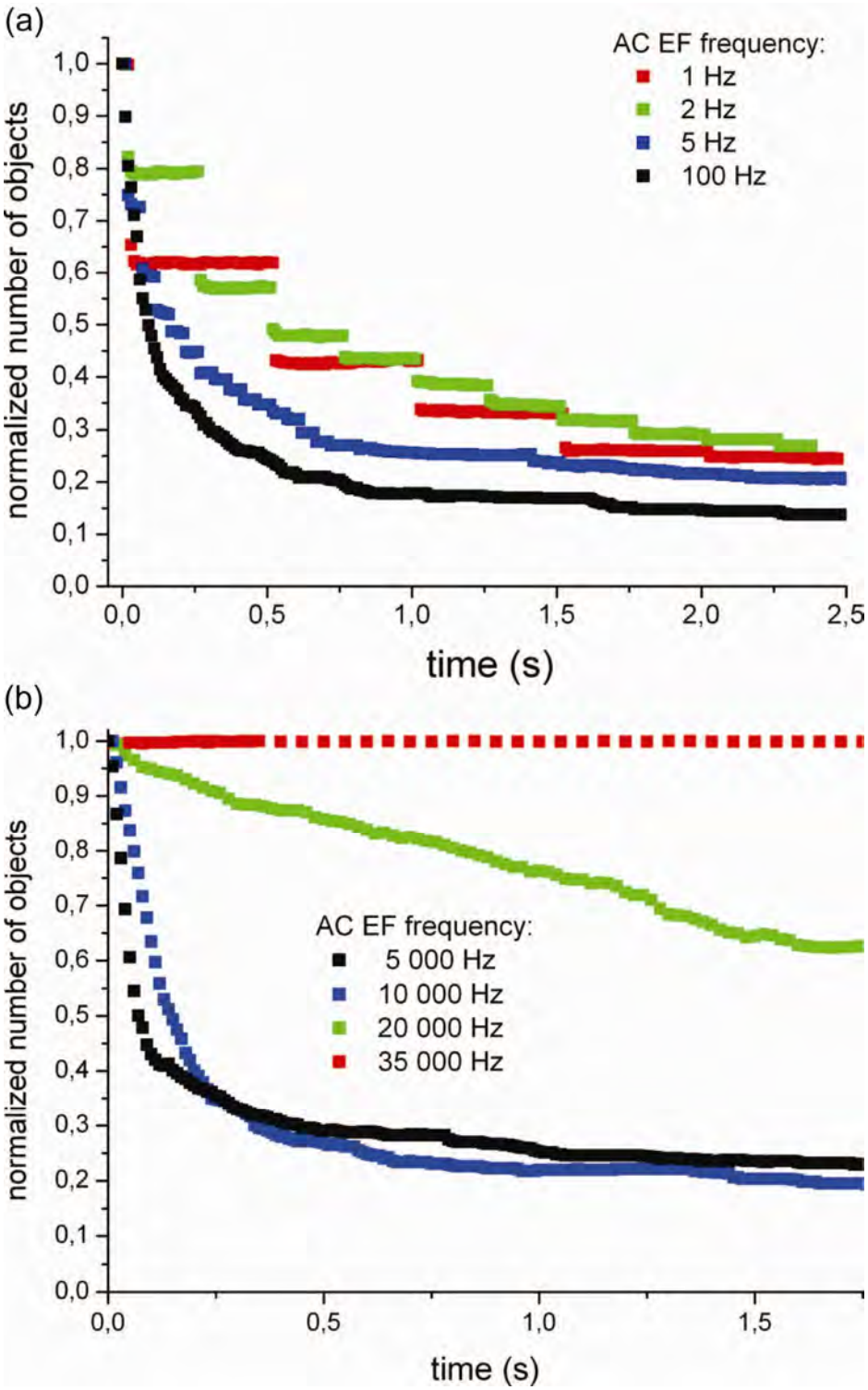

Fig. 132 Rate of electrocoalescence for droplets in microfluidic device. Dispersed phase is ultrapure water (Millipore). (a) Normalized number of objects as a function of time for low frequencies (1 Hz – 100 Hz). For 1 Hz and 2 Hz visible switching of polarization. (b) rate of electrocoalescence for high frequencies (5 000 Hz – 35 000 Hz). All results are taken for constant voltage *U*=500 V.

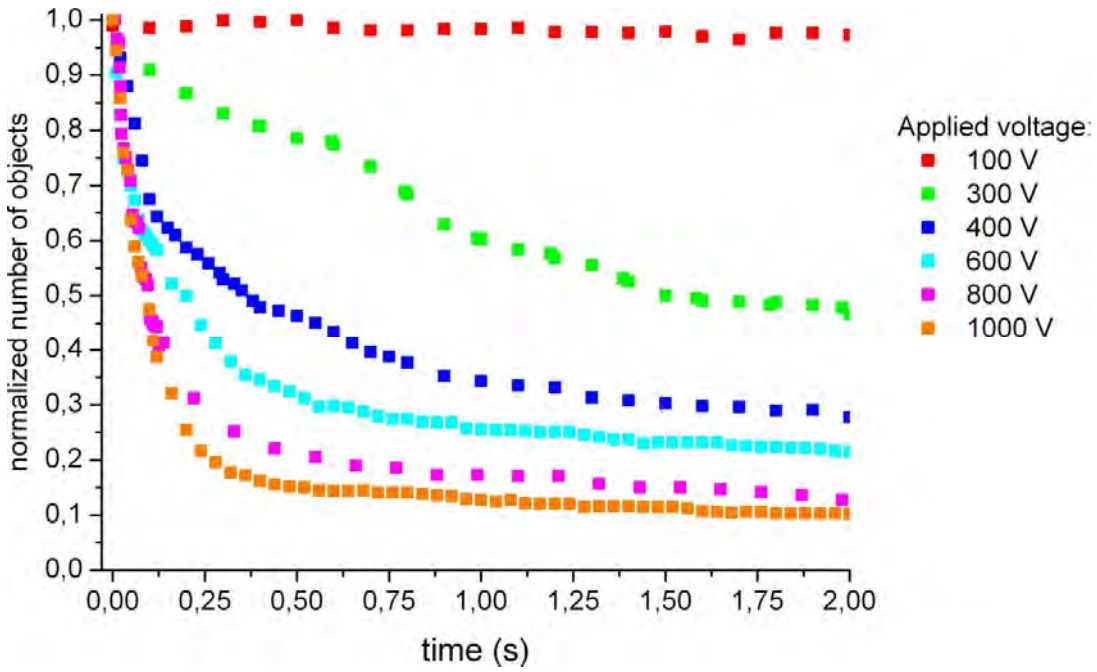

Fig. 133 Rate of electrocoalescence for ultrapure water and constant frequency *f*=20 Hz. Results for different voltage, from 100 V to 1000 V.

The influence of high frequency is presented on Fig. 132b. The results for 5 kHz and 10 kHz are quite similar. After fast decreasing of the water droplets in the beginning there is a clear plateau region, where approx. 20% of droplets did not merged. For 20 kHz shape of the plot is different, it is linear in all range of the time, i.e. the number of droplets which merge in a time unit is equal. Further increasing the frequency (35 kHz) caused that no electrocoalescence effect was observed. These experiments show that there is a critical frequency (approx. 25 kHz) for a pure water above the EC process disappear, i.e. the changes of external electric field are too fast to create a polarization of the water droplets.

The influence of applied voltage for a constant frequency (*f*=20 Hz) is presented in Fig. 133. For *U*=100 V there is no EC effect, the strength of electric field inside the channel is too small to polarize the droplets and accelerate EC process. For *U*=300V electrocoalescence process occurs and the dependency between normalized number of the objects and time is linear. The critical voltage for this frequency is probably around 200 V. Increasing the voltage shows that the higher applied voltage the more intense EC process: the intensity of EC process seems to scale like $\propto t^{-a}$. Above *U*=300V for each voltage there is a plateau region where there is no further coalescence of the droplets.

Qualitative results of electrocoalescence process are presented in Fig. 134, Fig. 135 and Fig. 136.

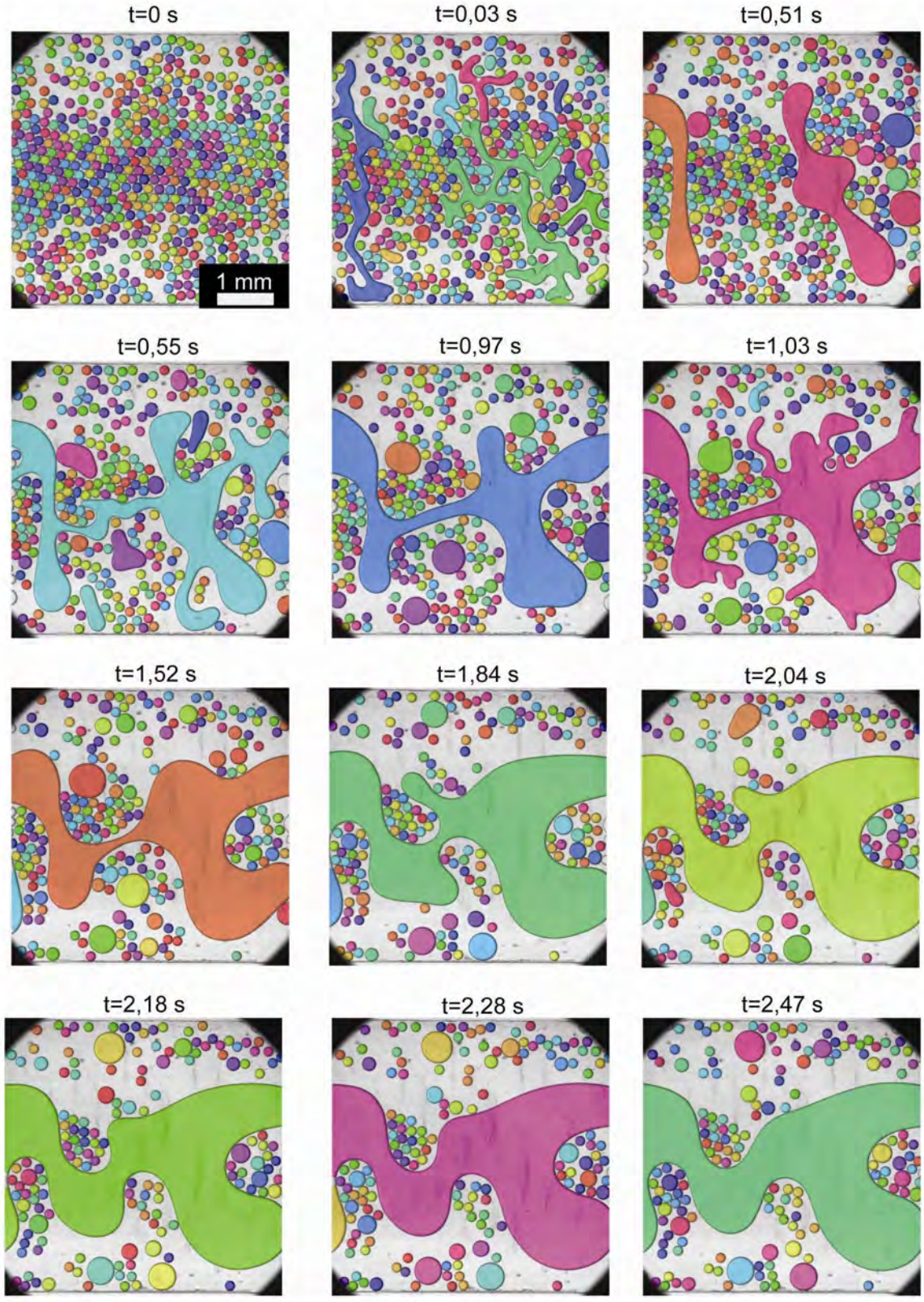

Fig. 134 Temporal dependency of the rate of electrocoalescence process for Millipore water. Video recorded for *U*=500V and frequency *f*=1 Hz. All images are after image analysis in MatLab software. After *t*=1.03 s there is no additional electrocoalescence process (a 'plateau' region).

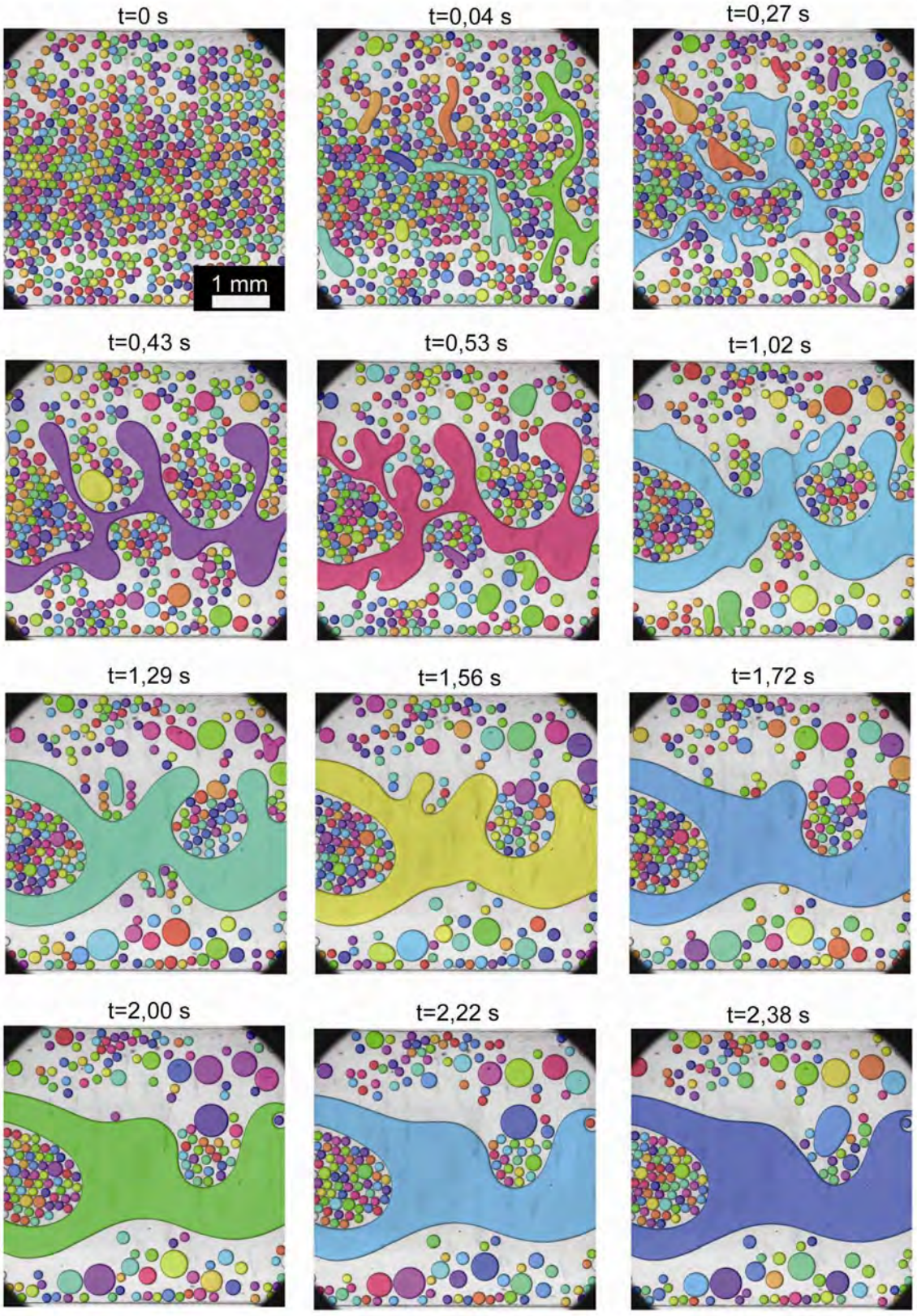

Fig. 135 Temporal dependency of the rate of electrocoalescence process for Millipore water. Video recorded for *U*=500V and frequency *f*=2 Hz. All images are after image analysis in MatLab software. After *t*=1.02 s there is no additional electrocoalescence process (a 'plateau' region).

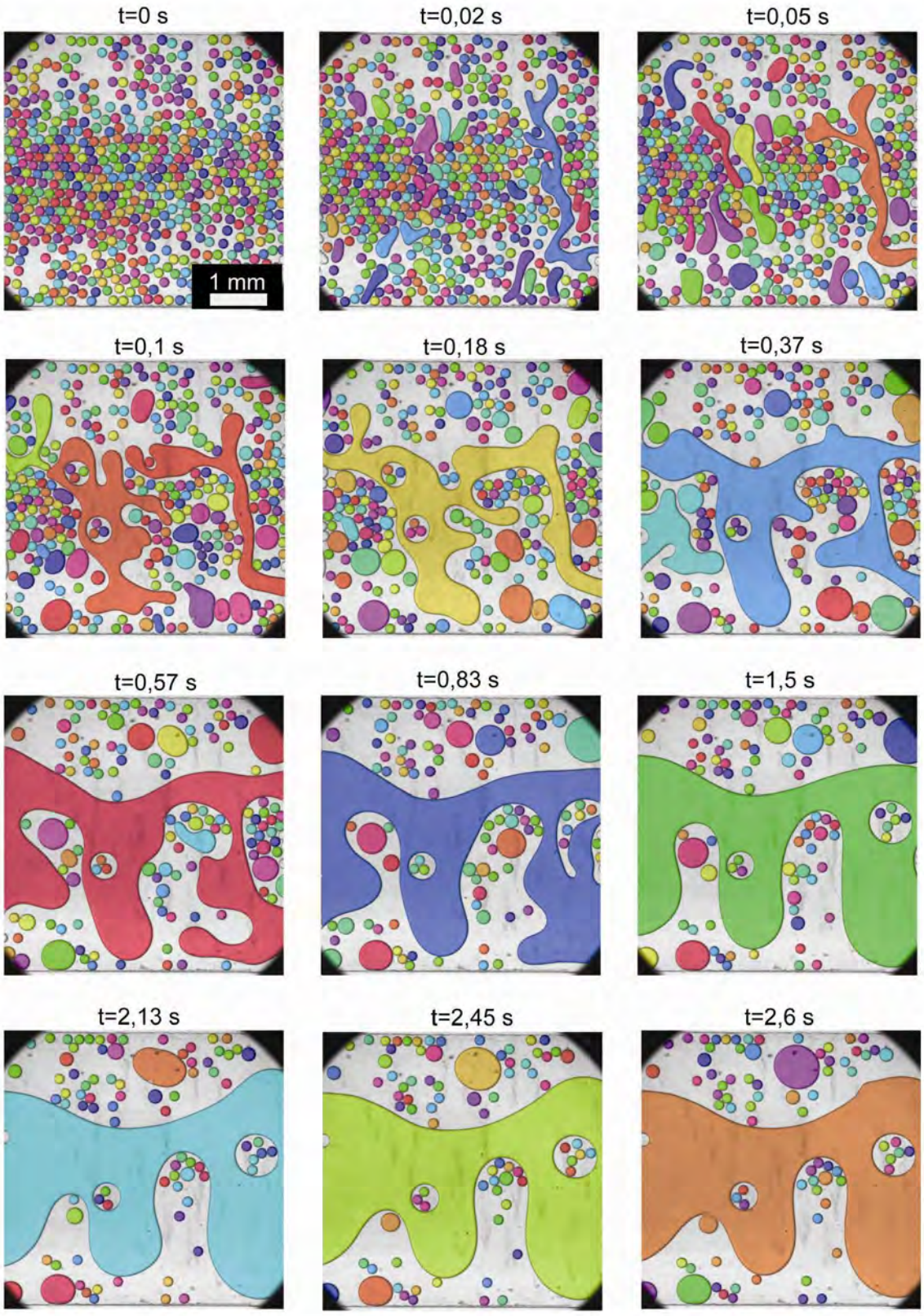

Fig. 136 Temporal dependency of the rate of electrocoalescence process for Millipore water. Video recorded for *U*=500V and frequency *f*=100 Hz. All images are after image analysis in MatLab software. After t=1.5 s there is no additional electrocoalescence process (a 'plateau' region).

They show a pictures of EC process after analysis in MatLab software. It is visible that for certain time the number of the objects do not change, yet the electric field is still working. On the plots (normalized number of objects versus time) it was visible as a “plateau” region.

3.4.2.8.4 Results for electrolyte solution

In this subchapter I present results from experiments with 10^{-4} M NaCl electrolyte solution. I plotted number of the objects found in every frame normalized by the number of the objects before coalescence (I called this ‘normalized number of objects’) as a function of applied voltage or frequency. To examine voltage and frequency influence on coalescence process I examined the time after 5% of the water droplets merged (or 95% was still randomly dispersed in the channel) and I called that time $t_{0,95}$, as shown in the Fig. 137.

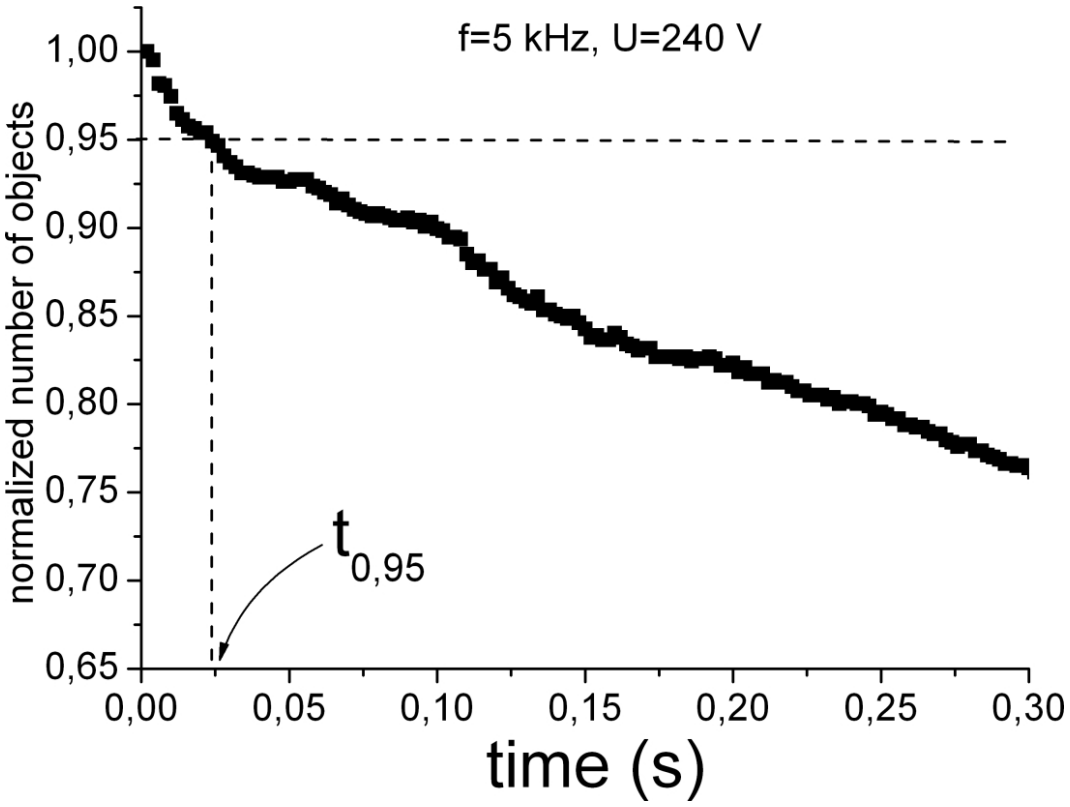

Fig. 137 Normalized number of objects as a function of time for *f*=5 kHz and *U*=240 V. In further analysis I discuss the time after 5% of total droplets in the channel coalesce or 95% is non-coalesced. I called that time $t_{0,95.}$

In Fig. 138a I plotted normalized number of objects as a function of time (t) for different frequencies and constant U_{CR} = 110 V.

In Fig. 138b I plotted the reciprocal of the $t_{0,95}$ as a function of frequency. In Fig. 138a it is clearly seen that coalescence intensity increase with frequency: the higher voltage frequency the faster is decreasing the number of the objects.

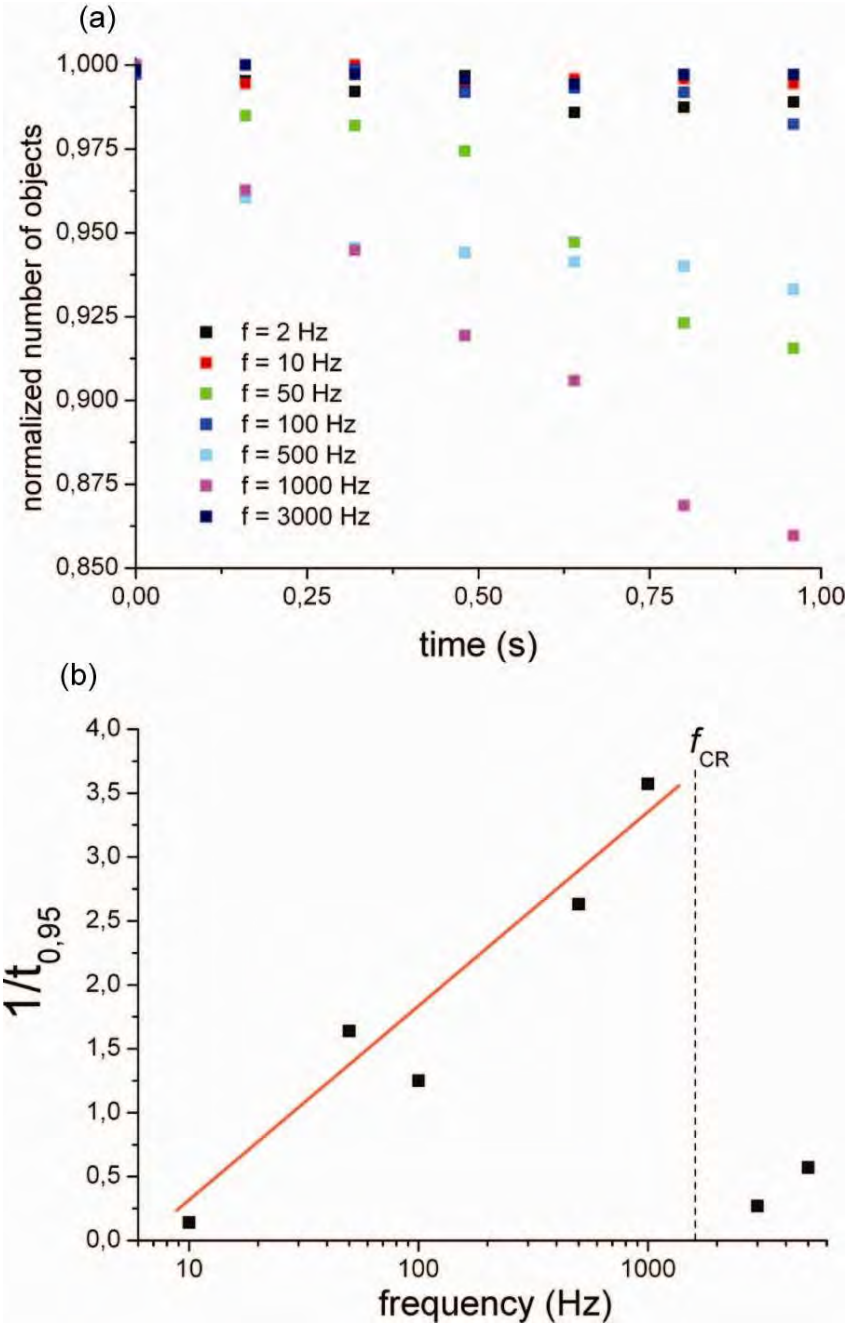

Fig. 138 Influence of the frequency on the electrocoalescence process. (a) Normalized number of objects as a function of time for a range of frequencies (from 2 Hz up to 5000 Hz) and for constant voltage U=110 V. (b) The reciprocal of $t_{0,95}$ as a function of frequency shows increasing rate of electrocoalescence process to critical frequency, above f_{CR} the rate decrease. The dependency between $(t_{0,95})^{-1}$ and frequency for $f<f_{CR}$ is linear.

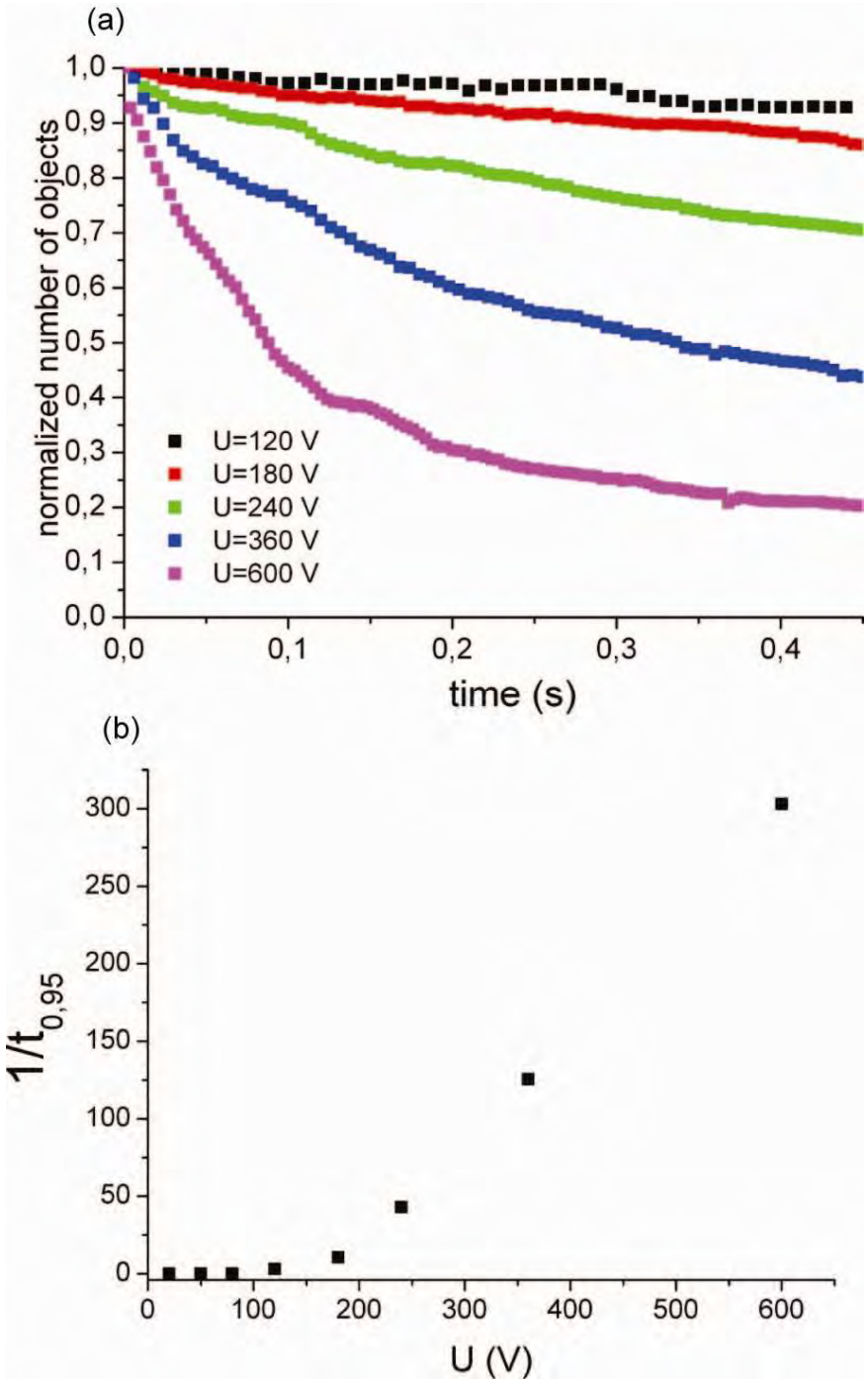

Fig. 139 Influence of applied voltage (U) on the rate of the electrocoalescence process (described as reciprocal of $t_{0,95}$). (a) When I increased the applied voltage, the rate of electrocoalescence also increased. (b) For voltage $U<U_{CR}$ the rate is relatively slow, after reaching the U_{CR} the rate is growing linearly.

In Fig. 138b I show that coalescence increase linearly with frequency till critical frequency (f_{CR}) what is in this case ca. 3 kHz. Above that f_{CR} intensity of the coalescence decreases.

In Fig. 139 I plotted number of the objects as a function of time for constant frequency (f = 5 kHz) and for voltages ranging from U = 120 V to U = 600 V.

The higher applied electric field the coalescence process is more effective, what can be clearly seen in Fig.139, where I plotted reciprocal of the $t_{0,95}$ versus voltage. Below certain critical voltage (U_{CR}) coalescence does not take place.

There is a sharp U_{CR} between stable region where coalescence do not occur and a region where EC takes place. Below that U_{CR} polarization force is too low to attract water droplets together or is too low to electrophoretically move ions over the Debye length.

I have found interesting that there is critical frequency f_{CR} above the electrocoalescence intensity decreases. I explain this phenomenon as follows.

Water droplets used in experiments contains ions Na^+ and Cl^-. Debye screening length (λ_D) in 10^{-4} NaCl solution is 30,4 nm, therefore ions have to separate for at least 30 nm to obtain macroscopic charge separation at the interface of water and oil. For frequencies below ca. 3 kHz distance that Cl^- ions made is higher than Debye length, whereas for frequencies above is lower than 30 nm (see Fig. 140).

The calculation from the Fig. 140 are in good agreement with observed dependence of $1/t_{0,95}$ versus time (Fig. 138). However in Fig. 138b it is shown that above 3 kHz there are points, what means that electrocoalescence occurs.

The explanation for this is that for electrocoalescence in microfluidic devices influence also several other factors like local arrangement of the droplets inside the channel, surface morphology (the channel has significant roughness due to finite diameter of the drill) and ‘turn-on effects’ (spikes) caused by HV amplifier. In experiments where I examined influence of NaCl concentration on the critical frequency I slowly increased voltage to avoid spikes.

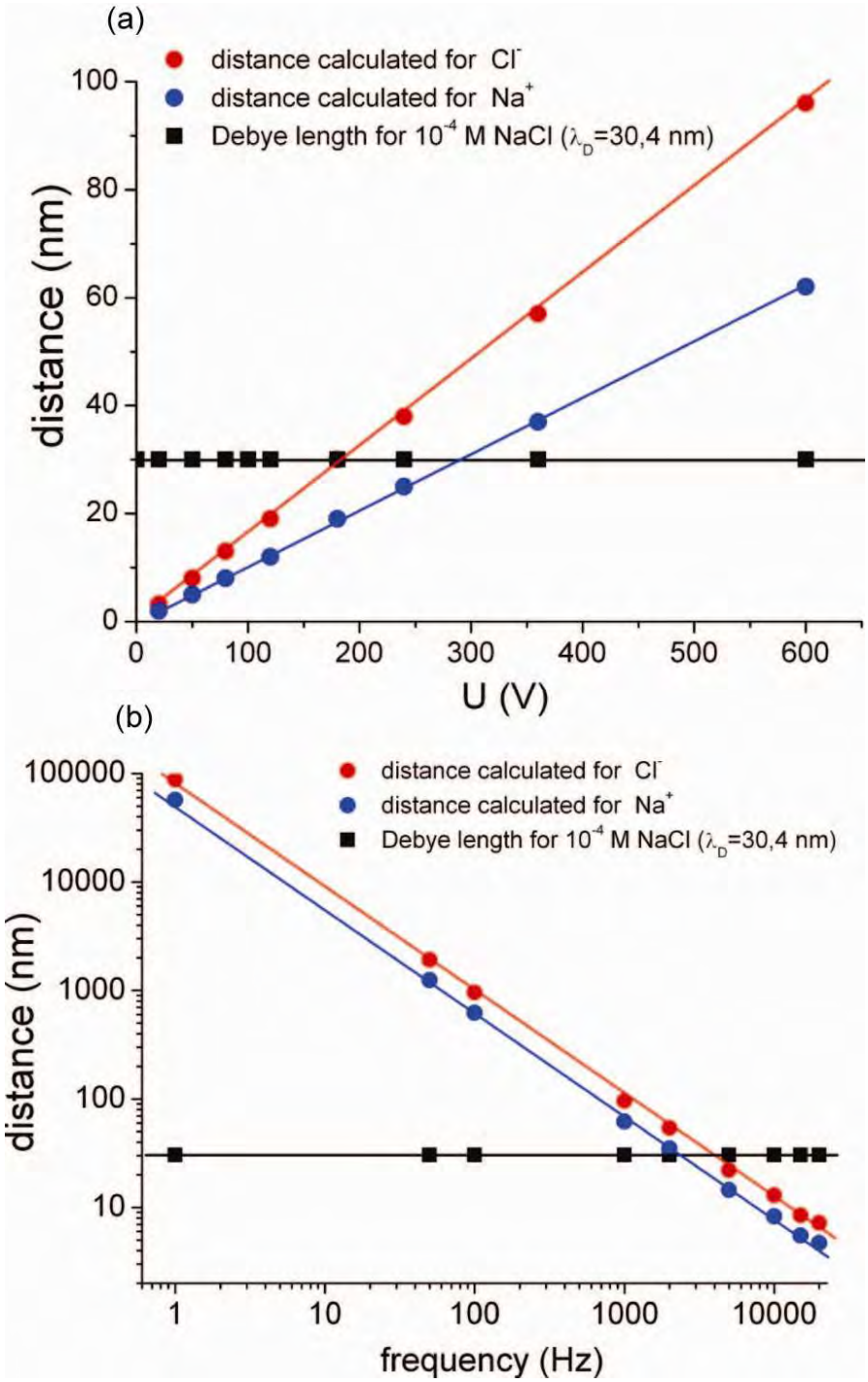

Fig. 140 Influence of applied voltage and frequency on electrocoalescence process. (a) distance of Na^+ and Cl^- ions calculated for known frequency, applied voltage and electrophoretic mobility. To polarize interface between water droplet and oil phase ions must separate over the Debye length (in this case ca. 30 nm). The separation occur for ca. *U*=180 V. For that voltage Cl^- ions separate over Debye length and increase rate of coalescence.
(b) For low frequencies the distance is higher than Debye length and the interface is polarized. As the frequency was increased, the separation distance decreased, till the critical frequency above the interface is not polarized due to ion separation.

3.4.2.9 SUMMARY

I proposed a simple and facile method for determination of the critical voltage (U_{CR}) and the critical frequency (f_{CR}) for electrocoalescence of water droplets in a microfluidic device. In contrary to other experiments I performed them in a stop-flow conditions to avoid hydrodynamic effects: shear stresses causes thinning of the oil film between water droplets and additionally accelerate the coalescence process.

I discovered that intensity of the electrocoalescence process—measured as the rate of decrease of the number of the droplets in time—depends on the applied electric field, which is in a good agreement with results from other experiments.

In literature several authors claim that there are optimal frequencies for EC process. However there is no agreement about the nature of this frequency. According to some authors AC or pulsed DC field can produce a vibration in the water droplet (droplet in external EF elongate and shrink after EF decreases), what can result in coalescence. The maximum intensity of drop vibration are at low frequencies, and vibration can disturb thin layer between water droplets thus can promote coalescence [19] [20] [34].

The investigations reported here give a new insights into behavior of water droplets in external EF at microscale. Using these experiments I showed that dynamic charge separation (dyCHASE) can influence the rate of electrocoalescence process. The parameters one can vary are: voltage, frequency and concentration of the ions.

As I demonstrated, dyCHASE phenomenon can be used not only for accelerating phase separation [35] or explaining the instabilities on the edge of free-standing smectic film [36] but also for explaining acceleration of the electrocoalescence process for low frequencies.

3.4.3 REFERENCES FOR CHAPTER 3.4

[1] J. C. McDonald, D. C. Duffy, J. R. Anderson, D. T. Chiu, H. Wu, O. J. A. Schueller, and G. M. Whitesides, Electrophoresis **21**, 27-40 (2000).
[2] Y. Xia and G. Whitesides, Annual Review of Materials Science **28**, 153-184 (1998).
[3] Y. Mourzina, D. Kalyagin, A. Steffen, and A. Offenhausser, Talanta **70**, 489-498 (2006).
[4] N. Nguyen, *Micromixers: Fundamentals, Design, and Fabrication* (William Andrew, 2008).
[5] C. Zhang, J. Xu, W. Ma, and W. Zheng, Biotechnology Advances **24**, 243-284 (2006).
[6] S. Cho, J. Godin, C. Chen, W. Qiao, H. Lee, and Y. Lo, Biomicrofluidics **4**, (2010).
[7] Y. Song, J. Hormes, and C. Kumar, Small **4**, 698-711 (2008).

[8] L. Y. Yeo, H. Chang, P. P. Y. Chan, and J. R. Friend, Small **7**, 12-48 (2011).
[9] N. Nguyen and S. T. Wereley, *Fundamentals And Applications of Microfluidics, Second Edition*, (Artech Print on Demand, 2006).
[10] J. D. Zahn, *Methods in Bioengineering: Biomicrofabrication and Biomicrofluidics*, 1st ed. (Artech House, 2009).
[11] D. Ogończyk, J. Węgrzyn, P. Jankowski, B. Dąbrowski, and P. Garstecki, Lab on a Chip **10**, 1324-1327 (2010).
[12] P. Jankowski, D. Ogonczyk, A. Kosinski, W. Lisowski, and P. Garstecki, Lab on a Chip **11**, 748-752 (2011).
[13] L. Derzsi, P. Jankowski, W. Lisowski, and P. Garstecki, Lab Chip **11**, 1151 (2011).
[14] S. Kakaç, B. Kosoy, D. Li, and A. Pramuanjaroenkij, *Microfluidics Based Microsystems: Fundamentals and Applications*, 1st ed. (Springer, 2010).
[15] A. M. Gañán-Calvo, Phys. Rev. Lett. **80**, 285 (1998).
[16] S. Anna, N. Bontoux, and H. Stone, Applied Physics Letters **82**, 364-366 (2003).
[17] M. Hashimoto, S. Shevkoplyas, B. Zasońska, T. Szymborski, P. Garstecki, and G. Whitesides, Small **4**, 1795-1805 (2008).
[18] J. Sjoblom, *Emulsions and Emulsion Stability: Surfactant Science Series/61*, 2nd ed. (CRC Press, 2005).
[19] J. Eow, M. Ghadiri, A. Sharif, and T. Williams, Chemical Engineering Journal **84**, 173-192 (2001).
[20] J. Eow and M. Ghadiri, Chemical Engineering Journal **85**, 357-368 (2002).
[21] H. Morgan and N. G. Green, *AC Electrokinetic: Colloids and Nanoparticles*, 1st ed. (Research Studies Press Ltd, 2002).
[22] M. Zagnoni and J. Cooper, Lab on a Chip **9**, 2652-2658 (2009).
[23] M. Zagnoni, C. Baroud, and J. Cooper, Physical Review E **80**, (2009).
[24] X. Niu, F. Gielen, A. deMello, and J. Edel, Analytical Chemistry **81**, 7321-7325 (2009).
[25] L. Fidalgo, G. Whyte, D. Bratton, C. Kaminski, C. Abell, and W. Huck, Angewandte Chemie-International Edition **47**, 2042-2045 (2008).
[26] K. Ahn, J. Agresti, H. Chong, M. Marquez, and D. Weitz, Applied Physics Letters **88**, (2006).
[27] W. Wang, C. Yang, and C. Li, Small **5**, 1149-1152 (2009).
[28] M. Chabert, K. Dorfman, and J. Viovy, Electrophoresis **26**, 3706-3715 (2005).
[29] C. Priest, S. Herminghaus, and R. Seemann, Applied Physics Letters **89**, (2006).
[30] L. Mazutis, A. Araghi, O. Miller, J. Baret, L. Frenz, A. Janoshazi, V. Taly, B. Miller, J. Hutchison, D. Link, A. Griffiths, and M. Ryckelynck, Analytical Chemistry **81**, 4813-4821 (2009).
[31] H. M. Evans, E. Surenjav, C. Priest, S. Herminghaus, R. Seemann, and T. Pfohl, Lab Chip **9**, 1933 (2009).
[32] A. R. Thiam, N. Bremond, and J. Bibette, Phys. Rev. Lett. **102**, 188304 (2009).
[33] J. Kralj, M. Schmidt, and K. Jensen, Lab on a Chip **5**, 531-535 (2005).
[34] J. Eow i M. Ghadiri, Colloids and Surfaces a-Physicochemical and Engineering Aspects **219**, 253-279 (2003).
[35] N. Ziębacz, S. Wieczorek, T. Szymborski, P. Garstecki, and R. Hołyst, Chemphyschem **10**, 2620-2622 (2009).
[36] T. Szymborski, O. Cybulski, I. Bownik, A. Żywociński, S. Wieczorek, M. Fiałkowski, R. Hołyst, and P. Garstecki, Soft Matter **5**, 2352-2360 (2009).

Chapter 4 Summary

In my PhD thesis I presented results of experiments performed for soft matter systems exposed to external electric fields. The experiments involved free-standing smectic films exposed to a radial, external AC electric field. The second set of experiments involved an oil in water emulsion in microfluidic device exposed to uniform AC electric field. For both cases I showed that AC electric field, for frequencies lower than critical, can separate ions on the interface (liquid crystal/air or water/oil) which results in electro-hydrodynamical instability (deformed LC islands) or polarization of the interface between water and oil (acceleration of the electrocoalescence process). Thus this phenomenon occurs in a highly dynamical conditions, it was called a dynamic charge separation – dyCHASE. Additionally, Natalia Zięba cz showed that the same mechanism can be applied in a different system, a mixture of polymer and liquid crystal. Charge separation in this case conduct to acceleration of phase separation.

Herein, I sum up the main results obtained in my PhD thesis:

i) Oscillating electric field introduce an electro-hydrodynamic instability which is visible as a periodical oscillations of the liquid crystalline island or a liquid crystalline meniscus. The mechanism is connected with the separation of ions (ionic impurities or artificially introduced ions) and macroscopic charging of the border of the island or meniscus. Due to highly dynamical process this phenomenon was called 'dynamic charge separation' or dyCHASE.

ii) There exist a sharp critical frequency f_{CR}: the process of deformation occurs only at frequencies lower than the critical value. I connected this critical frequency with the time needed to separate ions over the Debye screening length. For the frequency of oscillation equal or lower than critical ions separate over the Debye length thus they charge the interface of liquid crystal/air, liquid crystal/polymer or water/oil.

iii) The electro-hydrodynamical (EHD) model compared with the numerical data from experiment reveled that only three main forces are dominant in the instability: electric force F_e (which is also a driving force for the deformations), hydrodynamic resistance

force F_μ and line tension force F_σ. The inertia force, which was taken into account at the beginning, was omitted due to its small value (ca. 3%) in the optimal point A_{opt}.

iv) Using the EHD model and results from experiments it was possible to determine the value of line tension. Analysis of the single movie showed that line tension is decreasing as the length of arm is increasing. The value of line tension for every experiment (i.e. single movie) calculated for A_{opt} and plotted as a function of arm's length gave also a decreasing tendency. I connect this decreasing with the dissipation of the energy of the dislocation line. These values, however, lie in the order of magnitude of results obtained by other authors in different type of experiments.

v) With the use of EHD model it was possible to calculate (for a single arm and a single layer of molecules of liquid crystal) the induced charge Q. Analysis of single movies showed that induced charge is larger for a system doped with organic salt. The mean value of charge Q for a series of movies, for different addition of salt showed that increasing salt concentration increase also an induced charge.

vi) The experiments for a mixture of polymer/liquid crystal performed by Natalia Ziębacz indicate that dynamic charge separation is responsible for accelerating of phase separation process. The mechanism works regardless of type of liquid crystal or polymer matrix. The most striking observation was that the critical frequency f_{CR} above which no acceleration of phase separation was observed. The critical frequency in that experiment was f_{CR}≈25 Hz, what is in order of magnitude of frequencies observed in experiments with free-standing smectic films. Moreover, addition of the organic salt increased the acceleration process, which is in a good agreement with our model where the ions are responsible for the induced charge. Also, Natalia Ziębacz conducted experiment with DC electric field. The experiment gave similar results line in a FSSF pierced by a needle: the previously obtained domains of LC were destroyed.

vii) The last part of this thesis was to apply (and verify) the dyCHASE mechanism in a microfluidic system – a channel filled with water droplets. The results showed that increase the frequency of the EF increase the acceleration rate of the electrocoalescence process, up to a critical frequency f_{CR}, above which the rate is decreasing. For low frequencies ion separate over the Debye length thus polarize the

interface of water and oil. This polarization leads to electrostatic attraction of water droplets and accelerating of the electro-coalescence process.

In summary, the results presented in this thesis form a basis for interesting new developments of vistas to control non-equilibrium processes in soft matter systems with the use of oscillating electric fields.